

1994

Directional Wave Spectra using an Acoustic Doppler Current Profiler

William T. Stockhausen
College of William and Mary - Virginia Institute of Marine Science

Follow this and additional works at: <https://scholarworks.wm.edu/etd>



Part of the [Ocean Engineering Commons](#), and the [Oceanography Commons](#)

Recommended Citation

Stockhausen, William T., "Directional Wave Spectra using an Acoustic Doppler Current Profiler" (1994). *Dissertations, Theses, and Masters Projects*. Paper 1539617724. <https://dx.doi.org/doi:10.25773/v5-1w04-sg93>

This Thesis is brought to you for free and open access by the Theses, Dissertations, & Master Projects at W&M ScholarWorks. It has been accepted for inclusion in Dissertations, Theses, and Masters Projects by an authorized administrator of W&M ScholarWorks. For more information, please contact scholarworks@wm.edu.

**DIRECTIONAL WAVE SPECTRA
USING AN
ACOUSTIC DOPPLER CURRENT PROFILER**

**A Thesis
Presented to
The Faculty of the School of Marine Science
The College of William and Mary in Virginia**

**In Partial Fulfillment
Of the Requirements for the Degree of
Master of Arts**

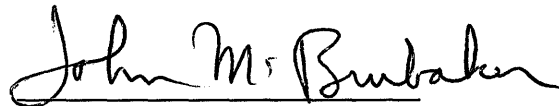
**by
William T. Stockhausen
1994**

This thesis is submitted in partial fulfillment of
the requirements of the degree of

Master of Arts

William T. Stockhausen

Approved, December 1993




John M. Brubaker, Ph.D.

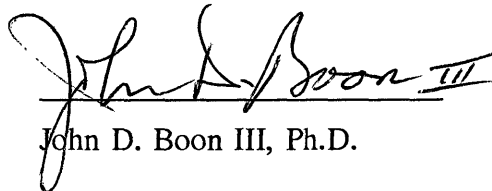
Committee Chairman / Advisor



Evon P. Ruzecki, Ph.D.



L. Donelson Wright, Ph.D.



John D. Boon III, Ph.D.



Leonard W. Haas, Ph.D.

DEDICATION

To my best friend, Victoria Farrington, whom I love dearly.

TABLE OF CONTENTS

	page
ACKNOWLEDGMENTS	vii
LIST OF TABLES	viii
LIST OF FIGURES	x
ABSTRACT	xix
1. INTRODUCTION	2
2. LITERATURE REVIEW	5
2.1 Instruments for directional wave spectra	7
2.2 Approaches to directional spectra estimation	15
Point estimation approaches	16
Function estimation approaches	23
3. ADCP OVERVIEW	33
3.1 Instrument description	33
3.2 ADCP directional wave spectra	36
3.3 ADCP sensitivity criteria	41
3.4 Statistical variability	45
4. DATA COLLECTION	53
4.1 Site description	53
4.2 Linear Array description	54
4.3 ADCP deployment	55

5. DATA PROCESSING	67
5.1 Linear Array processing	67
5.2 ADCP Data Processing	68
6. RESULTS PRIOR TO DIRECTIONAL SPECTRA	75
6.1 Mean observables	75
6.2 Time domain results	76
6.3 Cross spectra results	77
6.4 Nondirectional wave spectra results	79
7. DIRECTIONAL SPECTRA RESULTS AND ANALYSIS	97
7.1 Directional wave spectra results	97
7.2 Nondirectional wave frequency spectra results	100
7.3 Radiation stress angle	101
7.4 Mean wave direction	102
7.5 Directional width	102
7.6 Frequency-integrated directional spectra	104
7.7 H_{mo} and $\alpha_{xy,T}$	104
8. DISCUSSION	154
8.1 Analysis of ADCP autospectra-derived nondirectional wave spectra	155
8.2 Analysis of nondirectional wave spectra from ADCP directional spectra	157
9. SUMMARY AND CONCLUSION	168
APPENDIX A:	
DIRECTIONAL WAVE SPECTRA FOR SURFACE GRAVITY WAVES	170
A.1 Small Amplitude Surface Gravity Wave Theory	171
A.2 Linear Wave Spectrum Relationships	178

APPENDIX B: ADCP ORIENTATION	183
LITERATURE CITED	187
VITA	193

ACKNOWLEDGMENTS

This project would not have been possible without the unflagging help of my major professor, Dr. John Brubaker. John remained enthusiastic about this project from my first suggestion to its completion. He also always listened patiently to all my ideas (not necessarily an easy thing) and was primarily responsible for arranging the field deployment described herein. In this latter regard, I would also like to thank the personnel of the US Army Corps of Engineers Waterways Experiment Station Coastal Engineering Research Center Field Research Facility (FRF) at Duck, NC, particularly William Birkmeier, who allowed us to deploy the VIMS ADCP within the FRF pressure gage linear array and facilitated this deployment by letting us use the amphibious "LARC" at no cost. Tim Shannon, Danny Gouge, and Bob Gammisch at VIMS deserve thanks for participating in the deployment and retrieval of the instrument. Tim deserves an extra thanks for his design and construction of the cage in which the ADCP was deployed. In regard to data processing and analysis, I would like to extend my thanks to Dr. Charles Long at the FRF for providing the Linear Array directional wave spectra for comparison with the ADCP results. I would also like to thank the members of my committee (Dr.s Don Wright, Evon Ruzecki, John Boon, Larry Haas) for their help and support. Don Wright deserves special thanks for supporting some of the travel costs incurred during this project. Finally, Don and Dr. Al Kuo deserve thanks for supporting myself and this project during their tenures as chairman of the Physical Sciences department.

Finally, I'd like to thank my friend Aaron Adams for helping to round out my Marine Science education by giving me the chance to really get wet and do some biologically- and fisheries-oriented work with him.

LIST OF TABLES

	page
Table 3-1 ADCP operating parameters.	47
Table 4-1 ADCP initial and final deployment characteristics.	58
Table 4-2 ADCP data collected at US Army WES CERC FRF, Duck, North Carolina. P/E = # of pings per ensemble.	59
Table 4-3 ADCP configuration parameters for 6 pings/ensemble wave data collection. Parameters for which default values are used are not listed.	60
Table 4-4 Data intervals used for directional spectra estimation. ΔT = ADCP - LA start time.	61
Table 6-1 Data intervals used for directional spectra estimation. ΔT = ADCP - LA start time.	80
Table 6.1-1 Mean value of different observables for the data sets. Wind and current directions are relative to the wave coordinate system described in fig. 4-2. Headings are uncorrected for local magnetic deviation ($10^\circ W$).	81
Table 6.2-1 Case 1: ADCP Doppler velocity statistics. * = skew, kurtosis values significantly different from zero ($p < 0.01$).	82
Table 6.2-2 Case 2: ADCP Doppler velocity statistics. * = skew, kurtosis values significantly different from zero ($p < 0.01$).	83
Table 6.2-3 Case 3: ADCP Doppler velocity statistics. * = skew, kurtosis values significantly different from zero ($p < 0.01$).	84
Table 6.2-4 Case 4: ADCP Doppler velocity statistics. * = skew, kurtosis values significantly different from zero ($p < 0.01$).	85
Table 6.2-5 Case 5: ADCP Doppler velocity statistics. * = skew, kurtosis values significantly different from zero ($p < 0.01$).	86
Table 6.2-6 Case 6: ADCP Doppler velocity statistics. * = skew, kurtosis values significantly different from zero ($p < 0.01$).	87
Table 6.3-1 ADCP noise spectral densities from autospectra of bin 1.	88
Table 7.1-1 Case 1: IMLE directional spectra results.	109
Table 7.1-2 Case 2: IMLE directional spectra results.	113

Table 7.1-3 Case 3: IMLE directional spectra results.	117
Table 7.1-4 Case 4: IMLE directional spectra results.	121
Table 7.1-5 Case 5: IMLE directional spectra results.	125
Table 7.1-6 Case 6: IMLE directional spectra results.	129

LIST OF FIGURES

	page
Figure 2-1 Resolution functions for PRH buoy. 1: uniform weighting. 2: weighting for non-negative spectral estimate suggested by Longuet-Higgins, <i>et al.</i> (1963).	30
Figure 2-2 Resolution functions for a cloverleaf buoy. 1: uniform weighting. 2: weighting suggested by Cartwright and Smith (1964) to reduce negative sidelobe energy.	30
Figure 2-3 Attenuation of horizontal orbital velocity or perturbation pressure with depth. Plotted for values of $z/H = 0.1, 0.3, 0.5, 0.7, 0.9$	31
Figure 2-4 Attenuation of vertical orbital velocity with depth. Plotted for values of $z/H = 0.1, 0.3, 0.5, 0.7, 0.9$	31
Figure 2-5 Comparison of estimated waveheight spectrum for PRH buoy data. Spectra are: 1) extended MLE approach, 2) truncated Fourier series approach, 3) true spectrum.	32
Figure 2-6 Comparison of estimated waveheight spectrum for PRH buoy data. Spectra are: 1) extended MLE approach, 2) truncated Fourier series approach, 3) true spectrum.	32
Figure 3-1 Sketch of ADCP instrument.	48
Figure 3-2 Range-time sampling characteristics for ADCP.	48
Figure 3-3 MLE directional spectra estimates for ADCP and PUV instruments based on simulated cross spectra.	49
Figure 3-4 IMLE directional spectra estimates for ADCP and PUV instruments from simulated cross spectra.	49
Figure 3-5 ADCP performance parameterization with total depth = 10 m, $N = 1 \text{ m}^2$, $\alpha - \theta = 45^\circ$	50
Figure 3-6 ADCP performance parameterization with total depth = 20 m, $N = 1 \text{ m}^2$, $\alpha - \theta = 45^\circ$	51
Figure 3-7 ADCP performance parameterization with total depth = 20 m, $N = 1 \text{ m}^2$, $\alpha - \theta = 45^\circ$	51

Figure 3-8 ADCP performance parameterization with total depth = 30 m, $N = 1 \text{ m}^2$, $\alpha - \theta = 45^\circ$	52
Figure 3-9 ADCP performance parameterization with total depth = 30 m, $N = 1 \text{ m}^2$, $\alpha - \theta = 45^\circ$	52
Figure 4-1 Experiment site at the U.S. Army CERC Field Research Facility, Duck, North Carolina (Long and Oltman-Shay, 1991).	62
Figure 4-2 Inshore bathymetry and the Linear Array geometry at Duck, North Carolina (Long and Oltman-Shay, 1991).	63
Figure 4-3 ADCP orientation angle time history. P = pitch angle, R = roll angle, H = heading angle. Heading not corrected for local magnetic deviation (10° W).	64
Figure 4-4 Pier end 19.5 m wind speed for cases 1, 2, and 3. Solid vertical line = start of LA data interval. Dashed vertical line = start of ADCP data interval (if different from LA).	65
Figure 4-5 Pier end 19.5 m wind speed for case 4. Solid vertical line = start of LA data interval. Dashed vertical line = start of ADCP data interval (if different from LA).	65
Figure 4-6 Pier end 19.5 m wind speed for case 5. Solid vertical line = start of LA data interval. Dashed vertical line = start of ADCP data interval (if different from LA).	66
Figure 4-7 Pier end 19.5 m wind speed for case 6. Solid vertical line = start of LA data interval. Dashed vertical line = start of ADCP data interval (if different from LA).	66
Figure 5-1 Convergence of ADCP-type IMLE iteration for simulated ADCP cross spectra. S = true spectrum, 0 = MLE spectrum, 1, 10 = i th IMLE iterations. Frequency is 0.1 Hz.	74
Figure 5-2 Convergence of LA-type IMLE iteration for simulated ADCP cross spectra. S = true spectrum, 0 = MLE spectrum, 1, 10 = i th IMLE iterations. Frequency = 0.1 Hz.	74
Figure 6.2-1 Time series plot of ADCP Doppler velocity data for case 4 from bin 5 for 100 s. \square = beam 1. + = beam 2.	89

Figure 6.2-2 Time series plot of ADCP Doppler velocity data for case 4 from bin 5 for 100 s. □ = beam 3. + = beam 4.	89
Figure 6.3-1 Case 1: ADCP autospectra for each beam from bins 1,3,5: solid line = bin 1 autospectra, dashed line = bin 3 autospectra, dotted line = bin 5 autospectra.	90
Figure 6.3-2 Case 2: ADCP autospectra for each beam from bins 1,3,5: solid line = bin 1 autospectra, dashed line = bin 3 autospectra, dotted line = bin 5 autospectra.	90
Figure 6.3-3 Case 3: ADCP autospectra for each beam from bins 1,3,5: solid line = bin 1 autospectra, dashed line = bin 3 autospectra, dotted line = bin 5 autospectra.	91
Figure 6.3-4 Case 4: ADCP autospectra for each beam from bins 1,3,5: solid line = bin 1 autospectra, dashed line = bin 3 autospectra, dotted line = bin 5 autospectra.	91
Figure 6.3-5 Case 5: ADCP autospectra for each beam from bins 1,3,5: solid line = bin 1 autospectra, dashed line = bin 3 autospectra, dotted line = bin 5 autospectra.	92
Figure 6.3-6 Case 6: ADCP autospectra for each beam from bins 1,3,5: solid line = bin 1 autospectra, dashed line = bin 3 autospectra, dotted line = bin 5 autospectra.	92
Figure 6.4-1 Case 1: sea surface elevation frequency spectra from ADCP autospectra: + = from bin 1, x = from bin 3, ○ = from bin 5.	93
Figure 6.4-2 Case 2: sea surface elevation frequency spectra from ADCP autospectra: + = from bin 1, x = from bin 3, ○ = from bin 5.	93
Figure 6.4-3 Case 3: sea surface elevation frequency spectra from ADCP autospectra: + = from bin 1, x = from bin 3, ○ = from bin 5.	94
Figure 6.4-4 Case 4: sea surface elevation frequency spectra from ADCP autospectra: + = from bin 1, x = from bin 3, ○ = from bin 5.	94
Figure 6.4-5 Case 5: sea surface elevation frequency spectra from ADCP autospectra: + = from bin 1, x = from bin 3, ○ = from bin 5.	95

Figure 6.4-6 Case 6: sea surface elevation frequency spectra from ADCP autospectra: + = from bin 1, x = from bin 3, O = from bin 5.	95
Figure 6.4-7 Ratio of bin 1 to bin 5 wave frequency spectra for each case. Cases identified in plot legend.	96
Figure 6.4-8 Ratio of bin 3 to bin 5 wave frequency spectra for each case. Cases identified in plot legend.	96
Figure 7.4-9 Case 1: surface plot of normalized LA IMLE directional spectra.	106
Figure 4-10 Case 1: surface plot of normalized ADCP IMLE directional spectra.	106
Figure 7.4-11 Case 1: topographic plot of normalized LA IMLE directional spectra.	107
Figure 7.4-12 Case 1: topographic plot of normalized ADCP IMLE directional spectra.	108
Figure 7.4-13 Case 2: surface plot of normalized LA IMLE directional spectra.	110
Figure 7.4-14 Case 2: surface plot of normalized ADCP IMLE directional spectra.	110
Figure 7.4-15 Case 2: topographic plot of normalized LA IMLE directional spectra.	111
Figure 7.4-16 Case 2: topographic plot of normalized ADCP IMLE directional spectra.	112
Figure 7.4-17 Case 3: surface plot of normalized LA IMLE directional spectra.	114
Figure 7.4-18 Case 3: surface plot of normalized ADCP IMLE directional spectra.	114
Figure 7.4-19 Case 3: topographic plot of normalized LA IMLE directional spectra.	115
Figure 7.4-20 Case 3: topographic plot of normalized ADCP IMLE directional spectra.	116
Figure 7.1-13 Case 4: surface plot of normalized LA IMLE directional spectra.	118
Figure 7.1-14 Case 4: surface plot of normalized ADCP IMLE directional spectra.	118

Figure 7.1-15 Case 4: topographic plot of normalized LA IMLE directional spectra.	119
Figure 7.1-16 Case 4: topographic plot of normalized ADCP IMLE directional spectra.	120
Figure 7.1-17 Case 5: surface plot of normalized LA IMLE directional spectra.	122
Figure 7.1-18 Case 5: surface plot of normalized ADCP IMLE directional spectra.	122
Figure 7.1-19 Case 5: topographic plot of normalized LA IMLE directional spectra.	123
Figure 7.1-20 Case 5: topographic plot of normalized ADCP IMLE directional spectra.	124
Figure 7.1-21 Case 6: surface plot of normalized LA IMLE directional spectra.	126
Figure 7.1-22 Case 6: surface plot of normalized ADCP IMLE directional spectra.	126
Figure 7.1-23 Case 6: topographic plot of normalized LA IMLE directional spectra.	127
Figure 7.1-24 Case 6: topographic plot of normalized ADCP IMLE directional spectra.	128
Figure 7.1-25 Comparison of the magnitude of the largest peak (S_p) in the LA and ADCP directional spectra for each case.	130
Figure 7.1-26 Comparison of the period associated with the largest peak (T_p) in the LA and ADCP directional spectra for each case.	130
Figure 7.1-27 Comparison of the direction associated with the largest peak (θ_p) in the LA and ADCP directional spectra for each case.	131
Figure 7.2-1 Case 1: Comparison of the estimated wave frequency spectra from the LA IMLE ("o"), the ADCP IMLE ("+"), and the ADCP bin 5 autospectra ("x").	132
Figure 7.2-2 Case 2: Comparison of the estimated wave frequency spectra from the LA IMLE ("o"), the ADCP IMLE ("+"), and the ADCP bin 5 autospectra ("x").	132
Figure 7.2-3 Case 3: Comparison of the estimated wave frequency spectra from the LA IMLE ("o"), the ADCP IMLE ("+"), and the ADCP bin 5 autospectra ("x").	133

Figure 7.2-4 Case 4: Comparison of the estimated wave frequency spectra from the LA IMLE ("o"), the ADCP IMLE ("+"), and the ADCP bin 5 autospectra ("x").	133
Figure 7.2-5 Case 5: Comparison of the estimated wave frequency spectra from the LA IMLE ("o"), the ADCP IMLE ("+"), and the ADCP bin 5 autospectra ("x").	134
Figure 7.2-6 Case 6: Comparison of the estimated wave frequency spectra from the LA IMLE ("o"), the ADCP IMLE ("+"), and the ADCP bin 5 autospectra ("x").	134
Figure 7.2-7 Ratio of wave frequency spectra derived from LA IMLE spectra to that from the ADCP IMLE spectra for each case (legend lists case #).	135
Figure 7.2-8 Comparison of the magnitudes of the largest peak in the wave frequency spectra ($S_{p,f}$) derived from the LA and ADCP IMLE spectra for each case.	136
Figure 7.2-9 Comparison of the frequencies of the largest peak in the wave frequency spectra ($f_{p,f}$) derived from the LA and ADCP IMLE spectra for each case.	136
Figure 7.3-1 Case 1: Comparison of the radiation stress angles $\alpha_{xy}(f)$ from the LA ("+" and ADCP ("o") directional wave spectra.	137
Figure 7.3-2 Case 2: Comparison of the radiation stress angles $\alpha_{xy}(f)$ from the LA ("+" and ADCP ("o") directional wave spectra.	137
Figure 7.3-3 Case 3: Comparison of the radiation stress angles $\alpha_{xy}(f)$ from the LA ("+" and ADCP ("o") directional wave spectra.	138
Figure 7.3-4 Case 4: Comparison of the radiation stress angles $\alpha_{xy}(f)$ from the LA ("+" and ADCP ("o") directional wave spectra.	138
Figure 7.3-5 Case 5: Comparison of the radiation stress angles $\alpha_{xy}(f)$ from the LA ("+" and ADCP ("o") directional wave spectra.	139
Figure 7.3-6 Case 6: Comparison of the radiation stress angles $\alpha_{xy}(f)$ from the LA ("+" and ADCP ("o") directional wave spectra.	139
Figure 7.3-7 Errors in the ADCP-derived radiation stress angle $\alpha_{xy}(f)$ relative to the LA-derived radiation stress angle for each case (see legend).	140
Figure 7.4-1 Case 1: Comparison of the mean directions $\Theta(f)$ from the LA ("+" and ADCP ("o") directional wave spectra.	141
Figure 7.4-2 Case 2: Comparison of the mean directions $\Theta(f)$ from the LA ("+" and ADCP ("o") directional wave spectra.	141

Figure 7.4-3 Case 3: Comparison of the mean directions $\Theta(f)$ from the LA ("+") and ADCP ("o") directional wave spectra.	142
Figure 7.4-4 Case 4: Comparison of the mean directions $\Theta(f)$ from the LA ("+") and ADCP ("o") directional wave spectra.	142
Figure 7.4-5 Case 5: Comparison of the mean directions $\Theta(f)$ from the LA ("+") and ADCP ("o") directional wave spectra.	143
Figure 7.4-6 Case 6: Comparison of the mean directions $\Theta(f)$ from the LA ("+") and ADCP ("o") directional wave spectra.	143
Figure 7.4-7 Errors in the ADCP-derived mean direction $\Theta(f)$ relative to the LA-derived mean direction for each case (see legend).	144
Figure 7.5-1 Case 1: Comparison of the directional widths $\Delta(f)$ from the LA ("+") and ADCP ("o") directional wave spectra.	145
Figure 7.5-2 Case 2: Comparison of the directional widths $\Delta(f)$ from the LA ("+") and ADCP ("o") directional wave spectra.	145
Figure 7.5-3 Case 3: Comparison of the directional widths $\Delta(f)$ from the LA ("+") and ADCP ("o") directional wave spectra.	146
Figure 7.5-4 Case 4: Comparison of the directional widths $\Delta(f)$ from the LA ("+") and ADCP ("o") directional wave spectra.	146
Figure 7.5-5 Case 5: Comparison of the directional widths $\Delta(f)$ from the LA ("+") and ADCP ("o") directional wave spectra.	147
Figure 7.5-6 Case 6: Comparison of the directional widths $\Delta(f)$ from the LA ("+") and ADCP ("o") directional wave spectra.	147
Figure 7.5-7 Errors in the ADCP-derived directional width $\Delta(f)$ relative to the LA-derived directional width for each case (see legend).	148
Figure 7.6-1 Case 1: Comparison of the frequency-integrated directional spectrum $S(\theta)$ from the LA (solid line) and ADCP (dotted line) directional wave spectra.	149
Figure 7.6-2 Case 2: Comparison of the frequency-integrated directional spectrum $S(\theta)$ from the LA (solid line) and ADCP (dotted line) directional wave spectra.	149
Figure 7.6-3 Case 3: Comparison of the frequency-integrated directional spectrum $S(\theta)$ from the LA (solid line) and ADCP (dotted line) directional wave spectra.	150

Figure 7.6-4 Case 4: Comparison of the frequency-integrated directional spectrum $S(\theta)$ from the LA (solid line) and ADCP (dotted line) directional wave spectra.	150
Figure 7.6-5 Case 5: Comparison of the frequency-integrated directional spectrum $S(\theta)$ from the LA (solid line) and ADCP (dotted line) directional wave spectra.	151
Figure 7.6-6 Case 6: Comparison of the frequency-integrated directional spectrum $S(\theta)$ from the LA (solid line) and ADCP (dotted line) directional wave spectra.	151
Figure 7.6-7 Comparison of the magnitude ($S_{p,d}$) of the largest peak in the LA- and ADCP-derived frequency-integrated directional spectra for each case.	152
Figure 7.6-8 Comparison of the direction ($\Theta_{p,d}$) of the largest peak in the LA- and ADCP-derived frequency-integrated directional spectra for each case.	152
Figure 7.7-1 Comparison of the significant waveheight (H_{m0}) from the LA and ADCP directional wave spectra for each case.	153
Figure 7.7-2 Comparison of the equivalent radiation stress angle ($\alpha_{xy,T}$) from the LA and ADCP directional wave spectra for each case.	153
Figure 8.1-1 Frequency dependence of ratio of estimated wave frequency spectra (bins 1:5) when nominal total depth is 8 m and actual total depth is: x = 7 m, + = 9 m. .	160
Figure 8.1-2 Frequency dependence of ratio of estimated wave frequency spectra (bins 1:5) when error in assumed bin depths is: x = +1 m, + = -1 m.	160
Figure 8.1-3 Simulated autospectra without tilt. + = bin 1, x = bin 3, o = bin 5.	161
Figure 8.1-4 Simulated autospectra with tilt. + = bin 1, x = bin 3, o = bin 5.	161
Figure 8.1-5 Ratio of sum of simulated autospectra with tilt to corresponding sum of autospectra without tilt. + = bin 1, x = bin 3, o = bin 5.	162
Figure 8.1-6 Effect of Q on ratios of ADCP wave frequency spectra: *, \square = ratios (bins 1:5,3:5) obtained for case 2; x,+ = modeled ratios (bins 1:5,3:5) with noise bias. .	162
Figure 8.2-1 Mean depths at LA pressure gage 191 for each case.	163
Figure 8.2-2 Nondirectional wave spectra for case 3 (from directional spectra): o = LA results, x,+ = ADCP results using total depth = 9,8 m respectively.	163
Figure 8.2-3 Nondirectional wave spectra for case 4 (from directional spectra): o = LA results, x,+ = ADCP results using total depth = 9,8 m respectively.	164

Figure 8.2-4 Comparison of peak magnitudes from directional wave spectra for case 3 (L = low freq., H = high freq.) and case 4. 8, 9 = assumed total depth (m). 164

Figure 8.2-5 Comparison of peak directions from directional wave spectra for case 3 (L = low freq., H = high freq.) and case 4. 8, 9 = assumed total depth (m). 165

Figure 8.2-6 Comparison of characteristic waveheight H_{m0} from directional wave spectra for case 3 and case 4. 8, 9 = assumed total depth (m). 165

Figure 8.2-7 Comparison of total radiation stress angle $\alpha_{xy,T}$ from directional wave spectra for case 3 and case 4. 8, 9 = assumed total depth (m). 166

Figure 8.2-8 Comparison of nondirectional frequency spectra derived from directional spectra for case 3: o = LA, + = ADCP using eq. 3.14, x = ADCP using eq.s 8.4-8.6. 167

Figure 8.2-9 Comparison of mean direction vs. frequency derived from directional spectra for case 3: o = LA, + = ADCP using eq. 3.14, x = ADCP using eq.s 8.4-8.6. 167

Figure B-1 Wave coordinate system (WCS) definition. 186

Figure B-2 Beam orientation in ADCP coordinate system (ACS). 186

ABSTRACT

The directional wave spectrum for surface gravity waves is an important characterization of the local wave field for studies in wave refraction/diffraction, wave/current interactions, longshore transport and coastal erosion, among others. Directional wave spectra using acoustic Doppler measurements have been presented by previous authors, but no direct comparison has been made with conventional approaches. Additionally, no previous author has presented models to relate acoustic Doppler measurements to the directional wave spectrum. In this thesis, the estimation of surface gravity wave directional spectra using a commercially available Acoustic Doppler Current Profiler (ADCP) is discussed. Models which relate cross spectra of acoustic Doppler measurements to the directional wave spectrum are developed. These models are incorporated with the Iterative Maximum Likelihood Estimate method to provide algorithms for directional wave spectra estimation. In addition, an estimator for the wave frequency spectrum based on autospectra of acoustic Doppler current measurements is developed. A sensitivity analysis for directional wave spectrum estimation using acoustic Doppler measurements is presented. Finally, directional wave spectra estimates from a field deployment of an RD Instruments model 1200 DR ADCP at the U.S. Army Corps of Engineers Waterways Experiment Station Coastal Engineering Research Center Field Research Facility at Duck, NC during October-November, 1992 are compared to corresponding spectra obtained from a linear array of pressure gages within which the ADCP was deployed. Comparisons are based on the directional wave spectra themselves, as well as on derived quantities such as wave frequency spectra, equivalent radiation stresses, mean direction and directional width, total radiation stress, and significant waveheight.

ADCP and linear pressure array directional wave spectra comparisons are on the whole favorable. Total radiation stress angles agreed with 5° . Significant wave heights agree to within 15%. Equivalent radiation stresses for both approaches exhibited similar trends with frequency. Comparisons between frequency spectra show excellent agreement at low frequencies (< 0.2 Hz). At higher frequencies, however, the ADCP results generally underestimate the linear array results, exhibiting a bias which increases with frequency. Similar results are evident in comparisons of the directional spectra themselves. This discrepancy appears to be due to ignoring changes in the total depth due to tidal variation and other causes when the ADCP directional wave spectra were computed.

DIRECTIONAL WAVE SPECTRA
USING AN
ACOUSTIC DOPPLER CURRENT METER

1. INTRODUCTION

The characteristics of the wave field impinging on the nearshore region have important consequences for a variety of coastal and estuarine processes. These processes include wave-current interactions, wave refraction and diffraction, surf zone dynamics, longshore and cross-shore (rip) currents, sediment suspension, transport of sediment, pollutants, and larvae, beach and coastline dynamics, navigation and shipping safety, and damage to coastal structures and coastal flooding. Investigation of many aspects of these processes requires an accurate knowledge of the wave field with respect to the distribution of wave energy in frequency and direction, i.e. the directional wave spectrum.

A number of *in situ* instrument arrays have been developed and used to measure wave spectra. These arrays fall into two basic categories: point arrays and spatially-distributed arrays. Point arrays measure time series of several characteristics of the wave field (e.g. horizontal velocity and pressure) at a single spatial location. Directional wave spectra can be estimated from cross spectra of these time series. Examples of this type of system are the pitch-and-roll buoy (Longuet-Higgins *et al.*, 1963), the slope array (Higgins, 1981), and the pressure sensor-current meter combination (Boon *et al.*, 1990). These systems provide "bulk" directional wave data but have relatively poor directional resolution (Herbers *et al.*, 1991). Spatially-distributed arrays typically measure time series of one characteristic of the wave field at several spatial locations simultaneously by using several instruments deployed at different locations. Cross spectra of the time series can again be used to estimate the directional wave spectrum. Wavestaffs (Barber, 1954), pressure sensors (Pawka, 1981 and Long and Oltman-Shay, 1991), and current meters (Allender *et al.*, 1989) have been used in spatially-distributed arrays. Spatially-distributed arrays are capable of yielding high directional resolution but are expensive to deploy and maintain. Additionally, wave statistics must be stationary over the extent of the array. This reduces their applicability in areas of topographic diversity or current shear (e.g. a field of sand waves or the mouth of an estuary).

It thus appears that existing point and array systems for measuring wave directional spectra are somewhat inadequate to measure directional spectra with high resolution affordably in nearshore areas of complex bathymetry or current shear. The ideal system would seem to be one consisting of a single instrument package (thus minimizing deployment and maintenance costs) which obtained array-like measurements (thus improving directional resolution). An instrument which recommends itself to this situation is a multi-beam acoustic Doppler current profiler (ADCP). The ADCP obtains array-like measurements of the along-beam component of the total current at different ranges along each acoustic beam. If the beam is tilted from the vertical, then measurements at different ranges correspond to measurements at different horizontal positions. Typically, each beam is pointed in a different direction, resulting in increased horizontal sampling. Consequently a single ADCP instrument can obtain spatially-distributed array-like measurements of the component of orbital wave velocity along each of its beams. Additionally, it is capable of profiling the mean current through the water column. This combination of mean and orbital current measurements makes the ADCP an attractive instrument for use in nearshore transport studies, for example.

ADCP Doppler velocity measurements are conventionally used to estimate low frequency (< 0.01 Hz) vertical profiles of current velocity. Estimates are typically averaged over tens to thousands of acoustic pulses and tens to hundreds of seconds to reduce associated random errors. Acoustic Doppler instruments have been used successfully for the past decade to obtain mean current measurements in a variety of oceanic environments. For example, ADCPs have been used to investigate current profiles in estuarine fronts (Brubaker and Simpson, 1988), the Somali current (Schott and Johns, 1987), the Strait of Gibraltar (Pettigrew *et al.* 1986), and the North Sea (Smith *et al.*, 1987).

Recently, however, interest has developed in using acoustic Doppler instruments to measure surface gravity wave directional spectra. Pinkel and Smith (1987) identified velocity fluctuations due to surface wave contamination in several data sets collected by two Doppler sonars deployed with nearly horizontally-pointed beams at 35 m depth from the FLIP platform 500 km west of Point Conception, California. Krogstad *et al.* (1988) obtained estimates of wave directional spectra in the North Sea from measurements by two horizontally-oriented orthogonal acoustic Doppler beams. Smith (1989) developed a tradeoff

study for wave spectra estimation based on horizontally-pointed ADCP beams. Herbers *et al.* (1991) field-tested a four-beam acoustic Doppler device for making nearshore surface wave measurements near the Scripps pier at La Jolla, California. The measured Doppler velocities yielded information similar to a PUV sensor at a single depth. Comparison with measurements from an array of pressure sensors in which the acoustic device was embedded yielded excellent agreement.

Finally, RD Instruments (1989a) and Terray *et al.* (1990) demonstrated that reasonable directional wave spectra could be obtained from an ADCP with inclined beams, using a conventional narrowband 4-beam RD Instruments ADCP deployed near the Scripps pier at La Jolla, California. However, no comparison was made between the ADCP-derived directional spectra and that derived from a more conventional approach (e.g. a pressure sensor array or a PUV meter). Consequently the "accuracy" of the ADCP-derived wave spectra, at least with respect to some standard approach, has not been determined.

This study is an attempt to assess the "accuracy" of ADCP-derived directional wave spectra by a comparison of directional wave spectra obtained from a linear array (LA) of pressure sensors at the U.S. Army Engineer Waterways Experiment Station (WES) Coastal Engineering Research Center (CERC) Field Research Facility (FRF) at Duck, North Carolina USA with those obtained from an RD Instruments model DR 1200 kHz narrowband ADCP located within the array during a deployment in October-November, 1992.

Chapter 2 consists of a review of instruments and estimation techniques which have been used to measure directional spectra of surface gravity waves. The application of ADCP measurements to directional spectra estimation is developed in chapter 3, as is a sensitivity analysis which indicates under what wave conditions one can reasonably expect to measure wave spectra with an ADCP. The field deployment at Duck, NC is discussed in chapter 4. Data processing for directional spectra from both ADCP and LA measurements is outlined in chapter 5. Processing results prior to directional spectra estimation are presented for six ADCP datasets in chapter 6. ADCP and LA directional spectra are compared for these six cases in chapter 7. Chapter 8 consists of a discussion of the results presented in chapters 6 and 7, with a particular emphasis on attempting to explain certain frequency-dependent biases noted between some results. Finally, a summary and conclusion are given in chapter 9.

2. LITERATURE REVIEW

The physical observables associated with surface gravity waves in the ocean--e.g. sea surface elevation, orbital velocity components, perturbation pressure--are stochastic variables which vary in time and space. If they can be considered stationary during a period of observation, then the directional wave spectrum provides an important statistical description of these observables. The directional wave spectrum describes the distribution of the variance of sea surface elevation as a function of wave frequency and direction of travel. It also describes, to second order in the wave slope, the directional wave energy spectrum; wave energy is proportional to sea surface variance to this order (Phillips, 1966). In fact, "wave spectrum" and "energy spectrum" are frequently used interchangeably.

The directional wave spectrum is an example of a multidimensional wavenumber/frequency (WF) spectrum (Davis and Regier, 1977). The surface gravity wave WF spectrum $S(\underline{k}, \omega)$ is the multi-dimensional Fourier transform of the spatial/temporal covariance of the sea surface elevation $R(\underline{r}, \tau)$ [note: an underbar is used to denote a 2-d vector in the horizontal plane]. If $\eta(\underline{x}, t)$ is the sea surface elevation as a function of horizontal position $\underline{x} = (x, y)$ and time t , then

$$R(\underline{r}, \tau) = \langle \eta(\underline{x} + \underline{r}, t + \tau) \eta(\underline{x}, t) \rangle \quad (2.1)$$

where $\langle \rangle$ denotes an ensemble average and $R(\underline{r}, \tau)$ and $S(\underline{k}, \omega)$ constitute a Fourier transform pair defined by

$$\begin{aligned} R(\underline{r}, \tau) &= \frac{1}{(2\pi)^3} \int d^2k d\omega S(\underline{k}, \omega) \exp[i(\underline{k} \cdot \underline{r} - \omega \tau)] \\ S(\underline{k}, \omega) &= \int d^2r d\tau R(\underline{r}, \tau) \exp[-i(\underline{k} \cdot \underline{r} - \omega \tau)] \end{aligned} \quad (2.2)$$

The horizontal (angular) wavenumber $\underline{k} = (k_x, k_y)$ is the Fourier transform conjugate to the horizontal spatial separation $\underline{r} = (r_x, r_y)$, and the (angular) frequency ω is the conjugate to the

temporal separation τ . The wavenumber magnitude and the frequency are linked for small amplitude surface gravity waves by the dispersion relationship (see Appendix A)

$$\omega^2 = g k \tanh(kh) \quad (2.3)$$

where k is the wavenumber magnitude, g is the acceleration due to gravity, and h is the total depth of water. As a consequence, the directional wave spectrum is nonzero only on the surface defined by the dispersion relation and can also be described as a function by frequency ω and direction of travel $\theta = \arctan^{-1}(k_y/k_x)$ alone.

It is not possible to estimate the spatial/temporal sea surface covariance function $R(\underline{r}, \tau)$ directly from measurements made by an *in situ* array. Such arrays typically sample the wave field very sparsely spatially, so R might be estimated at a very small number of spatial separations \underline{r} . Additionally, an array may measure observables other than sea surface elevation, such as orbital velocity components or wave slopes, which are linearly-related to the wave field. Such observables are related to the wave spectrum $S(\underline{k}, \omega)$ through their cross spectra (see appendix A for a detailed discussion). If $f_i(t)$, $f_j(t)$ are time series of the i th, j th instruments of an array, located at \underline{x}_i, z_i and \underline{x}_j, z_j respectively, then the frequency cross spectrum of these measurements, $C_{ij}(\omega)$, is related to the directional wave spectrum by

$$C_{ij}(\omega) = \frac{1}{(2\pi)^2} \int d^2k F_i(\underline{k}, \omega) F_j^*(\underline{k}, \omega) S(\underline{k}, \omega) \exp[i\underline{k} \cdot (\underline{x}_i - \underline{x}_j)] \quad (2.4)$$

or, using the dispersion relation to reduce the dimensionality of the integral,

$$C_{ij}(\omega) = \int d\theta F_i(\omega, \theta) F_j^*(\omega, \theta) S(\omega, \theta) \exp[i\underline{k}(\omega, \theta) \cdot (\underline{x}_i - \underline{x}_j)] \quad (2.5)$$

In the above equations, F_i is the *transfer function* defining the proportionality between the wavenumber/frequency components of the observable measured by instrument i and the wavenumber/frequency components of the sea surface elevation with frequency ω and wavenumber $\underline{k}(\omega, \theta)$ (i.e. travelling in direction θ). In addition to ω and θ , F_i may also depend on the instrument depth.

For any realizable *in situ* array, there is an infinite number of functions which fit the data via the model defined by eq. 2.5. Additionally, the $C_{ij}(\omega)$ computed from the measured time series contain errors due to statistical fluctuations and instrument noise. The problem of

estimating the directional wave spectrum from *in situ* array data becomes that of finding the function $\hat{S}(\omega, \theta)$ which fits the measured $C_{ij}(\omega)$ according to some predefined criteria.

Investigators have used a variety of both instruments to measure observables related to the wave field and estimation techniques to extract directional wave spectra from the resultant data. Instruments which have been used to make measurements for wave spectra estimation are discussed in the following literature review. While some estimation techniques are briefly alluded to in the review, only the directional spectra estimation techniques used in this study will be discussed at length.

2.1 Instruments for directional wave spectra

Many different types of instruments have been used to measure a number of physical properties associated with surface gravity waves which contain information related to the waveheight spectrum. These physical properties include the sea surface elevation η , the sea surface slopes and curvatures along orthogonal directions (η_x, η_y) and $(\eta_{xx}, \eta_{yy}, \eta_{xy})$, the wave-induced pressure perturbations p , the orbital velocity components (u, v, w) , spatial derivatives of the horizontal orbital velocity components (u_x, u_y, v_x, v_y) and the projection of the orbital velocity onto a particular direction. Earle and Bishop (1984) provide a general discussion of a number of instruments used to collect wave data, including wavestaffs, subsurface pressure sensors, and wave orbital velocity sensors. Kinsman (1984) also discusses a number of instruments, including stereophotography and free-floating buoys.

Because sea surface elevation is conceptually the most straightforward measurement for determining directional wave spectra, the wavestaff is perhaps the simplest wave-measuring instrument. Wavestaffs directly measure the temporal evolution of the sea surface elevation at a single point in space. The wavestaff is partially immersed in the sea and forms part of an electronic circuit which produces voltage or current changes proportional to either the submerged or unsubmerged staff length. The three main types of wavestaffs are resistance wire staffs, capacitance staffs, and electromagnetic transmission line staffs (Earle and Bishop, 1984).

Measurements of sea surface elevation from a single instrument yield a non-directional wave spectrum which describes the distribution of wave energy with wave frequency or period. To obtain directional information, a spatially distributed array of wavestaffs is

required. Wavestaffs have been used to estimate directional wave spectra by Barber (1954) and Regier and Davis (1977) in the field and by Mobarek (1965) and Jeffreys *et al.* (1981) in the laboratory. Other instruments which have been used to directly measure sea surface elevation include inverted fathometers (mounted on a submerged, hovering submarine, de Leonibus, 1963) and laser altimeters (Allender *et al.*, 1989).

As a wave-measuring instrument, the wavestaff has several disadvantages. Since it must actually pierce the sea surface, in water depths over a few feet it must be deployed from an existing structure (e.g. a pier or offshore structure) if it is to remain stationary. This structure, however, will modify the wavefield through reflection and diffraction. Care must be taken in locating the wavestaff(s) to avoid measuring waves modified by the fixed structure. Additionally, wavestaff measurements can be corrupted by biofouling (Allender *et al.*, 1989). This may require frequent maintenance and cleaning of deployed wavestaffs.

Wavestaff arrays also suffer from several other disadvantages. The first is expense. The directional resolution of the wavestaff array is related directly to its geometry. Resolution of long wavelength wavetrains with slightly different directions by conventional Fourier processing requires array sizes comparable to the wavelength. Such large arrays are expensive to deploy and maintain (Seymour *et al.*, 1979). In addition, the wave field must be spatially homogeneous over the array extent. This may not be a valid assumption in the nearshore region if the bathymetry is not uniform.

Free-floating buoys are another means of obtaining directional wave information. The pitch/roll/heave (abbreviated PRH here) wave buoy includes a vertical accelerometer and pitch and roll sensors. The twice-integrated accelerometer measurements yield sea surface elevation as a function of time. The pitch and roll time series then yield information on the gradient of the sea surface-i.e. the wave slopes η_x and η_y . The wave buoy is an example of a "point" instrument array, as opposed to a spatially-distributed instrument array, from which directional wave data can be obtained. Pitch/roll/heave buoys have been used to obtain directional spectra by a number of investigators, including Longuet-Higgins, Cartwright, and Smith (1963), and Lygre and Krogstad (1986).

The PRH buoy suffers, however, from fundamentally poor directional resolution. The first 3 complex coefficients of a Fourier series expansion of the directional wave spectrum at a given frequency can be obtained from the cross-spectra of sea surface elevation and the

wave slopes (Longuet-Higgins *et al.*, 1963). The truncated Fourier series using these (possibly weighted) coefficients is the estimated directional spectrum. The energy from a single direction (the directional response) is smeared over about 88° for uniform weighting of the expansion coefficients, which also introduces negative energy in sidelobes (fig. 2-1). The energy is spread over about 130° when the coefficients are weighted so the estimated spectrum is nonnegative (fig. 2-1). The directional resolution of wavetrains coming from different directions is thus fairly poor. However, if the spectrum is known to be narrow directionally, the mean direction and spectrum width can be estimated (Longuet-Higgins *et al.*, 1963).

It should be noted that floating buoys will be sensitive only to waves in a particular band of wavelengths. This band is dependent on the details of the buoy shape and construction, as well as the sensitivity of the measurements it makes. Energy at short wavelengths will not be reliably estimated because the buoy's inertia makes it insensitive to the short term accelerations of such waves. Accelerations due to long wavelengths will be smaller than the instrument noise level, so energy at long wavelengths will not be reliably estimated. Additionally, the buoy design will make its motion resonant to certain period waves. The interpretation of spectra from floating buoys is thus dependent on accurate knowledge of the frequency response calibration of the pitch, roll, and heave sensors and the frequency response of the entire buoy.

Nevertheless, such buoys are a popular means of obtaining gross wave information because they are relatively inexpensive and easy to deploy. Many commercially available buoys similar to the pitch/roll/heave buoy were evaluated in terms of their directional spectra by Allender, *et al.* (1989). They reported problems with stability in high seas for several of the buoys tested. Overall, however, they found that comparisons for significant waveheight, mean or peak period, and wave direction at the spectral peak were "reassuringly good", although for individual buoys there were some significant differences for sub-classes of the data.

Cartwright and Smith (1964) extended the idea of the pitch/roll/heave buoy by creating a "cloverleaf" buoy, essentially three pitch/roll/heave buoys arranged in an equilateral triangle and attached to a welded tubular framework. The cloverleaf buoy is capable of estimating the sea surface curvatures (η_{xx} , η_{yy} , η_{xy}) in addition to the sea surface elevation and

slopes obtainable from a single buoy. The theoretical response of the cloverleaf buoy to wave energy from a single direction (see fig. 2-2) is about half as wide as that of the PRH buoy (Oltman-Shay and Guza, 1984).

Cartwright and Smith (1964) found their cloverleaf buoy results "reasonable", but did not compare them directly to wave spectra from a PRH buoy. Mitsuyasu *et al.* (1975) derived wave spectra for both the cloverleaf buoy and the PRH buoy contained as a subset of the cloverleaf data. They found, on the whole, spectra from both buoys to be quite similar. Where significant differences existed, they found that poor accuracy in the calculation of the curvature components for the cloverleaf buoy contributed "non-negligible errors" to the data. Oltman-Shay and Guza (1984) noted that "the theoretically higher resolution of the cloverleaf buoy has not been shown to be realizable in field applications." In practice, then, the cloverleaf buoy is found to have resolution equivalent to that of the PRH buoy.

A third instrument used for directional spectra estimation is the submerged pressure recorder, which measures the wave-induced pressure fluctuations at the sensor depth. Most pressure sensors use the deflection of a mechanical element to detect the *in situ* pressure. In electrically recording sensors, this deflection changes the inductance (inductive transducers), voltage (piezoelectric transducers), or resistance (potentiometric or strain gage transducers) of an electrical circuit. This change is then recorded. The pressure calibration curve can then be used to interpret the electrical output in terms of the pressure. The recorded pressure can be absolute, gage, or differential depending on the internal pressurization of the mechanical sensor. If the pressure transducer is not compensated, ambient temperature variation can significantly influence the accuracy of the measurements. Bottom-mounted pressure sensor arrays have been used by Long and Hasselman (1979), Pawka (1983), Herbers and Guza (1990), and Long and Oltman-Shay (1991) to measure directional waveheight spectra. In these studies, the pressure sensors were arranged in a linear array parallel to the shoreline, but other configurations are possible.

One disadvantage of the submerged pressure recorder is that the pressure fluctuations due to waves are attenuated with depth (see fig. 2-3). For wavelengths on the order of the total depth or shorter, the attenuation factor is approximately $\exp(kz)$, where k is the wavenumber magnitude and z is the sensor depth ($z < 0$). The pressure sensor acts as a low-pass filter of the sea surface elevation. As the sensor depth is increased, the width of this

low-pass filter is decreased and only the spectral content of longer wavelength waves can be measured. The instrument noise level consequently sets a limit on the ability to estimate high wavenumber (or frequency) spectral content. The sensor depth thus controls the shortest waves which can be analyzed. To measure energy at wavelengths on the order of the total depth or shorter, the pressure sensor must be deployed off the bottom. This requires that it be deployed from an existing structure, as are wavestaffs, if it is to remain in the same spatial position.

Pressure sensors are also used in point arrays. One such point array is the "slope" array (Seymour and Higgins, 1977). The slope array consists of four pressure sensors arranged in a parallelogram. The low-pass filtered sea surface slopes, as well as the low-pass filtered sea surface elevation, can be calculated from the slope array measurements. Because the slope estimates are based on finite differences between the four pressure sensors, the estimates are sensitive to noise for long wavelengths (compared to the sensor separation) and biased by sea surface curvature for short wavelength. The slope array thus operates well only in a limited frequency range. Within this range, the slope array formally has the same poor resolution as the PRH buoy (Oltman-Shay and Guza, 1984). Higgins *et al.* (1981), Grosskopf *et al.* (1983), and Otman-Shay and Guza (1984) have obtained directional spectra using slope array measurements.

Measurements of the wave orbital velocity field also yield information on the directional waveheight spectrum. The horizontal wave orbital velocity is attenuated with depth for short wavelengths like the wave-induced pressure fluctuations (fig. 2-3). The vertical orbital velocity has a different depth attenuation in shallow depths (fig. 2-4). The sensitivity of conventional current meters to energy at shorter wavelengths thus depends on the instrument depth and the instrument noise level. For long wavelengths, only the vertical velocity component w attenuates significantly with depth.

Although a number of current meters based on different designs exist, most wave orbital velocity measurements have been made with either electromagnetic current meters (EMCMs) or acoustic travel time current meters (ATTs). Electromagnetic current meters produce a magnetic field. Sea water flowing through the field changes the electric potential. Typical EMCMs measure the electric potential changes in two orthogonal directions to estimate the two components of velocity along these directions. The meter is usually oriented

so the two components are in the horizontal plane, i.e. u and v . Acoustic travel time current meters are based on the time it takes an acoustic pulse to travel between two transducers. Typical ATTs consist of two or three pairs of transducers, the axis of each pair is oriented orthogonally to the others. An ATT with three transducer pairs is consequently capable of measuring all three components of velocity.

Most current meters deployed for wave measurements have been located either on the bottom or on a fixed platform. These current meters have disadvantages similar to pressure sensors due to the attenuation of the orbital velocity with depth. In addition, the current meter itself distorts the flow field in a nonlinear manner. Current meters consequently must be extensively calibrated in the laboratory before they are deployed in the field. They have also been found susceptible to biofouling (Herbers *et al.*, 1991).

Nagata (1964) showed that the mean direction and spread of the spectrum could be estimated from the information available from a single current meter which measured the horizontal components of wave orbital velocity u and v . He also showed that a pressure sensor-UV current meter combination (PUV meter) yields directional spectra with resolution formally equivalent to a PRH buoy (fig. 2-1), as does a 3-axis (UVW) current meter.

Grosskopf *et al.* (1983), Krogstad *et al.* (1988), Allender *et al.* (1989), and Boon *et al.* (1990) have obtained directional spectra from PUV measurements. Allender *et al.* (1989) reported degraded spectral estimates due to biofouling for a PUV system located at 6 m depth. Obtaining directional spectra from 3-axis meters appears to be much less successful. Grosskopf *et al.* (1983) reported problems with a UVW meter due to orientation changes caused by heavy wave action. Additionally, because the UVW meter does not provide an estimate of the mean water depth--which may be significantly affected by tidal phase--there is an uncertainty converting measurements made at depth to the sea surface. Grosskopf *et al.* (1983) found that *in situ* wave gauges using a pressure sensor produced better estimated wave spectra than did a wave gauge using a vertical velocity sensor. Allender *et al.* (1989) abandoned attempts to use vertical current measurements to obtain directional spectra due to "data inconsistencies."

Simpson (1969) attempted an improvement, using additional current meters, on the poor resolution of the PUV meter similar to that which Cartwright and Smith (1964) attempted for the PRH buoy. Three EMCs were arranged in an isosceles right triangle with a pressure

sensor. In addition to p , u , and v measurements, spatial derivatives of the horizontal velocity components could also be computed based on finite differences. With this additional data, the array resolution was formally improved from that of a PUV meter or PRH buoy to that of the cloverleaf buoy (fig. 2-2), i.e. resolution was formally improved by a factor of about two. The actual results from the field deployment indicated that the signal to noise ratio of the velocity derivatives was less than anticipated, particularly in high sea conditions. This noise degradation was blamed on the creation of turbulence by the pier structure to which the array was attached.

A third type of current meter which has recently begun to be used to measure wave data is the acoustic Doppler current meter (ADCM). The ADCM measures current velocity along a particular direction by transmitting a pulse of acoustic energy in a pencil-shaped beam at a known frequency. Particles in the water column reflect the acoustic energy with different frequencies which depend on their radial motion relative to the ADCM (i.e. the Doppler effect). The ADCM detects this reflected energy and measures the average frequency shift within the ensonified volume. The ADCM current measurement is a weighted average of the radial fluid velocity over the ensonified volume. The minimum size of this volume depends on the length of the transmit pulse and the width of the beam.

Acoustic current meters based on the Doppler principle have several advantages over EMCMs and ATTs. These advantages include non-intrusiveness, linearity, less susceptibility to biofouling, and no requirement for calibration (Herbers *et al.*, 1991). Unlike EMCMs and ATTs, the ADCM is essentially a remote sensing device. It does not distort the flow field in the vicinity of its current measurement. The response of the ATT and the EMCM to the flow field is nonlinear and the meters are difficult to calibrate. The response of the ADCM to the flow field is a linear function of the speed of sound, which depends primarily on temperature and to a much lesser extent on salinity. An estimate of the temperature within 5°C is sufficient to determine the instrument response to 1% accuracy (Herbers *et al.*, 1991).

Herbers *et al.* (1991) used a 4-beam ADCM mounted on the sea floor to estimate the near-bottom u and v . Spatial derivatives of u and v could also be calculated, theoretically, from the Doppler velocity measurements, but these were expected to be limited by measurement errors due to the small spatial separation of between the Doppler measurements. A co-located pressure sensor allowed calculation of the directional

waveheight spectrum equivalent to a PUV meter or PRH buoy (fig. 2-1). A comparison of the non-directional spectra predicted by the ADCM measurements and measured by the co-located pressure sensor resulted in "excellent agreement", with gain errors less than 5% being somewhat better than those reported for similar comparisons between EM current meters and pressure sensors (Guza *et al.*, 1988).

Acoustic Doppler current meters which profile the flow field, known as acoustic Doppler current profilers (ADCPs), have the additional advantage that measurements are obtained at several different spatial positions with one instrument. Pinkel and Smith (1987) identified velocity fluctuations due to surface wave contamination in several data sets collected by two Doppler sonars deployed with nearly horizontally-pointed beams at 35 m depth from the FLIP platform 500 km west of Point Conception, Ca. This signal was apparently due to acoustic scattering by bubbles in the region 1 m below the surface which were advected by the orbital wave motion. Directional spectra were calculated using the two orthogonal beams to measure orthogonal components of the wave orbital velocity. This was an accidental result as the instruments had been designed to investigate horizontal current shear. Krogstad *et al.* (1988) used an ADCP with two orthogonal beams oriented horizontally in combination with a pressure sensor mounted at a depth of 14 m on an oil platform in the North Sea. Each beam had a beamwidth of 1.5° and was sampled at 25 positions 4.6 m apart. At this spacing, adjacent samples were 15% correlated. In addition, four Marsh-McBirney EMCs were included in the instrument array. These allowed estimation of directional spectra for a PUV system. Comparison of directional spectra computed from the ADCP+P and the PUV systems indicated that the ADCP+P was capable of producing directional spectra with a higher resolution than the PUV system. Smith (1989) developed a tradeoff study for wave spectra estimation based on horizontally-pointed ADCP beams, showing under what conditions this approach would be feasible.

These studies indicate the potential for using ADCP measurements to estimate directional spectra. The technique used by Pinkel and Smith (1987), and advocated by Smith (1989), is basically a deepwater technique and is inappropriate to the nearshore regime. The ADCP beam used is narrow in azimuth but wide in the vertical. In the nearshore regime, the wave signal would be contaminated by returns from the bottom. The system employed by Krogstad *et al.* (1988) would suffer from the same problem in relatively shallow water. The

one-range bin acoustic Doppler device used by Herbers *et al.* (1991) is not a current profiler and performs essentially as a PUV system; it has the same poor directional resolution as a PUV system.

RD Instruments (1989a) and Terray *et al.* (1990) obtained directional wave spectra using a 4-beam upward-looking, bottom mounted ADCP similar to the one used in this study. The instrument was deployed near the Scripps pier in La Jolla, California in 5.2 meters of water. Doppler velocities were sampled along each beam at 5 Hz and recorded at 1 Hz. Time series approximately 42 minutes in duration from range cells located 0.5, 1.5, 2.5, and 3.5 meters below the surface were used to compute cross spectra having approximately 40 degrees of freedom. The directional wave spectrum was estimated using a Maximum Likelihood Estimate (MLE) approach. Swell ($f = 0.1$ Hz) was seen to be propagating nearly directly onshore whereas higher frequency ($f = 0.25 - 0.35$ Hz) wind waves approached more obliquely from about 25° off the shore normal. These results were "in accord" with visual observations (RDI, 1989a), but an independent estimate of the directional spectra was not made.

The bottom-deployed, upward-looking ADCP used in this study (and in the RDI study) has a number of advantages over the other systems presented here. It is deployed on the sea floor, so there is no need to have an existing structure on which to mount it. Since it profiles the water column, it samples the Doppler velocity along its four beams at several different depths. The ADCP can sample to the surface, to within 15% of the total depth. The attenuation problems encountered by conventional bottom-deployed current meters will thus be partly avoided. It is expected that directional resolution should be better than a PUV meter or PRH buoy because the Doppler measurements are taken from spatially separated positions.

2.2 Approaches to directional spectra estimation

Techniques for estimating the directional wave spectrum fall into two categories with distinctly different approaches. One category might be termed "point estimation", the other might be termed "function estimation." Techniques in both categories can be formulated as solutions to variational problems. Those which fall into the point estimation category involve finding the (generally linear) relationship which minimizes the variance of the

estimated spectrum at a particular point in wavenumber/frequency space. This minimization is repeated for every point of interest in the spectrum. Davis and Regier (1977) provide a general discussion of point estimation techniques for arrays which measure sea surface elevation. Techniques which fall into the function estimation category involve finding the function which minimizes a particular functional based on the measured data and on additional constraints dictated, presumably, by the physics of the particular situation. Long (1986) presents a general discussion on the techniques in this category.

Two approaches to directional spectra estimation are used in this study, while a third was attempted but the results were unsatisfying and the approach was dropped. The Maximum Likelihood Estimator (MLE) is an example of a data adaptive point estimation technique which has been used in many studies (e.g. Davis and Regier, 1977, Oltman-Shay and Guza, 1984, and Isobe *et al.*, 1984) because of its flexibility and simplicity. The Iterative Maximum Likelihood Estimator (IMLE) is a refinement on the MLE which produces an estimate which is a "possible" spectrum (Pawka, 1983). The IMLE has been used in a number of studies (e.g. Pawka, 1983, Oltman-Shay and Guza, 1984, and Long and Oltman-Shay, 1991) because it offers the possibility of higher resolution than the MLE at a modest increase in computational expense. Directional spectra from both the ADCP and the Linear Array were estimated using these two techniques. Only the IMLE results are presented, since these constitute "higher resolution" results. I also attempted to implement the Generalized Inverse approach of Herbers and Guza (1990), an example of a function estimation approach, to produce directional spectra estimates from ADCP data. While this approach has several features which make it attractive, including a statistically-motivated fit to the cross spectra and the possibility of incorporating topographic constraints, it is algorithmically and computationally expensive. A computer program was developed to implement this method, but the results obtained on simulated data indicated a problem which has not been resolved, despite several attempts to isolate the cause. Consequently, no directional spectra estimated using this method are presented.

Point estimation approaches

The point estimation category includes techniques which Davis and Regier (1977) call "*a priori*" and "data adaptive" model-independent techniques. These estimators are based

on a linear combination of the measured cross-spectra \hat{C}_{ij} at a given frequency ω , so that the estimated wavenumber/frequency spectrum $\hat{S}(\underline{k}, \omega)$ is given by

$$\hat{S}(\underline{k}, \omega) = \sum_{i,j} \hat{C}_{ij}(\omega) \gamma_{ij}(\underline{k}, \omega) \quad (2.6)$$

To make \hat{S} real, the coefficients γ_{ij} and γ_{ji} are complex conjugates. The problem of estimating \hat{S} at the point \underline{k}, ω (hence "point estimation") becomes that of "optimally" selecting the $n(n+1)$ unknown coefficients $\gamma_{ij}(\underline{k}, \omega)$ (n is the number of nonredundant array instruments). The difference between "a priori" and "data adaptive" estimation techniques is that, in the former techniques, the coefficients are data-independent and so can be determined before data collection whereas in the latter techniques they are data-dependent and so must be determined after data collection. Data adaptive techniques have the further proviso that the coefficients are separable, that is $\gamma_{ij}(\underline{k}, \omega) = \gamma_i(\underline{k}, \omega) \gamma_j^*(\underline{k}, \omega)$. This has the important consequence that the estimated spectra is nonnegative definite (Davis and Regier, 1977). The Maximum Likelihood Estimator (MLE) used in this study is an example of the data adaptive point estimation techniques.

If c_{ij} denotes the "noise" in the estimate \hat{C}_{ij} , which is assumed to be an unbiased estimator of C_{ij} , then it can be shown from equations 2.4 and 2.6 that the mean value of the spectral estimator for a data adaptive estimator is given by

$$\langle \hat{S}(\underline{k}, \omega) \rangle = \int d^2 k' S(\underline{k}', \omega) W(\underline{k}, \underline{k}'; \omega) \quad (2.7)$$

where

$$W(\underline{k}, \underline{k}'; \omega) = \left| \sum_i G_i(\underline{k}, \omega) \gamma_i(\underline{k}, \omega) \right|^2 \quad (2.8)$$

and

$$G_i(\underline{k}, \omega) = F_i(\underline{k}, \omega) \exp(i \underline{k} \cdot \underline{x}_i) \quad (2.9)$$

The variance of the data adaptive directional spectra estimator is given by

$$\sigma^2(\underline{k}, \omega) = \langle [\hat{S}(\underline{k}, \omega) - \langle \hat{S}(\underline{k}, \omega) \rangle]^2 \rangle = \sum_{i,j} |\gamma_{ij}(\omega, \theta)|^2 \langle |c_{ij}|^2 \rangle \quad (2.10)$$

In deriving eq. 2.10, the cross-spectral noise is assumed to be independent for different sensors.

From eq. 2.7, the mean spectral estimate is a "smeared" version of the true spectrum. The spectral estimate is biased by the function W , which is called the wavenumber window and which determines the resolution of the array (Davis and Regier, 1977). "High resolution" spectra are obtained when W approximates a Dirac δ -function centered at $\underline{k} = \underline{k}'$. It can be seen from the form of W that the resolution is intimately related to the array geometry given by the set of non-redundant $\{\underline{x}_j\}$. Noise rejection is measured by eq. 2.10 and is quadratic in the weights applied to the cross-spectra in the spectrum estimate.

Optimal designs for directional wave spectra estimation should thus seek to minimize the spectral smearing by maximizing the resolution and minimize the spectral variance by maximizing the noise rejection (Davis and Regier, 1977). For a given number of instruments in an array, resolution and noise rejection cannot be maximized at the same time. Resolution is maximized by having no redundant separations in the array, but noise rejection is maximized by having many redundant separations. Ideally, what Davis and Regier call *a priori* approaches attempt to maximize spectral resolution and noise rejection based on array design and *anticipated* characteristics of the spectrum, whereas data adaptive approaches attempt to maximize spectral resolution and noise rejection based on the data actually collected. Most of the "point estimate" approaches which have been developed, however, concentrate on maximizing resolution (Davis and Regier, 1977).

The data adaptive estimators developed by Davis and Regier for cross spectra of sea surface elevation are based on the Maximum Likelihood approach developed by Capon (1967) and Capon *et al.* (1969). Isobe *et al.* (1984) and Oltman-Shay and Guza (1984) extended this approach to cross spectra of observables which are linearly related to the wave field (i.e. observables which have linear transfer functions relative to the wave field).

Capon (1967) developed the Maximum Likelihood (hereafter ML) approach as a signal estimation algorithm, not as an estimator of the directional spectrum, for seismic waves in a noise background propagating through a field of detectors. The ML method was optimized to filter a plane wave signal in background noise propagating through an array of detectors. The ML filter passed the signal undistorted but suppressed the noise. The ML filter weights were constrained to pass a plane wave signal, in the absence of noise, with unit gain and no

phase change. Capon *et al.* (1969) took the variance of the ML filter output "tuned" to the wavenumber/frequency \underline{k}, ω as an estimate of the wavenumber/frequency spectrum $S(\underline{k}, \omega)$.

For a plane wave signal of variance $E(\omega)$ with wavenumber \underline{k}' in noise, the spectrum can be expressed as (Davis and Regier, 1977)

$$S(\underline{k}, \omega) = E(\omega) \delta[\underline{k} - \underline{k}'] \cdot S_N(\underline{k}, \omega) \quad (2.11)$$

where S_N is the background noise WF spectrum. Because the spectrum S and the wavenumber window W are both nonnegative definite, the bias in the estimated spectrum can be reduced by minimizing the estimate in eq. 2.7 subject to the constraint to pass the signal with unit gain and no phase change. For observables linearly related to the wave field, this constraint is consistent with the requirement that

$$1 = W(\underline{k}, \underline{k}; \omega) \quad (2.12)$$

The ML estimate of $S(\underline{k}, \omega)$, for a given ω , can be derived by minimizing the functional

$$\begin{aligned} \tilde{S}(\underline{k}, \omega) = & \int d^2k' S(\underline{k}', \omega) W(\underline{k}, \underline{k}'; \omega) \\ & + \lambda [1 - W(\underline{k}, \underline{k}; \omega)] \end{aligned} \quad (2.13)$$

where λ is a Lagrange multiplier for the constraint eq. 2.12. It can be shown (e.g., Davis and Regier, 1977 or Isobe *et al.*, 1984) that the ML estimator (MLE) of the directional spectrum, \hat{S}_{ML} which minimizes eq. 2.13 is given by

$$\hat{S}_{ML}(\underline{k}, \omega) = \frac{\kappa(\omega)}{\sum_{ij} G_i(\underline{k}, \omega) C_{ij}^{-1}(\omega) G_j(\underline{k}, \omega)} \quad (2.14)$$

where C^{-1} is the inverse of the matrix C whose elements are the C_{ij} and $\kappa(\omega)$ is a proportionality constant for each frequency at which the directional spectrum is estimated. Applying the dispersion relation, eq. 2.14 reduces to

$$\hat{S}_{ML}(\omega, \theta) = \frac{\kappa(\omega)}{\sum_{ij} G_i(\omega, \theta) C_{ij}^{-1}(\omega) G_j(\omega, \theta)} \quad (2.15)$$

A problem arises in applying the MLE to continuous spectra. The MLE is optimized to estimate the variance at a particular wavenumber whereas this energy is zero for a continuous spectrum (Davis and Regier, 1977). The energy detected by the ML filter then corresponds to some unknown wavenumber (or direction) band. The problem is how one assigns a size to this band. The approach usually applied to this problem is to renormalize the ML spectrum for each frequency of interest by computing the MLE estimates at points on a finely-spaced grid in wavenumber (direction) space, connecting these points with a smooth surface (curve), and adjusting the overall spectrum so that the total variance computed from the \hat{C}_{ij} is preserved by the MLE spectrum. This normalization also determines the proportionality constant κ .

The "high resolution" potential of the MLE approach is illustrated in fig.s 2-5 and 2-6. Cross spectra were simulated for the PRH buoy for two wave conditions, one in which directionally narrowband wave energy comes from a single direction and one in which it comes from two directions 90° apart. The MLE approach and the conventional approach of Longuet-Higgins *et al.* (1963, i.e. a truncated Fourier series expansion of the spectrum) were used to estimate the directional wave spectrum. The MLE spectrum reflects the true peak width much more closely than does the spectrum from the conventional approach for the spectrum with one peak (fig. 2-5), although both estimates reflect the peak position correctly. However, for the two-peaked case (fig. 2-6), the conventional approach yields only a single peak midway between the two peaks in the true spectrum. It cannot resolve the presence of both peaks in the two-peaked case whereas the MLE spectra correctly reflects the positions of both peaks.

Davis and Regier (1977) evaluated the MLE along with several other proposed techniques using simulated cross-spectra from several types of spectra, including directional spikes, cosine power distributions, a cosine power + step distribution, and an isotropic spectrum. The array geometry reflected that of a six element wavestaff array on the spar buoy FLIP. The MLE performed well for spectra with narrow peaks. For broad spectra the MLE spectra contained "spurious fine structure and artificial peaks." Pawka (1983) noted that while the MLE yielded accurate estimates of the width and peak location for a unimodal narrowband spectrum, the MLE spectrum was biased low if a secondary peak was present in the true spectrum. Isobe *et al.* (1984) contrasted MLE spectra and spectra derived from

Longuet-Higgins et al. (1963) method for a variety of simulated *in situ* arrays, including PRH buoys, PUV meters, cloverleaf buoys and various other combinations of instruments. The MLE spectra tended to underestimate the peak height and width of the unimodal spectra, but performed better than the Fourier series expansion approach. For bimodal spectra, as Pawka (1983) had observed, the MLE underestimated the larger peak height, but it represented the subsidiary peak height well and resolved both peaks. The Fourier series expansion approach could only resolve both peaks for the cloverleaf buoy. They concluded that the MLE has "very high resolution power" and "holds substantial advantages in terms of convenience and simplicity..."

Herbers and Guza (1990) criticized the MLE and other approaches presented by Davis and Regier (1977) on the basis that the estimated spectra are not required to reproduce the measured cross-spectra to within some specified tolerance. The estimated spectra are consequently not necessarily possible spectra, in the sense that the estimated spectra is statistically consistent with the measured cross-spectra. In an attempt to address similar concerns, Pawka (1983) had earlier developed and tested the Iterative MLE (IMLE), an iterative approach to estimating the directional spectrum which attempts to improve the MLE spectrum so that the iterated spectrum essentially agrees with the measured cross-spectra. The IMLE was originally developed for sea surface elevation measurements, but Oltman-Shay and Guza (1984) extended the concept to other observables with linear transfer functions.

The IMLE is based on the idea that the smearing involved in eq. 2.7 is similar to that which occurs if the MLE spectrum \hat{S}_{MLE}^0 is taken as the true spectrum and a second MLE spectrum T_{MLE}^0 is estimated based on it. The smearing observed in this operation is used to compute the first IMLE spectrum \hat{S}_{MLE}^1 to improve the original MLE spectrum estimate. A third MLE spectrum T_{MLE}^1 is computed based on the first IMLE spectrum taken as "truth". The smearing observed between these spectra can be used to compute a second first iteration, \hat{S}_{MLE}^2 . This process continues until the original MLE spectrum, to some specified accuracy, is reproduced using the IMLE spectrum as the true spectrum. This convergence generally implies that the cross-spectra derived from the IMLE spectrum "agree" with the measured cross-spectra, but no statistical significance is attached to this agreement. Pawka (1983)

describes this process as a deconvolution of eq. 2.7. Oltman-Shay and Guza (1984) and Long and Oltman-Shay (1991) use an iteration of the form:

$$\hat{S}_{IMLE}^{i+1}(\omega, \theta) = \hat{S}_{IMLE}^{i-1}(\omega, \theta) \cdot \frac{|\lambda_i(\omega, \theta)|^{\beta+1}}{\gamma \lambda_i(\omega, \theta)} \quad (2.16)$$

where

$$\lambda_i(\omega, \theta) = \hat{S}_{IMLE}^o(\omega, \theta) - T^{i-1}_{MLE}(\omega, \theta) \quad (2.17)$$

and β and γ are user-defined constants which affect the rate of convergence.

The IMLE approach is obviously more computationally intensive than the MLE is, since the cross-spectral matrix C based on the IMLE spectrum and then MLE spectra based on this matrix are calculated each iteration. However, this cost is not prohibitive and the IMLE has been used in several studies now (e.g. Pawka, 1983; Oltman-Shay and Guza, 1984; and Long and Oltman-Shay, 1991).

Because an analytic relationship between the MLE or the IMLE and the true spectrum had not been developed, Pawka (1983) subjected both the MLE and the IMLE to an extensive series of tests involving deterministic and random simulation tests. A total of 960 unimodal and 800 bimodal spectral shapes were used to test the deterministic portion of the response of the two methods. He found that the IMLE showed improved performance relative to the MLE in all but 3.5% of the unimodal cases and 0.1% of the bimodal cases. The improvement was considered "particularly dramatic" for true directional spectra with broader forms. Pawka cautions, however, that the test cases illustrated that the convergence of the MLE spectrum based on the IMLE spectrum to the original MLE spectrum obtained from the measured cross-spectra did not always yield the true spectrum. Rather, the IMLE spectrum is simply one of a set of spectra which are consistent with the measured cross-spectra, within some accuracy. The expected performance of the IMLE and the MLE for spectral forms not tested was not known.

Oltman-Shay and Guza (1984) used deterministic spectra to compare the performance of the extended MLE and IMLE estimates in regards to background noise levels, directional mode spectra, and angular separations of the modes for PRH buoy-type measurements. The IMLE was found to have better resolution than the MLE, although it at times underestimated

the peak width. With bimodal peaks of equal amplitude (10° width at half maximum power), the IMLE was able to resolve both peaks to within 65° separation whereas the MLE was able to resolve them only within about 80° separation. For bimodal spectra where one peak had half the energy of the other, the IMLE was again able to resolve both peaks within 65° separation, but the MLE was only able to resolve the peaks within about 85° separation. On the other hand, conventional processing (i.e. the truncated Fourier series representation) could only resolve peaks separated by more than 120° . As with Pawka (1983), the IMLE approach was judged to be more successful than the MLE at representing the true spectrum for a wide number of spectral types.

Herbers and Guza (1990) note that although the IMLE techniques generate estimated spectra which agree with the measured cross-spectra to some specified accuracy, this accuracy is not based on a statistical qualification of the errors expected in the cross-spectra measurements. One cannot say, then, to what extent the estimated spectrum is *statistically* consistent with the measured cross-spectra.

Function estimation approaches

The second category of approaches to estimating the directional spectrum is the function estimation category. The third directional estimation technique used here for the ADCP data, the "generalized inverse" method of Herbers and Guza (1990), falls into this category. This category also includes techniques which involve model fitting (e.g. Longuet-Higgins *et al.*, 1963 and Cartwright, 1963), parameter fitting (e.g. Longuet-Higgins *et al.*, Cartwright and Smith, 1964, and Simpson, 1969), and other generalized inverse methods (e.g. Long and Hasselman, 1979). Some confusion may arise as to the distinction used here between "model fitting" and "parameter fitting" techniques, particularly since all models contain adjustable parameters. The term "model fitting" as used here refers to approaches which assume that the directional spectrum has a basic shape, such as a cosine power distribution. Specific model fitting approaches will not be discussed here. The term "parameter fitting" refers to approaches which represent the directional spectrum as an expansion in a set of basis functions, e.g. as a Fourier series expansion. Inverse modelling approaches can be model dependent (e.g. Long and Hasselman, 1979) or model independent (Herbers and Guza, 1990). Model fitting can, in fact, be viewed within the formalism of inverse modelling. However, "model fitting" implies a certain insensitivity to discrepancies between the model

results and the data which is not true of the inverse modelling techniques. The inverse modelling approaches are also, in some sense, data adaptive. Another approach which falls into the category of function estimation is the Maximum Entropy Method (Lygre and Krogstad, 1986). The Maximum Entropy Method (MEM) is data adaptive as well. Only the generalized inverse approach of Herbers and Guza (1990) will be discussed at length.

For surface gravity waves, the dependence of the cross-spectra on the underlying spectrum, given in eq. 2.5 for the individual cross-spectrum C_{ij} , can be succinctly abbreviated as

$$\mathbf{d}(\omega) = \int \mathbf{b}(\omega, \theta) S(\omega, \theta) d\theta \quad (2.18)$$

where \mathbf{d} is a column vector representing the set C_{ij} , \mathbf{b} is the column vector of "transfer functions" corresponding to \mathbf{d} , and S is the directional wave spectrum. As noted previously, the transfer functions \mathbf{b} relate the contribution to \mathbf{d} from wave energy at angular frequency ω and propagating in direction θ . For notational convenience, the dependence on ω will not be retained explicitly. The measured \mathbf{d} , denoted as $\tilde{\mathbf{d}}$, contains errors ϵ due to statistical fluctuations inherent in estimating the C_{ij} from finite length time series, instrument noise, and contamination from physical phenomena other than waves (e.g. turbulence).

Long (1986) gives a detailed discussion on the "inverse modelling" approach. According to Long, the problem of estimating the directional waveheight spectrum $S(\theta)$ (dropping ω from the notation for convenience) from a finite number of integral relationships of the form of eq. 2.18 is known as an "inverse" problem. An inverse problem arises whenever the observables of a physical system are related to a set of parameters which define the system by a set of known functionals such as eq. 2.18. Inverse modelling techniques were first applied to geophysical data by Backus and Gilbert (1967). The first application of this formalism to wave spectra estimation was by Long and Hasselman (1979).

Following Long (1986), the classification of the problem may be thought of in terms of linear algebra, if S is replaced by a linear model function with M parameters, i.e. $S(\theta)$ is given by

$$S(\theta) = \Phi^T(\theta) \mathbf{p} = \sum_{i=1}^M \Phi_i(\theta) p_i \quad (2.19)$$

where Φ is a M element column vector of basis functions and p is the M element column vector of parameters. With this model for the spectrum, the measured data \tilde{d} , reflecting the N integral equations summarized in eq. 2.18 and measurement noise ϵ , can be written as

$$\tilde{d} = d + \epsilon = A p + \epsilon \quad (2.20)$$

where A is an $N \times M$ matrix defined by

$$A = \int d\theta \mathbf{b} \Phi^T \quad (2.21)$$

Suppose A has full rank, denoted as Q . If the data set is smaller than the parameter set ($Q = N < M$), then the system is underdetermined and more than one p yields \tilde{d} . If the data set and the parameter set have equal dimensions ($Q = N = M$), then the parameters are uniquely determined. Since the measured data are noisy, though, the estimated parameter set may be extremely sensitive to these errors. If the data set is larger than the parameter set ($N > M = Q$), the system is overconstrained and probably inconsistent due to the errors ϵ . In this case, it is possible that *no* p yields the measured data. Finally, if the rank Q of A is less than both M and N , the system is both overconstrained and underdetermined. Thus the solution to eq. 2.21 may or may not exist, and if it does exist, it may not be unique.

It is possible, however, to construct a unique solution to eq. 2.21 based on the "generalized inverse" by adding constraints to the problem. For example, the solution \hat{p} may be required to be the "simplest" of a set of possible solutions. If H is the generalized matrix inverse to A , then the solution \hat{p} is

$$\hat{p} = H \tilde{d} = (H A) p + H \epsilon \quad (2.22)$$

and the data vector \hat{d} corresponding to \hat{p} is

$$\hat{d} = A \hat{p} = (A H) \tilde{d} \quad (2.23)$$

The underlying parameters are seen "as through a glass, darkly", the matrix HA (eq. 2.22) being the "glass." The matrix HA is known as the "resolution matrix" and determines how well the underlying parameters can be reproduced. The matrix AH (eq. 2.23) is the "information matrix," and determines how well the data can be reconstructed (Long, 1986).

The parameter set for the directional spectrum $S(\theta)$ is actually of infinite dimension. One possible parameter set to represent the directional spectrum is the set of coefficients $\{p_n\}$ from the Fourier series expansion of the directional spectrum given by

$$S(\theta) = \sum_{n=-\infty}^{\infty} p_n \exp[in\theta] \quad (2.24)$$

where $p_{-n} = p_n^*$ because S is real. The expansion coefficients can be obtained by measuring integral quantities of the directional spectrum given by

$$p_n = \frac{1}{2\pi} \int_{-\pi}^{\pi} d\theta S(\theta) \exp[-in\theta] \quad (2.25)$$

If \vec{d} has N independent values, then at most N parameters can be determined from eq. 2.22. Thus not only is the data inaccurate, it is also inadequate to determine this countably infinite parameter set. It may, however, be possible to use the physics of the particular problem at hand to reduce the dimensionality of the parameter set for S by introducing suitable constraints on the solution. Model fitting by assuming a particular functional form for S , defined by a finite number of parameters, is an example of such a reduction by constraint. Alternative or additional constraints, such as requiring S to be non-negative, may also help reduce the dimensionality of the parameter set. In addition to satisfying the constraints, the solution for S should reflect the uncertainties in the data (Long, 1986). Thus disagreement between the data and the estimated spectrum, characterized by using the estimated spectrum in eq. 3.21 (or eq. 3.19), should be statistically consistent with the errors expected in the data.

It is not always apparent in the techniques which have been developed for directional spectra estimation what constraints and assumptions have been (sometimes implicitly) used. In addition, in many of the approaches (including the point estimation approaches discussed previously), there is no attempt to ensure that the estimated spectrum be consistent with the data in a statistically significant sense. As Long (1986) argues, a coherent approach to spectral estimation should include both of these characteristics.

The inverse modelling approaches of Long and Hasselman (1979) and Herbers and Guza (1990) possess several advantages which the other approaches to directional spectra

estimation do not. The inverse modelling approaches are applicable to spatially distributed array measurements, as well as to point array measurements (there is some difficulty applying Longuet-Higgins *et. al.*'s (1963) Fourier series expansion approach as well as Lygre and Krogstad's (1986) MEM approach to spatially-distributed array data). Inverse modelling approaches can incorporate the constraint that the spectrum be nonnegative, as well as possible additional constraints based on the physics of the particular situation (e.g. shadowing by an island or refractive effects). Of the approaches mentioned so far, only the MEM (Lygre and Krogstad, 1986) incorporates the non-negativity of the spectrum as a constraint. For the other approaches, if the estimated spectrum *was* nonnegative definite, this was a consequence of the wavenumber window used, and thus merely fortuitous, not of a constraint applied *a priori* to the spectrum. Finally, the inverse modelling approaches are the only ones which produce a spectrum which is constrained to be *statistically* consistent, at some level, with the measured cross-spectra. The IMLE approaches of Pawka (1983) and Oltman-Shay and Guza (1984) are essentially based on achieving a specified level of agreement between the measured cross-spectra and the cross-spectra computed from the estimated spectrum, but this agreement is not interpreted statistically.

The inverse modelling approach is based on finding the "best" nonnegative function which fits the data at some statistical confidence level. The estimated spectrum is the solution to a variational problem, which may be cast as minimizing the functional

$$J[S] = \alpha \{ \rho^2 - (\bar{\mathbf{d}} - \mathbf{d}[S])^T \mathbf{V}^{-1} (\bar{\mathbf{d}} - \mathbf{d}[S]) \} + \beta \int d\theta \{ S(\theta) - |S(\theta)| \}^2 + R[S] \quad (2.26)$$

where $\bar{\mathbf{d}}$ is again the measured cross-spectra data, $\mathbf{d}[S]$ is the cross-spectra corresponding to S (based on eq. 2.18 or eq. 2.20), \mathbf{V} is the covariance matrix corresponding to the measured cross-spectra, ρ^2 is the chi-square value corresponding to the desired confidence level for fitting the measured cross spectra, and α and β are Lagrange multipliers. The first term in the equation corresponds to the constraint that S be statistically consistent with the data at the given confidence level. The second term corresponds to the constraint that the spectrum be nonnegative. The third term, $R[S]$, determines what is meant by the "best" function of those which meet the other constraints. Additional constraints which apply in particular situations can be incorporated by additional Lagrange multipliers. The estimated

directional spectrum at frequency ω , then, is that function \hat{S} which minimizes the functional J .

The "best" function is chosen to minimize some "nasty" property of the directional spectrum $S(\theta)$, subject to the other constraints (Long and Hasselman, 1979). Long and Hasselman (1979) sought a spectrum which was the best approximation to a particular model S_m consistent with the other constraints. They consequently chose the form

$$R[S] = \int d\theta \{S(\theta) - S_m(\theta)\}^2 \quad (2.27)$$

to express the nastiness of the spectrum.

Herbers and Guza (1990) sought a spectrum which is the "smoothest" spectrum consistent with the other constraints. Consequently, they chose a form which minimizes the "roughness" of the spectrum, where they define the roughness as

$$R[S] = \int d\theta \left\{ \frac{d^2 S}{d\theta^2} \right\}^2 \quad (2.28)$$

This approach has been applied by Provost and Salmon (1986) to hydrographic data to estimate the three-dimensional geostrophic velocity field and by Constable *et al.* (1987) to electromagnetic sounding data. This expression for the "nastiness" has the advantage that it is model independent, so that features which are reflected in the estimated spectrum are not consequences of the particular model chosen. As such, Herbers and Guza (1990) argue, this approach is more objective than that of Long and Hasselman (1979). They also contend that this approach reduces "spurious" structure in the estimated spectrum. "High resolution" spectral estimates from the MLE or the MEM can include peaks which do not correspond to the true spectrum but are caused by the sensitivity of the techniques to noise in the data. Herbers and Guza (1990) argue that the transfer functions b in eq. 2.18 make the measured cross-spectra relatively insensitive to the spectrum shape. Gross features are reflected in d , but rapid oscillations in the spectrum are simply smoothed out and estimates of such structure are completely arbitrary. The nastiness measure selected thus ensures that only features which are reflected in the data will be reflected in the spectrum. Features which are "fundamentally" unresolvable will remain that way.

Herbers and Guza (1990) compared their approach with that of Long and Hasselman (1979) using the same true spectrum (a unimodal $\cos^{20}(\theta/2)$ spectrum) and the same simulation approach (simulating cross spectra from a pressure sensor array with statistical fluctuations consistent with either 30 or 180 degrees of freedom) as the latter study. The estimated spectra produced by minimizing the roughness measure in eq.2.28 matched the true spectrum shape much better than the results presented by Long and Hasselman (1979) for both 30 and 180 degrees of freedom in the cross-spectra. Their results also produced very minimal sidelobes, if at all. For the spectrum shape used, at least, the model independent approach of Herbers and Guza (1990) outperformed the model dependent approach of Long and Hasselman (1979).

The generalized inverse approach was attempted for this study is identical to the Herbers and Guza (1990) approach which incorporates topographic constraints. These constraints require that the directional spectrum $S(\theta)$ be identically zero outside m open intervals of direction $\{\theta_1^m, \theta_2^m\}$ which are defined *a priori*. Since little wave energy is typically reflected from the beach at the experiment site (Long and Oltman-Shay, 1991), a topographic constraint requiring that $S(\theta)$ be zero for seaward propagating directions was incorporated here. However, tests using simulated cross spectra failed to achieve adequate results and this approach was dropped. Given the algorithmic complexity of this method, I'm sure that the failure of my implementation of this method to produce reasonable results reflects an implementation error and not a fundamental inconsistency in applying the method to ADCP data.

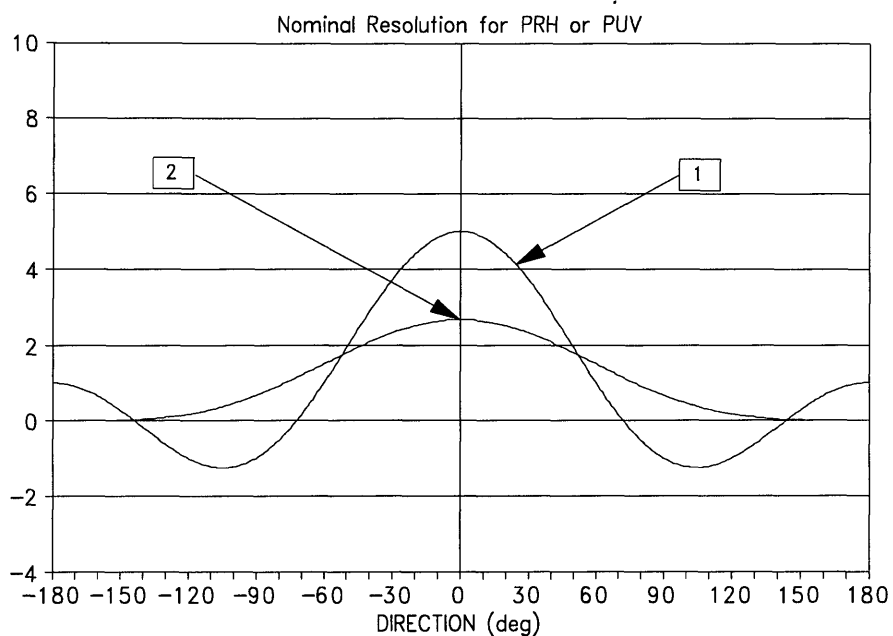


Figure 2-1 Resolution functions for PRH buoy. 1: uniform weighting. 2: weighting for non-negative spectral estimate suggested by Longuet-Higgins, *et al.* (1963).

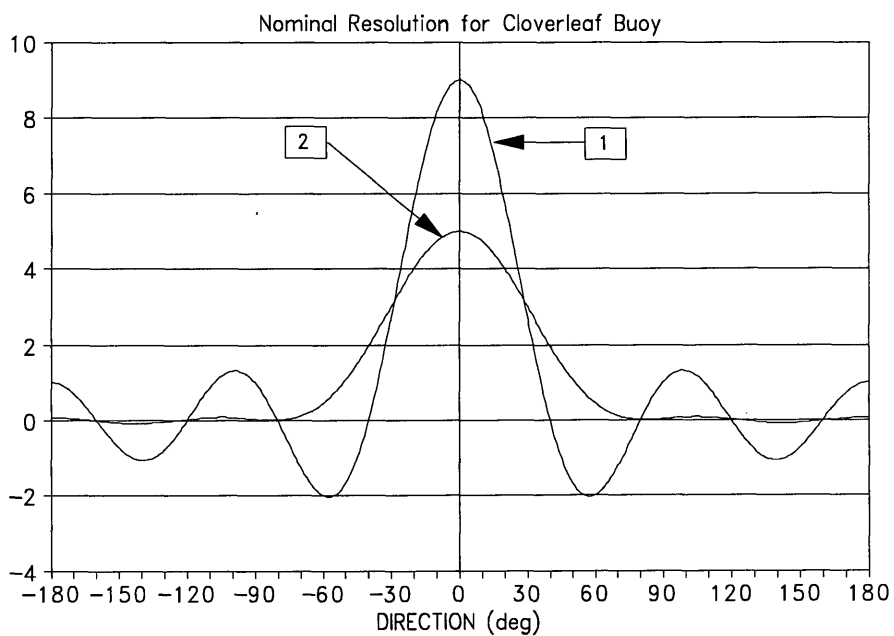


Figure 2-2 Resolution functions for a cloverleaf buoy. 1: uniform weighting. 2: weighting suggested by Cartwright and Smith (1964) to reduce negative sidelobe energy.

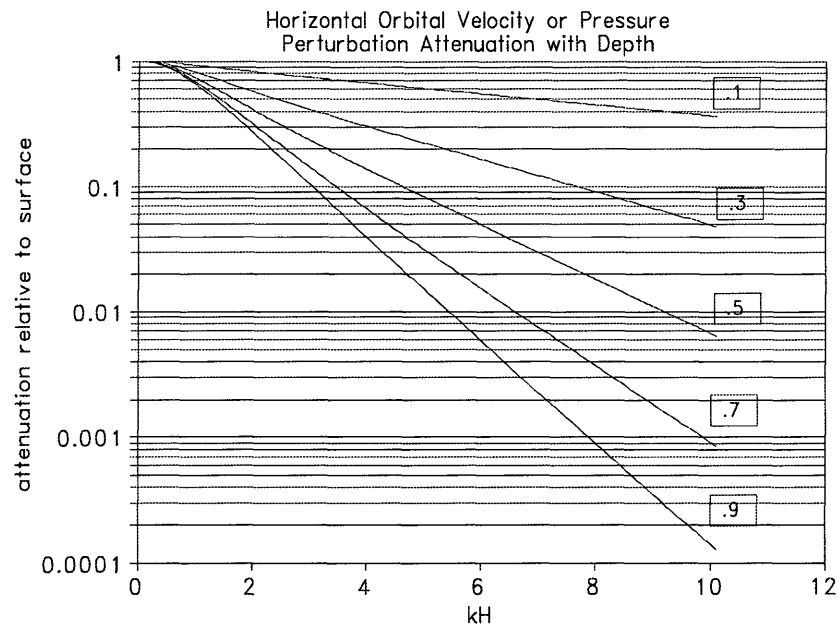


Figure 2-3 Attenuation of horizontal orbital velocity or perturbation pressure with depth. Plotted for values of $z/H = 0.1, 0.3, 0.5, 0.7, 0.9$.

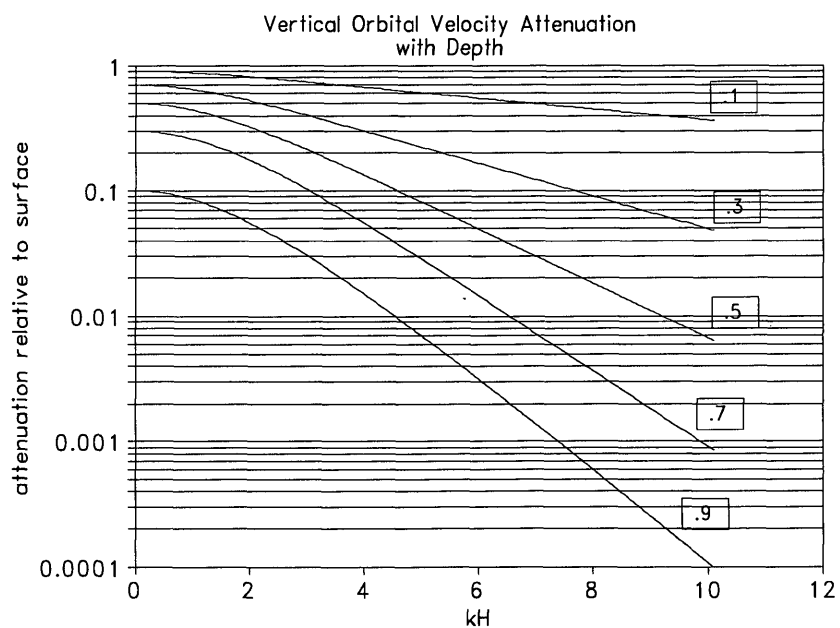


Figure 2-4 Attenuation of vertical orbital velocity with depth. Plotted for values of $z/H = 0.1, 0.3, 0.5, 0.7, 0.9$.

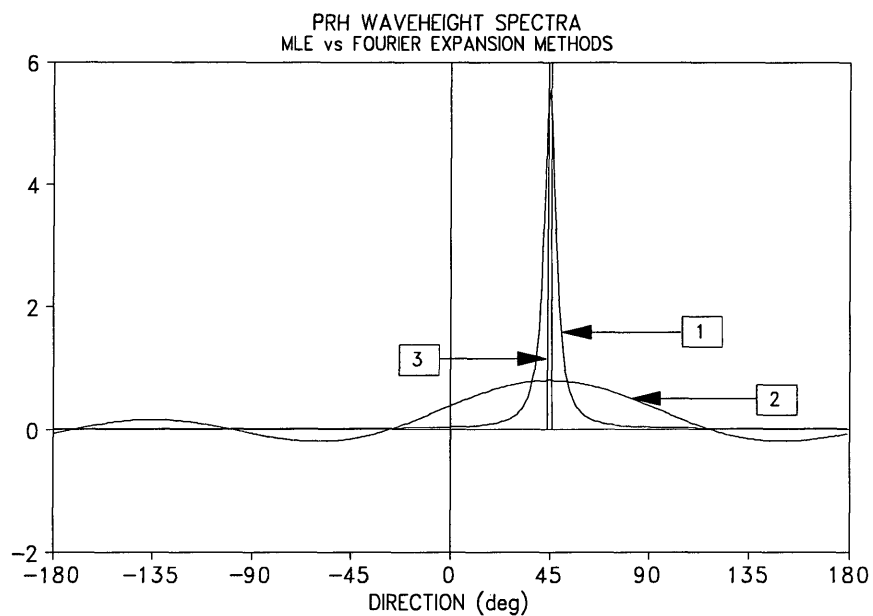


Figure 2-5 Comparison of estimated waveheight spectrum for PRH buoy data. Spectra are: 1) extended MLE approach, 2) truncated Fourier series approach, 3) true spectrum.

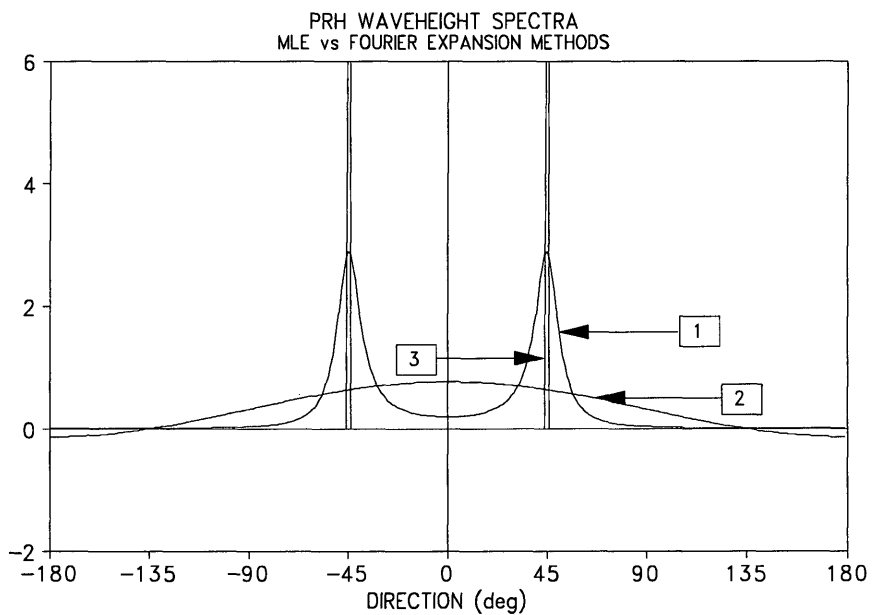


Figure 2-6 Comparison of estimated waveheight spectrum for PRH buoy data. Spectra are: 1) extended MLE approach, 2) truncated Fourier series approach, 3) true spectrum.

3. ADCP OVERVIEW

The ADCP used in this experiment is an RD Instruments model DR 1200 kHz narrowband ADCP. A description of the instrument and its operating principles is given in this section. Equations relating the cross spectra of ADCP time series to the directional wave spectrum are developed and a sensitivity analysis is presented which indicates the range of waveheights for which the ADCP can be expected to yield meaningful directional spectra.

3.1 Instrument description

The RD Instruments model DR Acoustic Doppler Current Profiler consists of four ceramic transducers which can produce narrow beams of acoustic energy. The overall configuration is sketched in fig. 3-1. Each transducer is tilted 30° from a common vertical axis. The four are mounted in a square so that the beams form, in the horizontal, an outward extension of the diagonals of the square. This is known as the *Janus* configuration. The RDI model DR also has a flux gate compass to measure heading and two pendulum sensors to measure pitch and roll. An AC power supply and data logger are external to the RDI DR model.

The operating parameters of the VIMS ADCP, compiled from the RDI model DR Technical Manual (RDI, 1991) and Practical Primer (RDI, 1989b), are listed in table 3-1. It operates at a transmit frequency of 1228.8 kHz and has a nominal range of 30m. The sampling characteristics of the ADCP are given in terms of vertical distances based on a 30° beam inclination. The minimum transmit pulse length is 1 vertical meter, which corresponds to a pulse length of 1.47 ms. The minimum depth cell, or receive pulse length, is 1 vertical meter also. The 3 dB beamwidth is 1.4° and the average sidelobe is 42 dB down from the peak for the transmit beam power. The same aperture is used for the receive beam, so the average two-way sidelobe is over 80 dB down from the peak.

The ADCP makes current measurements by transmitting pulses, or "pings", of acoustic energy through the water column and receiving the backscattered energy (RDI, 1989b). The

transmitted energy occupies a very narrow frequency band and has a pulselength of a few milliseconds. It is focussed into a narrow pencil-like "beam" to give it directionality.

As the energy propagates away from the ADCP in the beam direction, some of it is scattered from small particles (e.g. suspended sediment, plankton) in the water column which are assumed to be convected at the fluid velocity. Part of this scattered energy is reflected back towards the ADCP, which then acts as a receiver and measures the reflected signal. Because the signal is transmitted over a finite length of time and because the beam has a finite width, the received signal consists of energy scattered by particles in a range and direction interval, rather than at a single range and direction (fig. 3-2).

The time between transmit and receive gives the distance (or "range") interval at which the received energy was scattered. If a particle which reflects the acoustic energy back to the ADCP is moving towards or away from it, the frequency of the backscattered energy is changed. This frequency change, the Doppler effect, is proportional to both the radial velocity of the particle relative to the ADCP and the frequency of the transmitted pulse. Because energy reflected by a number of particles (which may be moving with slightly different radial velocities) contributes to it, the received signal actually has a frequency spectrum--rather than a single frequency. The spectrum represents, in some sense, a weighted distribution of the particle velocities in the volume of fluid illuminated by the pulse at an instant in time. The "weight" attached to each particle velocity in the spectrum corresponds to the energy which that particle reflected. The observed spectrum, however, is a convolution of the frequency window determined by the acoustic pulselength and the "true" frequency spectrum. Because the pulselength is very short, the frequency window is very wide and the observed spectrum width is primarily due to the short pulselength, not to any intrinsic width of the true spectrum (RDI, 1989b).

The RDI model DR ADCP estimates the frequency shift in a multi-step process (RDI, 1989b). The received signal is first shifted to an intermediate frequency and filtered by a wideband filter. The signal is then frequency-shifted and filtered again, this time by a narrowband, variable frequency "tracking" filter which shifts the signal to a frequency band near zero where it is digitized. The in-phase and quadrature signal components are maintained during this process. The digitized signal can then be considered as a complex signal, with the real and imaginary components equal to the in-phase and quadrature

components, respectively.

The mean frequency of the filtered/demodulated signal could be estimated by computing the first moment of the spectrum calculated using an FFT approach. Instead, the model DR ADCP uses time domain processing based on the covariance approach developed by Rummler (1968) and Miller and Rochwarger (1972) to estimate the mean frequency. If the signal $s(t)$ can be regarded as a complex gaussian process, then the phase of the signal autocovariance is proportional to the first moment of the spectrum. The autocovariance at a single time lag τ (much less than the pulselength) is estimated by averaging the Rummler product $s(t+\tau)s^*(t)$ over a time interval usually chosen as equal to the transmit pulse length (RDI, 1989b). This increases the volume of fluid which contributes to the Doppler velocity estimate, as illustrated in fig. 3-2. The resulting Doppler velocity estimate is regarded as corresponding to the center of the fluid volume, which is referred to as a range of depth "bin." In this study, bin centers were separated by 1.155 m along each beam. Velocity estimates from adjacent bins in a beam are approximately 15% correlated due to the overlap of the fluid volumes sampled for such bins (RDI, 1989b).

Theriault (1986) has derived an expression for the Cramer-Rao bound (a theoretical lower bound) on the Doppler frequency error variance. He shows that the variance of the error in the single ping Doppler frequency estimate is a function of the pulselength and the signal-to-noise ratio (SNR), defined as the ratio of the signal variance to the instrument noise variance. This expression, written for the Doppler velocity rather than the Doppler frequency, is

$$\sigma_v^2 = \left(\frac{c}{4\pi f_o}\right)^2 \frac{1}{T^2 SNR^2} \cdot \frac{SNR^2}{36 SNR + 30} \quad (3.1)$$

where c is the speed of sound, f_o is the transmit frequency, and T is the pulselength. Since the ADCP signal-to-noise ratio is typically high, the term involving the SNR simply reduces to unity. Using the ADCP parameters from table 3-1, $c = 1500$ m/s, and assuming high SNR, the minimum velocity standard deviation per ping will be 6.6 cm/s. A more realistic estimate of the Doppler velocity error variance for the ADCP used in this experiment is obtained by multiplying eq. 3.1 by a factor of 1.5 (RDI, 1989b). The estimate variance can be reduced by a factor of $1/N$ by averaging N pings together. The estimate variance can also be

decreased by increasing the pulselength. However, this is not desirable for orbital velocity measurements, since a longer pulselength implies increasing the spatial area over which the velocity estimate is smoothed. Bias errors are on the order of 0.5 - 1.0 cm/s (RDI, 1989b).

By detecting the Doppler frequency change, the ADCP makes a measurement equivalent a spatially-averaged measurement of the radial fluid velocity relative to the instrument at a known range and direction. The ADCP profiles the water column along the beam by measuring the mean frequency of the reflected signal at different times, corresponding to different ranges. It thus obtains measurements somewhat equivalent to a linear array of conventional one-axis current meters oriented along the beam direction.

Two beams, pointed in opposite horizontal directions, allow estimation of the horizontal fluid velocity parallel to the beams and the vertical velocity with one acoustic ping. With the *Janus* configuration, horizontal velocity estimates in two orthogonal directions can be calculated, as can two estimates of the vertical velocity. This approach allows one to estimate currents whose spatial scale is larger than the separation of the fluid volumes sampled by each beam to obtain the Doppler velocities. This aliases spatial energy with smaller scales but is valid for mean current measurements in areas where horizontal shear is not significant. For this experiment, the smaller spatial scales (i.e. waves) are of interest, so Doppler information from the individual beams is not combined on a ping-to-ping basis. At times it will be necessary to refer to a specific range or depth bin within a specific beam. Although the terminology is still somewhat unwieldy, I will use the shorthand "bin/beam pair" to refer to a specific bin within a specific beam.

3.2 ADCP directional wave spectra

The general form for the cross spectra of the wave-related ADCP measurements is derived in this section. As discussed in the previous section, the single ping Doppler velocity estimate obtained for a given bin/beam pair can be modelled as a weighted average of the radial component (relative to the beam direction) of particle velocities. It is assumed here that this weighting is dependent only on the position of each particle relative to the center of the bin and does not vary from ping to ping. This is equivalent to assuming that all particle scattering cross-sections are similar and that none are appreciably larger than the rest (i.e. no specular reflectors are considered). For generality, suppose that an ADCP beam is pointed

at the horizontal azimuth angle α (relative to some x -axis) and inclined from the vertical by the angle β . Let $b(\underline{x}', z'; \underline{x}, z)$ denote the weighting in the rangebin centered at \underline{x}, z to a particle at position \underline{x}', z' . The contribution to the ADCP Doppler velocity for this bin from a small volume at \underline{x}', z' will then be the true velocity of the particle at this position projected onto a unit vector $\underline{\phi}$ from the ADCP transducer to \underline{x}', z' , weighted by b . The total Doppler velocity measured by the ADCP will be the integral of this quantity over the water column, plus noise. If the velocity field is $\underline{u}(\underline{x}, z, t)$, then the Doppler velocity V_d estimated at the rangebin centered at \underline{x}, z at time t is

$$V_d(t; \underline{x}, z) = \int d^2x' dz' b(\underline{x}', z'; \underline{x}, z) [\underline{\phi}(\underline{x}', z') \cdot \underline{u}(\underline{x}', z', t)] \cdot N_d(\underline{x}, z, t) \quad (3.2)$$

where N_d is the ADCP noise at time t for the rangebin in question.

The velocity \underline{u} includes the mean and turbulent components as well as orbital velocities. The wave component of the Doppler velocity, V_{wd} is related to the stochastic sea surface Fourier amplitudes $dB_\eta(\omega, \theta)$ (using the notation developed in Appendix A) by

$$\begin{aligned} V_{wd}(t; \underline{x}, z) &= \int d^2x' dz' b(\underline{x}', z'; \underline{x}, z) \sum_{i=1}^3 [\phi_i(\underline{x}', z') f_i(\underline{x}', z', t)] \\ &\cdot \int d\omega d\theta \exp\{i[\underline{k}(\omega, \theta) \cdot \underline{x}' - \omega t]\} dB_\eta(\omega, \theta) \\ &\times \sum_{i=1}^3 \phi_i(\underline{x}', z') F_i(\omega, \theta, z') \\ &\cdot \int d^2x' dz' b(\underline{x}', z'; \underline{x}, z) \int d\omega d\theta \exp\{i[\underline{k}(\omega, \theta) \cdot \underline{x}' - \omega t]\} dB_\eta(\omega, \theta) \\ &\times (-\omega) \left\{ [\phi_1 \cos\theta + \phi_2 \sin\theta] \frac{\cosh[k(z'-h)]}{\sinh[kh]} - i \phi_3 \frac{\sinh[k(z'-h)]}{\sinh[kh]} \right\} \end{aligned} \quad (3.3)$$

where the ϕ_i are the components of the unit vector $\underline{\phi}$ and $[f_1, f_2, f_3]$ are the wave-related parts of $[u, v, w]$, $[F_1, F_2, F_3]$ are the transfer functions associated with $[u, v, w]$, and h is the total water depth.

The wave-related temporal cross correlation $R^{wd}_{ij}(\tau)$ at time interval τ between bin/beam pairs located at \underline{x}_i, z_i and \underline{x}_j, z_j is defined as

$$R^{wd}_{ij}(\tau) = \langle V_{wd}(t+\tau; \underline{x}_i, z_i) V_{wd}(t; \underline{x}_j, z_j) \rangle \quad (3.4)$$

Substituting eq. 3.3 into eq. 3.4 yields:

$$\begin{aligned}
R^{wd}_{ij}(\tau) &= \sum_{p,q=1}^3 \int d^2x' dz' b(\underline{x}', z', \underline{x}_p, z_p) \phi_p(\underline{x}', z') \\
&\quad \times \int d^2x'' dz'' b(\underline{x}'', z'', \underline{x}_q, z_q) \phi_q(\underline{x}'', z'') \\
&\quad \times \langle f'_p(\underline{x}', z', t, \tau) f'_q(\underline{x}'', z'', t) \rangle
\end{aligned} \tag{3.5}$$

and using eq.s A.36 and A.37, one obtains

$$\begin{aligned}
R^{wd}_{ij}(\tau) &\cdot \frac{1}{2\pi} \int d\omega d\theta e^{-i\omega\tau} S(\omega, \theta) \\
&\quad \times \sum_{p,q=1}^3 \int dz' F_p(\omega, \theta, z') \int d^2x' b(\underline{x}', z', \underline{x}_p, z_p) \phi_p(\underline{x}', z') e^{i\underline{k}\underline{x}'} \\
&\quad \times \{ \int dz'' F_q(\omega, \theta, z'') \int d^2x'' b(\underline{x}'', z'', \underline{x}_q, z_q) \phi_q(\underline{x}'', z'') e^{i\underline{k}\underline{x}''} \}.
\end{aligned} \tag{3.6}$$

The wave-related cross spectra $C^{wd}_{ij}(\omega)$ for this pair of bin/beam pairs is related to the cross correlation $R^{wd}_{ij}(\tau)$ of the respective time series by

$$R^{wd}_{ij}(\tau) = \frac{1}{2\pi} \int d\omega C^{wd}_{ij}(\omega) e^{-i\omega\tau} \tag{3.7}$$

By comparison with eq. 3.6, the ADCP wave-related cross spectra is seen to be related to the directional wave spectrum by

$$\begin{aligned}
C^{wd}_{ij}(\omega) &\cdot \int d\theta S(\omega, \theta) \\
&\quad \times \left\{ \sum_{p=1}^3 \int dz' F_p(\omega, \theta, z') \int d^2x' b(\underline{x}', z', \underline{x}_p, z_p) \phi_p(\underline{x}', z') e^{i\underline{k}\underline{x}'} \right\} \\
&\quad \times \left\{ \sum_{q=1}^3 \int dz'' F_q(\omega, \theta, z'') \int d^2x'' b(\underline{x}'', z'', \underline{x}_q, z_q) \phi_q(\underline{x}'', z'') e^{i\underline{k}\underline{x}''} \right\}.
\end{aligned} \tag{3.8}$$

which has the canonical form:

$$C^{wd}_{ij}(\omega) = \int d\theta G_i(\omega, \theta) G_j^*(\omega, \theta) S(\omega, \theta) \tag{3.9}$$

The complexity of the ADCP cross spectra is due to two factors. The first is that the ADCP measures the radial component of the velocity field along each beam. If the beams are not directed horizontally or vertically, this velocity component includes a mixture of u ,

v , and w components. The second complicating factor is that the ADCP samples a volume in space, not a point. To simplify the modelling, it is assumed that the dimensions of the sampling volume are small radially and very small azimuthally relative to the wavelengths of interest. The sampling volume is then small enough to be regarded as a point, $b(\underline{x}', z'; \underline{x}, z)$ becomes a delta function centered at \underline{x}, z , and the form of the cross spectra simplifies greatly. For this assumption, with a given beam direction specified by the angles α and β , the radial unit vector $\underline{\phi}$ becomes $\underline{\phi}(\alpha, \beta)$ where

$$\underline{\phi}(\alpha, \beta) = \begin{bmatrix} \cos\alpha \sin\beta \\ \sin\alpha \sin\beta \\ \cos\beta \end{bmatrix} \quad (3.10)$$

The ADCP cross spectra, for beam directions specified by α_i, β_i and α_j, β_j , then becomes

$$\begin{aligned} C^{wd}_{ij}(\omega) &= \int d\theta S(\omega, \theta) \exp\{i\mathbf{k} \cdot (\underline{x}_i - \underline{x}_j)\} \left[\frac{\omega}{\sinh(kh)} \right]^2 \\ &\times \{ \cos(\alpha_i - \theta) \sin\beta_i \cosh[k(z_i, h)] - i \cos\beta_i \sinh[k(z_i, h)] \} \\ &\times \{ \cos(\alpha_j - \theta) \sin\beta_j \cosh[k(z_j, h)] - i \cos\beta_j \sinh[k(z_j, h)] \} \end{aligned} \quad (3.11)$$

The ADCP autospectra, i.e. the diagonal terms of the cross spectra, is given by

$$\begin{aligned} A^{wd}(\omega; z_i, \alpha_i, \beta_i) &= C^{wd}_{ii}(\omega) \\ &= \int d\theta S(\omega, \theta) \omega^2 \\ &\times \left\{ \cos^2(\alpha_i - \theta) \sin^2\beta_i \frac{\cosh^2[k(z_i, h)]}{\sinh^2[kh]} + \cos^2\beta_i \frac{\sinh^2[k(z_i, h)]}{\sinh^2[kh]} \right\} \end{aligned} \quad (3.12)$$

If the vertical inclination angle β_i is identical for each ADCP beam (i.e. the ADCP is not tilted relative to the vertical), then an estimate of the nondirectional wave frequency spectrum can be obtained from the autospectra of two rangebins located at the same depth but in beams directed orthogonally to each other in the horizontal plane (e.g., adjacent beams in the Janus configuration). For such a situation, the α_i 's in eq. 3.12 corresponding to the different beams differ by $\pi/2$. From eq. 3.12, then, the sum of the two autospectra is independent of angle and proportional to the integral of the directional wave spectrum over direction, i.e. the nondirectional wave frequency spectrum. Based on this, an estimate of the nondirectional wave spectrum is given by:

$$\hat{S}(\omega; z) = \frac{A^{wd}(\omega; z, \alpha, \beta) + A^{wd}(\omega; z, \alpha + \frac{\pi}{2}, \beta)}{\omega^2 \left\{ \sin^2 \beta \frac{\cosh^2[k(z \cdot h)]}{\sinh^2[kh]} + 2 \cos^2 \beta \frac{\sinh^2[k(z \cdot h)]}{\sinh^2[kh]} \right\}} \quad (3.13)$$

where the subscripts have been dropped. Note that the estimated wave frequency spectrum is depth dependent, due to possible biases in the autospectrum, although the true spectrum is not.

To test the feasibility of obtaining directional spectra estimates from ADCP measurements, ADCP cross spectra were simulated for several types of directional spectra (unimodal and bimodal) using eq. 3.11. MLE and IMLE spectra were computed from the simulated cross spectra using eq.s 2.15 and 2.17 with

$$G_i(\omega, \theta) = \exp\{i \mathbf{k}(\omega, \theta) \cdot \mathbf{x}_i\} \frac{\omega}{\sinh[kh]} \times \{\cos(\alpha_i - \theta) \sin \beta_i \cosh[k(z_i \cdot h)] - i \cos \beta_i \sinh[k(z_i \cdot h)]\} \quad (3.14)$$

A sample result is shown in fig.s 3-3 and 3-4. The true directional spectrum is bimodal, with peaks centered at -45° and at $+30^\circ$, and has a small uniform "noise" floor. The modes are gaussian-shaped; the mode at -45° has a one- σ width of 3° and its peak is twice as high as the mode at $+30^\circ$, which has a one- σ width of 10° . The frequency used was 0.3 Hz. The ADCP cross spectra were simulated for four beams with rangebins at 2 and 4 m depths in a total depth of 10 m. For comparison, the cross spectra of a PUV meter at 9 m depth was also simulated and similarly used to estimate the directional spectra. The results for the MLE show that the estimated ADCP directional spectra correctly reproduces the peak positions but underestimates their amplitudes. In the PUV results, however, the peaks are unresolved, with the resulting unimodal spectrum skewed toward the wider peak at $+30^\circ$. The IMLE results are more striking. The mode at -45° is almost exactly reproduced in the ADCP directional spectrum. The other mode is very nearly reproduced, but the IMLE technique does over-resolve the single peak into a double peak. On the other hand, the IMLE spectrum estimated from the PUV cross spectra gives only a very slight indication that wave energy is propagating at two, rather than one, directions. Although certainly not conclusive, these results indicate the potential for obtaining better-resolved directional spectra from ADCP measurements than from PUV measurements. To some extent, whether the indicated

resolution is actually achievable will depend on sensor noise levels and statistical variability, as well as on how well the ADCP measurements are reflected by the spatial δ -function weighting used to develop the ADCP transfer functions.

3.3 ADCP sensitivity criteria

To some extent, the ability to obtain good directional spectra estimates from ADCP data depends on noise levels in the ADCP relative to the wave orbital velocity "signal". Sensitivity criteria for orbital velocity measurements made by the ADCP can be developed. The first step in estimating the wave directional spectrum from the ADCP measurements is to form cross- and autospectra from the data for each pair of rangebins. Following Smith (1989), a reasonable sensitivity criterion for the ADCP is that a narrow-band wave "signal" in the Doppler velocity auto- and cross-spectra should be larger than the noise level in order to make directional wave spectra estimation feasible. One is thus interested in the dependence of the ratio

$$R = \frac{A^{wd}(\omega ; z, \alpha, \beta)}{Q(\omega)} \quad (3.15)$$

on the wave climate and on system parameters such as ping averaging and nyquist frequency. In the equation, A^{wd} is the wave-related ADCP velocity autospectral density from eq. 3.12 at radian frequency ω for a rangebin at depth z in a beam "pointed" with horizontal azimuth α and vertical inclination β . Q is the ADCP spectral noise level. An expression for this ratio can be developed in terms of a narrow-band waveheight and the ADCP noise per ping.

In the limit of high signal-to-noise ratio, Theriault's (1986) expression for the variance of the ADCP noise (eq. 3.1) becomes

$$\sigma_v^2 = \left(\frac{c}{4\pi f_0 T} \right)^2 \quad (3.16)$$

where c is the speed of sound, f_0 is the ADCP operating frequency, and T is the transmit/receive pulse length. Using the following relations between the pulse length T , the alongbeam rangebin size ΔR , and the vertical rangebin size ΔR_v ,

$$\Delta R = \frac{1}{2} c T \quad (3.17)$$

$$\Delta R_z = \Delta R \cos \beta$$

where β is the angle of beam inclination from the vertical, the expression for the ADCP noise variance becomes

$$\sigma_v^2 = \left(\frac{c^2 \cos \beta}{8 \pi f_0 \Delta R_z} \right)^2 \quad (3.18)$$

The noise is assumed to be normally-distributed white noise and independent between different rangebins. Actually, rangebins along the same beam are correlated if they are closer than ΔR apart. For the RDI ADCP, adjacent rangebins are about 15% correlated (RDI, 1989b). This correlation is small and is ignored in this analysis, although in data processing adjacent rangebins are excluded from the cross spectra matrix. For the nominal ADCP parameters listed in table 3-1, the single ping variance is expected to be approximately 100 (cm/s)² for this ADCP.

If each n pings are ensemble averaged before recording, then the noise level per ensemble becomes

$$\langle (\Delta V)^2 \rangle = \frac{\sigma_v^2}{n} \quad (3.19)$$

The noise variance per ensemble is related to the two-sided noise spectral density $Q(\omega)$ by

$$\langle (\Delta V)^2 \rangle = \frac{1}{2\pi} \int_{-\omega_n}^{\omega_n} Q(\omega) d\omega \quad (3.20)$$

where ω_n is the radian nyquist frequency. For white noise, Q is constant. This relation can consequently be inverted to yield

$$Q = \frac{2\pi \langle (\Delta V)^2 \rangle}{2 \omega_n} = \frac{\pi \sigma_v^2}{n \omega_n} \quad (3.21)$$

As shown in section 3.2, the wave-related Doppler velocity autospectrum at radian frequency ω in the rangebin centered at depth z can be expressed in terms of the waveheight spectrum by

$$A^{wd}(\omega; z, \alpha, \beta) = \int d\theta T(\omega, \theta; z, \alpha, \beta) S(\omega, \theta) \quad (3.22)$$

where the transfer function T in the limit of a delta function ADCP velocity response is

$$T(\omega, \theta; z, \alpha, \beta) = \left[\frac{\omega}{\sinh[kh]} \right]^2 \times \{ \cos^2(\alpha - \theta) \sin^2 \beta \cosh^2[k(z \cdot h)] + \cos^2 \beta \sinh^2[k(z \cdot h)] \} \quad (3.23)$$

The ratio of A^{wd} to Q depends on the nature of the directional spectrum at the frequency in question. Two situations are rather easily considered here: a line spectrum in direction and a directionally-uniform spectrum. The directional spectrum in the first situation can be expressed as

$$S_L(\omega, \theta) = S(\omega) \delta[\theta - \theta'(\omega)] \quad (3.24)$$

where $S(\omega)$ is the magnitude of the directional spike at frequency ω and θ' is the direction of wave approach at this frequency. In the second situation, the directional spectrum is simply

$$S_u(\omega, \theta) = \frac{1}{2\pi} S(\omega) \quad (3.25)$$

In the case where the spectrum is given by eq. 3.24, the autospectrum becomes, after integration,

$$A^{wd}(\omega; z, \alpha, \beta) = S(\omega) T(\omega, \theta'(\omega); z, \alpha, \beta) \quad (3.26)$$

In the case where the spectrum is directionally-uniform (eq. 3.25), the autospectrum becomes

$$A^{wd}(\omega; z, \alpha, \beta) = S(\omega) \left[\frac{\omega}{\sinh[kh]} \right]^2 \times \left\{ \frac{1}{2} \sin^2 \beta \cosh^2[k(z \cdot h)] + \cos^2 \beta \sinh^2[k(z \cdot h)] \right\} \quad (3.27)$$

$$= S(\omega) T(\omega, \alpha \pm 45^\circ; z, \alpha, \beta)$$

If $\theta'(\omega)$ in eq. 3.26 is chosen so that $\alpha - \theta'(\omega) = \pm 45^\circ$, then eq. 3.27 and eq. 3.26 are identical. Since the four ADCP beams are directed in a Janus configuration, this condition represents the situation where a line-spectrum wavetrain is most misaligned with *any* of the beams. The following analysis consequently addresses both the line spectrum and the omnidirectional spectrum.

Using eq.s 3.21 and 3.27 in eq. 3.15, the ratio of the Doppler velocity spectrum "signal" to the ADCP noise spectrum becomes

$$R = \frac{A^{wd}(\omega; z, \alpha, \beta)}{Q} \quad (3.28)$$

$$= \left\{ \frac{4n\omega_n S(\omega)}{2\pi} \right\} \frac{1}{2} \sigma_v^{-2} T(\omega, \alpha \pm 45^\circ; z, \alpha, \beta)$$

For purposes of plotting, R is turned into a "signal-to-noise ratio" defined by

$$SNR = 10 \log_{10} R \quad (3.29)$$

The dependence of SNR on rangebin depth and wave frequency is illustrated in figures 3.5 through 3.9. Nominal ADCP parameters from Table 3-1 are used to compute the noise variance. In each of the plots, the factor $N = (4n\omega_n S(\omega))/2\pi = 1 \text{ m}^2$. If the Nyquist frequency is 0.5 Hz and $n = 6$, then $S(\omega) = .083 \text{ m}^2/\text{Hz} = 830 \text{ cm}^2/\text{Hz}$ corresponds to the plotted curves. Using the Pierson-Moskowitz functional form for the nondirectional wave spectrum (Apel, 1987), this spectral density is achieved in a fully-developed sea at frequencies of 0.1, 0.2, and 0.3 Hz when 19.5 m wind speeds are 9, 5.5, and 5 m/s, respectively. The plotted functions thus correspond to reasonable situations. For conditions where N is not 1 m^2 , the corresponding curves shift up or down by

$$\Delta SNR = 10 \log_{10} [N] \quad (3.30)$$

These curves thus allow one to estimate minimum performance criteria for different ADCP rangebins.

Characteristic of the dependence of the SNR (fig.s 3-5 through 3-9) are several features which are familiar from linear wave theory. The first is the attenuation of the wave-related Doppler velocity signal with the depth of the rangebin for a given frequency wave. This is due to the well-known attenuation of orbital velocity with depth. For short period waves (say $T < 4 \text{ s}$ for the depths illustrated), this attenuation is exponential in both horizontal and vertical components. For long period waves the attenuation is much less dramatic and chiefly consists of the linear decay of the vertical component of the orbital velocity. This, of course, reflects the different characteristics of the orbital velocities of "deep water" and "shallow water" waves. The second feature is that, at least near the surface, the "signal" is larger from high frequency waves than from low frequency waves of the same amplitude. This reflects

the dependence of the orbital velocity on both the wave amplitude and the wave frequency. It thus appears that information on the higher frequency waves will be limited to the near surface rangebins.

A reasonable requirement for the "signal-to-noise" ratio is that the ratio is at least 5 dB. Continuing the example given above, and if the total depth is 20 m, then one should be able to detect the wave signal of any period wave up to nyquist in the rangebin at 2 m depth, waves with period greater than 3.5 s in the rangebin at 6 m depth, waves with period greater than 5 s in the rangebin at 10 m, and waves with period greater than 15 s in the rangebin at 18 m depth (fig.s 3-7,8). On the basis of this analysis, it appears that the ADCP is capable of making measurements with sufficient accuracy to allow wave spectra estimation if the wave spectral density $S(\omega)$ is high enough.

3.4 Statistical variability

Even in the absence of sensor noise, cross spectra computed from time series contain errors due to statistical fluctuations. It can be shown (Jenkins and Watts, 1969) that, ignoring the bias introduced by the finite length of the time series involved, the covariance between the estimated cross spectra \tilde{C}_{ij} and \tilde{C}_{kl} is given by

$$Cov[\tilde{C}_{ij}, \tilde{C}_{kl}] = \frac{2}{N_{dof}} C_{ik} C_{jl} \quad (3.31)$$

where N_{dof} is the number of degrees of freedom in the estimate of the cross spectra. The magnitude of the expected statistical fluctuations decreases as the square root of the number of degrees of freedom. For a given frequency resolution, the number of degrees of freedom will increase as the length of the time series increases. However, because the wave field can be considered stationary only over a limited time interval, the number of degrees of freedom for a given frequency resolution is limited. Statistical stability can be increased then only with a decrease in frequency resolution. Unfortunately, decreasing the frequency resolution increases the bias in the estimated cross spectra (Jenkins and Watts, 1969).

The sensitivity of the various directional spectra estimation techniques for the ADCP measurements is not known. This issue could be addressed via Monte-Carlo simulations to identify estimation trends with the number of degrees of freedom and to identify minimum requirements for the number of degrees of freedom required in the cross spectra estimates.

However, it is expected that the 150 degrees of freedom for the ADCP cross spectra computed in this study should result in reasonable stability.

Table 3-1 ADCP operating parameters.

operating frequency	1228.8 kHz
transducer diameter	54 mm
nominal range	30 m
3-dB beamwidth	1.4°
average (one way) sidelobe level	-42 dB
minimum transmit pulselength	1.47 ms
For 30° beam inclination:	
minimum vertical pulselength	1 m
minimum depth cell	1 m

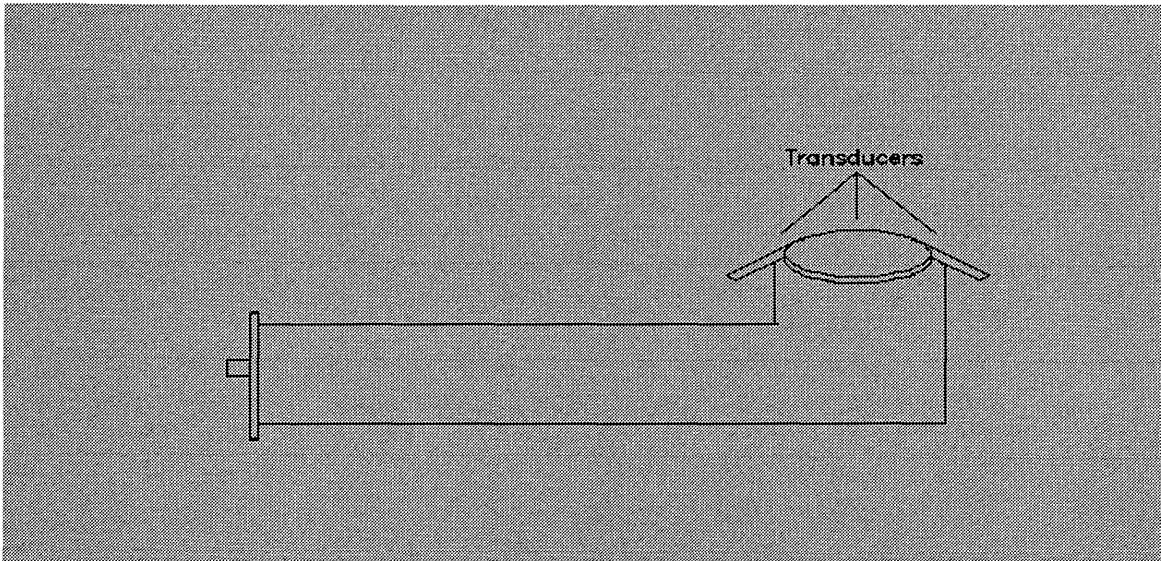


Figure 3-1 Sketch of ADCP instrument.

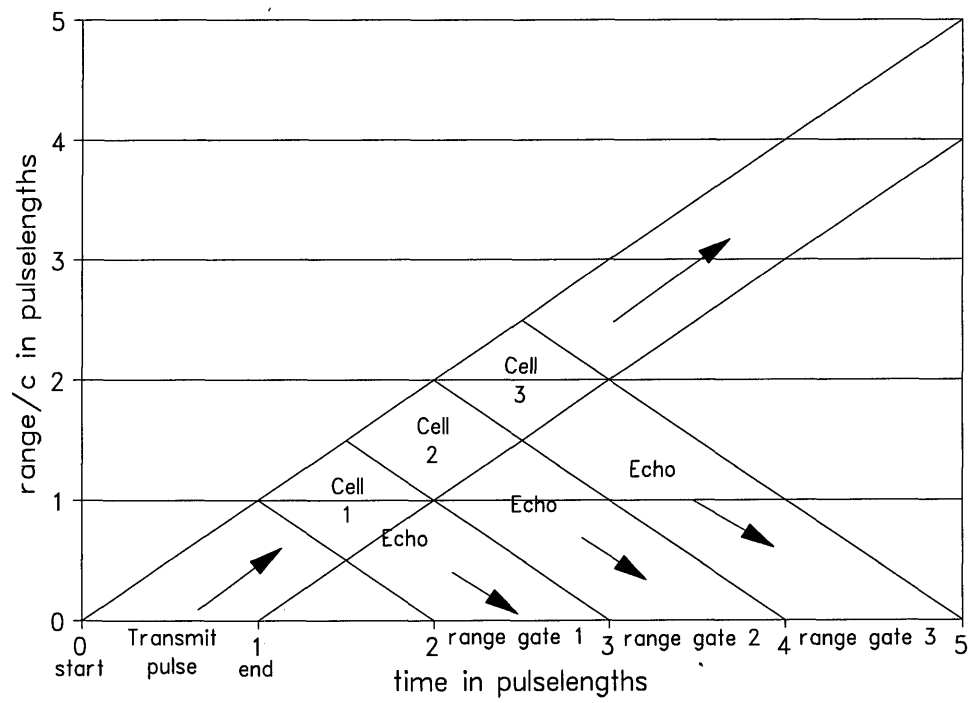


Figure 3-2 Range-time sampling characteristics for ADCP.

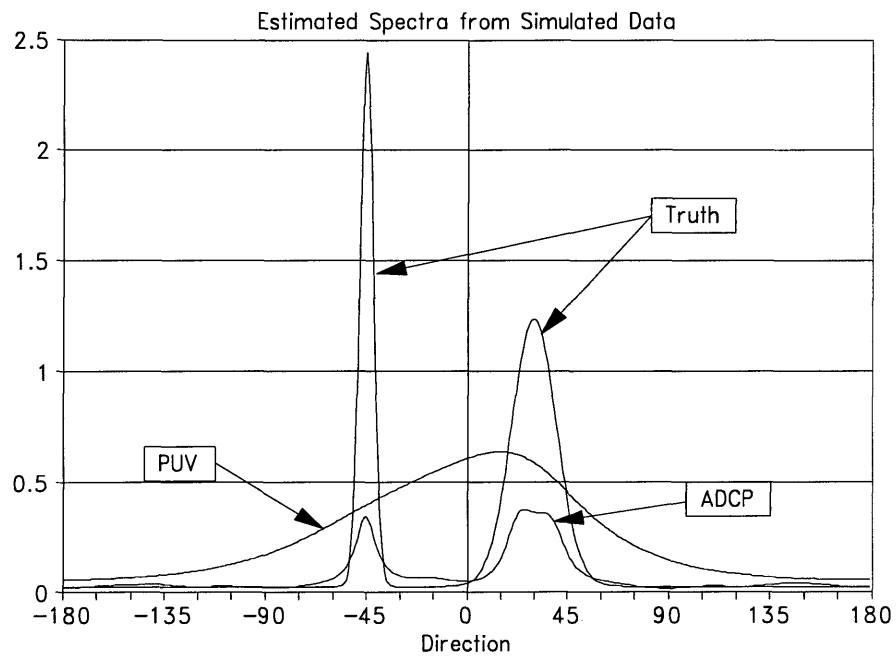


Figure 3-3 MLE directional spectra estimates for ADCP and PUV instruments based on simulated cross spectra.

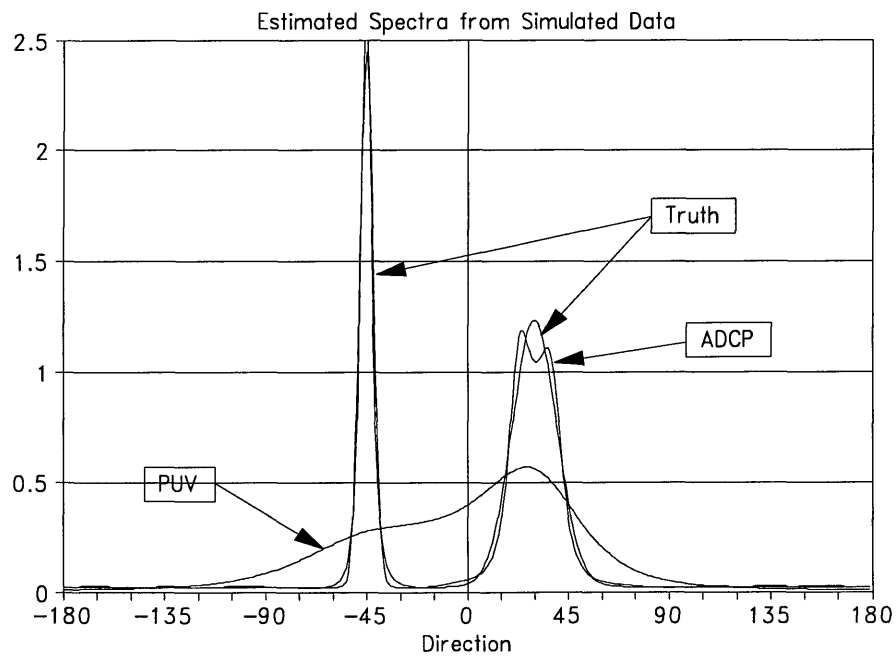


Figure 3-4 IMLE directional spectra estimates for ADCP and PUV instruments from simulated cross spectra.

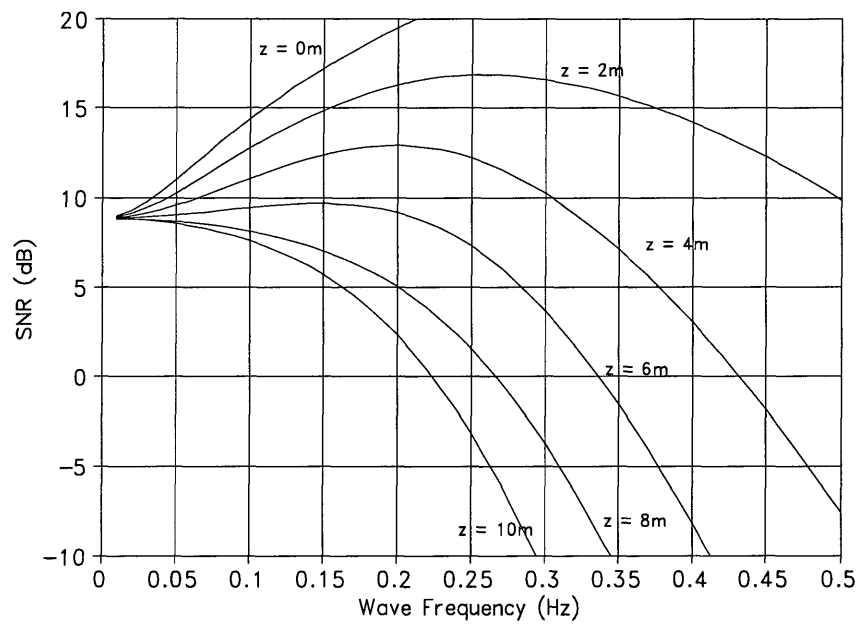


Figure 3-5 ADCP performance parameterization with total depth = 10 m, $N = 1 \text{ m}^2$, $\alpha - \theta = 45^\circ$.

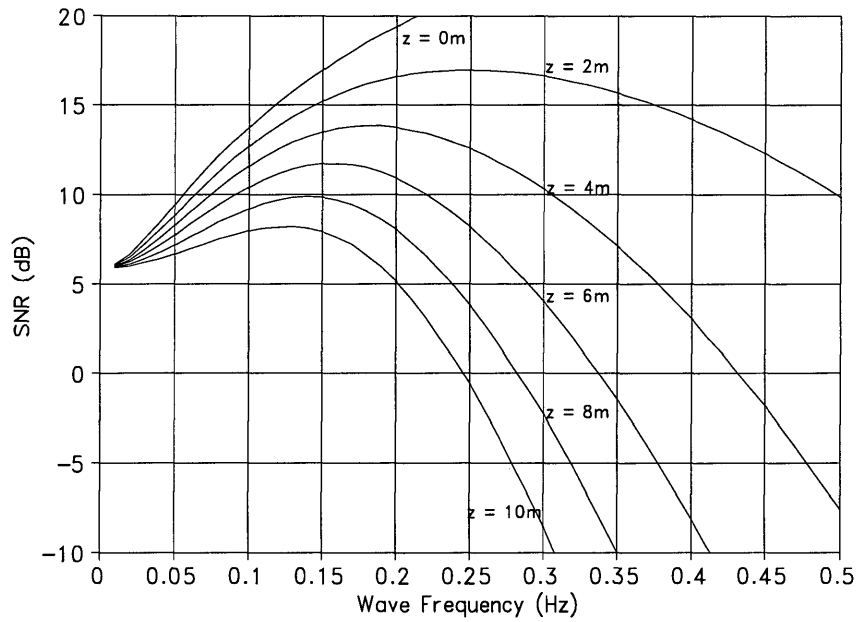


Figure 3-6 ADCP performance parameterization with total depth = 20 m, $N = 1 \text{ m}^2$, $\alpha - \theta = 45^\circ$.

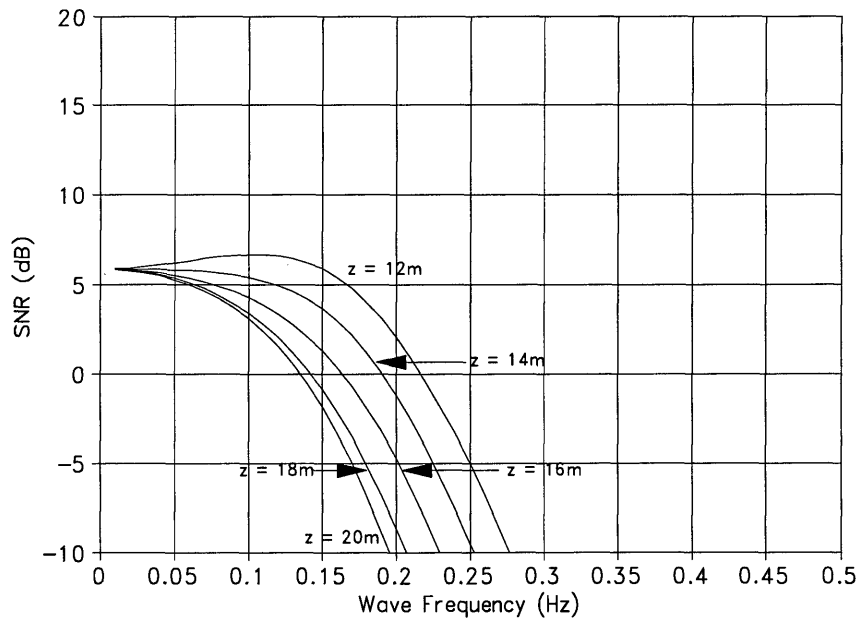


Figure 3-7 ADCP performance parameterization with total depth = 20 m, $N = 1 \text{ m}^2$, $\alpha - \theta = 45^\circ$.

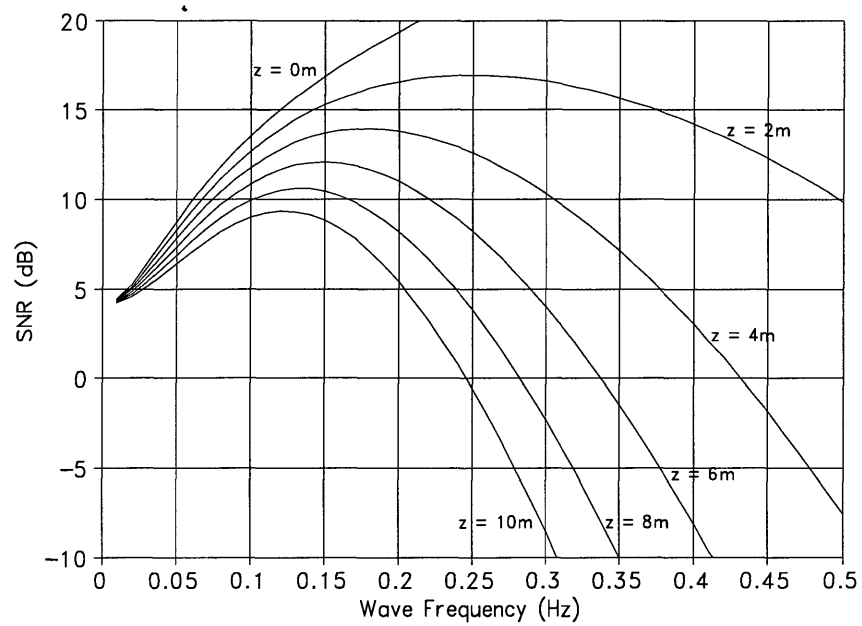


Figure 3-8 ADCP performance parameterization with total depth = 30 m, $N = 1 \text{ m}^2$, $\alpha - \theta = 45^\circ$.

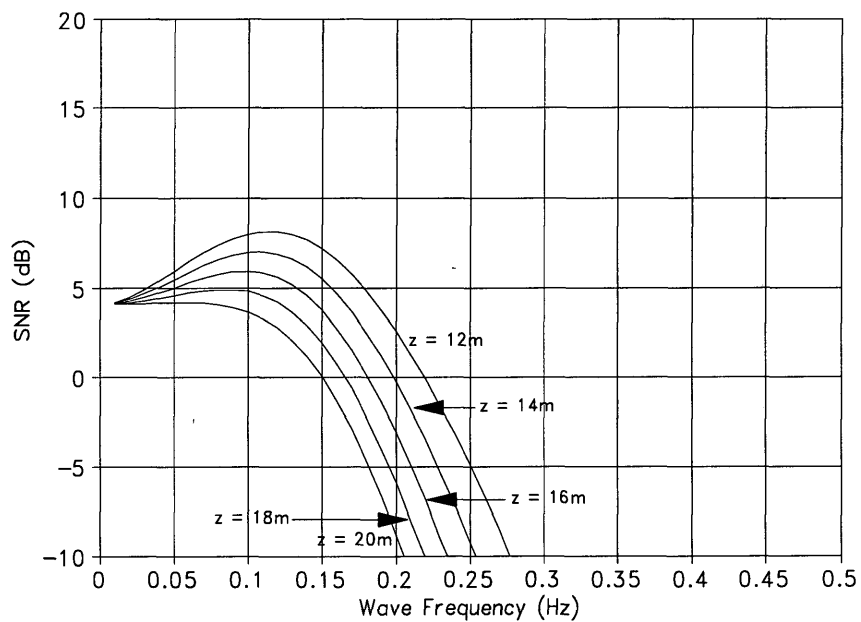


Figure 3-9 ADCP performance parameterization with total depth = 30 m, $N = 1 \text{ m}^2$, $\alpha - \theta = 45^\circ$.

4. DATA COLLECTION

To test the suitability of using a conventional narrowband ADCP for directional wave spectra estimation, the RD Instruments 1200 kHz model DR narrowband ADCP operated by the College of William and Mary's Virginia Institute of Marine Science/School of Marine Science (VIMS/SMS) was deployed from October 28, 1992 to November 11, 1992 near the U.S. Army Corps of Engineers Waterways Experiment Station (WES) Coastal Engineering Research Center (CERC) Field Research Facility (FRF) at Duck, North Carolina. This site was chosen because the FRF operates a linear array of nine pressure sensors at the site, from which it obtains directional spectra estimates every six hours. This allows a comparison of the ADCP-derived directional wave spectra with that of a more conventional, high resolution system.

4.1 Site description

A detailed description of the site, together with supporting references, is given in Long and Oltman-Shay (1991). The FRF consists of 175 acre site at Duck, North Carolina. It comprises one main lab and office building, a garage and storage building, and a 561 m long pier which extends into the nearshore zone (Birkemeier *et al.* 1985). The FRF site (fig. 4-1) is situated on an open coastline which is nearly straight for tens of kilometers on either side of it. As a consequence, waves can approach the site from a 180° arc centered on 70° N, the direction of the seaward-facing shore normal. Birkemeier *et al.* (1985) indicated that the mean direction of wave approach during October-December was 60° N, with a mean waveheight of 1 m.

The adjacent continental shelf is broad (nearly 100 km wide), narrowing to the south where Cape Hatteras extends eastward. The 100 m isobath approaches to within 80 km of the site in a south-southeast direction. The characteristic bottom slope is approximately 1 meter per kilometer, but numerous randomly-situated features on 1-10 km horizontal scales and 10 m vertical scales complicate the offshore bathymetry. Significant refraction effects

are consequently expected for longer period (10 s and up) waves propagating across the shelf. The bathymetry is much more regular, however, within a few kilometers of the FRF site. Close to shore (300 m), a complex bar system exists. The bathymetry is also complicated in the immediate vicinity of the pier, due to scouring around the pier pilings.

4.2 Linear Array description

A comprehensive description of the Linear Array characteristics and data collection is given in Long and Oltman-Shay (1991). A summary of that description is given here.

The nine instrument linear array is located approximately 800 m offshore, just seaward of the 8 m depth contour, which it parallels (fig. 4-2). The end of the array closest to the pier is offset from the pier axis approximately 200 m upshore. The array is located far enough offshore and away from the pier to assure that the wave field is not affected by the inshore bathymetry or the pier. The wave field is consequently spatially homogeneous over the array, a requirement for directional spectra estimation. Additionally, the array is located outside the normal surf zone so that linear theory can be applied in all but the most energetic situations.

The linear array consists of nine Senso-Metric Model SP973(C) pressure transducers mounted 0.7 m off the bottom. Each transducer uses a piezoelectric strain gage to measure the displacement of a pressure-sensitive diaphragm relative to an evacuated cavity. The manufacturer's stated accuracy for the transducers of ± 0.25 percent of full scale (25 psi) corresponds to ± 4.3 cm of water in a static water column. Annual site calibrations indicate a stable field accuracy of 0.6 cm, comparable to the least significant bit (0.7 cm) in digitization.

The linear array spacing is dictated by the desire to obtain optimum resolution for waves in the frequency range 0.54 to 0.32 Hz. The array length is 255 m while the minimum gage spacing is 5 m. The remaining gages are distributed along the array on the whole to obtain as many unique spacings as possible (given spacing distances in multiples of the minimum gage spacing), but several redundant spacings are included for error checking. Absolute positions of the gages are surveyed using the FRF's Coastal Research Amphibious Buggy with a Zeiss Elta-2 total station. It is estimated that positioning errors result in a wave direction uncertainty of $\pm 0.3^\circ$.

Data is routinely collected daily at 0100, 0700, 1300, and 1900 hours. Measurements are taken at a 2 Hz rate from each gage for 8,192 s (approximately 2 hours, 16 minutes) resulting in 16,384 data points per gage. Several error checking procedures are used to test that the data collected is both temporally and spatially homogeneous prior to estimating the directional spectrum. The error checking also identifies any gages which malfunction during the data collection interval.

4.3 ADCP deployment

The VIMS ADCP (RD Instruments 1200 kHz model DR) was deployed near the pier-end of the Linear Array on October 28, 1992 and removed on November 18 using the FRF's amphibious LARC. The ADCP was housed in a custom-built instrument cage which was secured to the bottom by three 10 ft metal pipes which were sandblasted into place. Power was supplied to the ADCP from the FRF pier via a submerged cable. This cable also provided a communications link to control ADCP operation and record data using an ATT 6386SX/EL WGS PC temporarily housed in a "command center" at the seaward end of the pier.

Total depth, instrument depth, and orientation angles were measured at deployment and recovery using divers and the ADCP itself (table 4-1). Measurements by divers at deployment indicated that the total water depth was 26 ft (~8 m) and that the ADCP transducers were located at a depth of 23 ft (~7 m). During data collection, a blanking interval of 0.5 m and a range cell of 1 m were used, so the nominal depth of the first range bin was 5.5 m. Diver measurements concerning the initial orientation of the ADCP indicated that its heading was 148° N, pitch was approximately 1° aft, and roll was nonexistent. Initial ADCP readings indicated that the heading was 139° N, pitch was 2.4°, and roll was 1.1°. Diver and ADCP pitch and roll measurements were taken as consistent with each other. The total depth on retrieval was 27ft, the transducer depth was 24 ft, and the heading was 145° N as measured by divers. The ADCP-measured heading prior to retrieval was 147° N, while the pitch and roll angles were 3.0° and 1.8°, respectively. The initial and final diver heading measurements (estimated error $\pm 5^\circ$) indicated that the ADCP platform did not shift or twist appreciably during the deployment. The initial and final ADCP pitch and roll measurements support this conclusion. However, the heading, as measured by the ADCP flux gate compass,

changed by almost 10° over the deployment. Since the instrument frame on which the ADCP was deployed was secured using 10' aluminum rods sandblasted into the bottom, it is questionable whether this change reflects a real change in the ADCP orientation.

The time history of the ADCP-measured orientation angles (fig. 4-3) indicates that the heading changed twice by several degrees in a step-like fashion during the deployment. Since these step changes were not reflected in the pitch and roll time series, as would be expected if the ADCP had actually changed orientation suddenly, this is possibly indicative of some problem with the ADCP flux gate compass. However, because the discrepancies between the ADCP-measured headings and the diver-measured values were fairly small, the ADCP-measured orientation angles were used to determine the ADCP orientation for the directional spectra processing.

ADCP data collection is summarized in table 4-2. For the deployment, ADCP data was collected in two modes: a fast sampling mode (data recorded at 1 Hz) for directional spectra estimation and a slow sampling mode (data recorded at 0.1 Hz) to investigate long period nearshore current phenomena. Two ping averaging lengths, 4- and 6-ping averages per ensemble, were used in the fast sampling mode. The variance due to "white" instrument noise is expected to be 33% lower for the 6-ping averaged data, with respect to the 4-ping averaged data. For this study, only 6-ping averaged data has been analyzed. The ADCP configuration parameters for the 6-ping sampling are listed in table 4-3.

Six data sets were selected from the collected ADCP Doppler velocity data for directional spectra processing (table 4-4). Directional wave spectra estimates computed from the corresponding (routinely collected) Linear Array (LA) data were obtained from Dr. Charles Long at the FRF (table 4-4).

Although it was possible to synchronize the ADCP and LA data sets in two cases, in the majority of cases synchronization was not possible (table 4-4). The maximum time interval between the beginning of the ADCP and LA data sets is 199 minutes (case 5). This lack of synchronization introduces the possibility that the wave field might have changed enough between the four unsynchronized ADCP and LA collection intervals to significantly alter the wave field, consequently invalidating comparisons between spectra from the two arrays. Although this possibility exists, time series (fig.s 4-4 through 4-7, representing 34 minute vector averages of the mean FRF pier end 19.5 m wind data) indicate that the measured wind

field, at least, might be described as "dramatically" different during the intervals over which the LA and ADCP data was collected only in case 4. In this case (see fig. 4-5), the wind speed increased approximately from 6 to 8 m/s and then decreased to 6 m/s during the ADCP data collection interval, while during the LA data collection interval the wind speed dropped approximately from 7 to 3 m/s. However, since the Linear Array and ADCP directional spectra results for this case are fairly similar (sect. 7.1, fig.s 7.1-13-16), it is doubtful that the wave field changed significantly between the collection intervals.

Table 4-1 ADCP initial and final deployment characteristics.

method	type	total depth (ft)	transducer depth (ft)	Heading (° N)	Pitch (°)	Roll (°)
diver	initial	26	23	148	1	0
ADCP	initial	---	---	139	2.4	1.1
diver	final	27	24	145	---	---
ADCP	final	---	---	147	3.0	1.8

Table 4-2 ADCP data collected at US Army WES CERC FRF, Duck, North Carolina.
P/E = # of pings per ensemble.

start date	time (EST)	end date	time (EST)	P / E	ensemble rate (Hz)	# ensembles collected	# bins collected
10-28	17:41	10-28	18:39	1	2.39	8436	12
10-28	19:50	10-29	14:06	4	1.00	65739	8
10-30	20:01	10-30	22:26	6	1.00	8690	8
10-30	22:33	10-31	11:25	6	1.00	46321	8
10-31	12:11	11-03	10:54	95	0.10	25457	8
11-03	10:58	11-03	14:23	6	1.00	12298	8
11-03	14:33	11-04	08:01	95	0.10	6289	8
11-04	09:24	11-05	10:43	95	0.10	9116	8
11-05	12:38	11-08	13:34	95	0.10	26260	8
11-08	15:41	11-08	18:11	6	1.00	9003	8
11-08	18:39	11-11	08:14	95	0.10	22172	8
11-11	13:39	11-11	15:57	6	1.00	8310	8
11-11	16:26	11-18	09:15	95	0.10	57894	8

Table 4-3 ADCP configuration parameters for 6 pings/ensemble wave data collection. Parameters for which default values are used are not listed.

Configuration Parameter	Description
V000010	Time between pings (min,sec,hundredths) (value = 0.1s)
L0	depth cell (2^L m) (value = 1m)
J005	blank after transmit (LSD = 0.1 m) (value = 0.5 m)
Q008	number of depth cells (value = 8)
O095	output data selector
P00006	pings per ensemble (value = 6)
R00000100	time between ensembles (hr,min,sec,hundredths) (value = 1s)
FH00255	Bottom tracking turned "off"

Table 4-4 Data intervals used for directional spectra estimation.
 ΔT = ADCP - LA start time.

case	Linear Array			ADCP		ΔT (hr:min)
	date	time (EST)	# failed sensors	date	time (EST)	
1	10-30	19:00	0	10-30	20:01	+1:01
2	10-31	01:00	0	10-31	01:00	0
3	10-31	07:00	0	10-31	07:00	0
4	11-03	13:00	0	11-03	10:58	-2:02
5	11-08	19:00	1	11-08	15:41	-3:19
6	11-11	13:00	0	11-11	13:39	+0:39

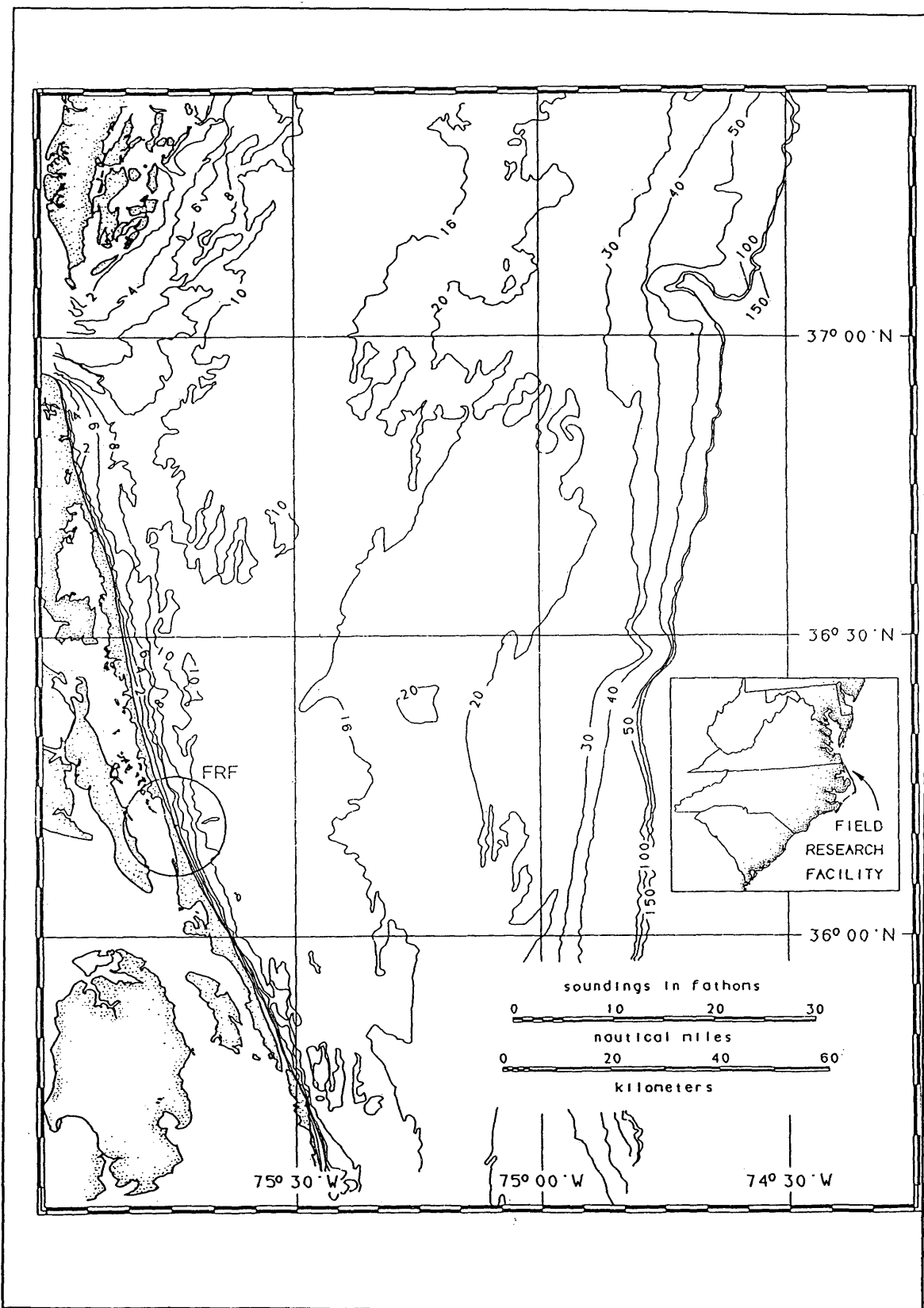


Figure 4-1 Experiment site at the U.S. Army CERC Field Research Facility, Duck, North Carolina (Long and Oltman-Shay, 1991).

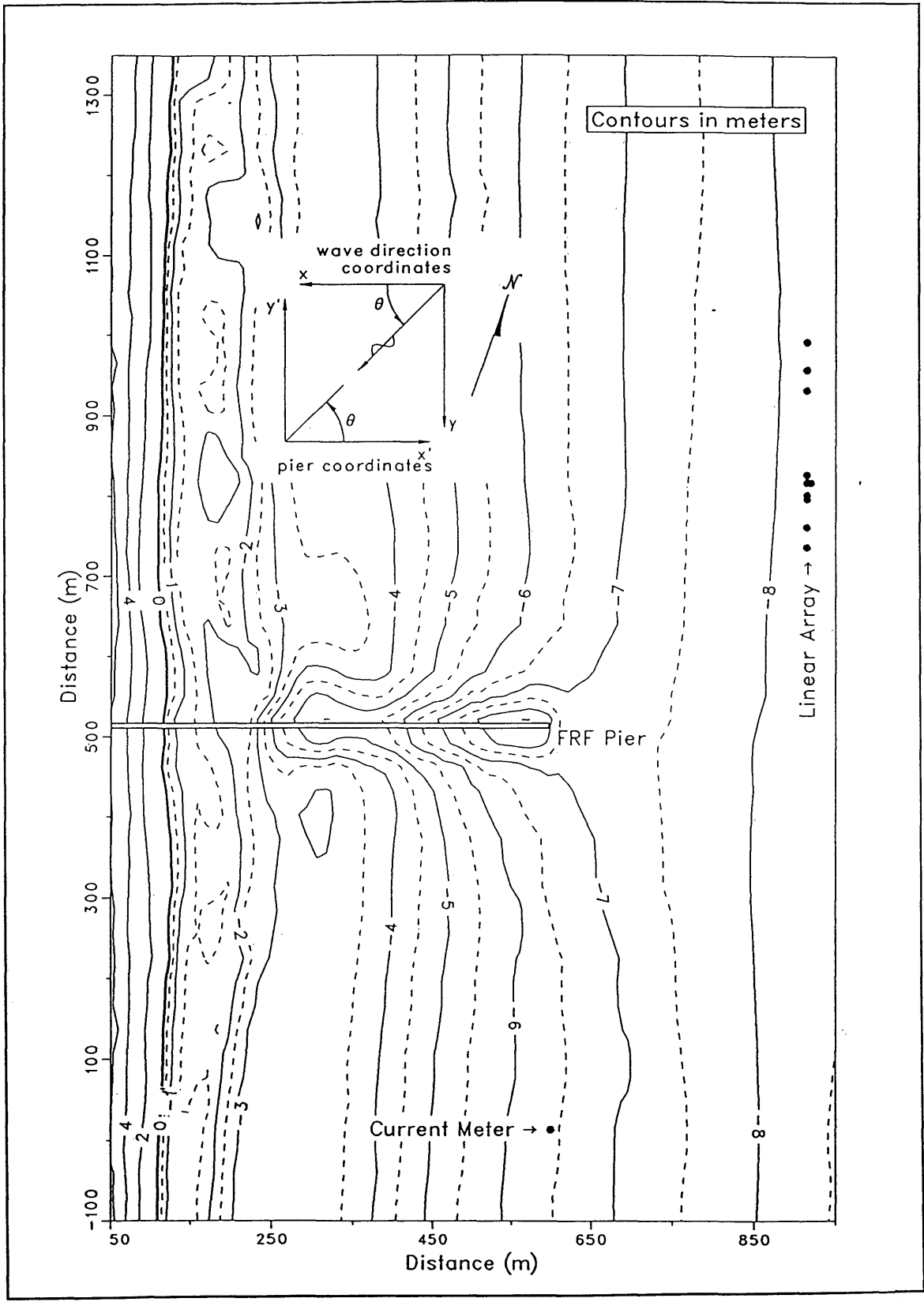


Figure 4-2 Inshore bathymetry and the Linear Array geometry at Duck, North Carolina (Long and Oltman-Shay, 1991).

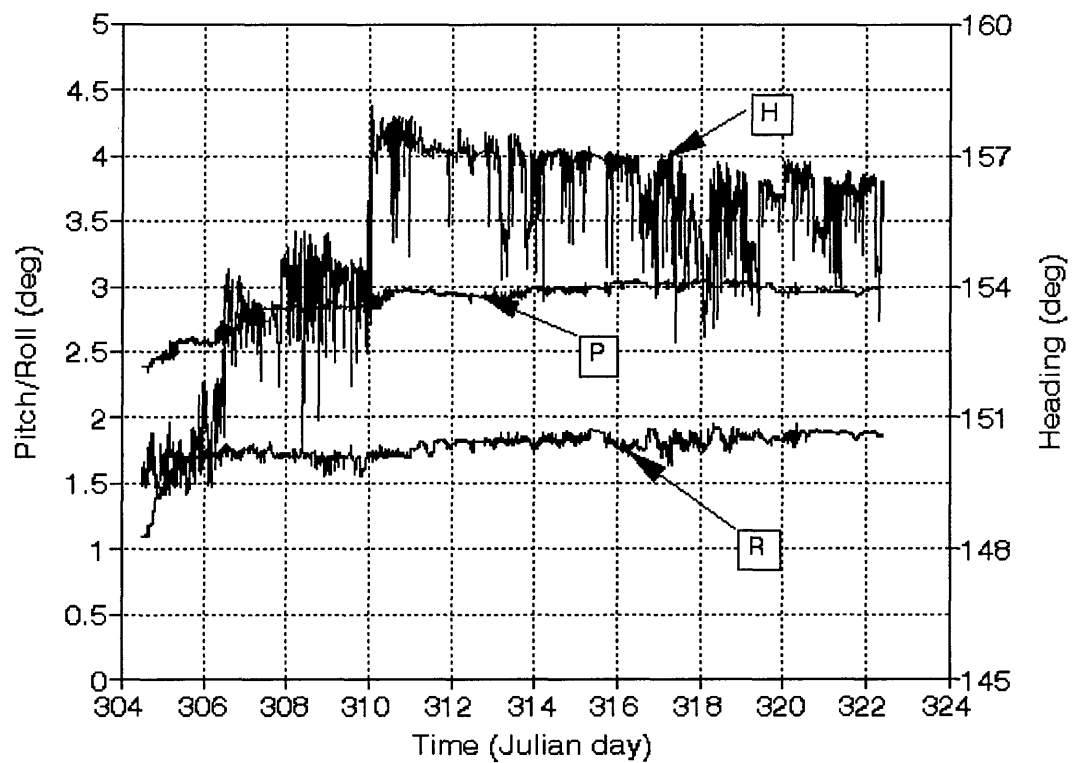


Figure 4-3 ADCP orientation angle time history. P = pitch angle, R = roll angle, H = heading angle. Heading not corrected for local magnetic deviation (10° W).

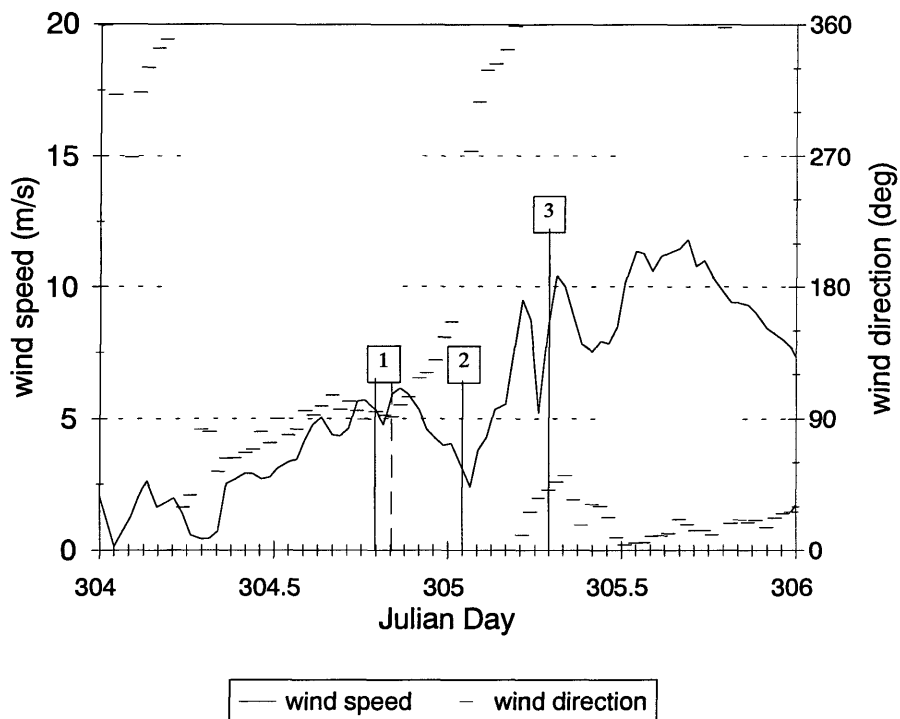


Figure 4-4 Pier end 19.5 m wind speed for cases 1, 2, and 3. Solid vertical line = start of LA data interval. Dashed vertical line = start of ADCP data interval (if different from LA).

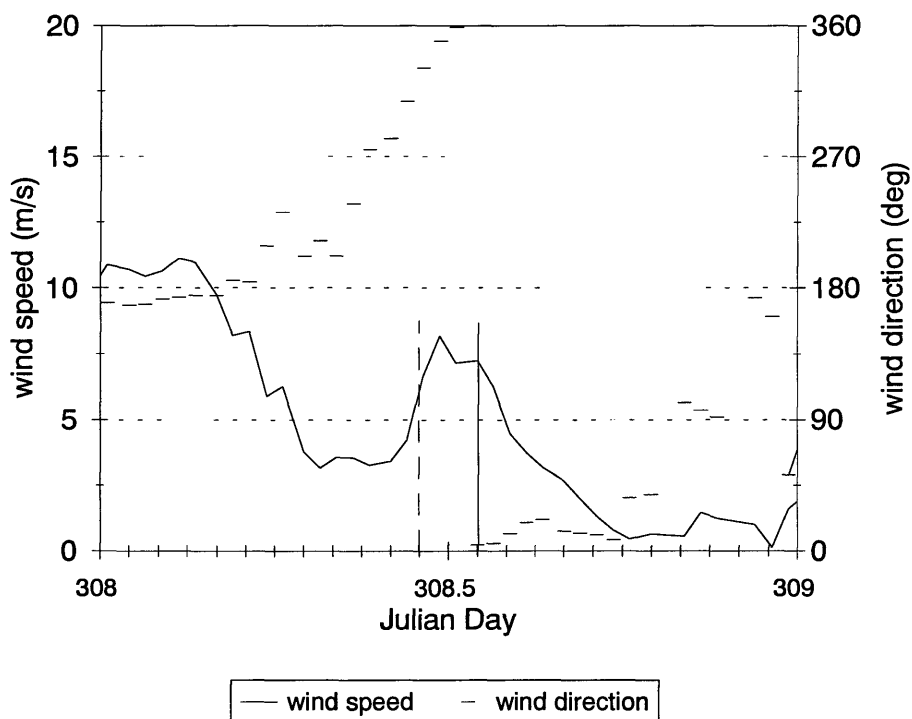


Figure 4-5 Pier end 19.5 m wind speed for case 4. Solid vertical line = start of LA data interval. Dashed vertical line = start of ADCP data interval (if different from LA).

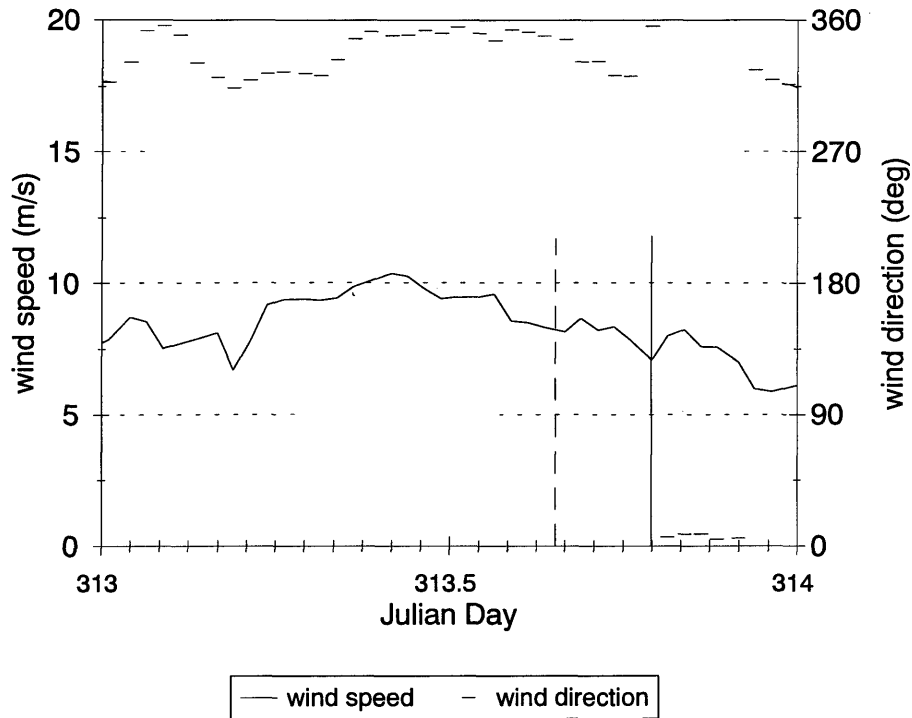


Figure 4-6 Pier end 19.5 m wind speed for case 5. Solid vertical line = start of LA data interval. Dashed vertical line = start of ADCP data interval (if different from LA).

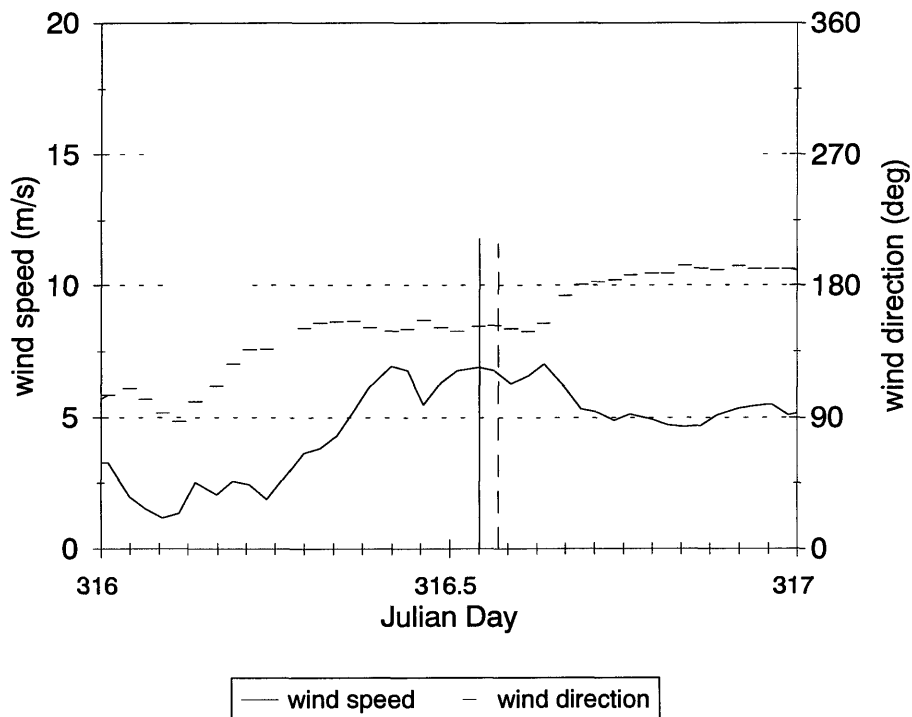


Figure 4-7 Pier end 19.5 m wind speed for case 6. Solid vertical line = start of LA data interval. Dashed vertical line = start of ADCP data interval (if different from LA).

5. DATA PROCESSING

To compare the directional spectra estimated from ADCP data with that of a conventional approach for high resolution spectra, IMLE directional wave spectra were computed for six pairs of ADCP and Linear Array data sets (table 4.4). The data processing involved in estimating the directional wave spectra from the ADCP and the Linear Array data is discussed in this chapter.

5.1 Linear Array processing

IMLE directional spectra estimation using the Linear Array data was performed at the Army Corps of Engineers Waterways Experiment Station (WES) Coastal Engineering Research Center (CERC) Field Research Facility (FRF) at Duck, NC, USA by Dr. Charles Long as part of routine oceanographic data processing. Processing of the Linear Array (LA) data is discussed in detail by Long and Oltman-Shay (1991). As such, only a brief synopsis of the process is included here.

As noted in section 4.1, each LA data set consists of 16,384 data points sampled at 2 Hz from each of nine pressure gages (8192 s time interval). Before the data set was used to estimate directional spectra, it had to pass several error-checking procedures which attempted to indicate whether gages had malfunctioned or the data was spatially inhomogeneous or temporally nonstationary (conditions which invalidate the assumptions used in computing directional spectra). Error checking indicated problems in only one case (case 5, table 5.1) of those considered here, which consisted of one malfunctioning gage. The time series of the malfunctioning gage was omitted from the directional spectra processing for this case, which reduced the directional resolution, particularly at higher frequencies (i.e. higher wavenumbers). The directional spectrum is normally computed for frequencies up to 3.18 Hz, but for this case the directional spectrum was computed for frequencies only up to 0.28 Hz.

After error checking was completed, the frequency cross spectra of the time series data

was computed. This was accomplished in several steps. First, each time series was broken into 15 sections of 2048 data points which overlapped adjacent sections by 1024 data points. Each section was tapered using a Kaiser-Bessel window to reduce leakage. Each section was then fast Fourier transformed to the frequency domain. Initial frequency cross spectra estimates for each pair of gages and each section were computed by multiplying the frequency transform of one gage by the complex conjugate of the frequency transform of a second gage. Intermediate resolution cross spectra were obtained by averaging the results over sections. Final resolution cross spectra were obtained by averaging results over 10 adjacent frequency bands. This resulted in cross spectra with frequency resolution of 0.0976 Hz and at least 150 degrees of freedom. The Chi-square confidence intervals on the autospectra are approximately 19% at the 95-percent confidence level and 15% at the 90-percent level.

Directional wave spectra $S_{LA}(\omega, \theta)$ were computed from the cross spectra at each sampled frequency from 0.54 to 0.318 Hz (if all nine gages are included) using the Iterative Maximum Likelihood Estimation (IMLE) method described in section 2.2. The directional wave spectra for the six cases were provided to me as ASCII data files by Dr. Charles Long at the FRF.

The six LA IMLE directional spectra were plotted as 3-d surface and contour plots normalized to the largest magnitude in the directional spectrum. To facilitate the comparison of the ADCP and LA results, several summary functions and parameters were computed. These calculations are discussed in chapter 7, where the directional spectra and associated results are presented.

5.2 ADCP Data Processing

Directional spectra estimates were computed for six time intervals of ADCP data. The ADCP time intervals were selected to agree as closely as possible to the time intervals used to produce the Linear Array directional wave spectra estimates (table 5.1). The ADCP time series data from selected bin/beam combinations was processed in a manner similar to that of the Linear Array data to minimize differences in the final directional wave spectra estimates due solely to processing artifacts.

Each ADCP data interval selected consisted of 8192 data points sampled at 1 Hz (6 ping

ensemble averages) from each of the four beams for range bins 1,3,5. The length of time used for the data interval is identical to that for the Linear Array data. The range bins used correspond to nominal depths of 5.5, 3.5 and 1.5 m below the surface. Data for range bins 2,4,6,7,8 (corresponding to nominal depths of 4.5, 2.5, and 0.5 below the sea surface, and 0.5 and 1.5 m above the sea surface) was also recorded for each beam during data collection, but was not included for directional spectra estimation for several reasons. Given its proximity to the surface, range bin 6 was probably contaminated by specular reflection from the sea surface. Consequently, Doppler velocity measurements from this bin reflected the phase speed of the waves, not the along-beam component of orbital velocity modeled in the ADCP transfer function. Bins 7 and 8 nominally corresponded to positions above the sea surface. Acoustic energy received in these bins was thus reflected from the sea surface. Data from these bins is consequently also unusable. Finally, the time series from bins 2 and 4 are correlated with that from the adjacent bins which were used in the directional spectra estimation. Since the estimation techniques do not account for this correlation, this data was dropped from inclusion in the directional wave spectrum estimate.

The time series data for each selected bin/beam combination was detrended using a quadratic fit to remove longer period trends associated with tidal cycles. Statistical moments for each time series were computed to assess data quality.

Cross spectra for different bin/beam combinations (bins 1, 3, and 5) were computed using an approach similar to that used for the Linear Array data to obtain the same final resolution. Each data interval was divided into 15 sections of 1024 data points, each with an overlap of 512 points, and tapered using a Hanning window (rather than a Kaiser-Bessel window as for the Linear Array, but this should have little effect on subsequent analysis). Each section was then fast Fourier transformed to the frequency domain using the following convention:

$$\tilde{s}_m^n(k \Delta f) = \sum_{j=0}^{N-1} s_m^n(j \Delta t) \exp(i 2 \pi \frac{k j}{N} \Delta t) \quad (5.1)$$

where m denotes the bin/beam combination, n denotes the section (1..15), $k = 0..N/2$ is the frequency index, j denotes the time index, Δt is the sampling interval, Δf is the frequency sampling interval ($\Delta f = (N \Delta t)^{-1}$), and N is 1024. Intermediate resolution frequency cross

spectra were formed by computing the product of the transform of one bin/beam pair with the conjugate of the transform of another bin/beam pair for corresponding sections (normalized to retain variance as in Bendat and Piersol, 1971), then averaging the results over the 15 sections:

$$C_{ij}^{int}(k \Delta f) = \frac{1}{15} \sum_{n=1}^{15} \frac{[\tilde{s}_i^n(k \Delta f) \tilde{s}_j^n(k \Delta f)^*]}{T_{eqv}} \quad (5.2)$$

where T_{eqv} is a variance normalizing factor equal to the integral of the square of the Hanning tapering function. Final resolution cross spectra were obtained, as for the Linear Array, by averaging 10 adjacent frequency bins. The resulting cross spectra have the same frequency resolution (.0097 Hz), number of degrees of freedom (>150), and the same sampled frequencies (up to the 0.5 Hz Nyquist limit for the ADCP data) as the Linear Array cross spectra. The ADCP noise spectral density for each beam was estimated by averaging the autospectra from all four beams of the lowest bin over frequencies higher than 0.4 Hz up to the Nyquist limit.

Prior to directional wave spectra estimation, nondirectional frequency spectra were estimated from the sum of the autospectra (denoted here as $C_{ii}(\omega)$) of each beam ($i = 1-4$) for rangebins 1, 3, and 5 using (see eq. 3.13 also):

$$\hat{S}(\omega) = \frac{\frac{1}{2} \sum_{i=1}^4 [C_{ii}(\omega) - Q]}{\omega^2 \left\{ \sin^2 \beta \frac{\cosh^2[k(z \cdot h)]}{\sinh^2[kh]} + 2 \cos^2 \beta \frac{\sinh^2[k(z \cdot h)]}{\sinh^2[kh]} \right\}} \quad (5.3)$$

The nominal inclination angle $\beta = 30^\circ$ and the nominal depth z (-5.5, -3.5, and -1.5 for bins 1, 3, and 5 respectively) were used to compute eq. 5.3 for each bin. The autospectra are biased by the ADCP white noise level, so Q , a noise factor of $10 \text{ (cm/s)}^2/\text{Hz}$, was subtracted from each of the autospectra at all frequencies. The actual ADCP spectral noise level was about $22 \text{ (cm/s)}^2/\text{Hz}$ (see section 6.3), so this represents only a partial correction to the noise bias. To further minimize effects due to the ADCP noise in the frequency spectra estimates, the estimate was taken as zero unless the autospectra of all four beams (for a given depth)

were greater than a threshold value of 80 (cm/s)²/Hz--roughly four times the ADCP noise spectral density.

At each frequency sampled between 0.054 and 0.318 Hz (identical to the Linear Array treatment), an 8x8 cross spectra matrix $C(\omega)$ was formed using the cross spectra between all four beams in the mid-depth and near surface bins (3 and 5). Nondirectional spectra computed from the near-bottom bin, bin 1, appeared significantly biased with respect to those computed from bins 3 and 5 (see section 6.4), so cross spectral values involving beams from bin 1 were excluded in forming the cross spectra matrix.

In an attempt to reduce the effects due to the ADCP noise in the autospectra, the cross spectra matrix was edited when diagonal elements (autospectra) did not meet a threshold criterion of 80 (cm/s)²/Hz. Editing consisted of reducing the cross spectra matrix by eliminating the row and column in which the deficient diagonal element occurred. If the matrix had less than four elements in it, the directional spectrum at the frequency in question was taken as zero.

If the edited cross spectra matrix $C'(\omega)$ passed the tests, the unnormalized MLE directional spectrum $S'_{MLE}(\theta; \omega)$ was computed using (see sect.s 2.2 and 3.2):

$$S'_{MLE}(\theta; \omega) = \frac{1}{\sum_{i,j} G'_i(\omega, \theta) C'^{-1}_{ij}(\omega) G'_j(\omega, \theta)} \quad (5.4)$$

where

$$G'_i(\omega, \theta) = \exp\{i \mathbf{k}(\omega, \theta) \cdot \mathbf{x}_i\} \frac{\omega}{\sinh[kh]} \times \{\cos(\alpha_i - \theta) \sin\beta \cosh[k(z_i \cdot h)] - i \cos\beta \sinh[k(z_i \cdot h)]\} \quad (5.5)$$

The i th bin/beam position (x_i, z_i) and the orientation angles α_i and β_i are computed from the nominal values using the ADCP pitch, roll, and heading angles averaged over the 8192 s time interval (appendix B). The unnormalized MLE directional spectrum $S'_{MLE}(\theta; \omega)$ and ADCP noise bias $Q = 20$ (cm/s)²/Hz were used to calculate estimates of the diagonal elements of the edited cross spectral matrix $C'(\omega)$ using the MLE spectrum as the true spectrum (see eq. 3.12)

$$\hat{C}'_{ii}(\omega) = \int d\theta |G_i(\omega, \theta)|^2 S'_{MLE}(\theta; \omega) \cdot Q \quad (5.6)$$

A frequency-dependent normalization factor $\kappa(\omega)$ was computed from the ratio of the geometric means of the estimated and measured diagonal elements of the cross spectra matrix at each frequency:

$$\kappa(\omega) = \frac{\{\prod_{i=1}^n C'_{ii}(\omega)\}^{1/n}}{\{\prod_{i=1}^n \hat{C}'_{ii}(\omega)\}^{1/n}} \quad (5.7)$$

The normalized MLE directional spectrum $S_{MLE}(\omega, \theta)$ was then computed by

$$S_{MLE}(\omega, \theta) = \kappa(\omega) S'_{MLE}(\theta; \omega) \quad (5.8)$$

The IMLE directional spectrum for each sampled frequency was computed from the corresponding MLE directional spectrum using the iteration

$$S_{IMLE}^i(\omega, \theta) = \left[\frac{S_{IMLE}^{i-1}(\omega, \theta)}{T_{MLE}^{i-1}(\omega, \theta)} \right]^\beta S_{IMLE}^{i-1}(\omega, \theta) \quad (5.9)$$

where $S_{IMLE}^0(\omega, \theta)$ is $S_{MLE}(\omega, \theta)$ and $T_{MLE}^{i-1}(\omega, \theta)$ is the normalized MLE directional spectrum computed using an estimated cross spectra matrix given by

$$\hat{C}'_{jk}{}^{i-1}(\omega) = \int d\theta G_j(\omega, \theta) S_{IMLE}^{i-1}(\omega, \theta) G_k(\omega, \theta) \cdot Q \quad (5.10)$$

The value of the parameter β in eq. 5.9 was selected as 0.4.

The iterative scheme used for the ADCP IMLE is different from that used to compute the LA IMLE directional spectra. The iterative scheme used for the LA IMLE directional spectra is a "slow approach" (Oltman-Shay and Guza, 1984) method which requires considerable computer time if 50 iterations are used (as in Oltman-Shay and Guza, 1984). The iterative scheme used here converges much more quickly to what appears to be an acceptable estimate of the directional spectrum, at least for the test cases considered (see

fig.s 5-1,2 for a sample result). The values 20 and 1 were used for the parameters γ and β in the LA-type IMLE iteration (fig. 5-2, as suggested in Oltman-Shay and Guza, 1984 for eq. 2.16).

After each iteration, the resulting IMLE spectrum was renormalized using the approach outlined above for the MLE directional spectrum. The iteration was terminated after one of the following conditions applied: 1) 10 iterations had occurred, or 2) the convergence criterion

$$R_{conv} = \frac{\int d\theta |\hat{S}_{IMLE}^i(\omega, \theta) - \hat{S}_{IMLE}^{i-1}(\omega, \theta)|}{\int d\theta |\hat{S}_{IMLE}^i(\omega, \theta)|} \quad (5.11)$$

fell below a threshold of .05.

The resulting IMLE directional spectra were plotted as 3-d surface and contour plots normalized to the largest magnitude in the directional spectrum. To facilitate the comparison of the ADCP and LA results, several summary functions and parameters were computed. These calculations are discussed in chapter 7 where the directional spectra and the associated results are presented.

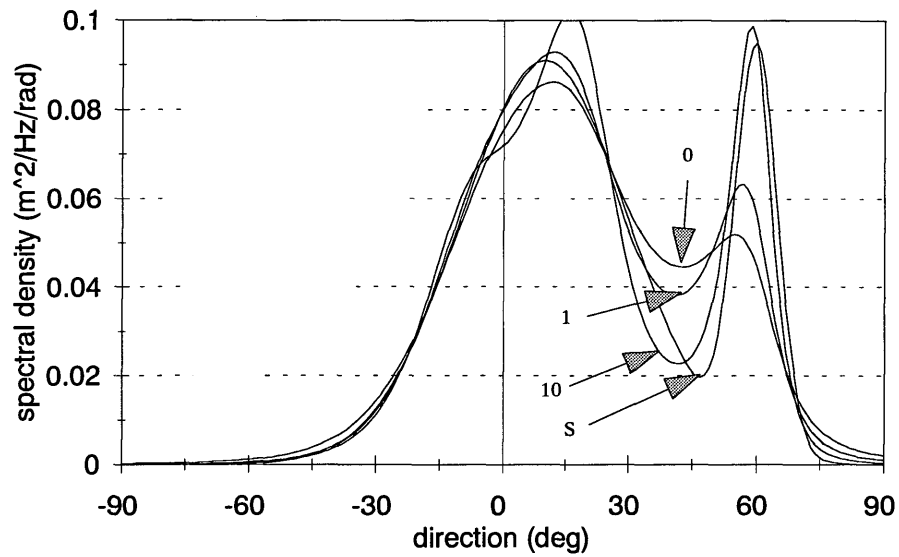


Figure 5-1 Convergence of ADCP-type IMLE iteration for simulated ADCP cross spectra. S = true spectrum, 0 = MLE spectrum, 1, 10 = i th IMLE iterations. Frequency is 0.1 Hz.

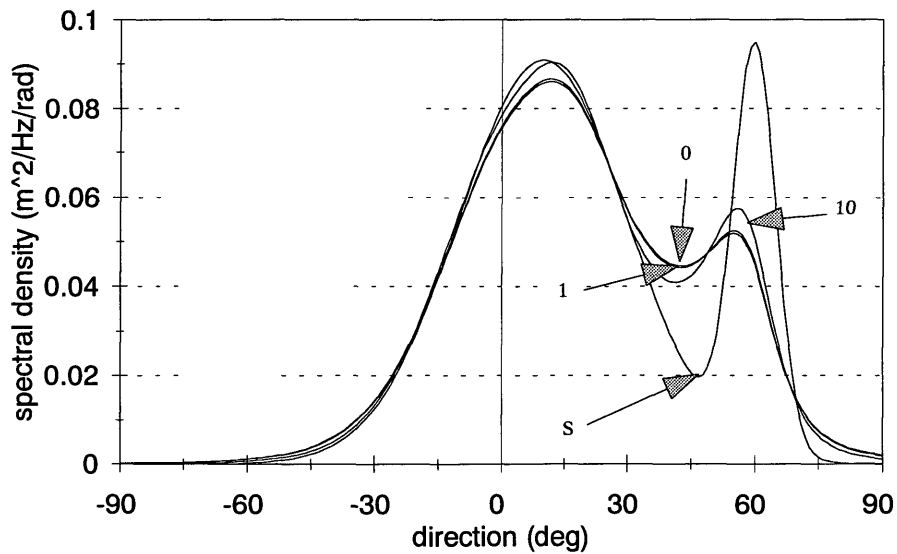


Figure 5-2 Convergence of LA-type IMLE iteration for simulated ADCP cross spectra. S = true spectrum, 0 = MLE spectrum, 1, 10 = i th IMLE iterations. Frequency = 0.1 Hz.

6. RESULTS PRIOR TO DIRECTIONAL SPECTRA PROCESSING

Results associated with processing the six selected ADCP data sets (table 6-1, which repeats table 4-4) to estimate IMLE directional wave spectra are presented in this and the subsequent chapter. In this chapter, results from processing steps prior to actually computing the directional spectra are presented. Mean observables associated with each case are presented first, in section 6.1. Time domain results from the ADCP data sets are then presented in section 6.2. Cross spectra results for the ADCP data sets are presented in section 6.3, while corresponding estimates of the nondirectional wave frequency spectra (computed as outlined in section 5.2) are given in section 6.4. In chapter 7, the ADCP and the LA IMLE directional wave spectra are presented and compared. Several integral properties of the directional wave spectrum (e.g. frequency spectra, significant waveheight) are also presented and compared for each case.

6.1 Mean observables

Wind speed and direction, current speed and direction, total depth, and the ADCP orientation angles were the mean observables measured for each case (table 6.1-1). Dr. Charles Long at the FRF provided the average wind velocities and total depths, which were computed over the LA data interval for each case. The mean current and mean ADCP orientation angles were computed by averaging over the ADCP data interval for each case. In addition, the mean current (from ADCP measurements) was averaged over depth as well.

Mean wind speeds measured at the end of the FRF pier (table 6.1-1) varied from 2.2 m/s (case 2) to 9.4 m/s (case 3). Wind directions in table 6.1-1 are given in the wave coordinate system (fig. 4-2), so wind directions of 0° represent winds blowing directly onshore and directions of 90° represent winds blowing alongshore to the south. Winds with onshore components blew in five out of the six cases (all except case 2), while the accompanying alongshore components were southerly in four out of the six cases (all except cases 1 and 6).

Mean currents (table 6.1-1) ranged in speed from 3.8 (case 1) to 39.0 cm/s (case 5). The

measured currents are primarily alongshore, with northerly and southerly components equally represented among the six cases. There appears to be wind-induced forcing of the alongshore currents at the site (Dr. J. Brubaker, personal communication), but the data presented in table 6.1-1 is insufficient to draw any conclusion from.

The variation in water depth at gage no. 191 (one of the nine pressure gages in the LA, table 6.1-1), gives an indication of the tide changes which occurred during data collection. Mean depths range from 7.91 (case 6) to 9.02 m (case 4), while the depth change during data collection varies from 0.07 (case 4) to 0.55 m (case 3). By using a nominal depth of 8 m for all six data cases to estimate the directional wave spectra from the ADCP data (section 5.2), a source of error is apparently introduced into the ADCP directional spectra processing. However, the relation between the ADCP depth and the depth at gage 191 is not known, so this error cannot be corrected. In addition, the effect of such an error appears to be small (see below, section 6.4).

The mean ADCP orientation angles (pitch and roll, table 6.1-1) for each case indicate that the ADCP shifted somewhat during the deployment. This was not unexpected, and probably results from wave or tidally-induced stresses on the ADCP and its frame. The ADCP heading angle, however, changes by almost 9° over the six cases. As discussed in section 4.2, this is somewhat suspect and does not seem to agree with diver observations. However, means (over 8192 s for each case) of all three orientation angles were used to compute the directional spectra for each case.

6.2 Time domain results

The ADCP data for directional wave spectra estimation was examined in the time domain prior to cross spectra processing. Individual waves are apparent in typical ADCP Doppler velocity time series (fig.s 6.2-1,2), as are wave groups (fig. 6.2-1).

Statistics were calculated from the ADCP Doppler velocity time series for bins 1,3,5 (nominally 5.5, 3.5, and 1.5 m below mean sea level) from each beam (tables 6.2-1 through 6.2-6). The variance, skew, and kurtosis were calculated after quadratically detrending each 8192 s time series.

If the time series data were normally distributed, one would expect the calculated skew and kurtosis to both be zero (tables 6.2-1 through 6.2-6). Out of the 72 series examined for

all six cases, the kurtosis was significantly different from zero ($p < .01$) in only four of the time series. For cases 1, 2, 3, and 5, the skew was significantly different from zero ($p < .01$) in only two instances (out of 48, tables 6.2-1,2,3,5). On this basis, then, almost all of the time series from cases 1,2,3, and 5 are well-represented as normal random processes. For cases 4 and 6, however, the skew was significantly different from zero ($p < .01$) in 16 out of the 24 time series considered (tables 6.2-4,6). These time series are consequently not well-represented as normal processes. The departure from normality indicates that second or higher order effects may be important for the wave fields for these two cases.

The influence of wave velocities on the ADCP measurements is seen for each case in the increase in variance with decrease in depth (increase in bin #) for each beam. The opposite orientation of beams 1 and 2 and beams 3 and 4 is evidenced by the sign change in their respective mean values. The slightly tilted orientation (relative to vertical, see table 6.1-1) of the ADCP is partly responsible for the inequality in the magnitude of the mean values as well as the in the variances between the oppositely directed beam pairs. Otherwise, and except for sampling variability, one would expect these to be identical for oppositely pointed beams since the mean vertical velocity should be very small.

6.3 Cross spectra results

For each case, cross spectra were computed for each pair of time series from bins 1, 3, and 5 (72 pairs), as discussed in section 5.2. The resulting two-sided autospectra are presented in figures 6.3-1 through 6.3-6. The autospectra are distinguished as to bin, but not as to beam, since this would have resulted in overly cluttered plots. The confidence limits (150 degrees of freedom) for the autospectra are 1.21 (upper) and 0.84 (lower), expressed as multiplicative factors.

Several observations can be made regarding the autospectra for all six cases. Each displays at least one major peak in the frequency interval from 0.05 to 0.20 Hz, corresponding to long wave (swell) energy. At the low frequency peak it is usually possible to distinguish pairs of autospectra for a given bin which have very similar values. However, for each bin, the two pairs of autospectra have dramatically different spectral density levels. This results from the ADCP beam geometry and the principal propagation direction of the long waves (i.e. onshore). The ADCP beams are oriented so that beams 1 and 2 are primarily

perpendicular to the shore, while beams 3 and 4 are primarily parallel to the shore. Long waves are refracted as they approach the shore, and so approach nearly perpendicular to the shore. Consequently, one expects to find much more energy in beams 1 and 2, as opposed to beams 3 and 4, due to long waves (i.e. at low frequencies). Higher frequency (> 0.2 Hz, say) waves undergo less refraction over the shelf, so these waves are less likely than low frequency waves to be well-collimated, hence it is possible to find equal energy in all four beams at higher frequencies.

Additionally, the frequency-dependent attenuation of surface gravity wave particle velocities with depth (section 2.1, appendix A) is evident in the autospectra. Particle velocities decay exponentially with depth at high frequencies (> 0.3 Hz, say) while there is little depth dependence at low frequencies (< 0.1 Hz). One notes that the largest autospectra values are from bin 5 (the shallowest depth) at all frequencies, while the smallest values are from bin 1 (the deepest), at least until an apparent noise floor is reached at high frequencies. However, at low frequencies the *difference* between the largest autospectra values from bin 5 and bin 1 is small, while the difference increases with frequency until the autospectra from the lower bin reach the noise floor.

Finally, as just noted, the autospectra in bins 1 and 3 reach an apparent noise floor at high frequency (generally between 0.35 and 0.4 Hz for bin 1). Since surface wave-related particle velocities are exponentially attenuated with depth at high frequency, this corresponds to the white noise level associated with the ADCP Doppler velocity measurements. The spectral noise level estimated from the bin 1 autospectra (table 6.3-1) ranges from 20 (cm/s)²/Hz (case 4) to 25 (cm/s)²/Hz (case 5). The average spectral noise density for all six cases is 22 (cm/s)²/Hz, which compares reasonably well with the theoretical white noise level of 15 (cm/s)²/Hz (using eq.s 3.1 and 3.21).

The first three cases (fig.s 6.3-1,2,3) are perhaps the most interesting to focus on individually, since they correspond to data intervals collected within a 12 hour timespan. Beginning on the morning of Oct. 30 (julian day 304), the wind speed, with some fluctuations, increased from almost zero to a maximum of about 12 m/s some 42 hours later (fig. 4.4). The concurrent buildup of high frequency wind waves is evident in the autospectra. A low amplitude secondary peak in the case 1 autospectra, located between 0.3 and 0.35 Hz, increased in energy and shifted location to between 0.2 and 0.25 Hz in case 2.

It continued to increase in energy and shift location lower in frequency to between 0.15 and 0.2 Hz in case 3. By case 3, the high frequency peak is greater in amplitude than the low frequency peak associated with swell, which has remained at a constant magnitude.

6.4 Nondirectional wave spectra results

Estimates of the (two-sided) nondirectional wave frequency spectrum were computed for each case from the autospectra using the method outlined in sections 3.2 and 5.2 for bins 1, 3, and 5 separately (fig.s 6.4-1 through 6.4-6). The estimated nondirectional spectra for each case exhibit the broad features noted in the corresponding autospectra in the previous section. The most notable feature of the estimated wave frequency spectra is that, for each case, the relative amplitude of the results from bins 1 and 3 to that from bin 5 is both depth and frequency dependent, but the dependence appears to be the same in each case (fig.s 6.4-7 and 6.4-8). The estimated spectra from bin 1 is always greater than that from bin 3, which in turn is always greater than that from bin 5--although the discrepancy between the estimates from bins 3 and 5 is small. Additionally, the discrepancy increases with frequency. Since the estimated spectra should be identical for all three bins, except for statistical fluctuations, this behavior indicates a problem with either the processing of the data, the modelling of the data, or with the data itself.

Table 6-1 Data intervals used for directional spectra estimation.
 ΔT = ADCP - LA start time.

case	Linear Array			ADCP		ΔT (hr:min)
	date	time (EST)	# failed sensors	date	time (EST)	
1	10-30	19:00	0	10-30	20:01	+1:01
2	10-31	01:00	0	10-31	01:00	0
3	10-31	07:00	0	10-31	07:00	0
4	11-03	13:00	0	11-03	10:58	-2:02
5	11-08	19:00	1	11-08	15:41	-3:19
6	11-11	13:00	0	11-11	13:39	+0:39

Table 6.1-1 Mean value of different observables for the data sets. Wind and current directions are relative to the wave coordinate system described in fig. 4-2. Headings are uncorrected for local magnetic deviation (10°W).

case:		1	2	3	4	5	6
mean pier end wind	speed (m/s)	5.5	2.2	9.4	5.4	7.7	6.6
	dir. (deg)	-24	136	26	61	65	-81
mean ADCP horizontal velocity	speed (cm/s)	3.8	21.6	32.7	12.6	39.0	12.2
	dir. (deg)	98	-80	-84	88	-90	72
pressure gage 191 depth (m)	mean	8.65	8.66	8.89	9.02	8.73	7.91
	min	8.45	8.49	8.63	8.98	8.52	7.88
	range	0.42	0.34	0.55	0.07	0.38	0.10
mean ADCP orientation angles (deg)	Pitch	2.4	2.4	2.4	2.8	2.9	3.0
	Roll	1.1	1.1	1.1	1.7	1.8	1.8
	Heading	148.6	149.3	149.7	152.8	157.1	156.9

Table 6.2-1 Case 1: ADCP Doppler velocity statistics. * = skew, kurtosis values significantly different from zero ($p < 0.01$).

bin	beam	mean (cm/s)	variance (cm/s) ²	skew	kurtosis
1	1	-1.1	92	-.033	-.025
	2	2.7	82	.045	-.089
	3	-2.2	52	.031	.098
	4	3.8	54	.002	.029
3	1	-1.8	100	-.056	-.039
	2	2.4	92	.065	-.039
	3	-4.0	61	.045	-.012
	4	4.9	63	-.026	.070
5	1	-1.1	149	.024	-.084
	2	1.4	144	.030	-.034
	3	-3.4	114	-.010	-.067
	4	3.7	105	.001	.016

Table 6.2-2 Case 2: ADCP Doppler velocity statistics. * = skew, kurtosis values significantly different from zero ($p < 0.01$).

bin	beam	mean (cm/s)	variance (cm/s) ²	skew	kurtosis
1	1	-0.8	109	-.014	-.076
	2	3.7	105	.032	-.074
	3	-9.3	70	.002	.014
	4	11.7	69	-.062	.124
3	1	-2.0	120	.031	-.001
	2	3.5	118	-.029	-.091
	3	-9.9	81	-.017	-.028
	4	11.6	77	-.051	.124
5	1	-0.4	212	.001	-.074
	2	1.9	209	.000	-.134
	3	-9.7	172	-.002	-.063
	4	11.4	149	-.033	.023

Table 6.2-3 Case 3: ADCP Doppler velocity statistics. * = skew, kurtosis values significantly different from zero ($p < 0.01$).

bin	beam	mean (cm/s)	variance (cm/s) ²	skew	kurtosis
1	1	-2.7	214	.048	.066
	2	5.7	210	-.017	.001
	3	-13.8	135	.036	.110
	4	16.83	129	.007	-.052
3	1	-2.8	261	.060	.069
	2	5.0	264	-.027	.139*
	3	-14.8	180	.007	-.117
	4	17.1	168	-.039	.063
5	1	-3.0	481	.087*	-.045
	2	5.0	496	-.020	-.027
	3	-15.1	396	.043	-.054
	4	17.2	350	-.007	-.068

Table 6.2-4 Case 4: ADCP Doppler velocity statistics. * = skew, kurtosis values significantly different from zero ($p < 0.01$).

bin	beam	mean (cm/s)	variance (cm/s) ²	skew	kurtosis
1	1	1.8	307	-.103*	-.074
	2	-1.2	244	.119*	-.068
	3	5.1	191	.085*	-.071
	4	-5.8	222	-.052	-.125
3	1	1.7	336	-.096*	-.074
	2	-3.0	285	.094*	-.016
	3	6.1	232	.051	-.130
	4	-7.8	246	-.053	-.041
5	1	1.8	496	-.081*	-.049
	2	-2.7	459	.097*	-.031
	3	4.6	416	.035	-.130
	4	-6.1	394	-.049	-.088

Table 6.2-5 Case 5: ADCP Doppler velocity statistics. * = skew, kurtosis values significantly different from zero ($p < 0.01$).

bin	beam	mean (cm/s)	variance (cm/s) ²	skew	kurtosis
1	1	-2.9	227	.037	-.085
	2	6.7	205	.020	-.189*
	3	-16.4	121	.077*	-.048
	4	19.4	115	-.006	.036
3	1	-3.2	262	.012	-.049
	2	6.2	255	.009	-.094
	3	-17.2	161	.035	-.012
	4	20.1	144	-.015	.018
5	1	-2.4	444	.035	-.145*
	2	5.6	459	.005	-.169*
	3	-18.4	342	.035	-.083
	4	22.0	280	-.040	-.054

Table 6.2-6 Case 6: ADCP Doppler velocity statistics. * = skew, kurtosis values significantly different from zero ($p < 0.01$).

bin	beam	mean (cm/s)	variance (cm/s) ²	skew	kurtosis
1	1	1.7	201	-.139*	-.006
	2	-0.9	164	.168*	.008
	3	4.3	89	.051	-.048
	4	-3.6	109	-.104*	.086
3	1	0.6	225	-.134*	-.015
	2	-1.4	192	.127*	-.103
	3	3.5	111	.076*	-.036
	4	-3.8	122	-.082*	.023
5	1	6.5	316	-.145*	.006
	2	-7.8	295	.148*	-.008
	3	8.1	215	.017	-.099
	4	-8.0	203	-.048	-.021

Table 6.3-1 ADCP noise spectral densities from autospectra of bin 1.

case	ADCP spectral noise density ((cm/s) ² /Hz)
1	25
2	20
3	23
4	20
5	22
6	22

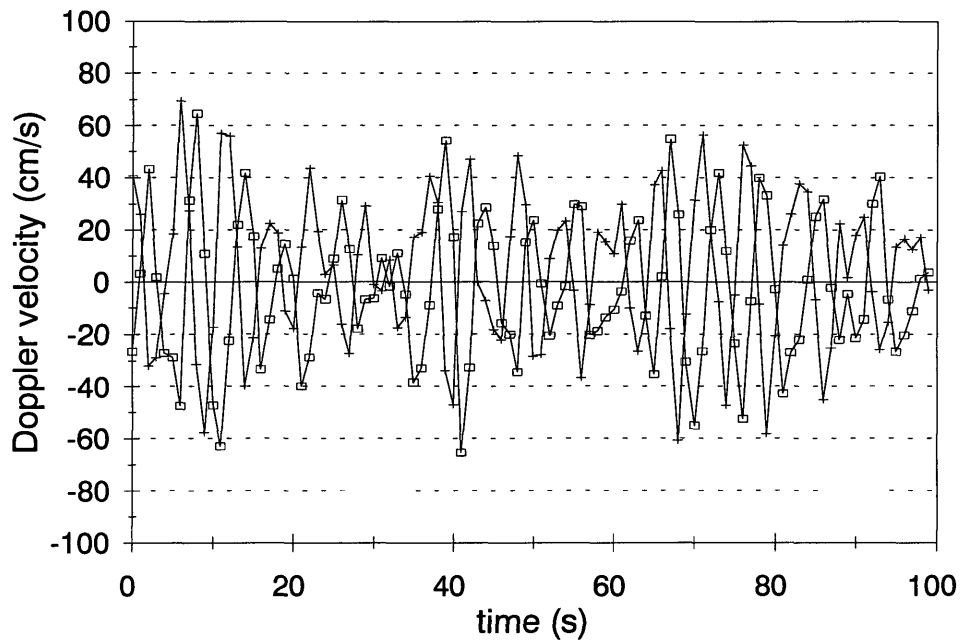


Figure 6.2-1 Time series plot of ADCP Doppler velocity data for case 4 from bin 5 for 100 s. \square = beam 1. + = beam 2.

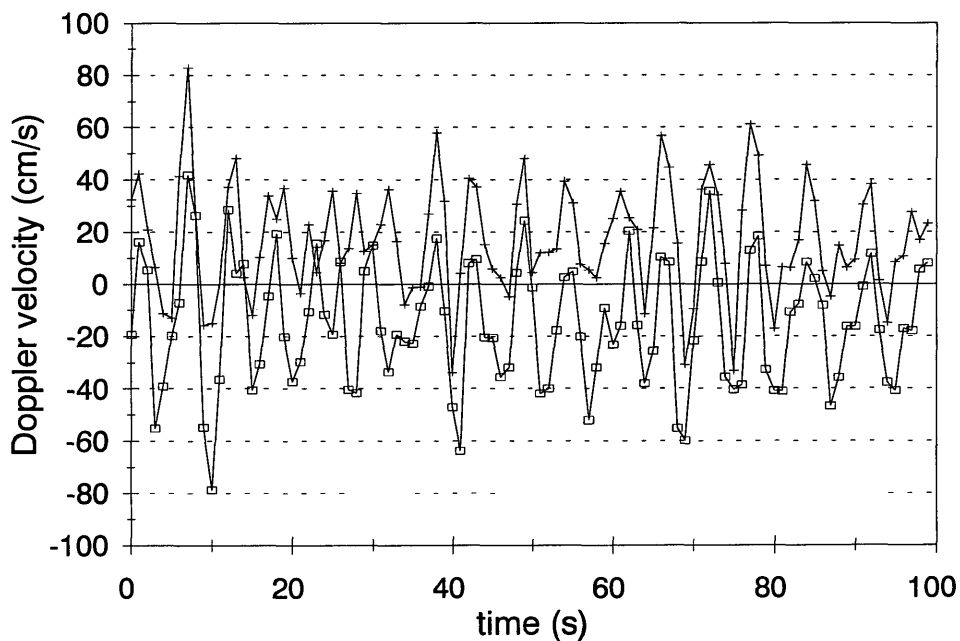


Figure 6.2-2 Time series plot of ADCP Doppler velocity data for case 4 from bin 5 for 100 s. \square = beam 3. + = beam 4.

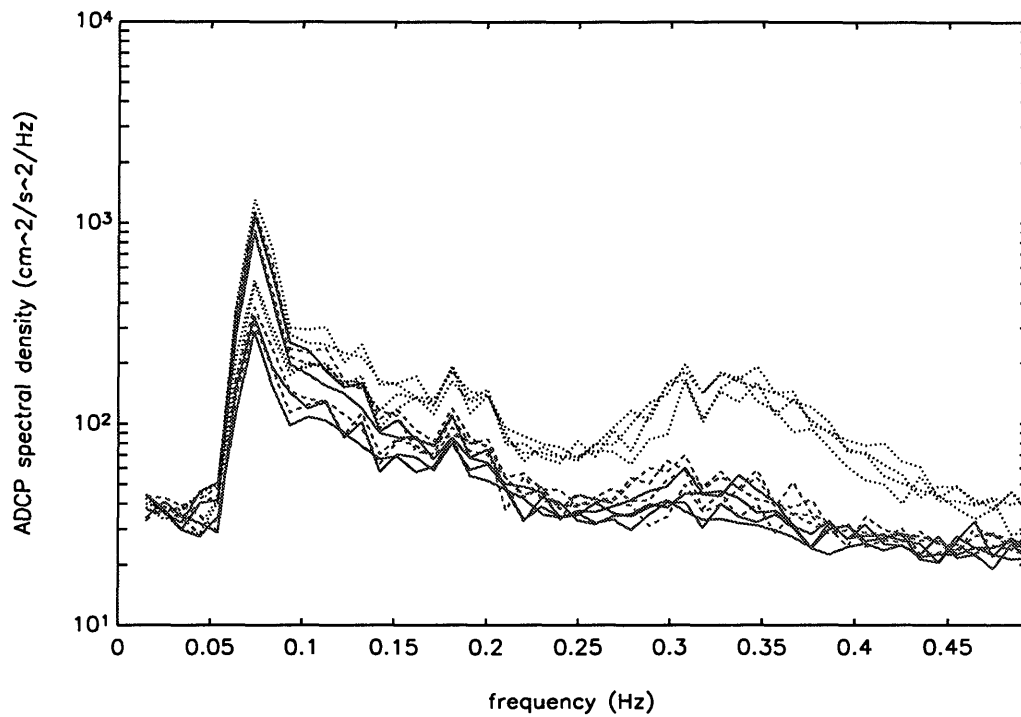


Figure 6.3-1 Case 1: ADCP autospectra for each beam from bins 1,3,5: solid line = bin 1 autospectra, dashed line = bin 3 autospectra, dotted line = bin 5 autospectra.

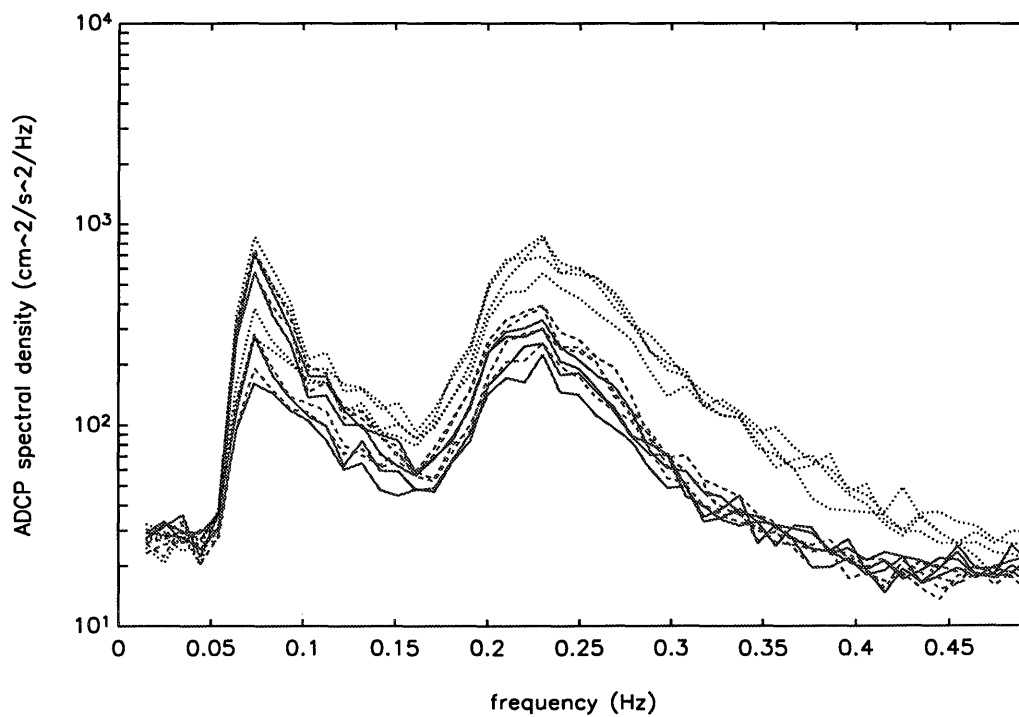


Figure 6.3-2 Case 2: ADCP autospectra for each beam from bins 1,3,5: solid line = bin 1 autospectra, dashed line = bin 3 autospectra, dotted line = bin 5 autospectra.

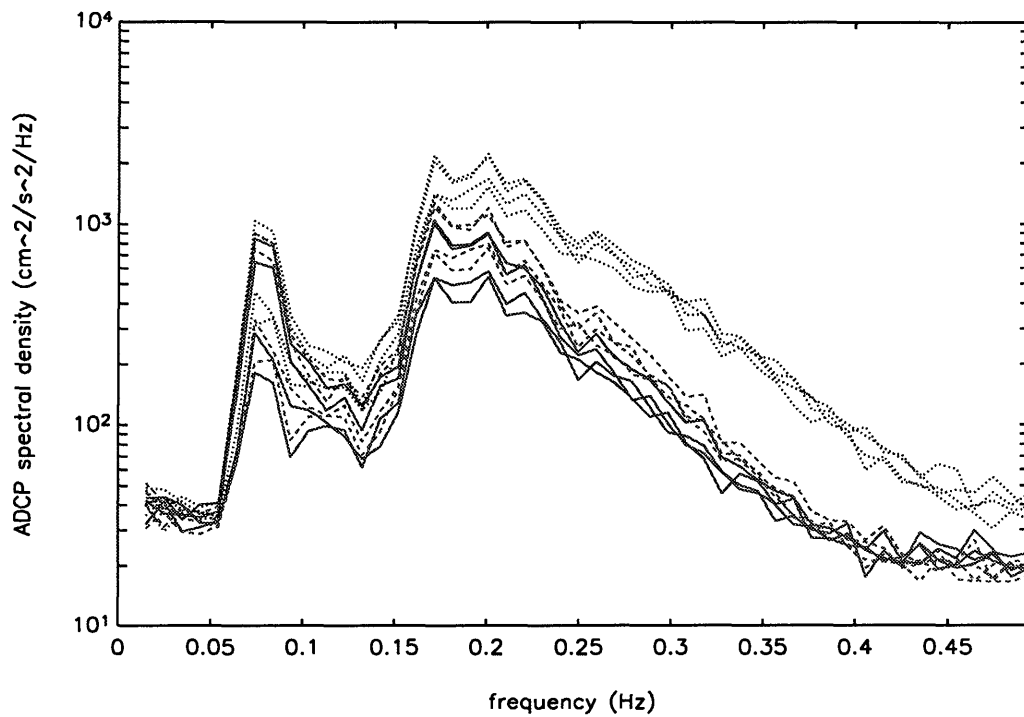


Figure 6.3-3 Case 3: ADCP autospectra for each beam from bins 1,3,5: solid line = bin 1 autospectra, dashed line = bin 3 autospectra, dotted line = bin 5 autospectra.

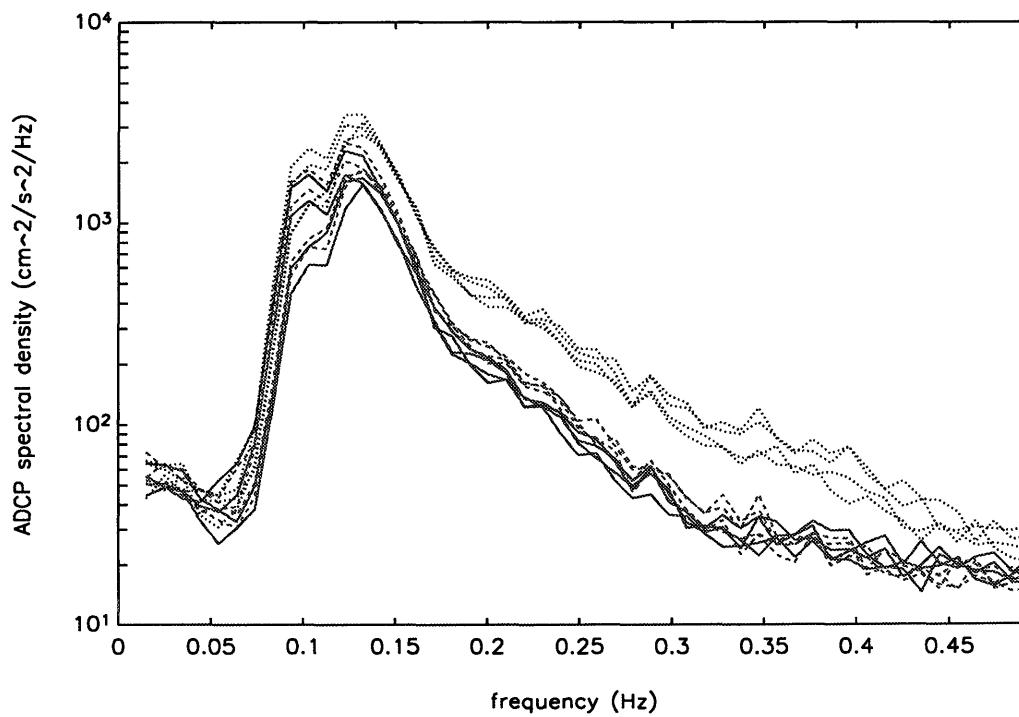


Figure 6.3-4 Case 4: ADCP autospectra for each beam from bins 1,3,5: solid line = bin 1 autospectra, dashed line = bin 3 autospectra, dotted line = bin 5 autospectra.

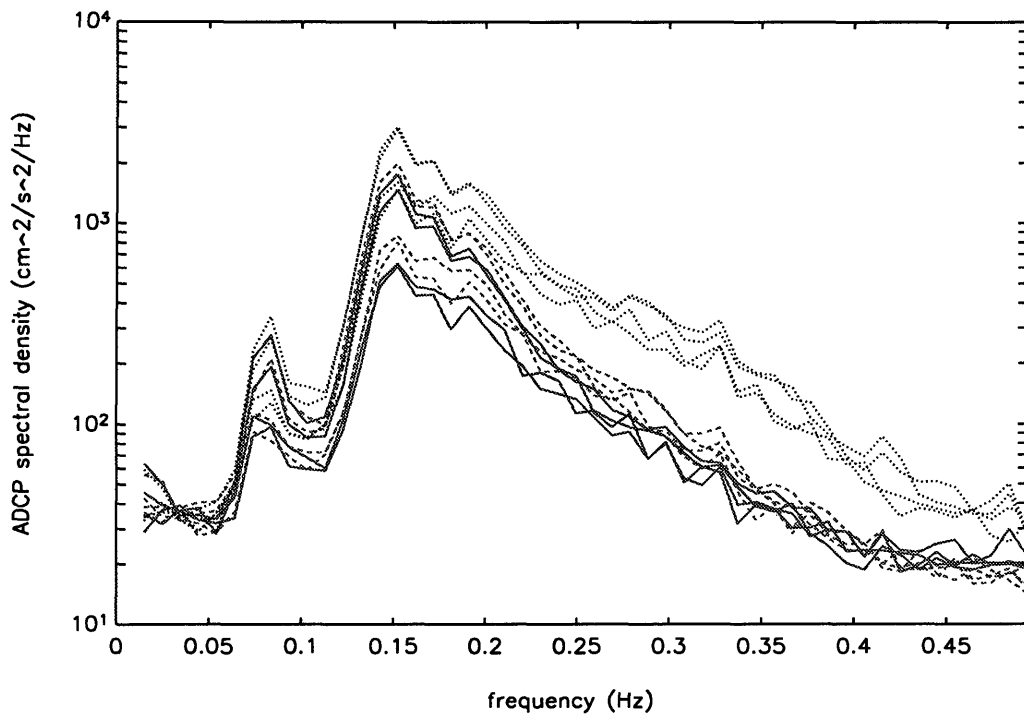


Figure 6.3-5 Case 5: ADCP autospectra for each beam from bins 1,3,5: solid line = bin 1 autospectra, dashed line = bin 3 autospectra, dotted line = bin 5 autospectra.

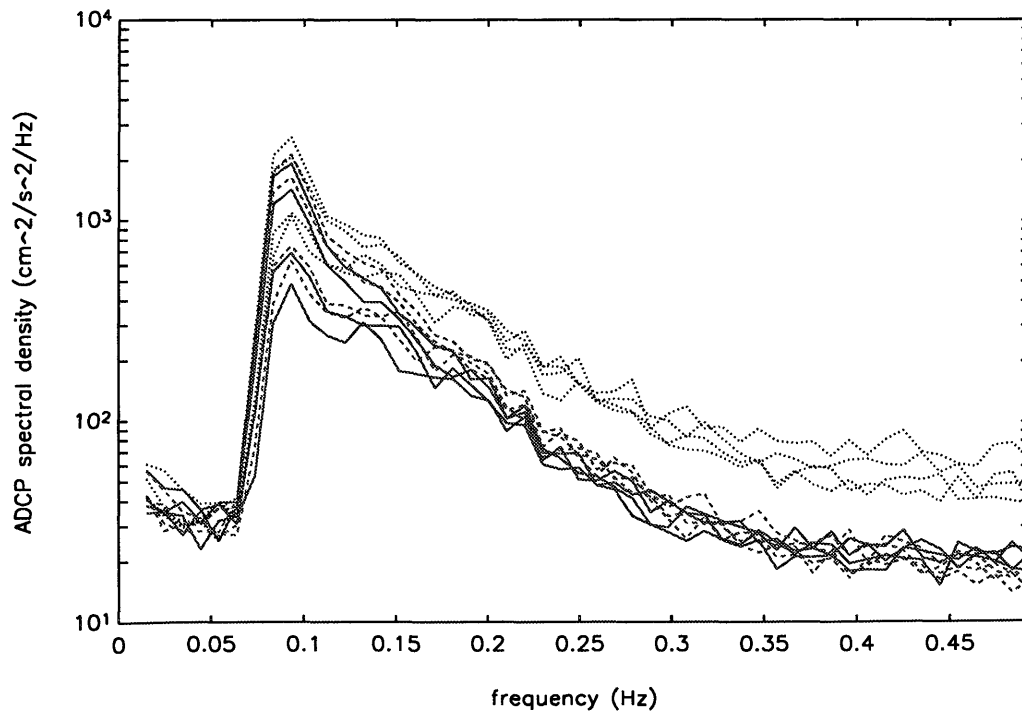


Figure 6.3-6 Case 6: ADCP autospectra for each beam from bins 1,3,5: solid line = bin 1 autospectra, dashed line = bin 3 autospectra, dotted line = bin 5 autospectra.

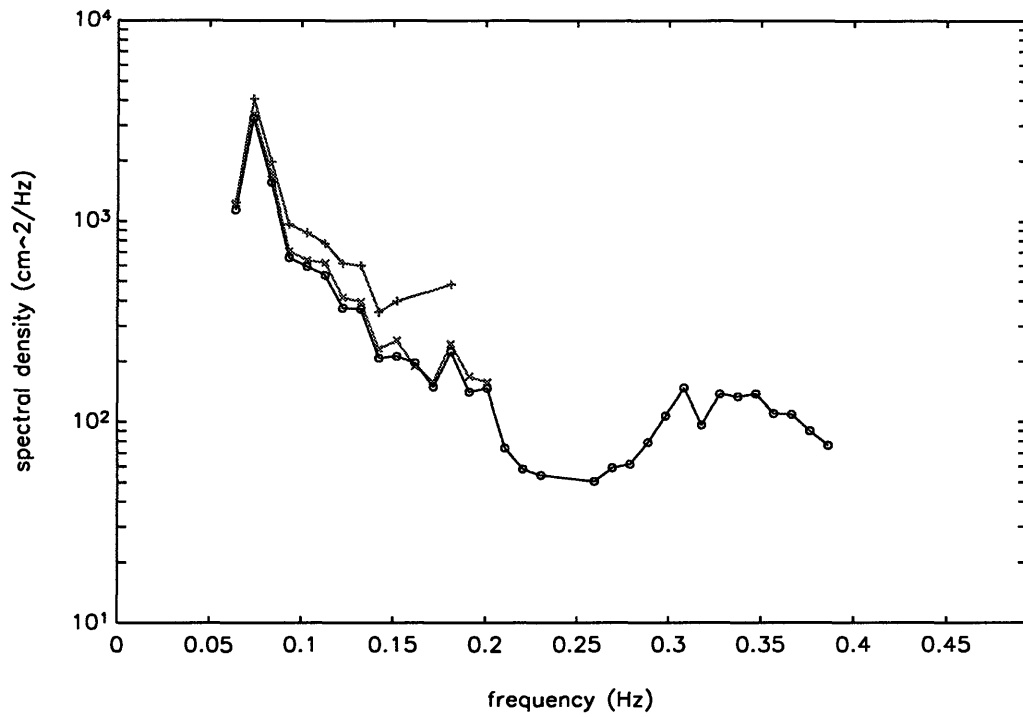


Figure 6.4-1 Case 1: sea surface elevation frequency spectra from ADCP autospectra: + = from bin 1, x = from bin 3, O = from bin 5.

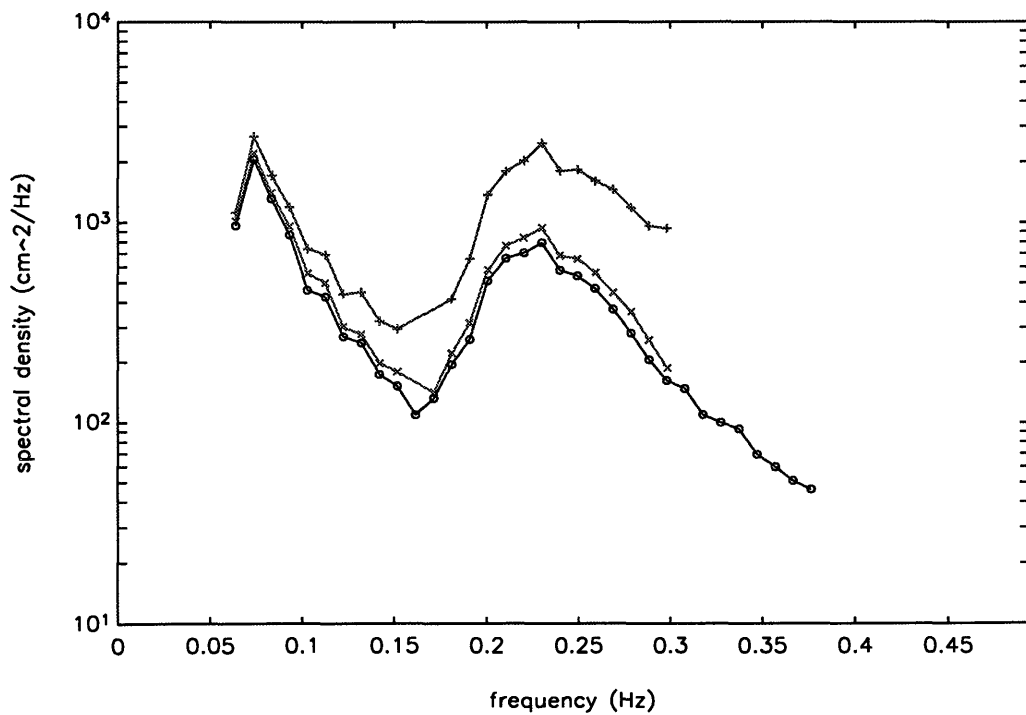


Figure 6.4-2 Case 2: sea surface elevation frequency spectra from ADCP autospectra: + = from bin 1, x = from bin 3, O = from bin 5.

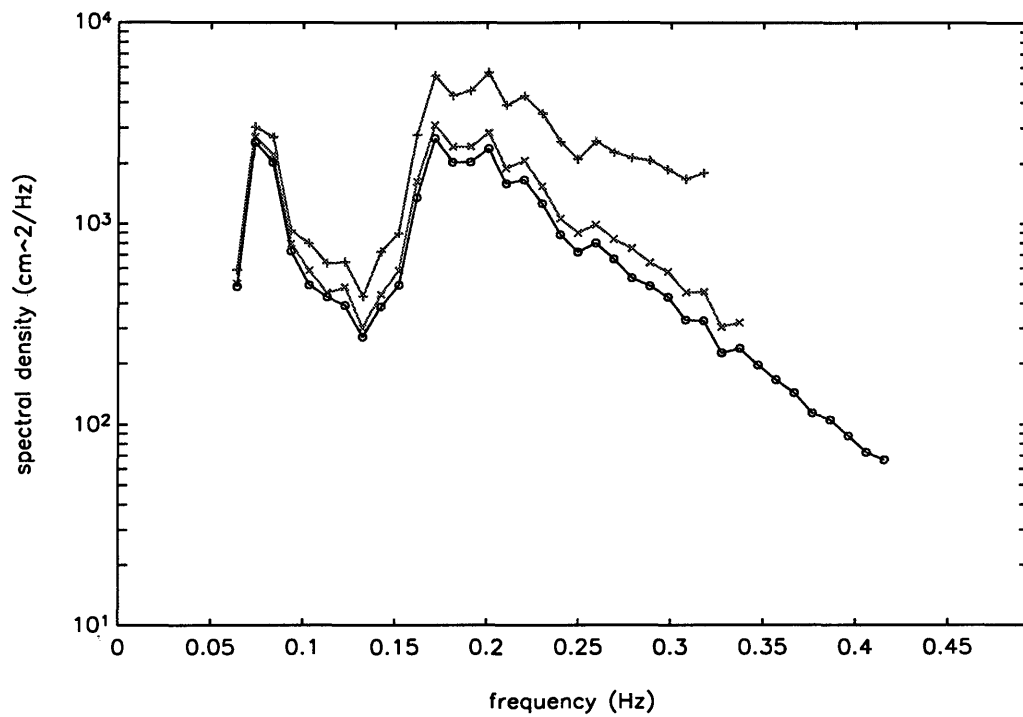


Figure 6.4-3 Case 3: sea surface elevation frequency spectra from ADCP autospectra: + = from bin 1, x = from bin 3, O = from bin 5.

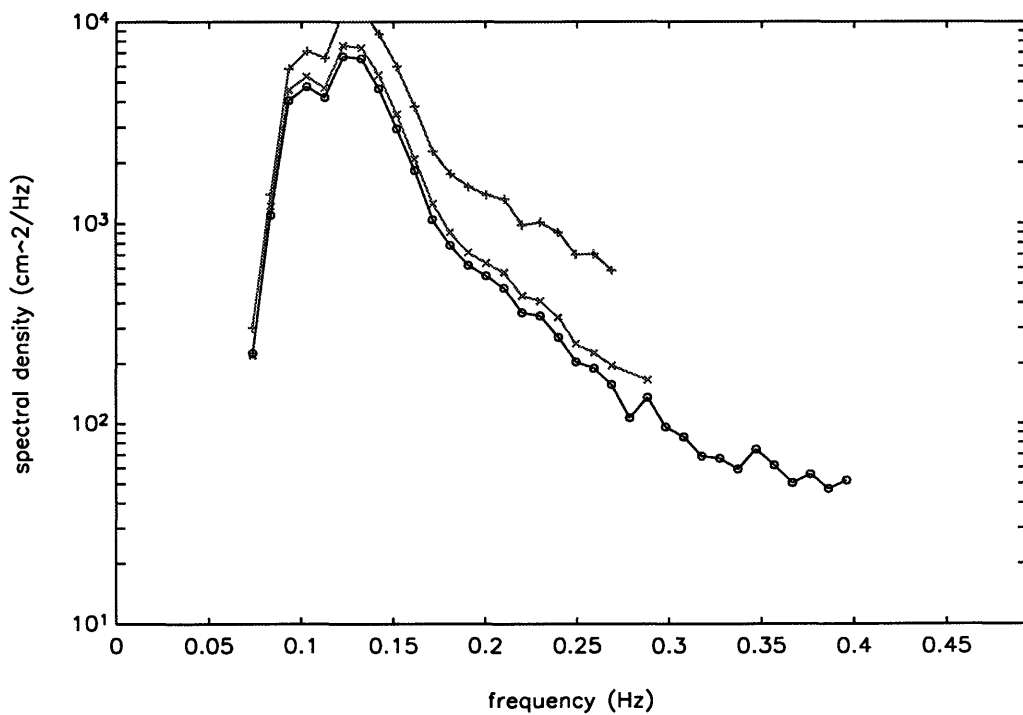


Figure 6.4-4 Case 4: sea surface elevation frequency spectra from ADCP autospectra: + = from bin 1, x = from bin 3, O = from bin 5.

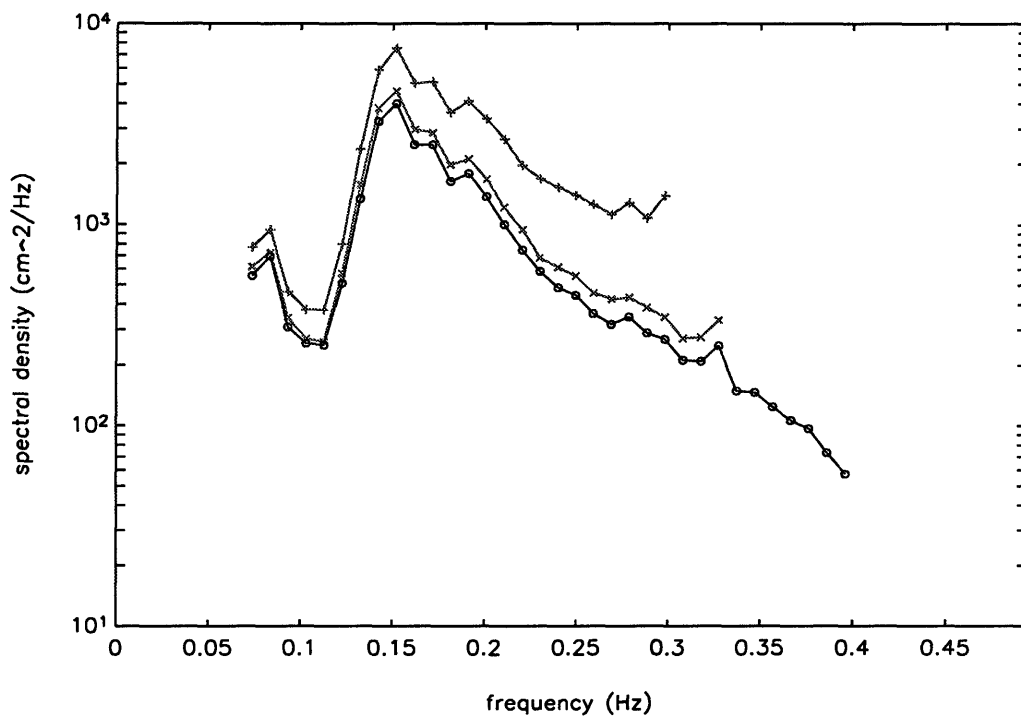


Figure 6.4-5 Case 5: sea surface elevation frequency spectra from ADCP autospectra: + = from bin 1, x = from bin 3, O = from bin 5.

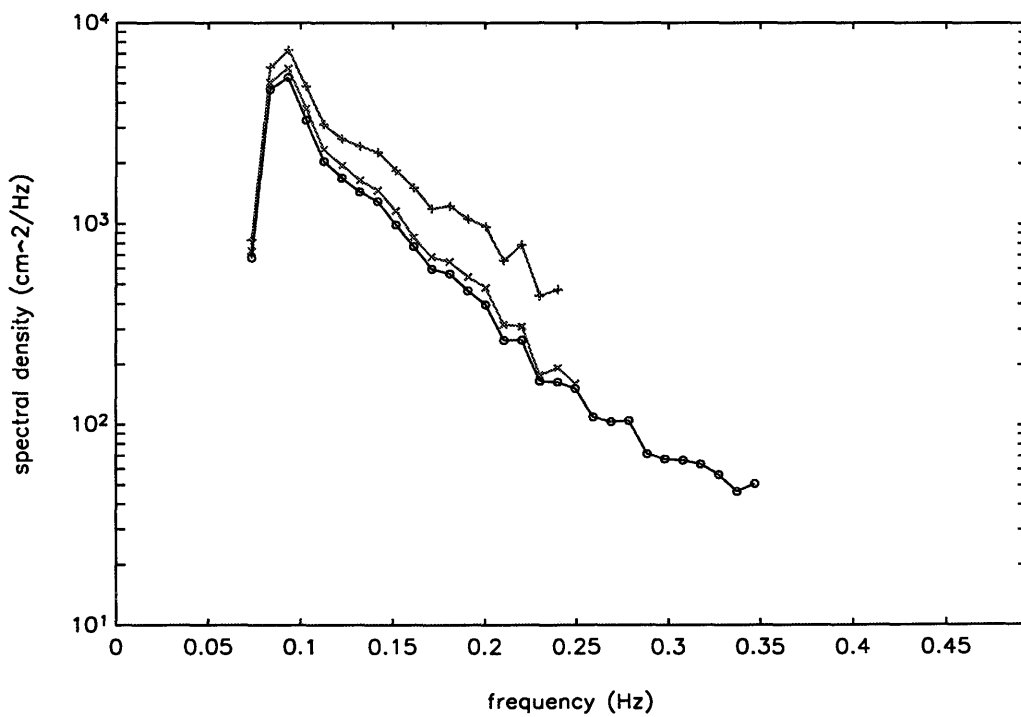


Figure 6.4-6 Case 6: sea surface elevation frequency spectra from ADCP autospectra: + = from bin 1, x = from bin 3, O = from bin 5.

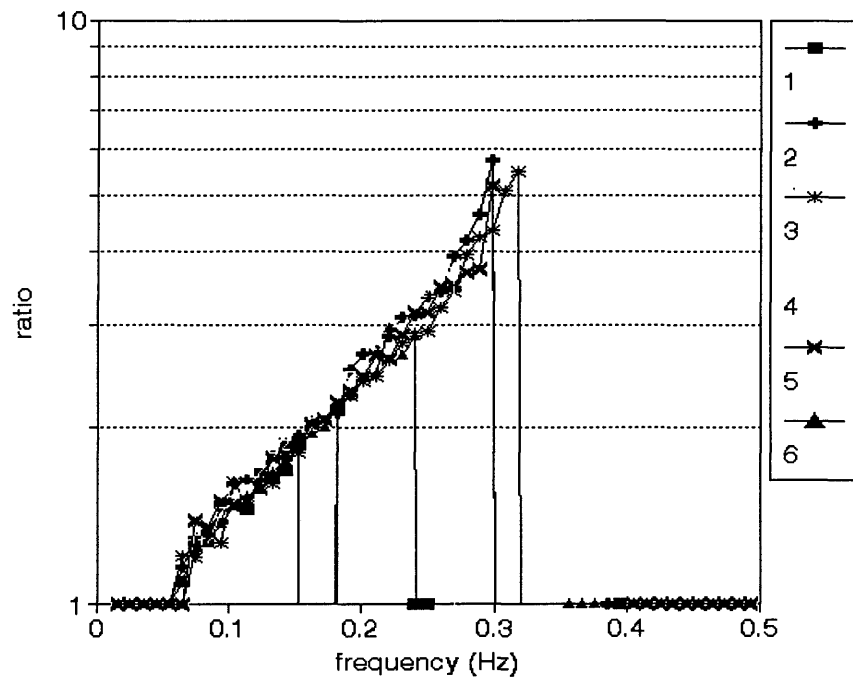


Figure 6.4-7 Ratio of bin 1 to bin 5 wave frequency spectra for each case. Cases identified in plot legend.

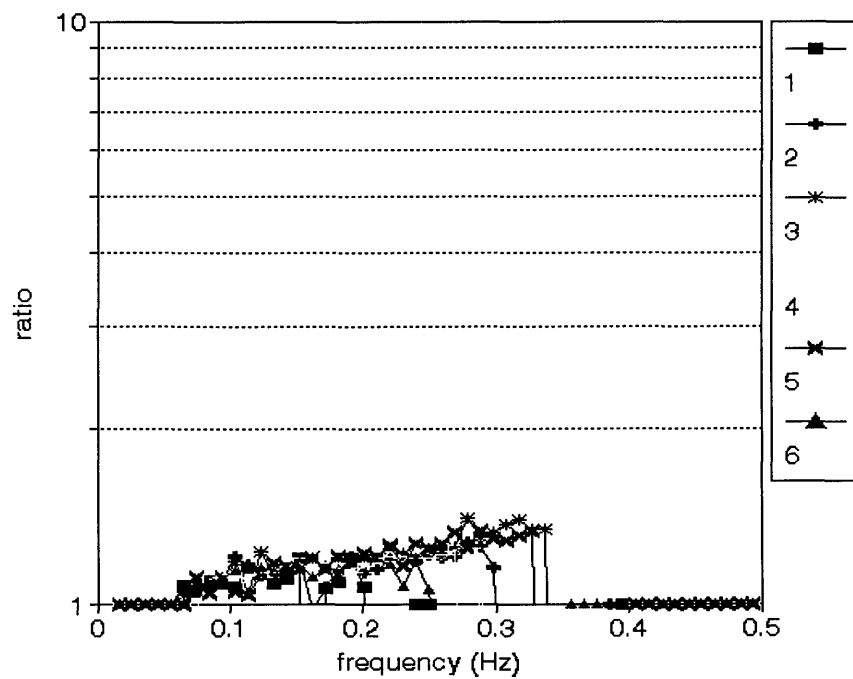


Figure 6.4-8 Ratio of bin 3 to bin 5 wave frequency spectra for each case. Cases identified in plot legend.

7. DIRECTIONAL SPECTRA RESULTS AND ANALYSIS

The estimated ADCP and LA IMLE directional spectra for the cases processed are presented and compared in the first section of this chapter. As will be seen, it is somewhat difficult to assess the accuracy of the ADCP directional spectra, relative to the LA directional spectra, based solely on surface and contour plots of the full directional wave spectrum. There are a number of important parameters of the wave field, such as the nondirectional frequency spectra $S(f)$ or the characteristic waveheight H_{mo} , which can be derived from the directional spectra. These parameters are often of more interest than the full directional spectra, particularly for engineering applications. To aid in the evaluation of the ADCP directional spectra, several integral properties of the directional wave spectrum are compared between the LA and ADCP results for each case. These integral properties include the nondirectional frequency spectrum $S(f)$ (sect. 7.2), the radiation stress angle $\alpha_{xy}(f)$ (sect. 7.3), the mean wave propagation angle $\Theta(f)$ (sect. 7.4), the directional width $\Delta(f)$ (sect. 7.5), the frequency-integrated directional spectrum $S(\theta)$ (sect. 7.6), and the characteristic waveheight H_{mo} and total radiation stress angle $\alpha_{xy,T}$ (sect. 7.7).

7.1 Directional wave spectra results

For each of the six cases selected (table 6.1), IMLE directional wave spectra were estimated from the ADCP cross spectra (see sect. 5.2 for details). The corresponding LA IMLE directional spectra were obtained from Dr. Charles Long at the U.S. Army Corps of Engineers' FRF (Duck, NC). They were estimated from the LA data sets using the method outlined in section 5.1.

The ADCP and LA directional spectra results are presented here as both 3-d surface plots and contour plots (fig.s 7.1-1 through 7.1-24). The directional spectra are plotted from -180° to 180° in direction and from 0.04 to 0.32 Hz in frequency. In case 5, one of the pressure sensors in the LA malfunctioned and its data was excluded from the directional spectra calculations. To avoid spatial aliasing, the LA IMLE directional spectrum for this case was

only computed to 0.28 Hz; however it is plotted here to 0.32 Hz as for the other cases. Each plot is normalized by the peak magnitude in the plotted directional spectrum. Contour plots are plotted using contours at factors of .10, .20, .30, .40, .50, .60, .70, .75, .80, .85, .90, and .95 of the peak spectral density. No formal theory exists for the errors associated with IMLE directional spectra estimates (Long and Oltman-Shay, 1991), so confidence intervals for the directional spectra cannot be calculated and thus are not included in the plots. The magnitude S_p , frequency f_p , period T_p , wavelength λ_p , and direction θ_p associated with the largest peak in the spectrum for both the ADCP and the LA IMLE directional spectra are listed in a separate table for each case (tables 7.1-1 through 7.1-6). For cases 2 and 3 (tables 7.1-2,3), where the wave energy was contained in two distinct modes--one at swell frequencies and one in the wind wave region--the parameters associated with the peak wave energy are listed for both the low frequency ("low f") and high frequency ("high f") modes. Some of these parameters are compared graphically for all six cases in figures 7.1-25 (S_p), 7.1-26 (T_p), and 7.1-27 (θ_p).

Wave energy in all six cases is characteristically located in the low frequency region ($f < 0.16$ Hz). Distinct wave energy modes at frequencies higher than 0.16 Hz occur only in cases 2 and 3. Low frequency wave energy is directed primarily within 10° of the onshore normal, although the direction associated with the peak energy for the LA results in case 1 is -16° . The high frequency wave energy modes in cases 2 and 3 appear at angles more oblique to the shore, up to 44° .

Overall, the ADCP directional spectra appear to reflect features in the LA directional spectra (taken here as the "true" distribution of wave energy) fairly well, although differences between the two are apparent for each case. Both the LA and ADCP directional spectra display single regions of observable wave energy ("modes") for cases 1, 4, 5, and 6 (compare fig.s 7.1-3,4, fig.s 7.1-15,16, fig.s 7.1-19,20, and fig.s 7.1-23,24). For cases 2 and 3, the LA and ADCP spectra both present dual (low and high frequency) modes (compare fig.s 7.1-7,8 and fig.s 7.1-11,12). In each of the six cases, the position of the 0.10 contours agree fairly well between the ADCP and LA spectra. Minor peaks occur in one directional spectrum which are not apparently reflected in the other (case 1, for example), but it is probably arguable that some of the minor peaks represent overfocussing of the IMLE procedure splitting a single broad peak, rather than actual distinct regions of wave energy.

The magnitude, period, and direction (S_p , T_p , θ_p) associated with the largest peaks in the LA and ADCP directional spectra agree fairly well for each case (tables 7.1-1 through 7.1-6 and fig.s 7.1-25,26,27). Peak magnitudes range from 1800 to 28,000 $\text{cm}^2/\text{Hz}/\text{rad}$ (fig. 7.1-25). Typical differences in peak magnitude between the two types of directional spectra are about 50%. Low frequency peaks in the ADCP spectra are typically larger than the corresponding peaks in the LA spectra, while the reverse is true for high frequency peaks. The period associated with the largest peaks in the directional spectra ranges from approximately 4.4 to 13.6 s (fig. 7-1.26), corresponding to wavelengths of 30 to 116 m. Typical differences in the frequency associated with the peak magnitude is less than 10%, while the largest discrepancy is less than 25% (case 4). The direction associated with the largest peak in the spectra varies from -30° to 45° (fig. 7.1-27). The largest difference in peak position is 20° , while the typical difference is less than 10° in absolute value.

The sequence of cases 1, 2, and 3 provide an indication of how well ADCP directional spectra can reflect dynamic changes in the existing wave field. The buildup of energy in the high frequency region during the approximately 12 hour time period for these cases, which was seen in the ADCP autospectra (sect. 6.3) and the ADCP wave frequency spectra (sect. 6.4), is also evident in both the LA and ADCP directional spectra for these cases (fig.s 7.1-1 through 7.1-12). In case 1, only an onshore-directed low frequency wave energy mode corresponding to swell is present (fig.s 7.1-1,2,3,4). This low frequency mode continues in cases 2 and 3 virtually unchanged. A high frequency mode (centered at about $f = 0.23$ Hz, $\theta = +25-30^\circ$) appears in the LA and ADCP directional spectra for case 2 (fig.s 7.1-5,6,7,8). In case 3, the peak of the high frequency mode has increased in energy (it is apparently larger than the peak of the low frequency mode, fig. 7.1-25), and shifted location to lower frequency ($f = 0.17$ Hz, fig. 7.1-26) and a larger "angle-of-attack" to the shore normal ($\theta = +40-45^\circ$, fig. 7.1-27).

The low frequency peak magnitude in the ADCP directional spectra varies from about 40% larger to 10% smaller and then back to 40% larger than the corresponding peak magnitude in the LA directional spectra for the three cases. Since this low frequency peak appears to be reasonably constant in the LA results, this variation may give some indication of the variability of the ADCP directional spectra. The frequency associated with this peak also appears to remain constant over the cases.

7.2 Nondirectional wave frequency spectra results

The nondirectional wave frequency spectra (or simply, the frequency spectra) $S(f)$ is related to the full directional wave spectra $S(f,\theta)$ by

$$S(f) = \int_{-\pi}^{\pi} S(f,\theta) d\theta \quad (7.1)$$

Nondirectional wave frequency spectra were computed from the IMLE directional spectra for both the LA and ADCP results by integrating the directional spectra over angle for each sampled frequency (fig.s 7.2-1 through 7.2-6). The wave frequency spectra calculated directly from the ADCP bin 5 autospectra (section 6.4) are included for each case as well. The frequency spectra are plotted as one-sided spectra. Unfortunately, confidence intervals cannot be calculated for the frequency spectra derived from the IMLE directional spectra. From a practical viewpoint, however, the three types of wave frequency spectra agree very well with each other.

The two types of frequency spectra derived from the ADCP data are almost identical in behavior for each case. The IMLE-derived spectra display a fairly constant (with frequency and among cases), small bias above the autospectra-derived wave frequency spectra. This bias originates in the normalization used for the MLE and IMLE directional spectra (section 5.2) and reflects the bias between the wave frequency spectra calculated from the autospectra for bins 3 and 5 (section 6.4).

The ADCP-derived wave frequency spectra agree with those calculated from the LA directional spectra particularly well at the low frequency peak observed for each case (fig.s 7.2-1 through 7.2-6). The only real disagreement at low frequencies (<0.2 Hz, say) between the ADCP-derived and the LA-derived wave frequency spectra occurs near the between the two low frequency peaks in case 5. However, even this disagreement is only about a factor of 2 (fig. 7.2-7). The agreement at higher frequencies (> 0.2 Hz) is more variable (fig. 7.2-7). In cases 1 and 6, the agreement at higher frequencies is good. In the other four cases, a discrepancy between the ADCP- and LA-derived wave frequency spectra begins at about 0.2 Hz and appears to increase with frequency. Based on the LA wave frequency spectra, the ADCP results appear to underestimate the energy at higher frequencies.

The agreement between both the magnitude $S_{p,f}$ and the period $T_{p,f}$ of the largest peak in the LA and ADCP frequency spectra is fairly good (fig.s 7.2-8,9). Although the peak magnitude is consistently underestimated in the ADCP results, relative to the LA results, the relative error is less than 10% in four out of the six cases (fig. 7.2-8)--and less than 50% in all six cases. The largest relative error occurs in case 3, which had the smallest period associated with the peak (fig. 7.2-9).

7.3 Radiation stress angle

One of the ways in which the directional content of the wave field can be summarized is by a frequency-dependent angle associated with the radiation stress. The off-diagonal component of the radiation stress tensor associated with the wave field, $S_{xy}(f)$, is important in the nearshore zone for longshore current generation and associated sediment transport (Bowen, 1969, Longuet-Higgins, 1970). It is related to the directional wave spectrum $S(f,\theta)$ by

$$S_{xy}(f) = \int_{-\pi}^{\pi} d\theta S(f,\theta) n(f) \sin(\theta) \cos(\theta) \quad (7.2)$$

where $n(f)$ is the ratio of the group speed to the phase speed of waves with frequency f (Thornton and Guza, 1986). The directional information in the directional wave spectrum can be collapsed into a single frequency-dependent angle $\alpha_{xy}(f)$, based on $S_{xy}(f)$, defined as

$$\sin(\alpha_{xy}(f)) \cos(\alpha_{xy}(f)) = \frac{S_{xy}(f)}{S(f) n(f)} \quad (7.3)$$

where $S(f)$ is the wave frequency spectrum (Thornton and Guza, 1986).

The radiation stress angle $\alpha_{xy}(f)$ was computed from the LA and ADCP directional spectra for each case using eq.s 7.2,3 (fig.s 7.3-1 through 7.3-6). The ADCP and LA results appear to be in good agreement. The ADCP results appear to reproduce the variation of α_{xy} with frequency apparent in the LA results (e.g. case 2, fig. 7.3-2). The difference between the ADCP and LA results as a function of frequency for each case appears to be respectable (fig. 7.3-7). The mean error (regardless of frequency) in the ADCP-derived angles, relative to the LA-derived angles, is -0.6° . The standard deviation is 4.7° . The largest disagreement

is about 15° (case 4), but this occurs at high frequency where little wave energy was detected.

7.4 Mean wave direction

Another way in which directional information can be summarized from the directional spectrum is by a frequency-dependent mean wave direction $\Theta(f)$, defined as

$$\Theta(f) = \frac{\int_{-\pi}^{\pi} d\theta \theta S(f, \theta)}{\int_{-\pi}^{\pi} d\theta S(f, \theta)} \quad (7.4)$$

To some extent, $\Theta(f)$ needs to be examined in conjunction with $S(f)$ since one intuitively expects the possible error in $\Theta(f)$ to be large when $S(f)$ is small (and possibly noise dominated).

The mean wave directions computed from the ADCP and LA directional spectra agree fairly well with each other (fig.s 7.4-1 through 7.4-6). For a given case, the ADCP-derived $\Theta(f)$ follows, for the most part, the same trend with frequency which occurs in the LA-derived results. The largest disagreement occurs in case 4 at high frequencies where $S(f)$ is small for both the LA and ADCP results (fig. 7.2-4), while agreement is fairly good at intermediate frequencies (fig. 7.4-4). At the lowest frequencies for this case, the ADCP results were set to zero because the ADCP directional spectrum was identically zero. No directional spectra were computed at the lowest frequencies sampled for the ADCP results because the ADCP cross spectra did not satisfy signal-to-noise requirements.

Even including the high frequency results from case 4, the errors in the ADCP-derived $\Theta(f)$ relative to the LA-derived $\Theta(f)$ (fig. 7.4-7) are comparable in size to the disagreement between ADCP- and LA-derived $\alpha_{xy}(f)$ (fig. 7.3-7). The mean difference is 0.6° and the standard deviation is 10°.

7.5 Directional width

A third characterization of the directional information contained in the directional wave

spectrum is an estimate of the frequency-dependent directional width $\Delta(f)$. There are several alternative definitions of this width, such as the *full width at half power* (defined as the arc subtended by the direction of the points which are at half the magnitude of the largest peak in the directional spectrum at frequency f , Oltman-Shay and Guza, 1984) or as a parameter characterizing a particular functional shape assumed for the directional spread of a peak (Mitsuyasu *et al.*, 1975). The first definition is useful if a single, unambiguous mode is present in the directional distribution of energy each frequency. The second is useful if this directional distribution of this mode fits the model (Long and Oltman-Shay, 1991). However, the directional spectra obtained here are clearly not unimodal in direction. Consequently, the definition used here is taken from Long and Oltman-Shay (1991) and has the advantage that it can be defined for distributions with any number of modes with any shapes. The frequency-dependent directional width $\Delta(f)$ is defined as the difference of the 75th and 25th percentiles (third and first quartiles) of the cumulative directional distribution of wave energy at the frequency f . Mathematically, $\Delta(f)$ is calculated as

$$\Delta(f) = \theta_{0.75,f} - \theta_{0.25,f} \quad (7.5)$$

where the percentile $\theta_{p,f}$ is defined as

$$I(f, \theta_{p,f}) = P \quad (7.6)$$

and the cumulative distribution $I(f, \theta)$ is defined as

$$I(f, \theta) = \frac{\int_{-\pi}^{\theta} d\theta S(f, \theta)}{\int_{-\pi}^{\pi} d\theta S(f, \theta)} \quad (7.7)$$

It again appears that the ADCP and LA results are in agreement over the six cases (fig. 7.5-1 through 7.5-6), although this agreement is certainly of a rougher nature than that obtained for $\alpha_{xy}(f)$ and $\Theta(f)$. At lower frequencies ($f < 0.2$ Hz), the ADCP results underestimate the directional width relative to the LA results, whereas the opposite is true at higher frequencies (fig. 7.5-7). The mean difference between the ADCP widths relative

to the LA results is -4° , while the standard deviation is 10° .

7.6 Frequency-integrated directional spectra

The final approach to summarizing the directional content of the directional wave spectrum used here is the frequency-integrated directional spectrum $S(\theta)$, which is the directional analog to the nondirectional frequency spectrum $S(f)$ (sect. 7.2). The frequency-integrated directional spectrum is defined as

$$S(\theta) = \int df S(f, \theta) \quad (7.8)$$

where the integration is from zero to 3.18 Hz. As with the nondirectional frequency spectrum, no confidence intervals can be assigned to $S(\theta)$ calculated from IMLE directional spectra.

The frequency-integrated directional spectra computed from the ADCP and LA IMLE directional spectra agree roughly with one another for each case (fig.s 7.6-1 through 7.6-6), although the agreement in certain cases can be termed better (e.g. case 6, fig 7.6-6) and in others can certainly be termed worse (case 3, fig. 7.6-3). The magnitude associated with the largest peak, $S_{p,d}$, in the ADCP frequency-integrated directional spectrum tended to be smaller than its counterpart in the LA spectrum (in four out of the six cases, fig. 7.6-7). The relative difference in magnitude between the ADCP and LA results was less than 20% in three cases (2,4,5) while the largest difference was almost 60% (case 3). The directions associated with the largest peak, $\Theta_{p,d}$ in the ADCP and LA frequency-integrated directional spectra agree to better than 10° in four out of the six cases (fig. 7.6-8), while the largest difference is less than 20° .

7.7 H_{mo} and $\alpha_{xy,T}$

The final two summary parameters, H_{mo} and $\alpha_{xy,T}$, considered here characterize the directional wave spectrum with a single number each. The characteristic waveheight H_{mo} is four times the variance of the sea surface elevation (Long, 1991). It can be computed from the directional wave spectrum $S(f, \theta)$ by (Long, 1991):

$$H_{mo}^2 = 16 \times \int df \int d\theta S(f, \theta) \quad (7.9)$$

where the integration over direction is from $-\pi$ to π . The total radiation stress angle $\alpha_{xy,T}$ characterizes the total directional distribution of wave energy as the frequency-dependent radiation stress angle $\alpha_{xy}(f)$ (sect. 7.3) characterized the directional distribution at each frequency. The total radiation stress angle $\alpha_{xy,T}$ is defined as (Thornton and Guza, 1986):

$$\alpha_{xy,T} = \frac{1}{2} \sin^{-1} \left\{ \frac{2 S_{xy,T}}{H_{mo}^2 \frac{n(f_{p,f})}{16}} \right\} \quad (7.10)$$

where the total off-diagonal radiation stress $S_{xy,T}$ is the frequency-integrated off-diagonal radiation stress

$$S_{xy,T} = \int df S_{xy}(f) \quad (7.11)$$

and $n(f_{p,f})$ is the ratio of the wave group to phase speed at the frequency $f_{p,f}$ of the largest peak in the nondirectional frequency spectrum $S(f)$. For both H_{mo} and $\alpha_{xy,T}$, the integration over frequency is from zero to 3.18 Hz.

The characteristic waveheights computed from the ADCP and LA directional spectra agree fairly well with each other for all six cases (fig. 7.7-1). The ADCP results are lower than the LA results in every case, but the largest relative error is only 25% (case 3). Similarly, the results for $\alpha_{xy,T}$ show good agreement between the ADCP and LA values for each case (fig. 7.7-2). The largest discrepancy is only 5°. It is perhaps noteworthy that similar trends in $\alpha_{xy,T}$ are exhibited through cases 1, 2, and 3 for both the ADCP and the LA.

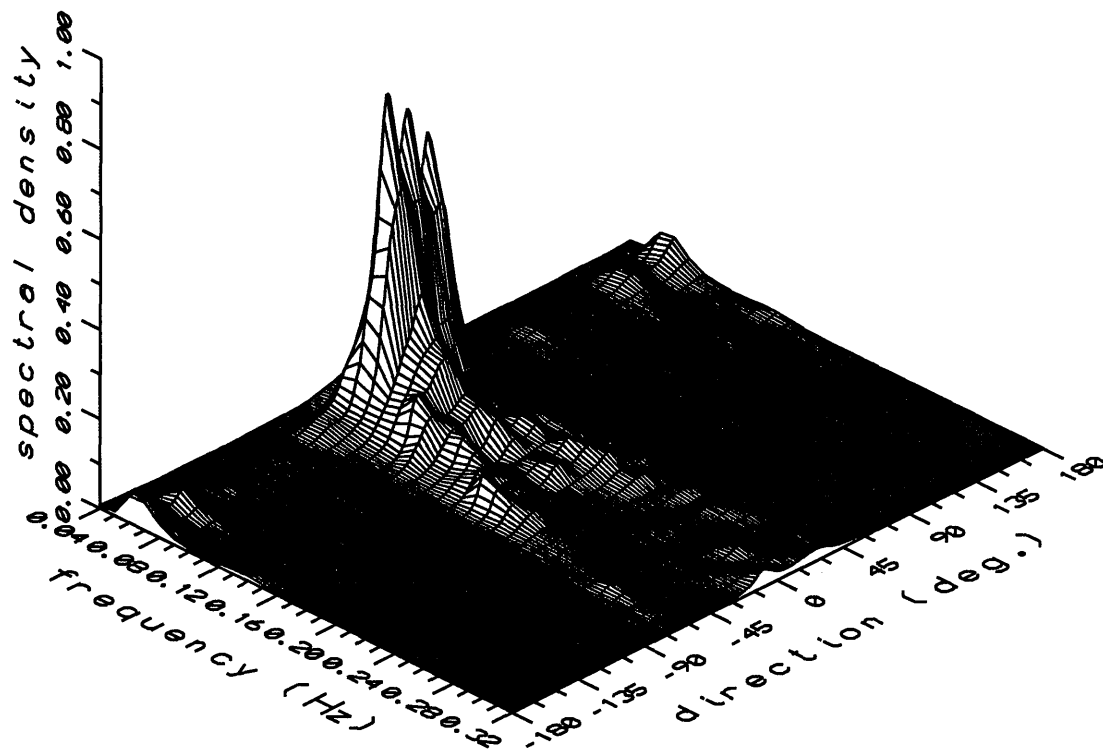


Figure 7.1-1 Case 1: surface plot of normalized LA IMLE directional spectra.

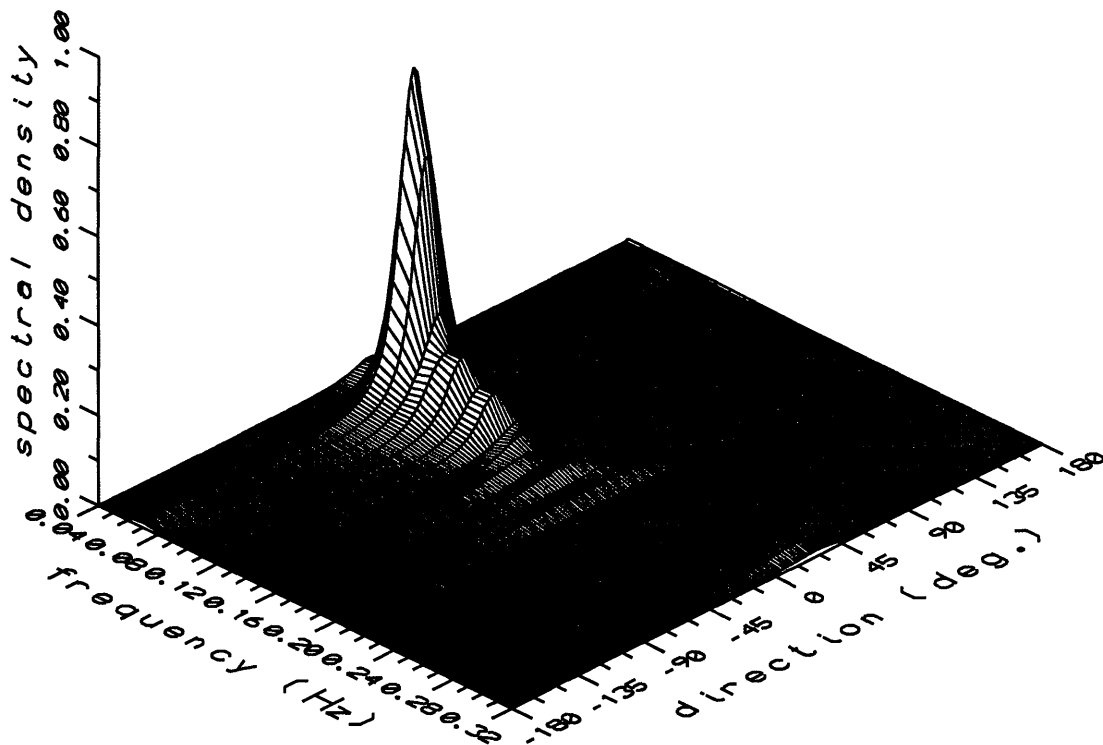


Figure 7.1-2 Case 1: surface plot of normalized ADCP IMLE directional spectra.

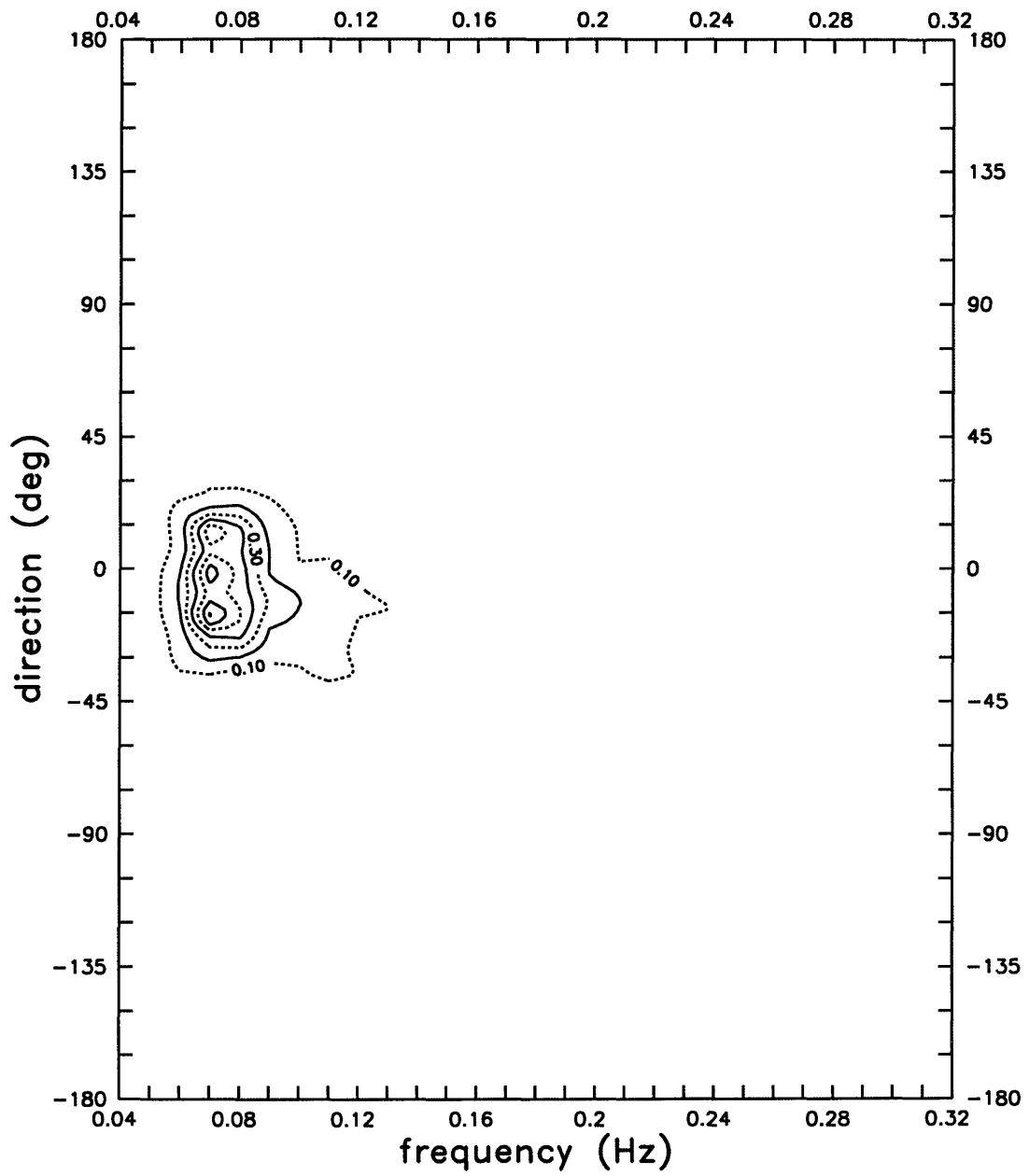


Figure 7.1-3 Case 1: topographic plot of normalized LA IMLE directional spectra.

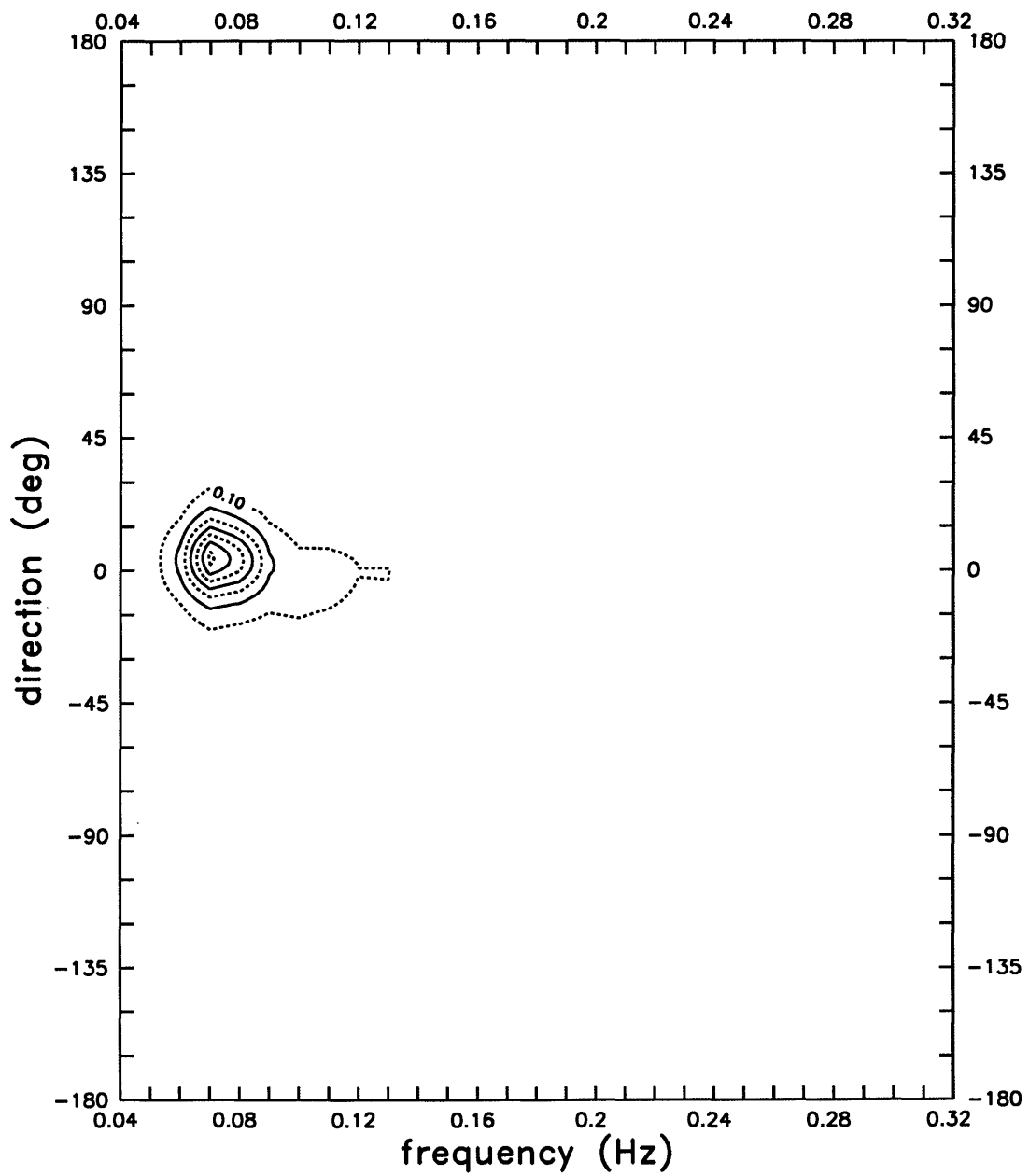


Figure 7.1-4 Case 1: topographic plot of normalized ADCP IMLE directional spectra.

Table 7.1-1 Case 1: IMLE directional spectra results.

	Linear Array results	ADCP results
S_p ($\text{cm}^2\text{-Hz}^{-1}\text{-rad}^{-1}$)	8660	12400
f_p (Hz)	.074	.074
T_p (s)	13.6	13.6
λ_p (m)	116	116
θ_p (deg)	-16	4

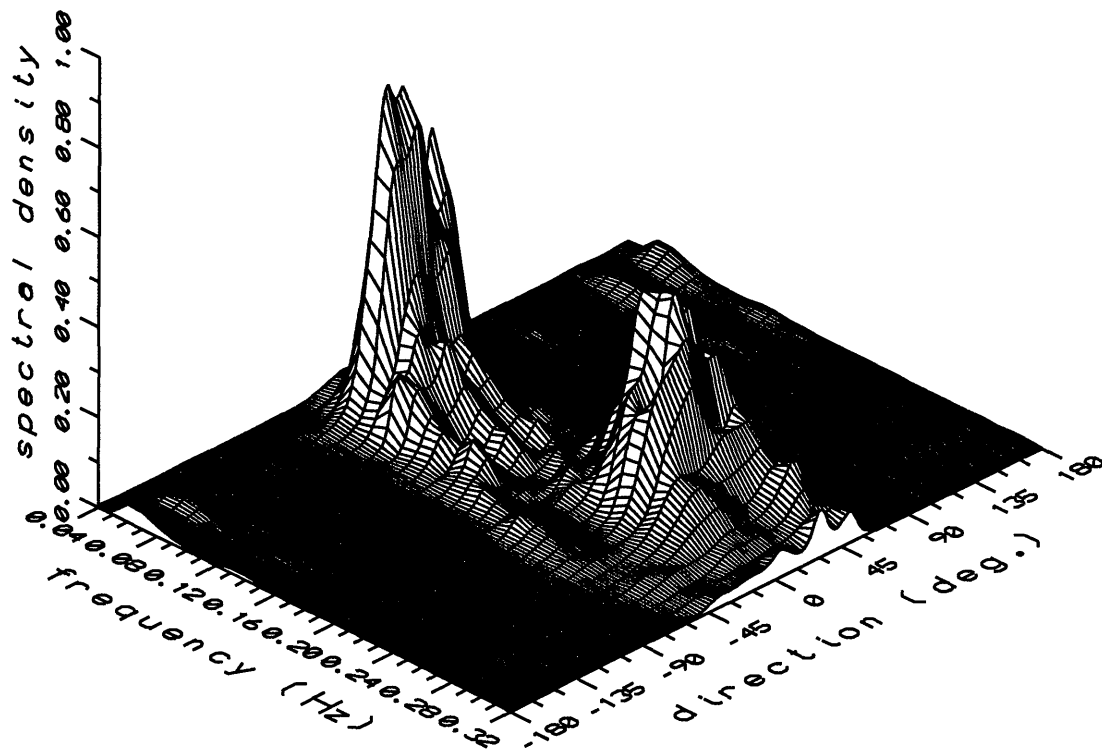


Figure 7.1-5 Case 2: surface plot of normalized LA IMLE directional spectra.

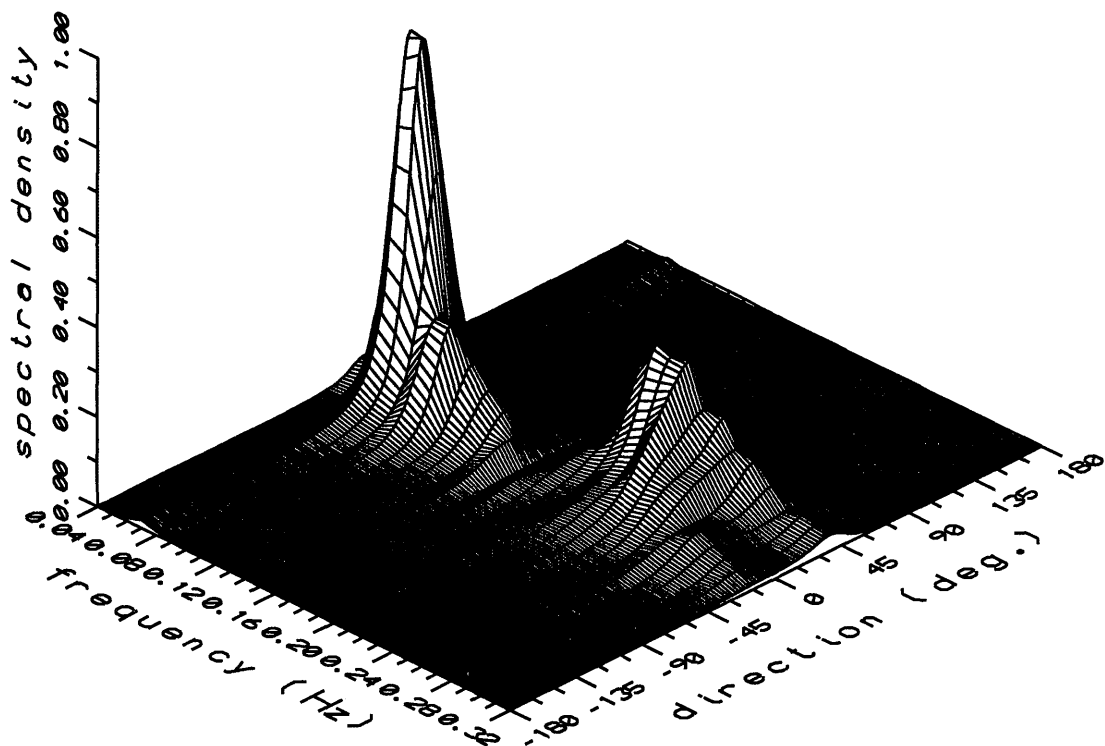


Figure 7.1-6 Case 2: surface plot of normalized ADCP IMLE directional spectra.

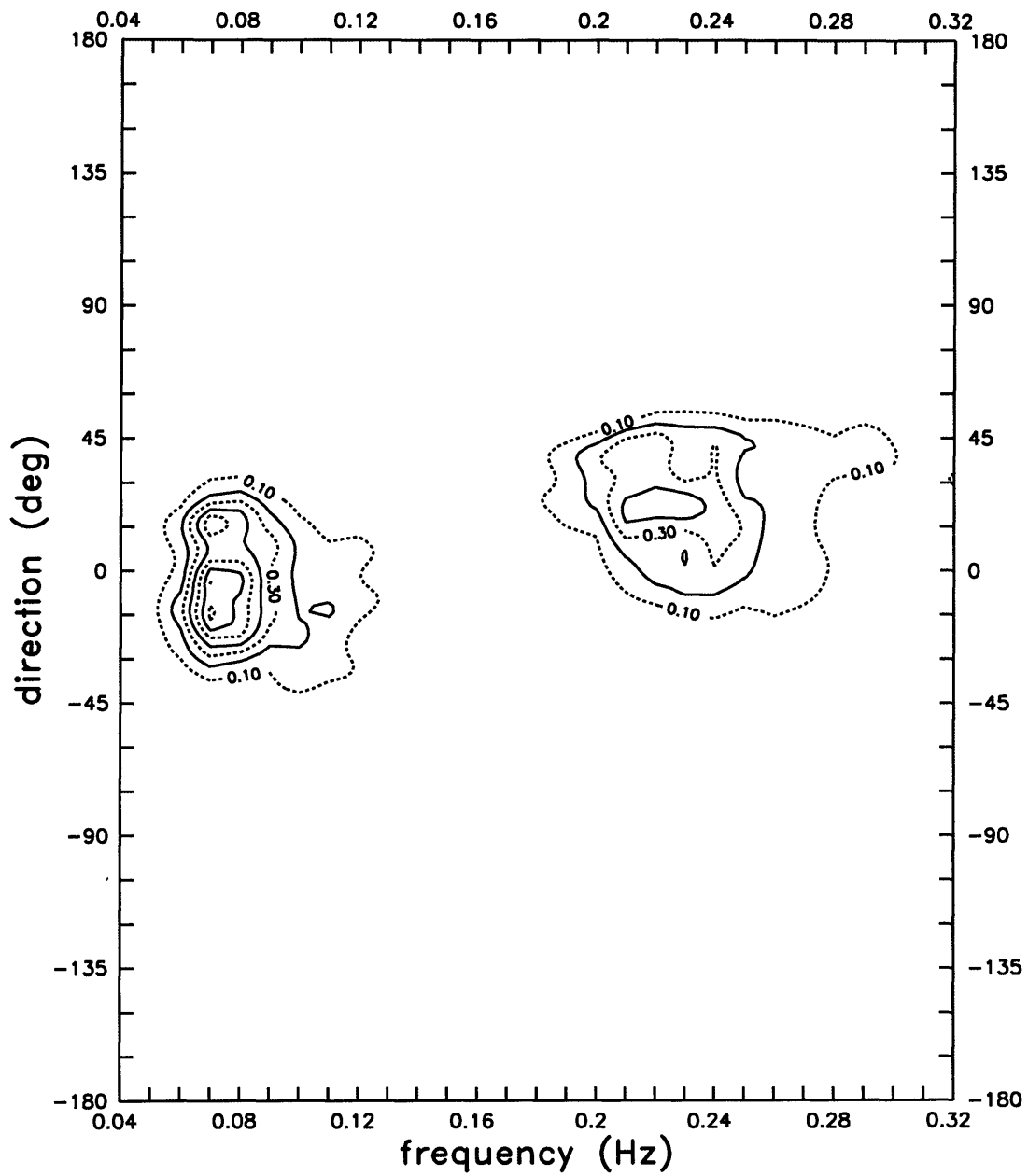


Figure 7.1-7 Case 2: topographic plot of normalized LA IMLE directional spectra.

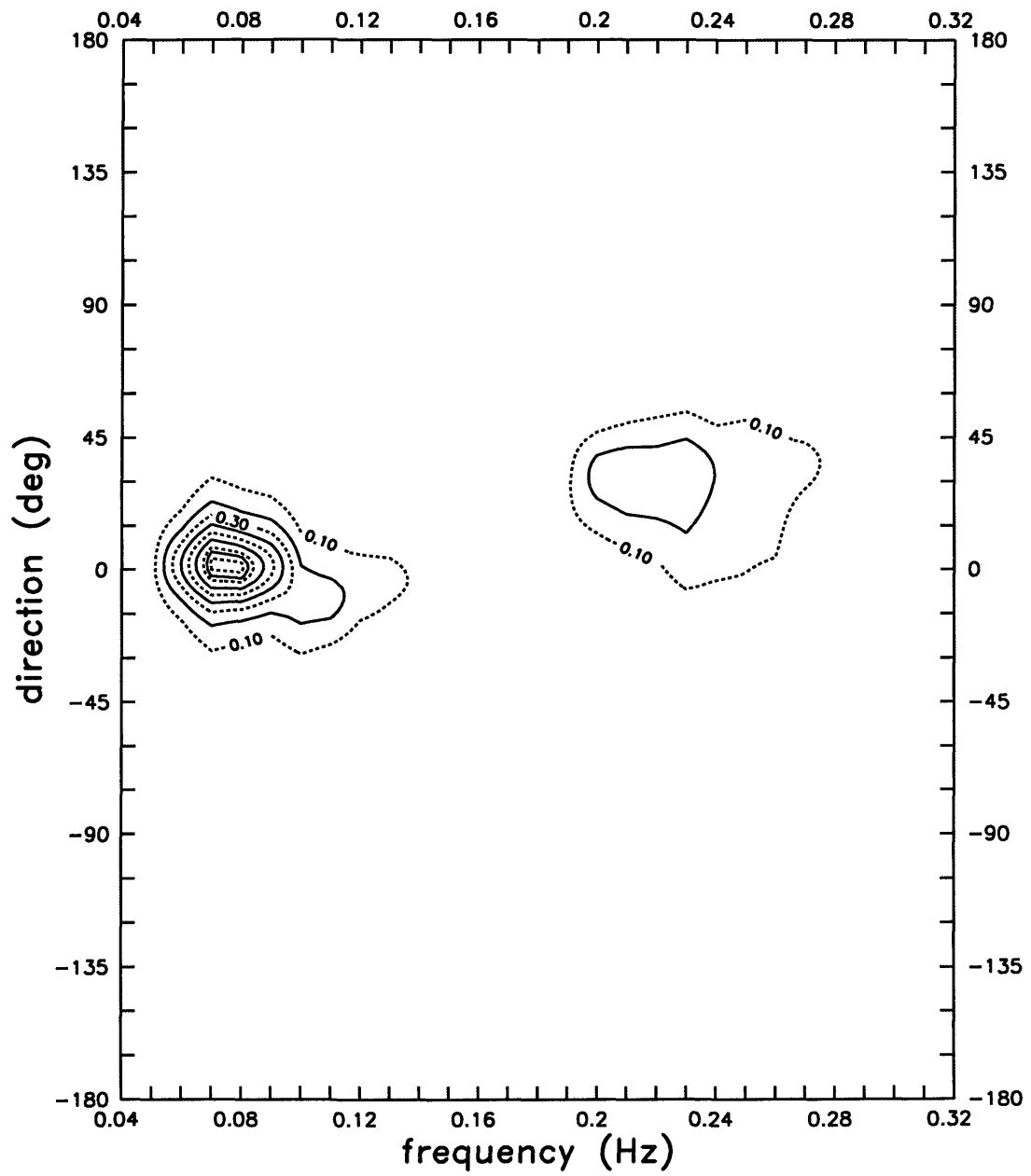


Figure 7.1-8 Case 2: topographic plot of normalized ADCP IMLE directional spectra.

Table 7.1-2 Case 2: IMLE directional spectra results.

	Linear Array results		ADCP results	
	low f	high f	low f	high f
S_p ($\text{cm}^2\text{-Hz}^{-1}\text{-rad}^{-1}$)	6560	3040	6890	1827
f_p (Hz)	.074	.230	.074	.210
T_p (s)	13.6	4.35	13.6	4.75
λ_p (m)	116	30	116	32
θ_p (deg)	-4	22	-2	31

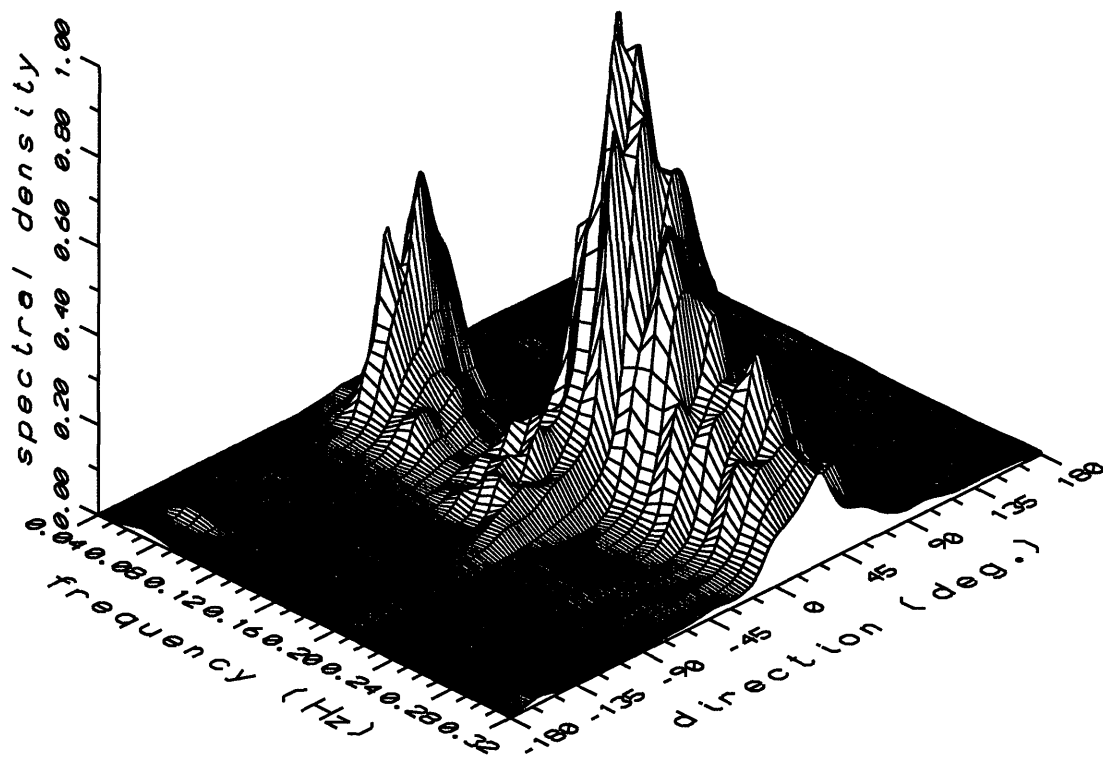


Figure 7.1-9 Case 3: surface plot of normalized LA IMLE directional spectra.

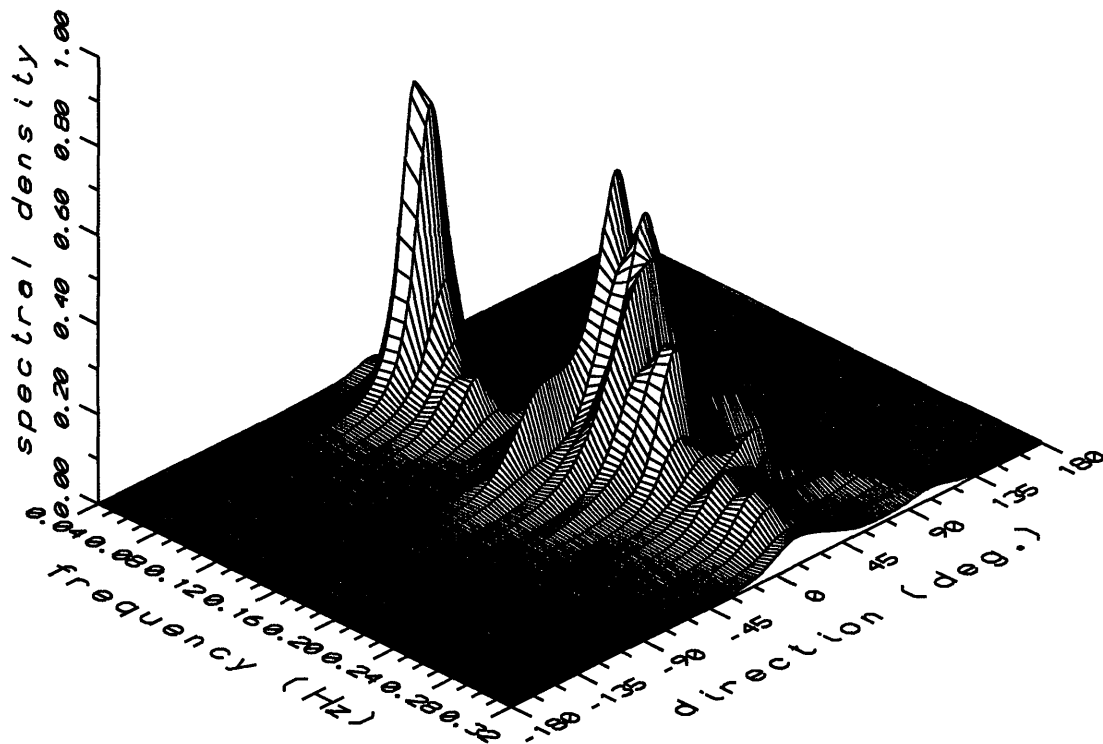


Figure 7.1-10 Case 3: surface plot of normalized ADCP IMLE directional spectra.

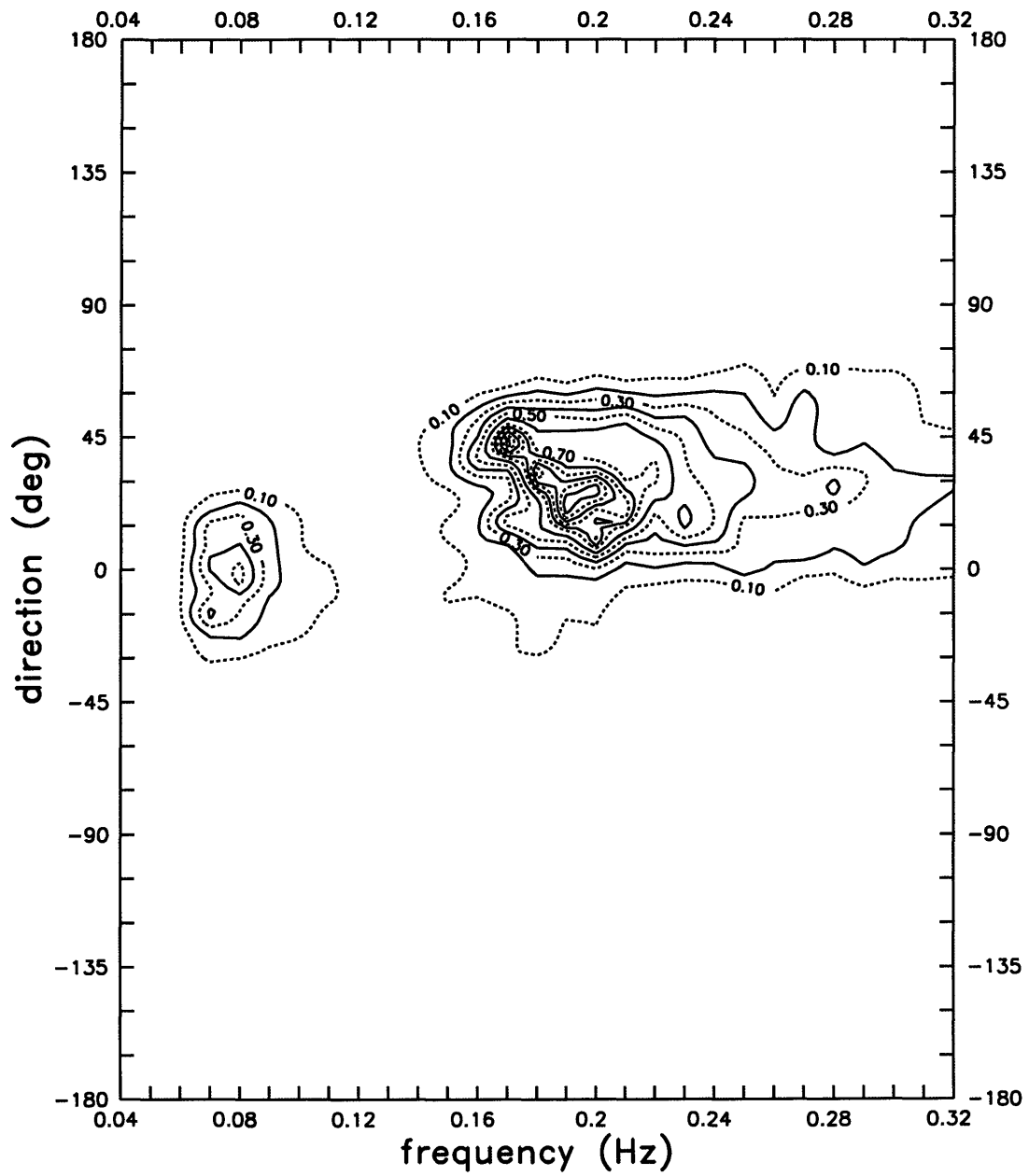


Figure 7.1-11 Case 3: topographic plot of normalized LA IMLE directional spectra.

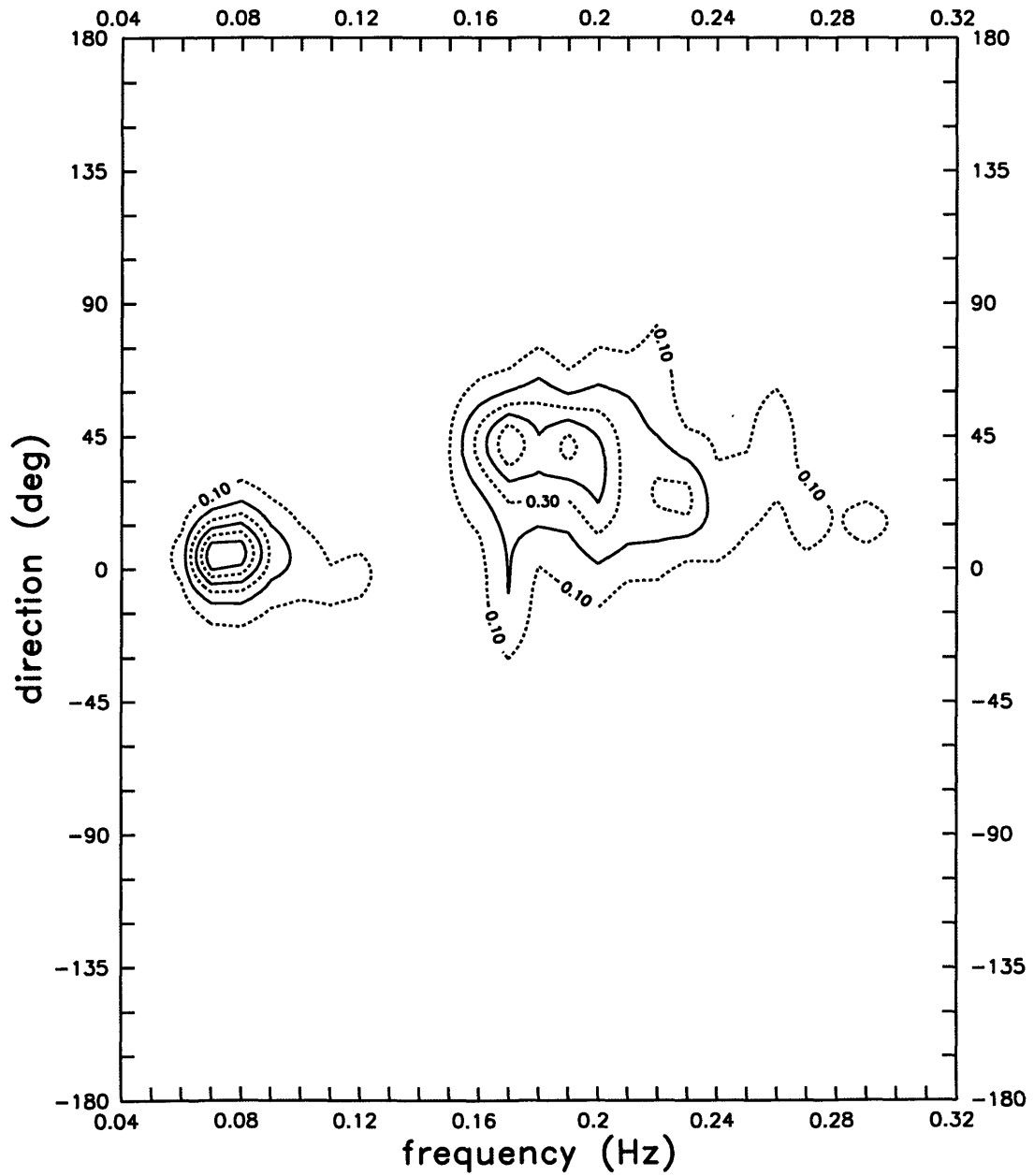


Figure 7.1-12 Case 3: topographic plot of normalized ADCP IMLE directional spectra.

Table 7.1-3 Case 3: IMLE directional spectra results.

	Linear Array results		ADCP results	
	low f	high f	low f	high f
S_p ($\text{cm}^2\text{-Hz}^{-1}\text{-rad}^{-1}$)	7389	11597	10233	6233
f_p (Hz)	.084	.171	.074	.171
T_p (s)	12.0	5.84	13.6	5.84
λ_p (m)	102	44	117	44
θ_p (deg)	-2	44	4	43

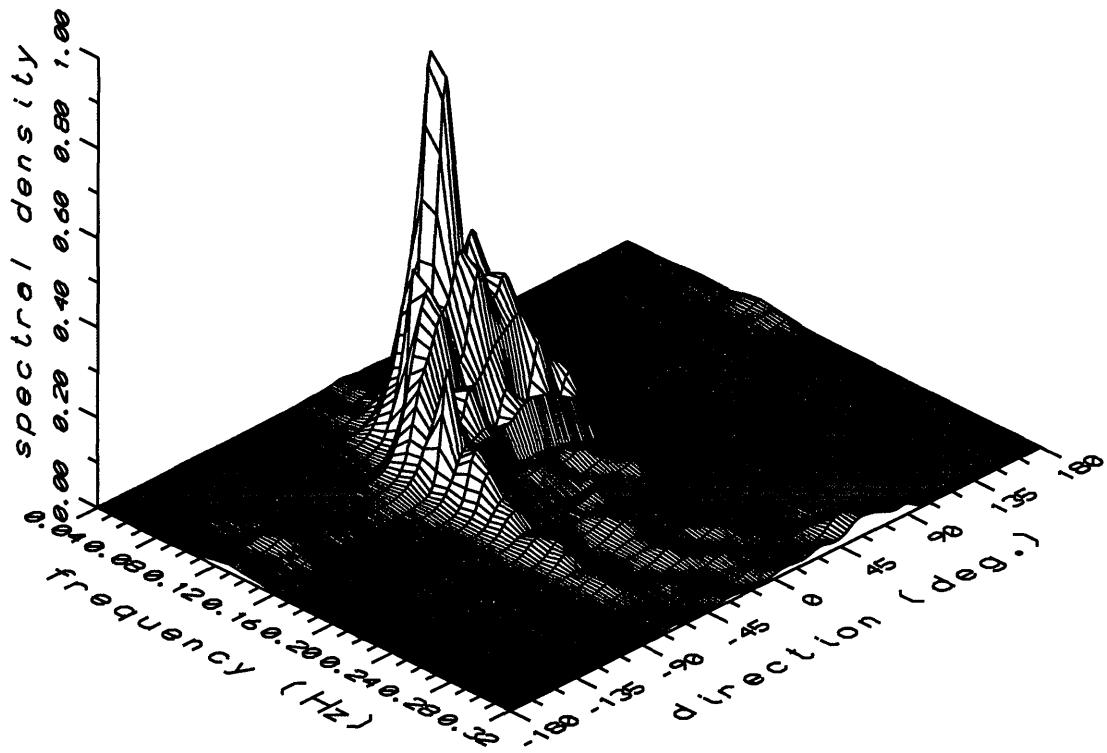


Figure 7.1-13 Case 4: surface plot of normalized LA IMLE directional spectra.

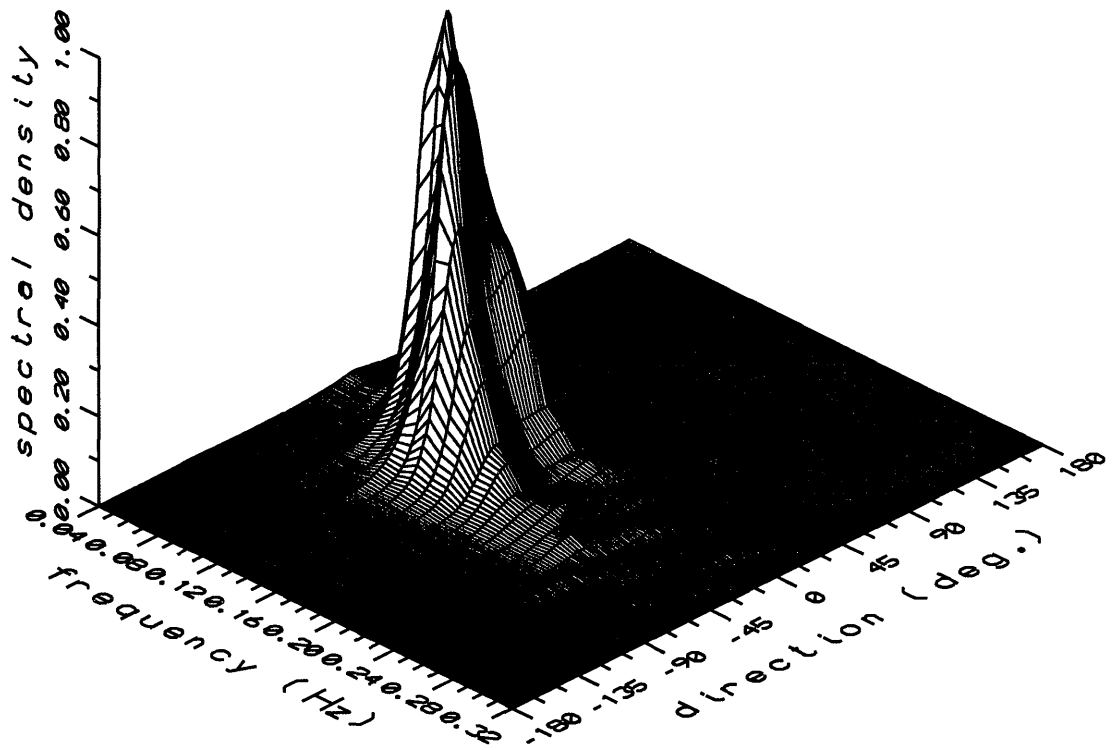


Figure 7.1-14 Case 4: surface plot of normalized ADCP IMLE directional spectra.

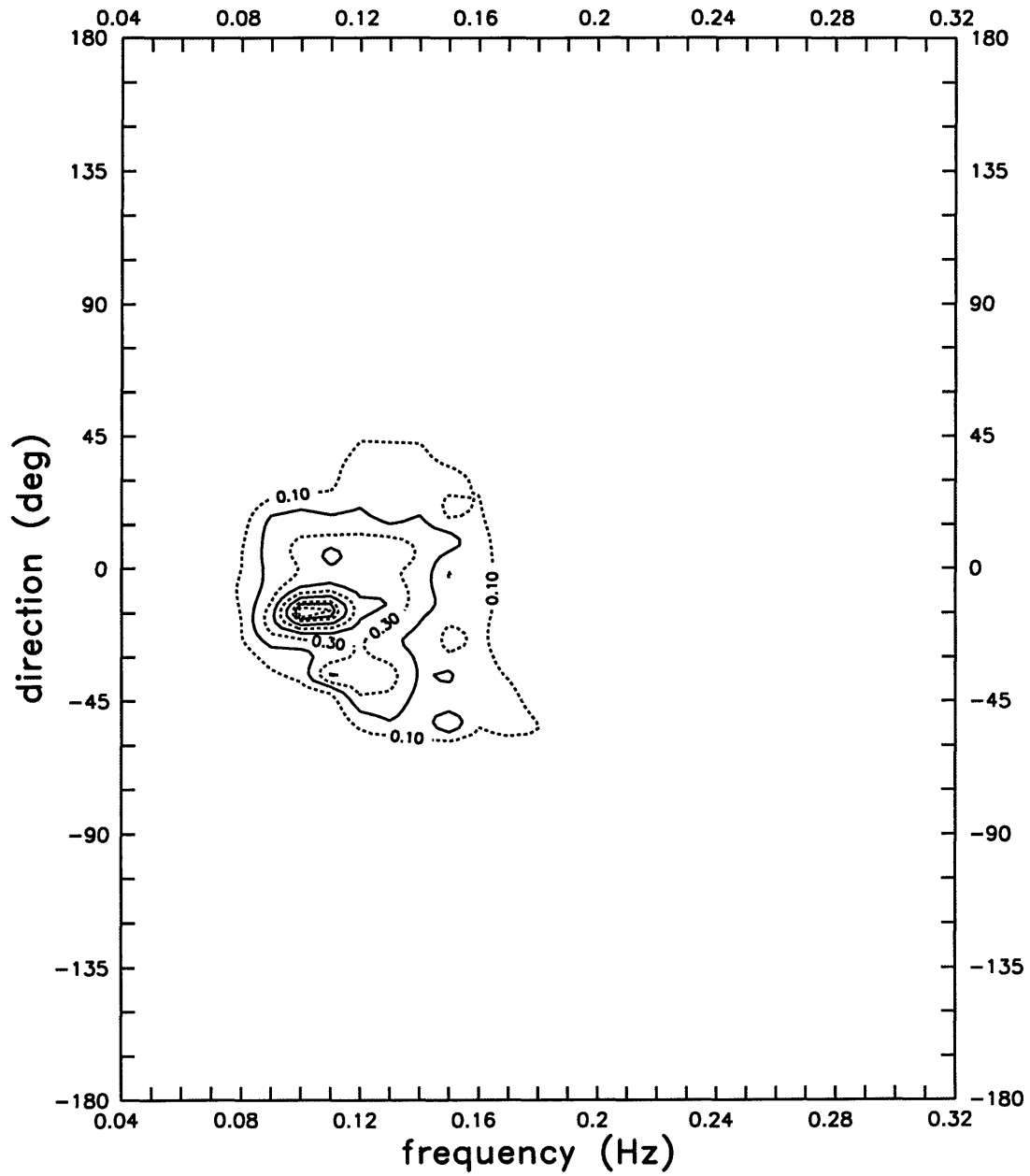


Figure 7.1-15 Case 4: topographic plot of normalized LA IMLE directional spectra.

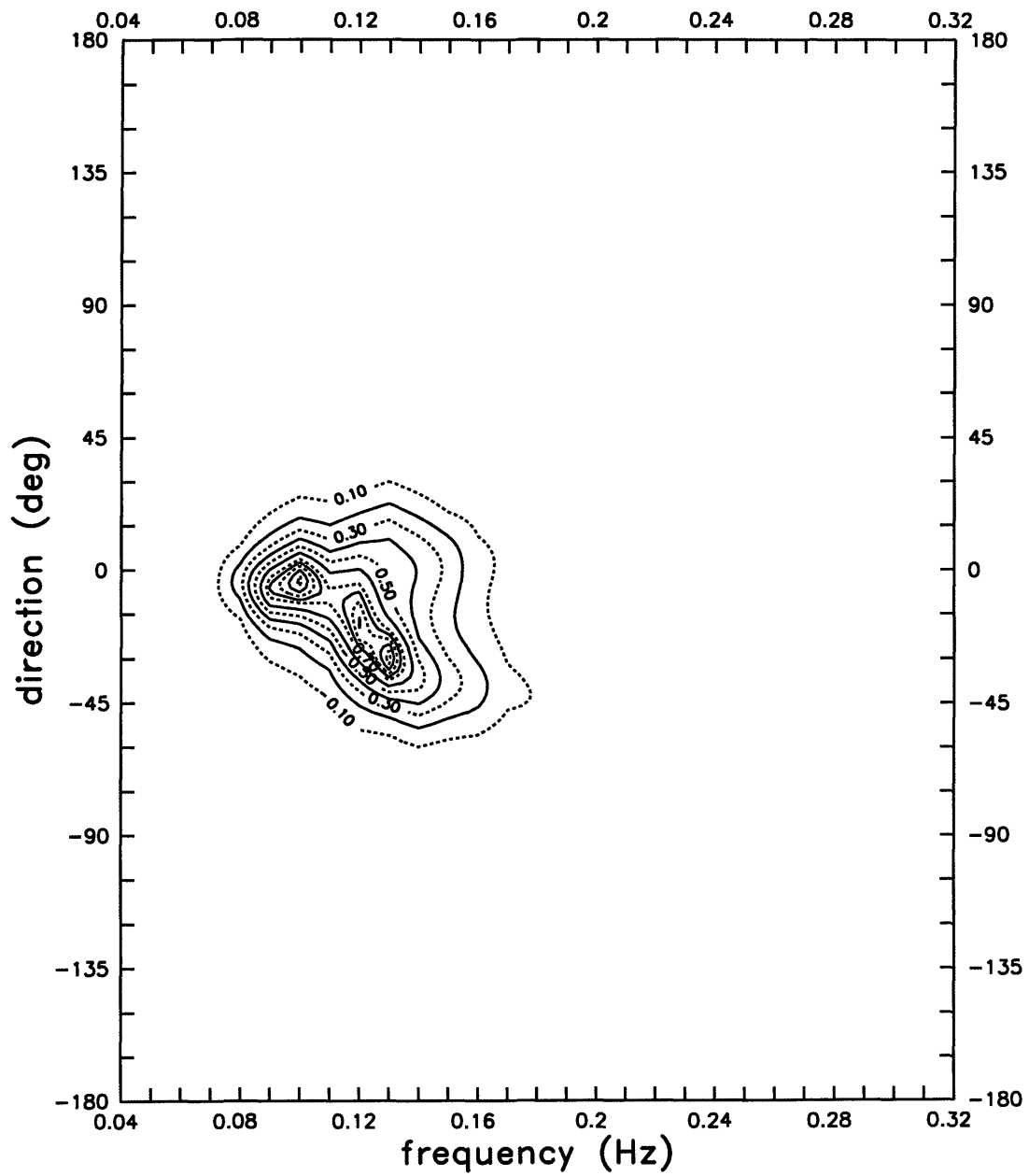


Figure 7.1-16 Case 4: topographic plot of normalized ADCP IMLE directional spectra.

Table 7.1-4 Case 4: IMLE directional spectra results.

	Linear Array results	ADCP results
S_p ($\text{cm}^2\text{-Hz}^{-1}\text{-rad}^{-1}$)	28400	18000
f_p (Hz)	.103	.132
T_p (s)	9.71	7.58
λ_p (m)	81	61
θ_p (deg)	-14	-30

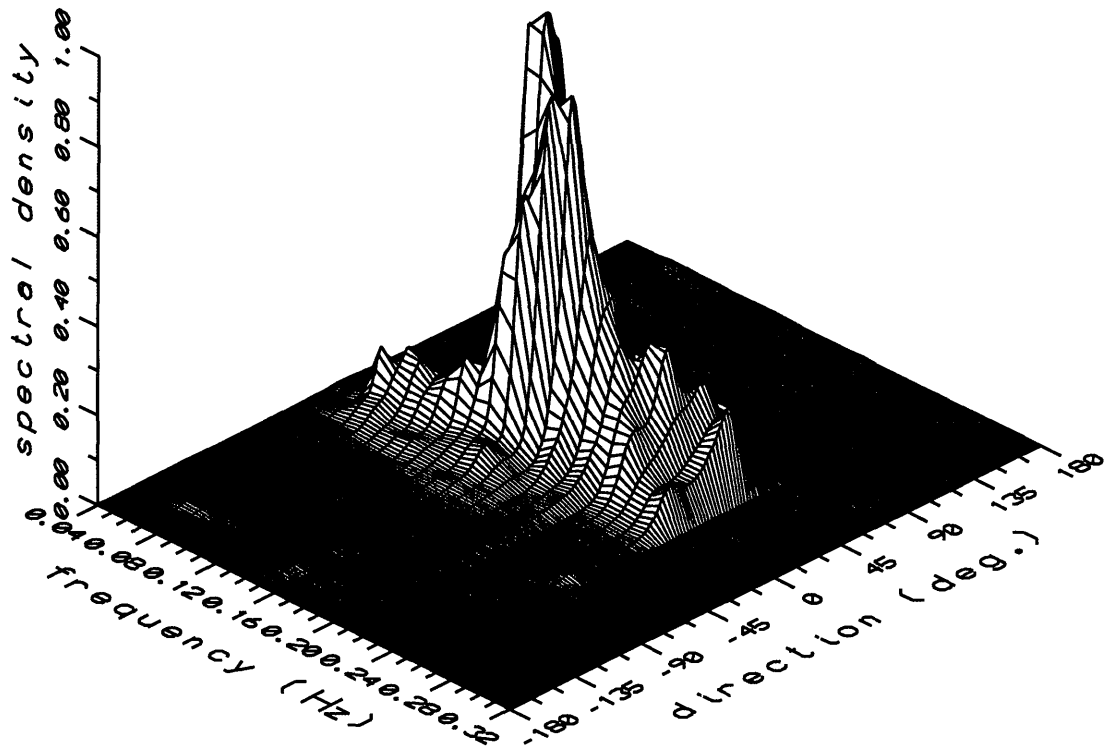


Figure 7.1-17 Case 5: surface plot of normalized LA IMLE directional spectra.

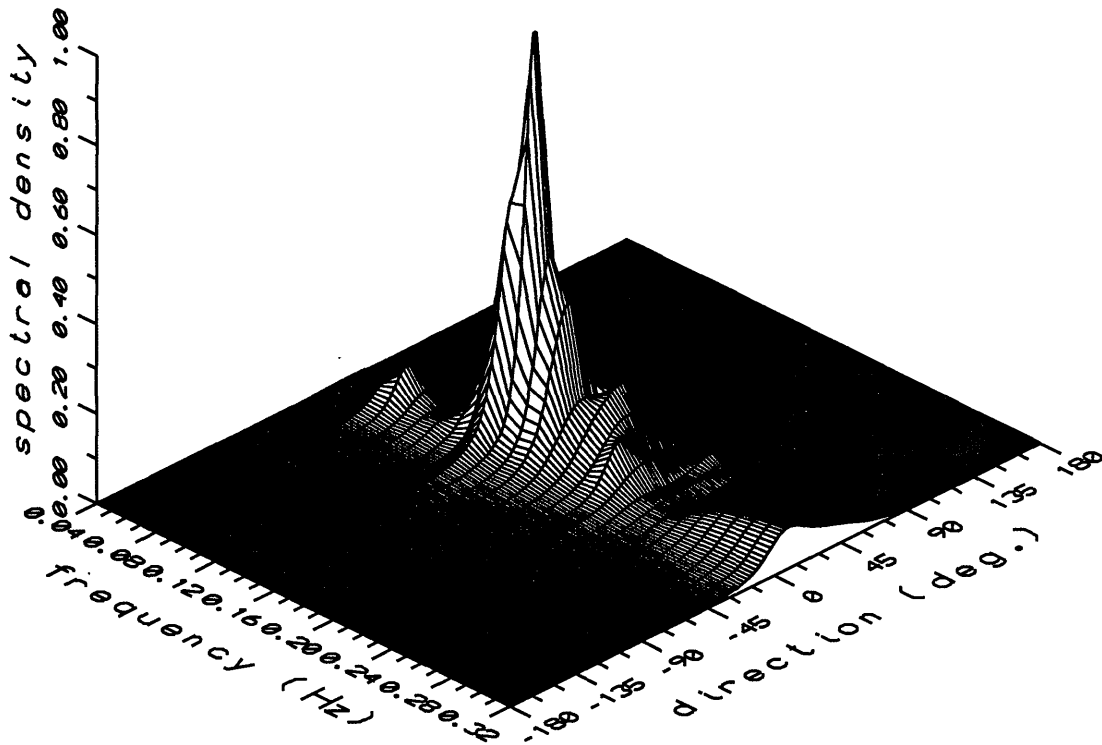


Figure 7.1-18 Case 5: surface plot of normalized ADCP IMLE directional spectra.

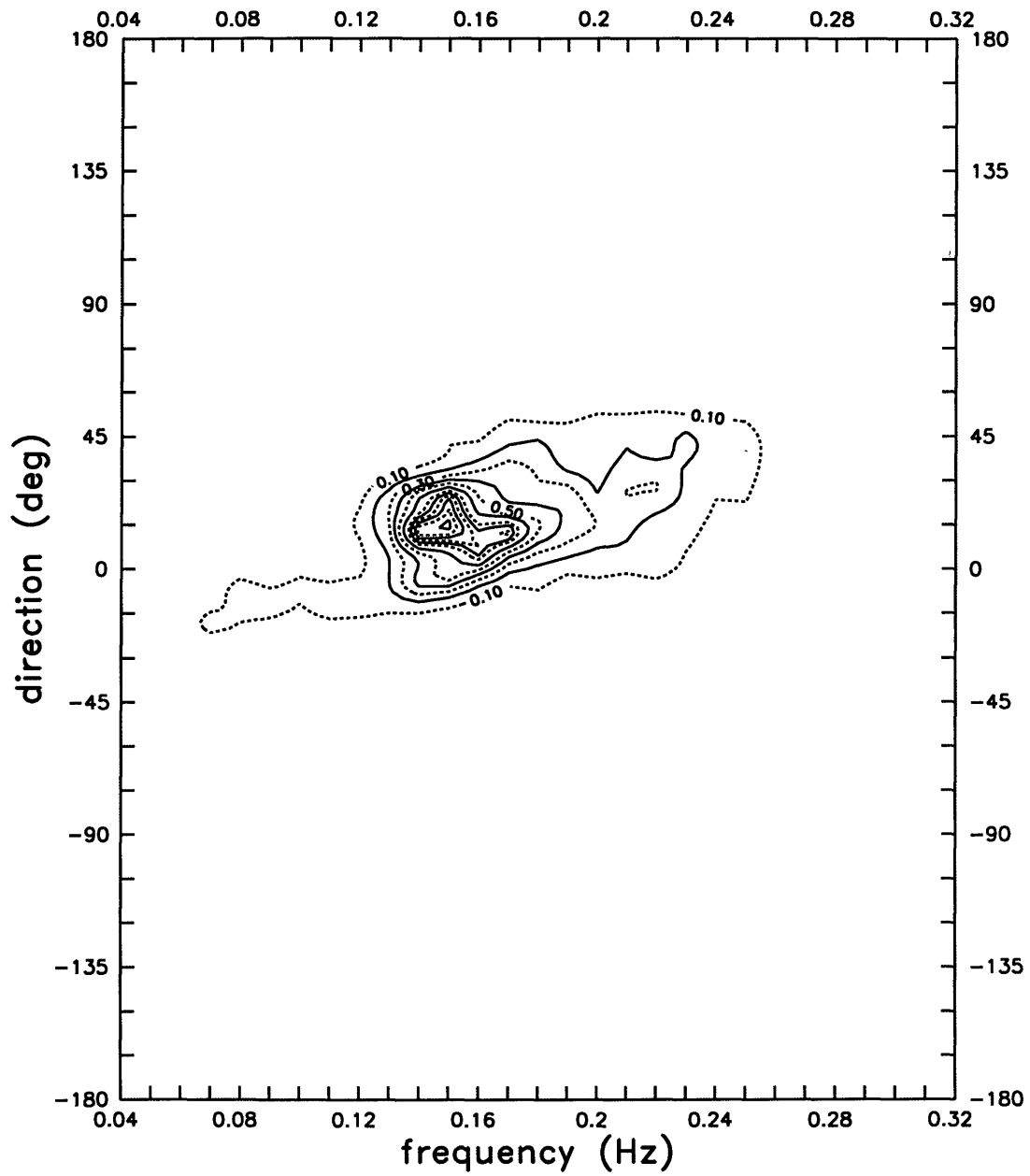


Figure 7.1-19 Case 5: topographic plot of normalized LA IMLE directional spectra.

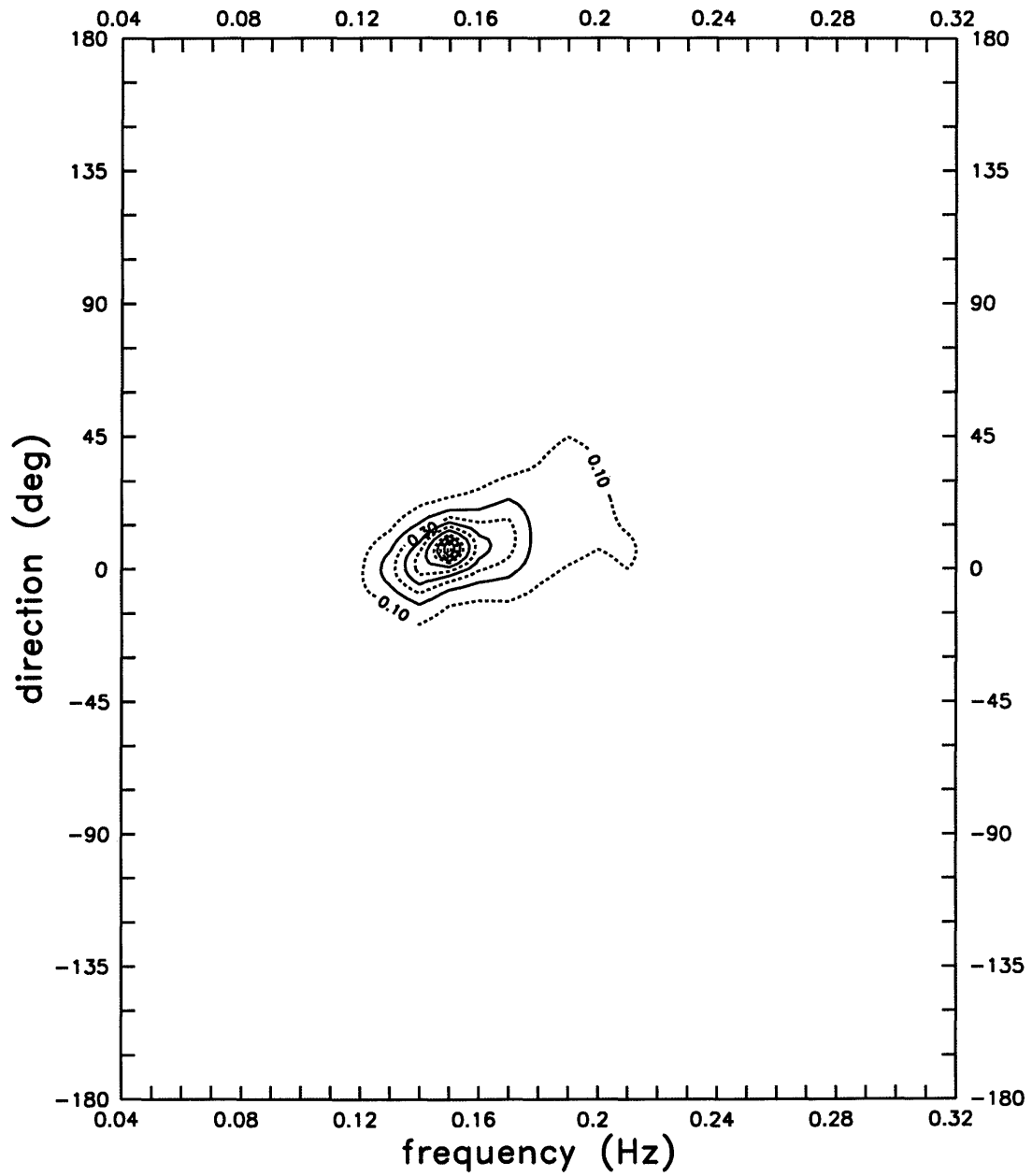


Figure 7.1-20 Case 5: topographic plot of normalized ADCP IMLE directional spectra.

Table 7.1-5 Case 5: IMLE directional spectra results.

	Linear Array results	ADCP results
S_p ($\text{cm}^2\text{-Hz}^{-1}\text{-rad}^{-1}$)	15700	23300
f_p (Hz)	.142	.152
T_p (s)	7.04	6.58
λ_p (m)	55	51
θ_p (deg)	12	7

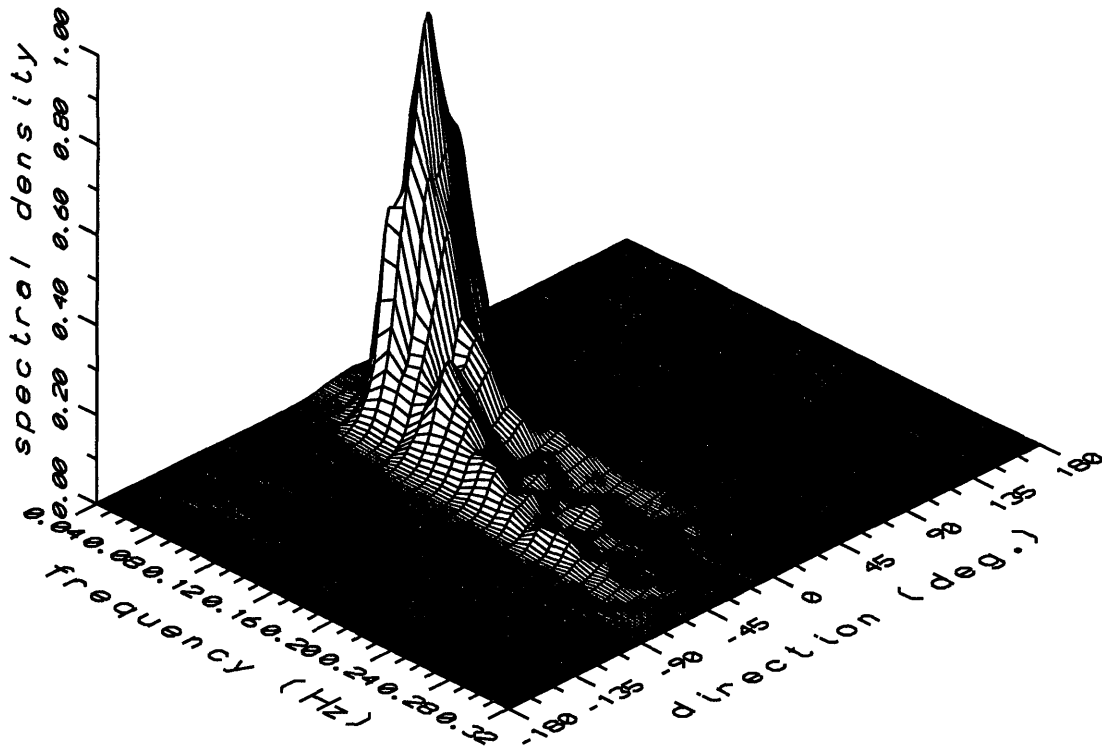


Figure 7.1-21 Case 6: surface plot of normalized LA IMLE directional spectra.

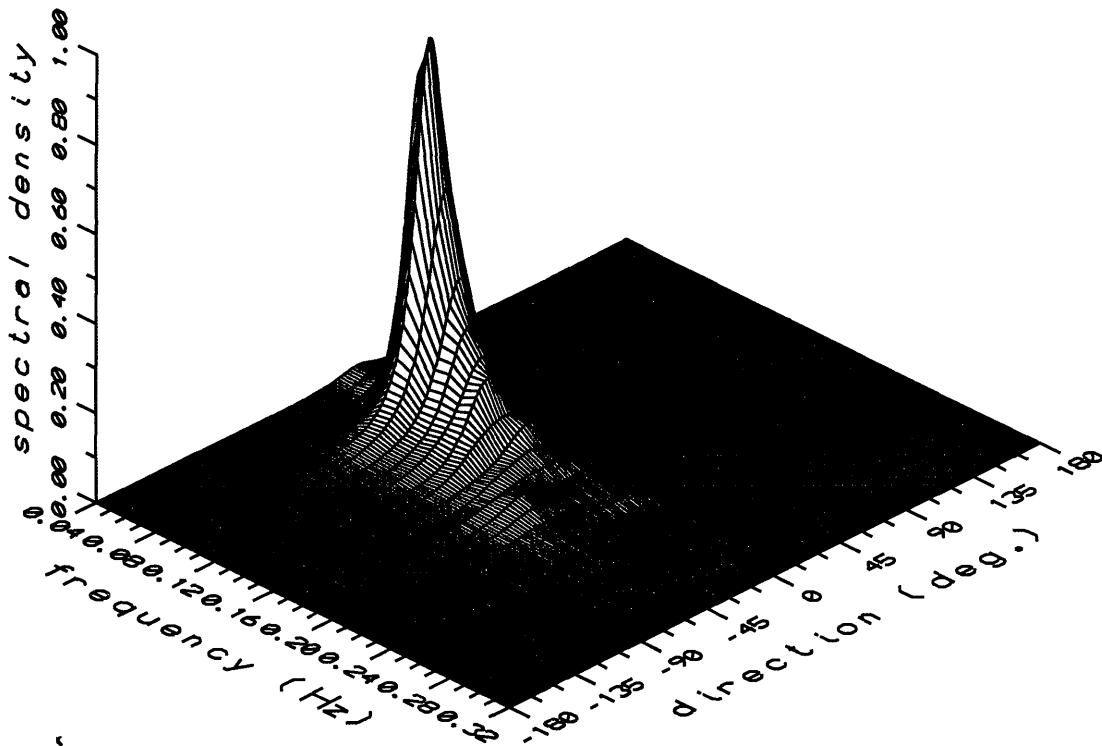


Figure 7.1-22 Case 6: surface plot of normalized ADCP IMLE directional spectra.

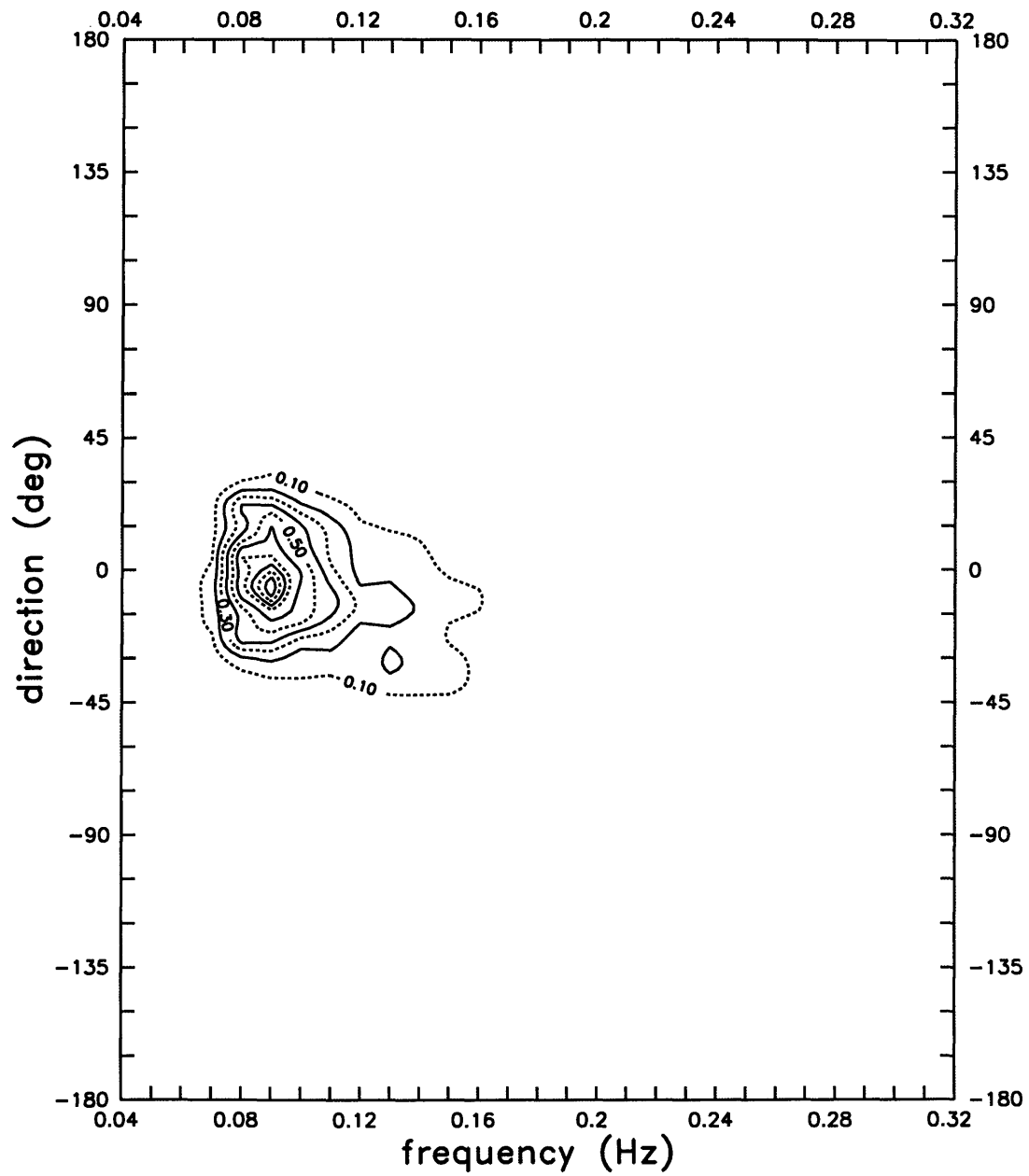


Figure 7.1-23 Case 6: topographic plot of normalized LA IMLE directional spectra.

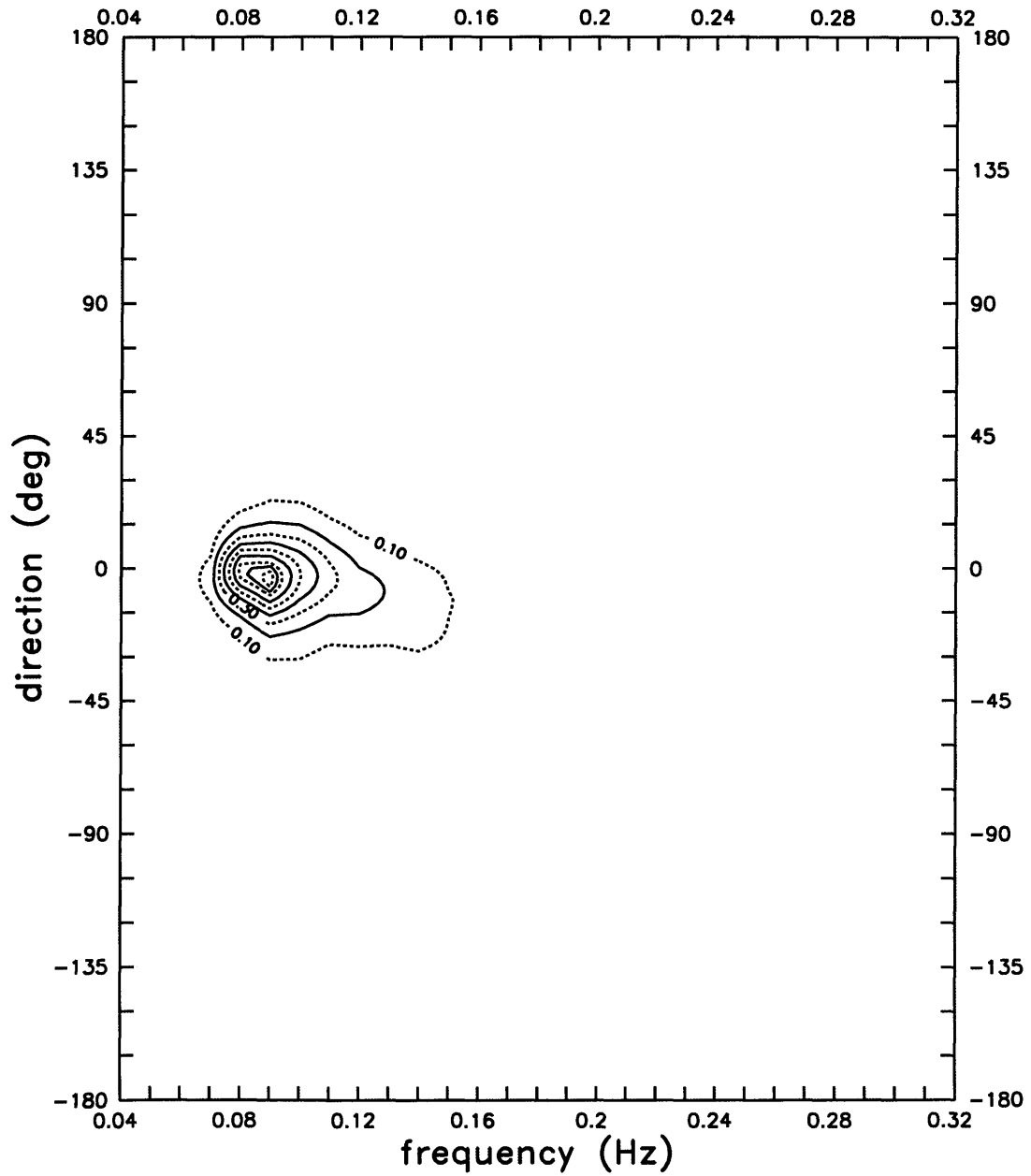


Figure 7.1-24 Case 6: topographic plot of normalized ADCP IMLE directional spectra.

Table 7.1-6 Case 6: IMLE directional spectra results.

	Linear Array results	ADCP results
S_p ($\text{cm}^2\text{-Hz}^{-1}\text{-rad}^{-1}$)	15100	21800
f_p (Hz)	.093	.084
T_p (s)	10.8	11.9
λ_p (m)	91	101
θ_p (deg)	-6	-1

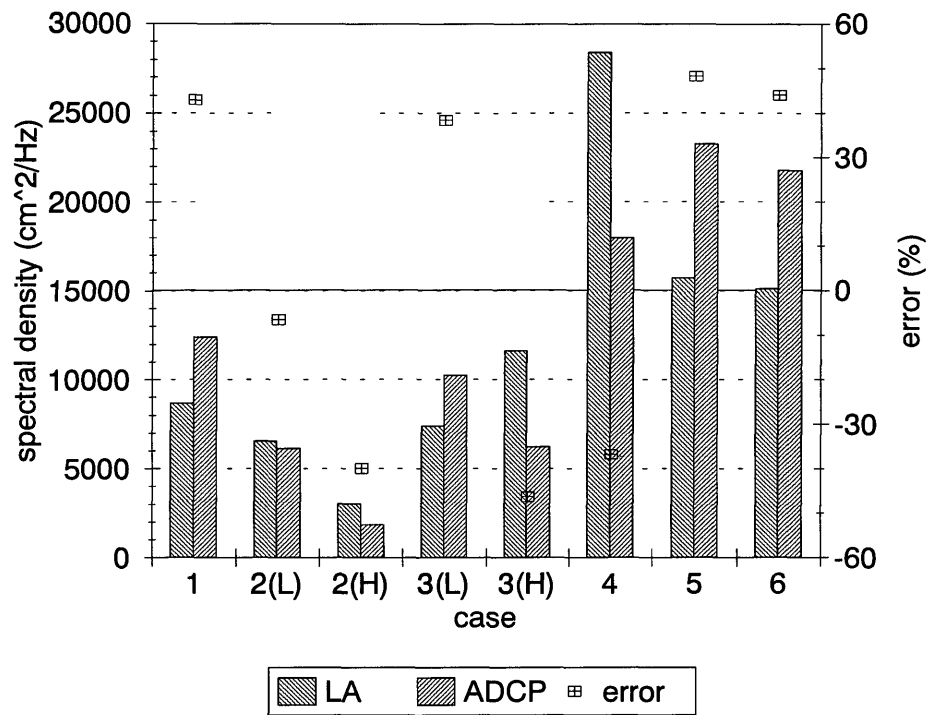


Figure 7.1-25 Comparison of the magnitude of the largest peak (S_p) in the LA and ADCP directional spectra for each case.

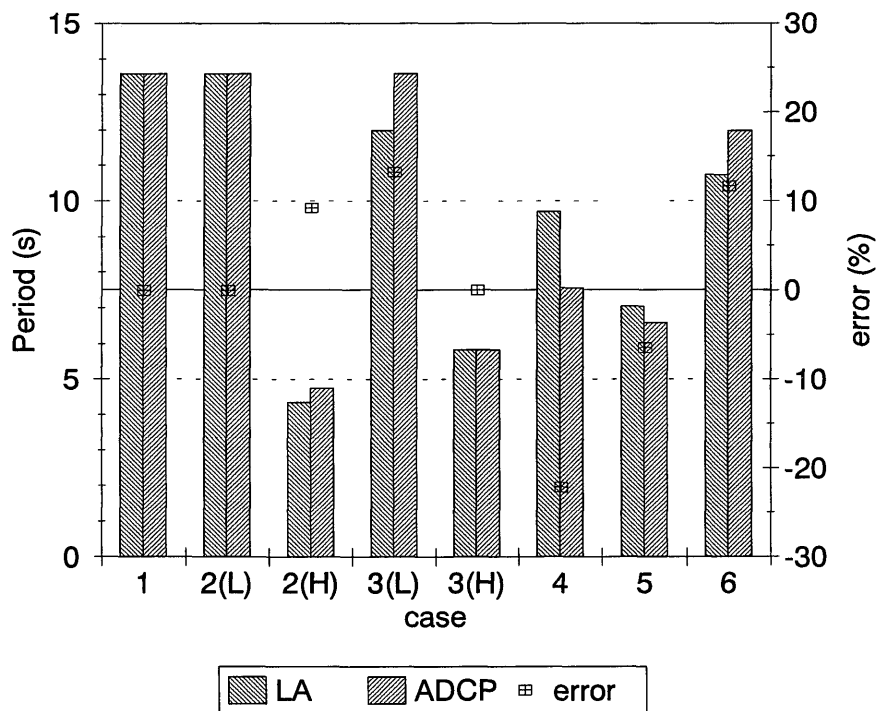


Figure 7.1-26 Comparison of the period associated with the largest peak (T_p) in the LA and ADCP directional spectra for each case.

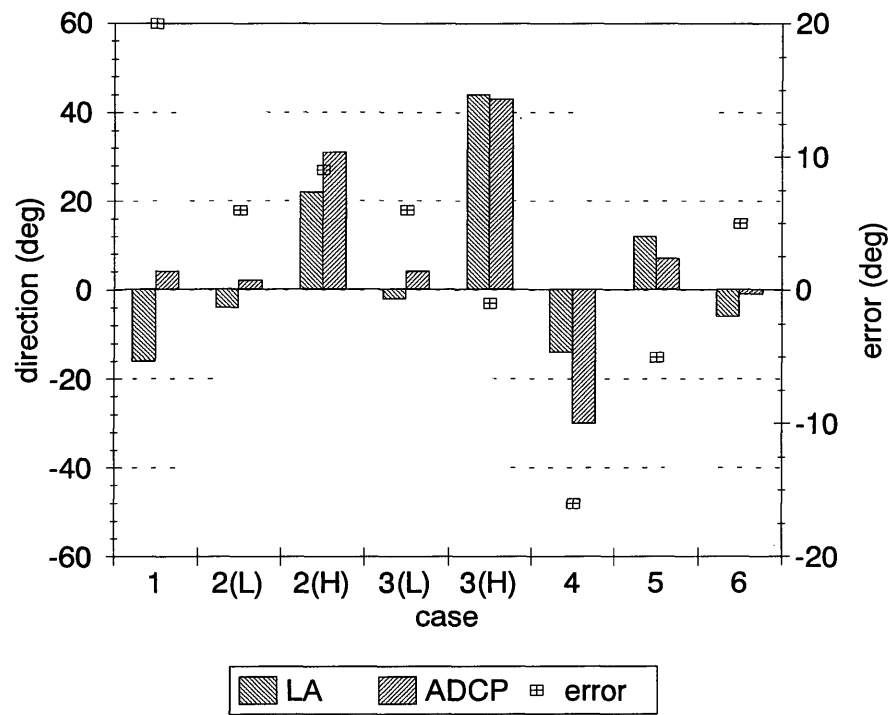


Figure 7.1-27 Comparison of the direction associated with the largest peak (θ_p) in the LA and ADCP directional spectra for each case.

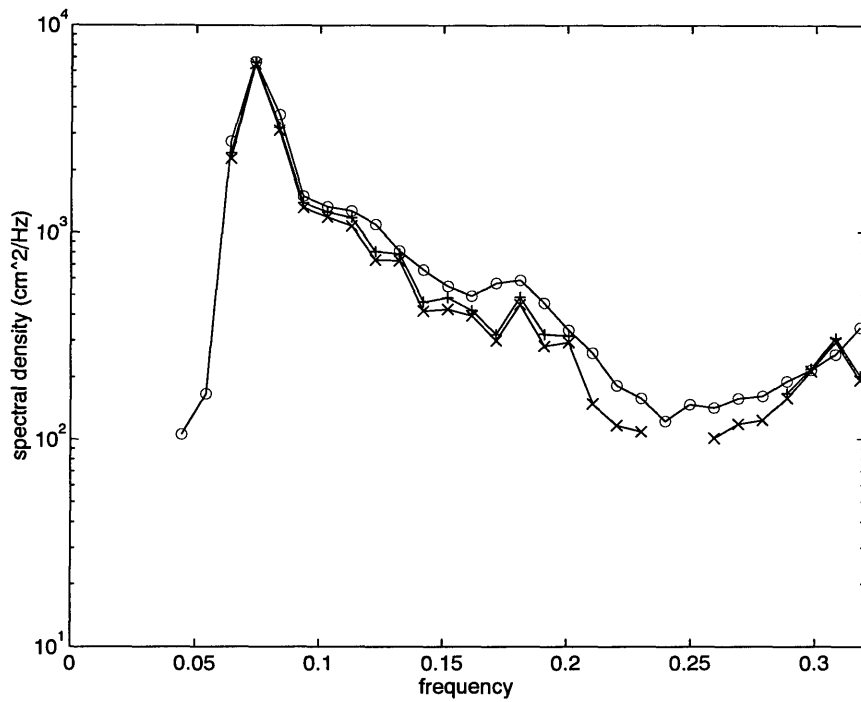


Figure 7.2-1 Case 1: Comparison of the estimated wave frequency spectra from the LA IMLE ("o"), the ADCP IMLE ("+"), and the ADCP bin 5 autospectra ("x").

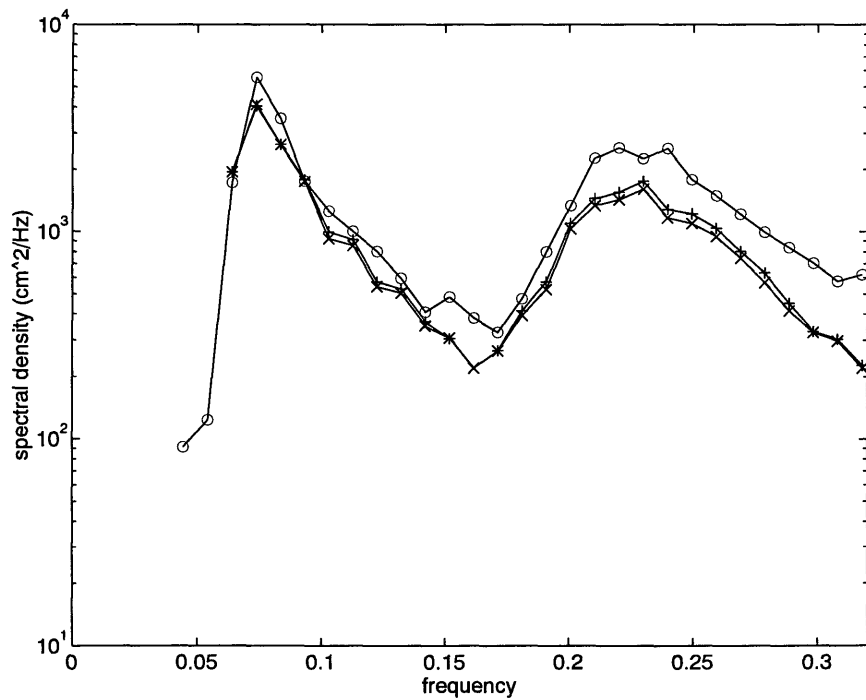


Figure 7.2-2 Case 2: Comparison of the estimated wave frequency spectra from the LA IMLE ("o"), the ADCP IMLE ("+"), and the ADCP bin 5 autospectra ("x").

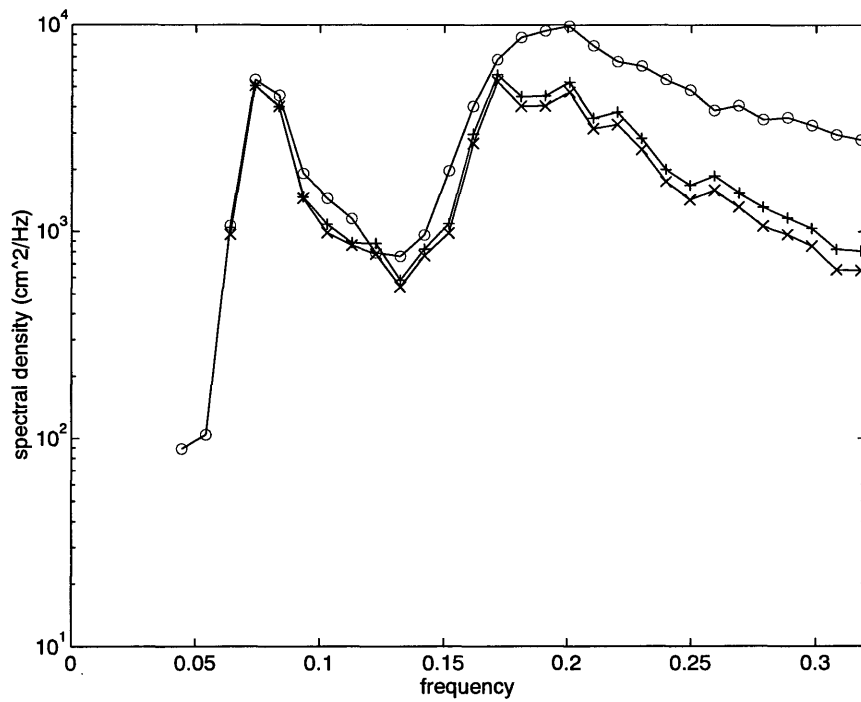


Figure 7.2-3 Case 3: Comparison of the estimated wave frequency spectra from the LA IMLE ("o"), the ADCP IMLE ("+"), and the ADCP bin 5 autospectra ("x").

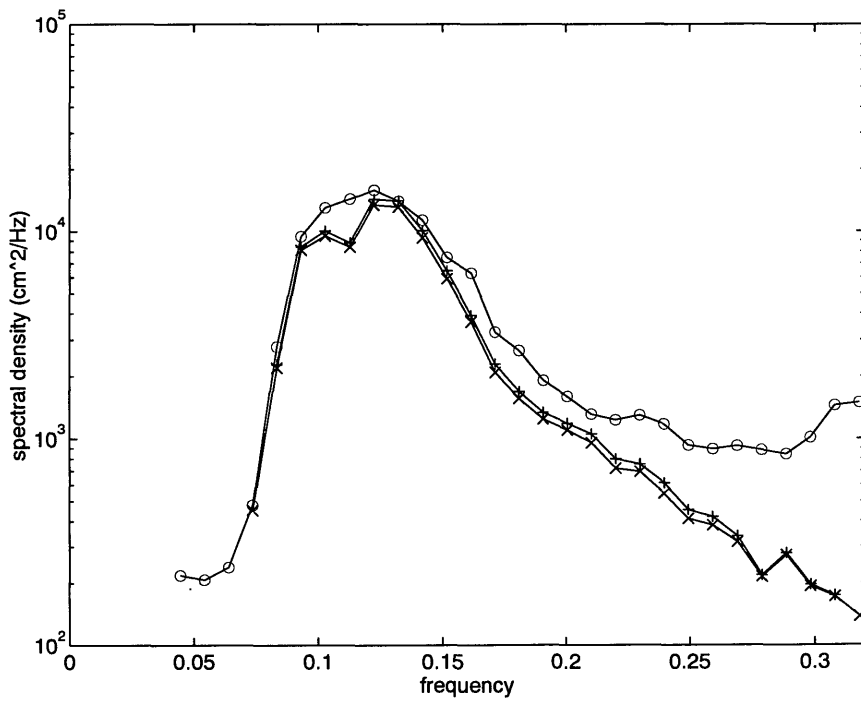


Figure 7.2-4 Case 4: Comparison of the estimated wave frequency spectra from the LA IMLE ("o"), the ADCP IMLE ("+"), and the ADCP bin 5 autospectra ("x").

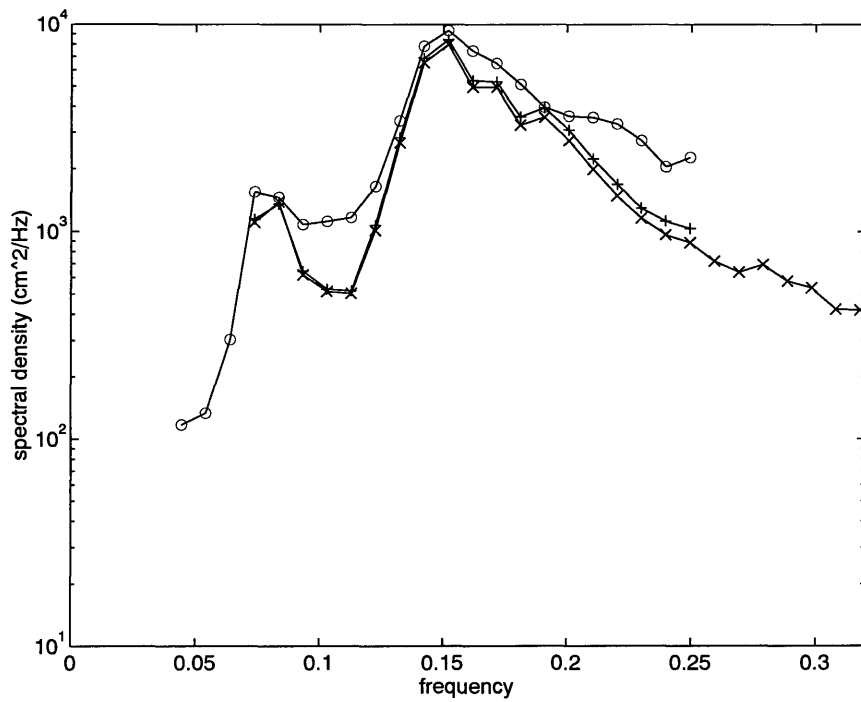


Figure 7.2-5 Case 5: Comparison of the estimated wave frequency spectra from the LA IMLE ("o"), the ADCP IMLE ("+"), and the ADCP bin 5 autospectra ("x").

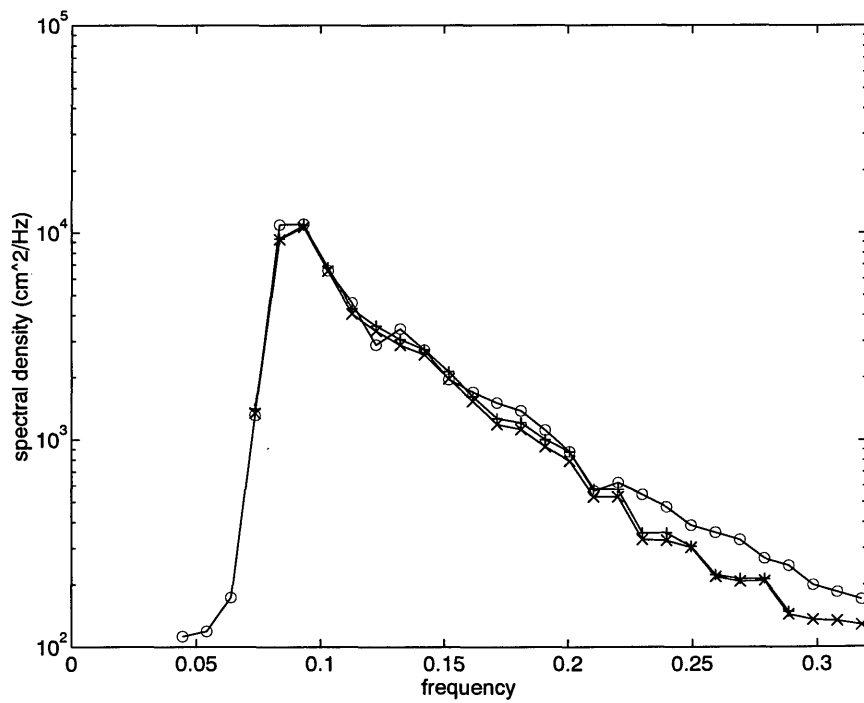


Figure 7.2-6 Case 6: Comparison of the estimated wave frequency spectra from the LA IMLE ("o"), the ADCP IMLE ("+"), and the ADCP bin 5 autospectra ("x").

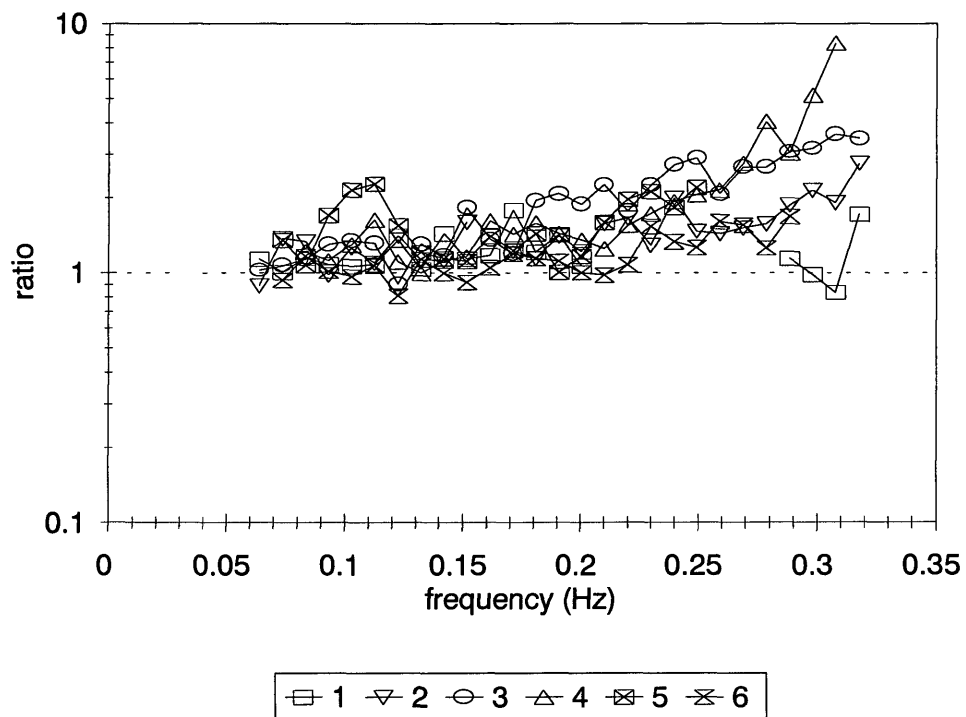


Figure 7.2-7 Ratio of wave frequency spectra derived from LA IMLE spectra to that from the ADCP IMLE spectra for each case (legend lists case #).

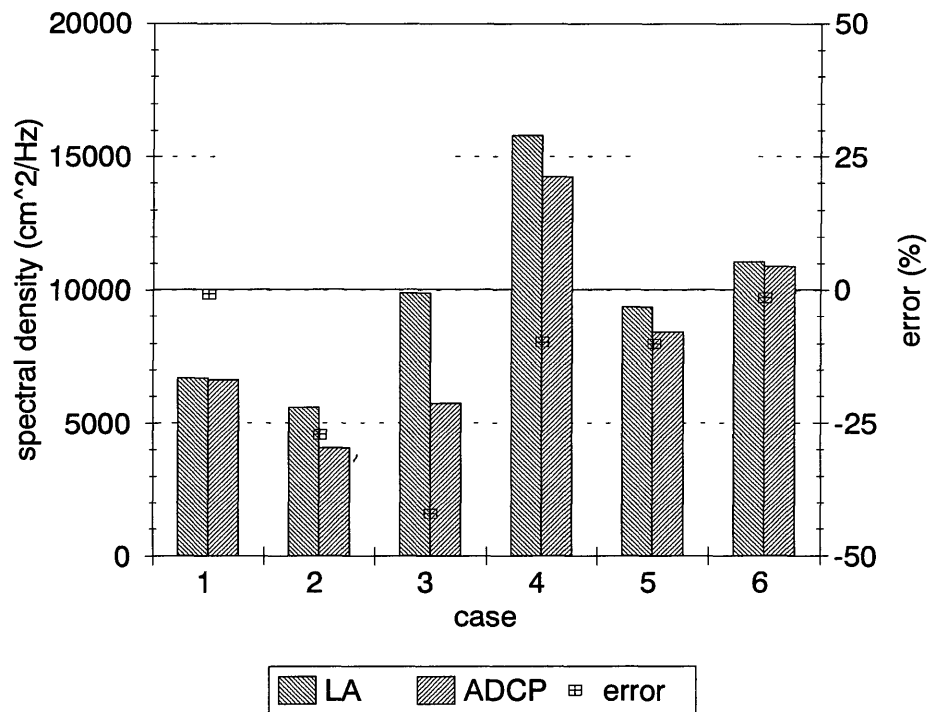


Figure 7.2-8 Comparison of the magnitudes of the largest peak in the wave frequency spectra ($S_{p,t}$) derived from the LA and ADCP IMLE spectra for each case.

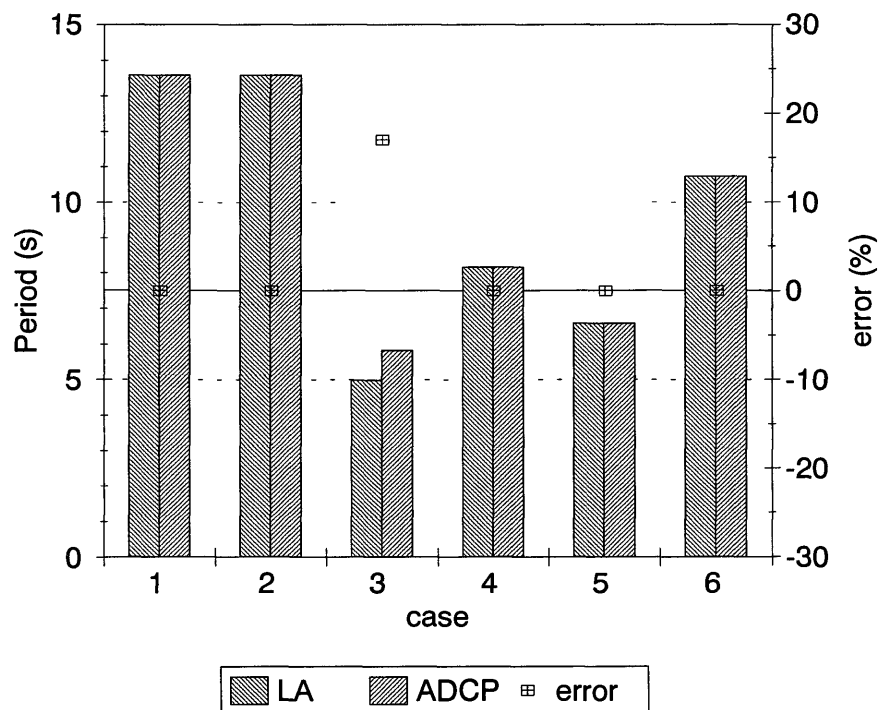


Figure 7.2-9 Comparison of the frequencies of the largest peak in the wave frequency spectra ($f_{p,t}$) derived from the LA and ADCP IMLE spectra for each case.

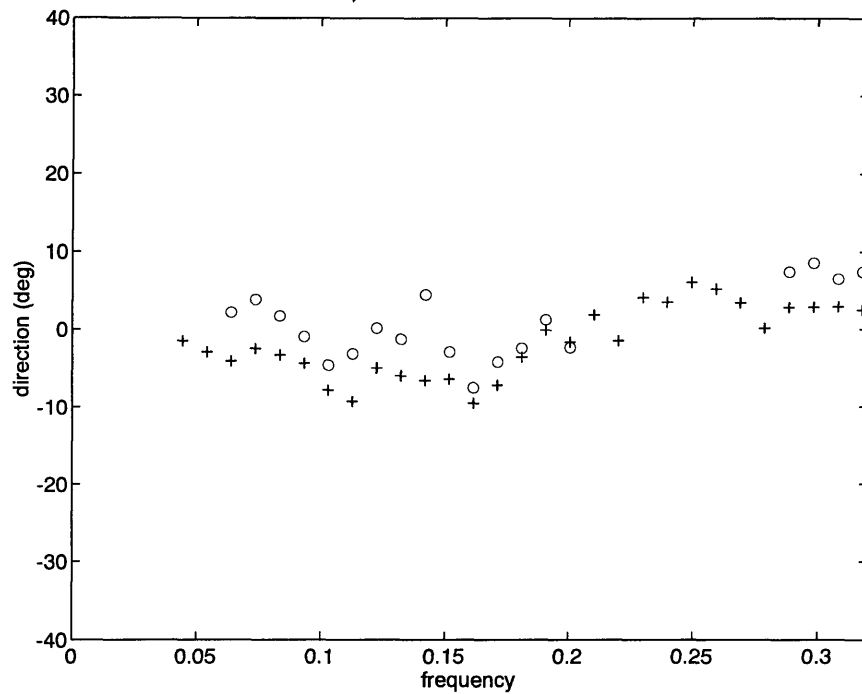


Figure 7.3-1 Case 1: Comparison of the radiation stress angles $\alpha_{xy}(f)$ from the LA ("+") and ADCP ("o") directional wave spectra.

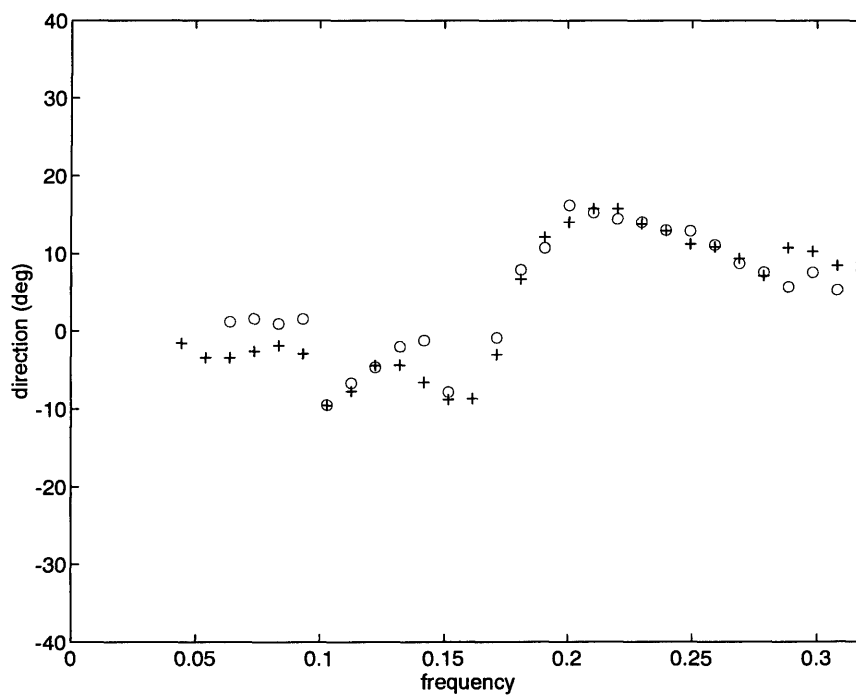


Figure 7.3-2 Case 2: Comparison of the radiation stress angles $\alpha_{xy}(f)$ from the LA ("+") and ADCP ("o") directional wave spectra.

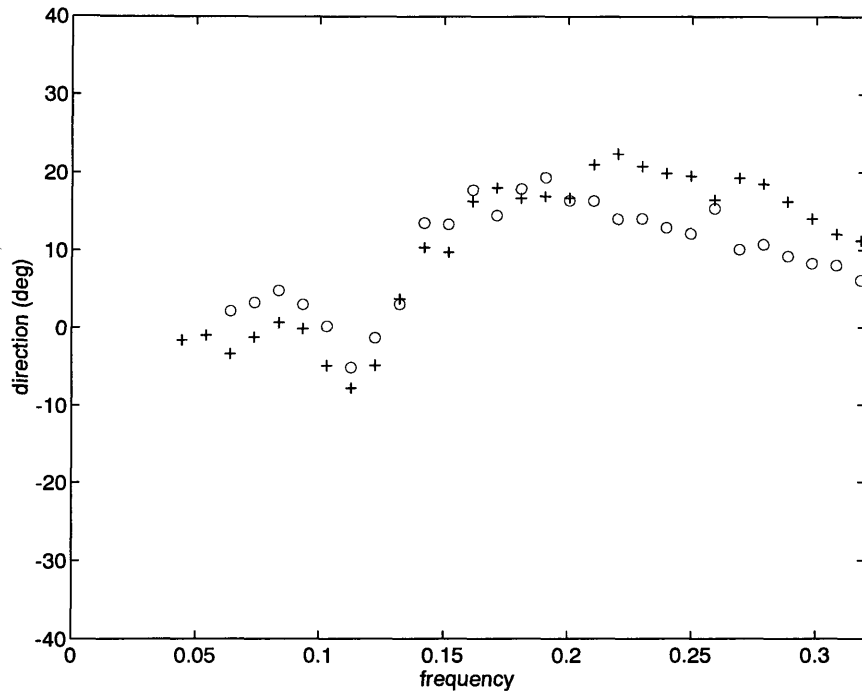


Figure 7.3-3 Case 3: Comparison of the radiation stress angles $\alpha_{xy}(f)$ from the LA ("+") and ADCP ("o") directional wave spectra.

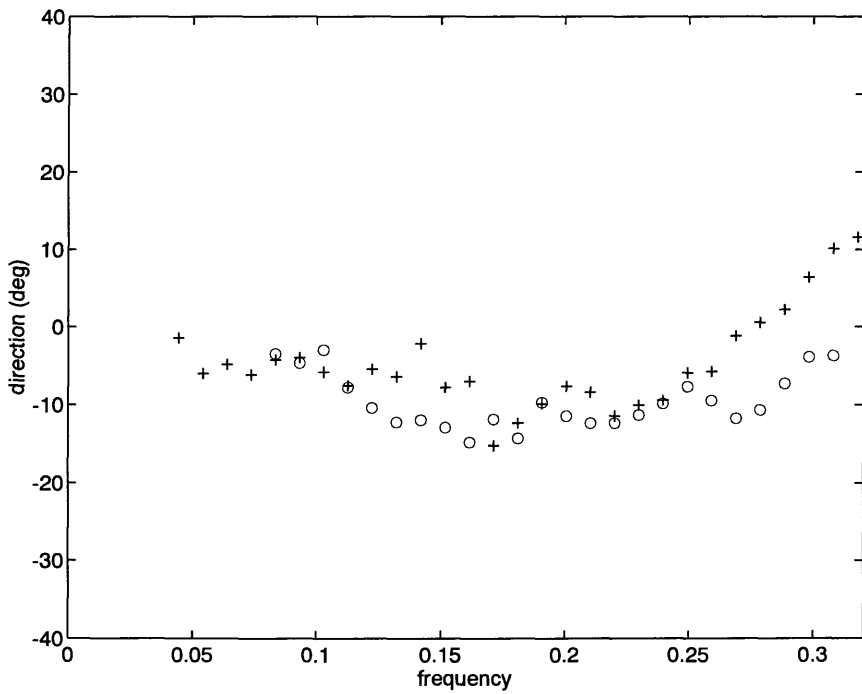


Figure 7.3-4 Case 4: Comparison of the radiation stress angles $\alpha_{xy}(f)$ from the LA ("+") and ADCP ("o") directional wave spectra.

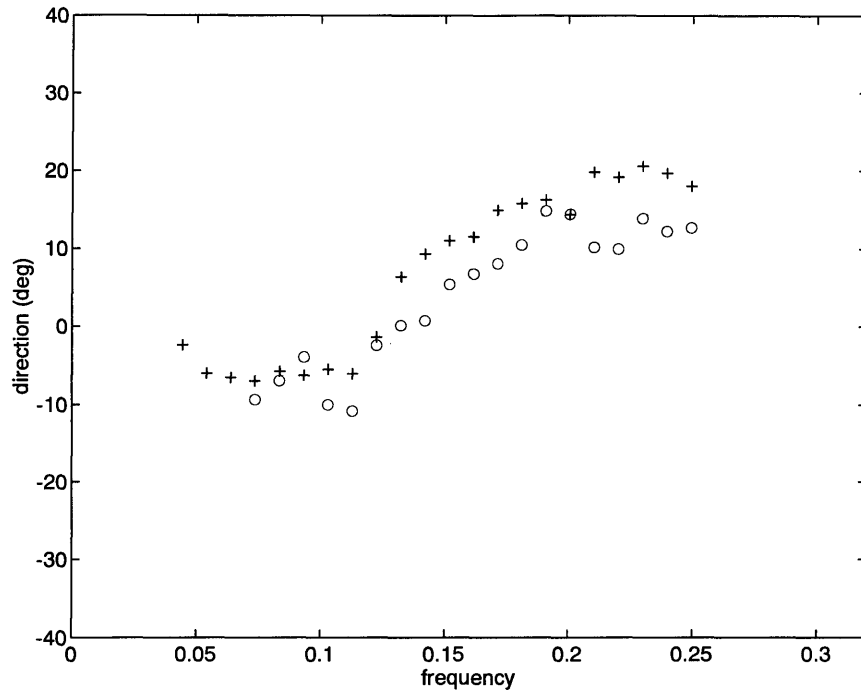


Figure 7.3-5 Case 5: Comparison of the radiation stress angles $\alpha_{xy}(f)$ from the LA ("+") and ADCP ("o") directional wave spectra.

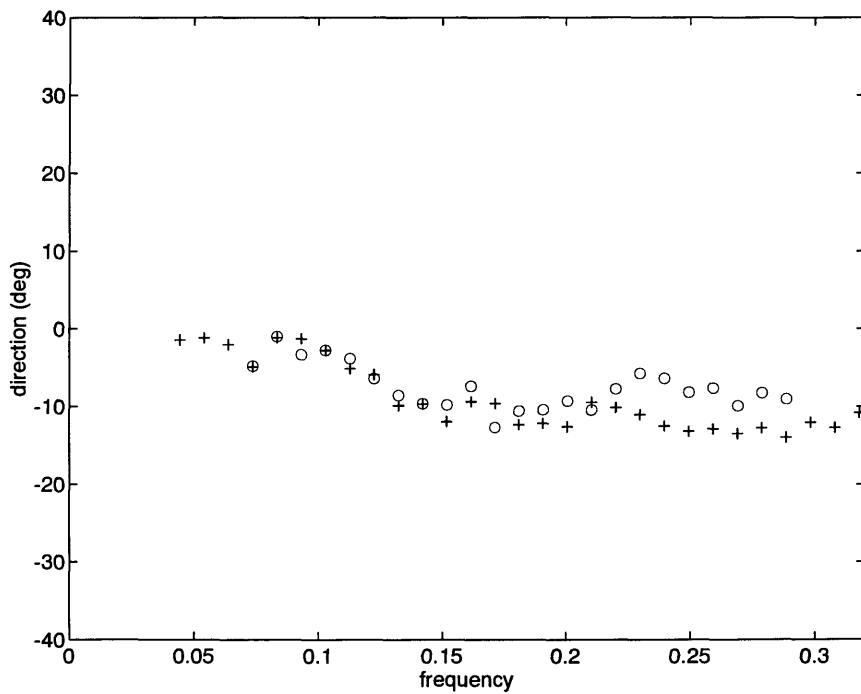


Figure 7.3-6 Case 6: Comparison of the radiation stress angles $\alpha_{xy}(f)$ from the LA ("+") and ADCP ("o") directional wave spectra.

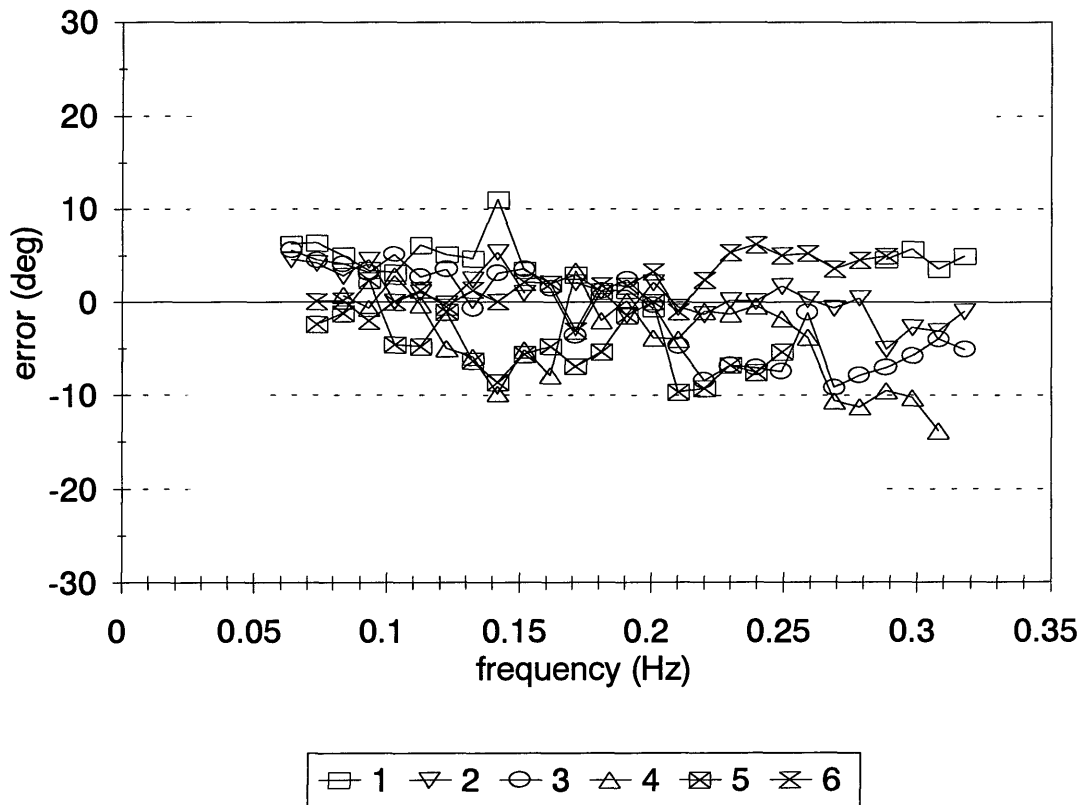


Figure 7.3-7 Errors in the ADCP-derived radiation stress angle $\alpha_{xy}(f)$ relative to the LA-derived radiation stress angle for each case (see legend).

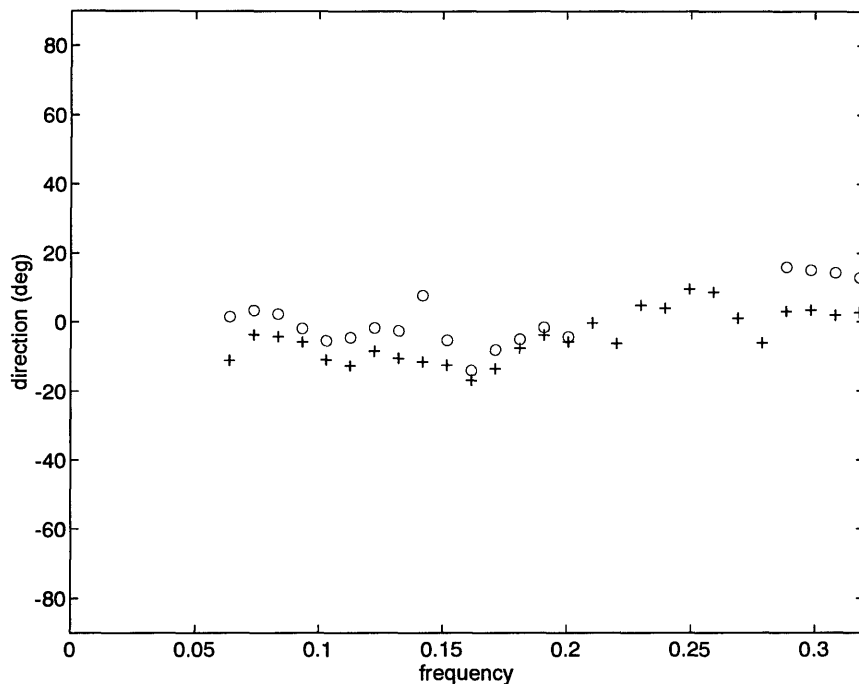


Figure 7.4-1 Case 1: Comparison of the mean directions $\Theta(f)$ from the LA (+) and ADCP (o) directional wave spectra.

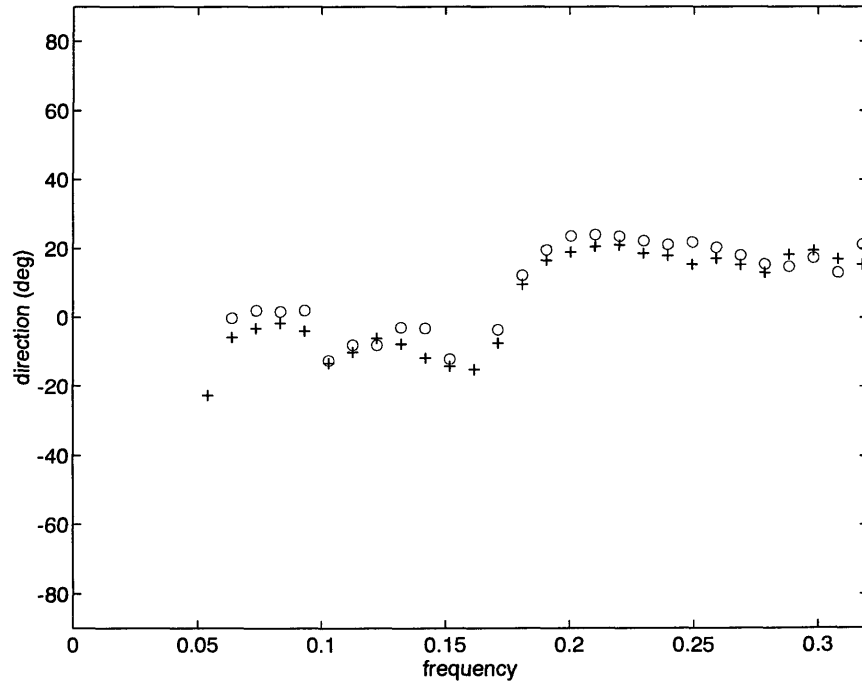


Figure 7.4-2 Case 2: Comparison of the mean directions $\Theta(f)$ from the LA (+) and ADCP (o) directional wave spectra.

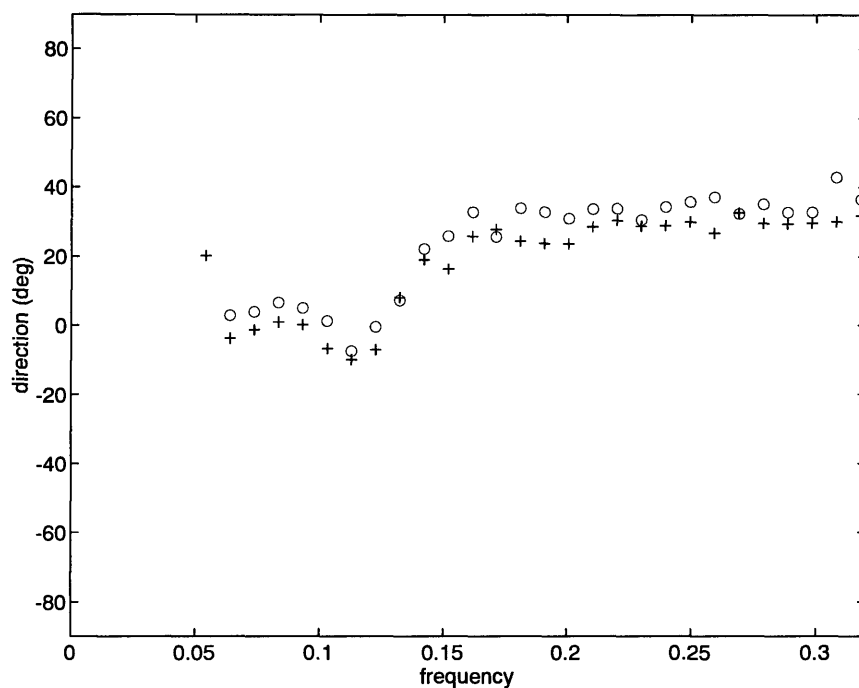


Figure 7.4-3 Case 3: Comparison of the mean directions $\Theta(f)$ from the LA ("+") and ADCP ("o") directional wave spectra.

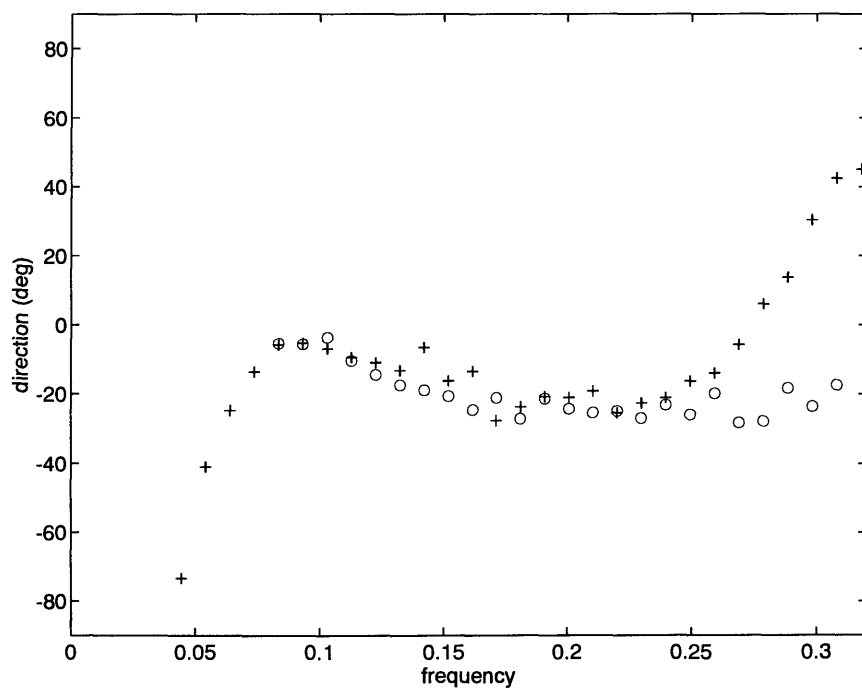


Figure 7.4-4 Case 4: Comparison of the mean directions $\Theta(f)$ from the LA ("+") and ADCP ("o") directional wave spectra.

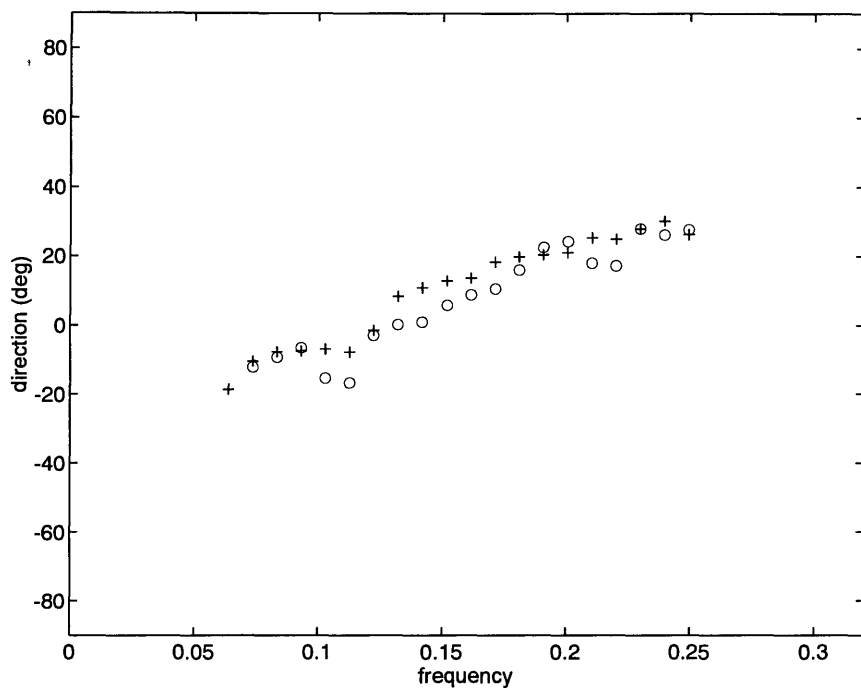


Figure 7.4-5 Case 5: Comparison of the mean directions $\theta(f)$ from the LA ("+") and ADCP ("o") directional wave spectra.

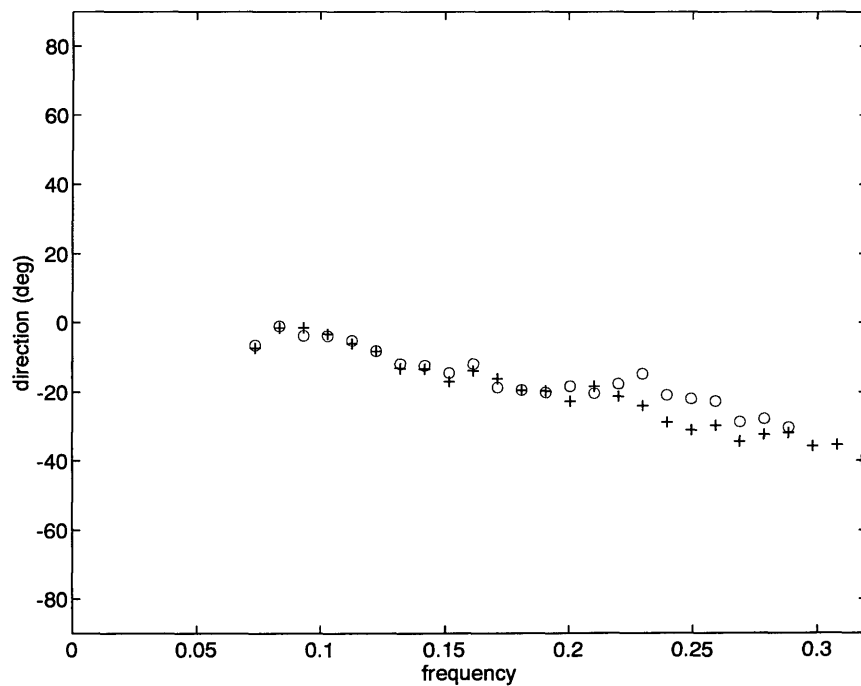


Figure 7.4-6 Case 6: Comparison of the mean directions $\theta(f)$ from the LA ("+") and ADCP ("o") directional wave spectra.

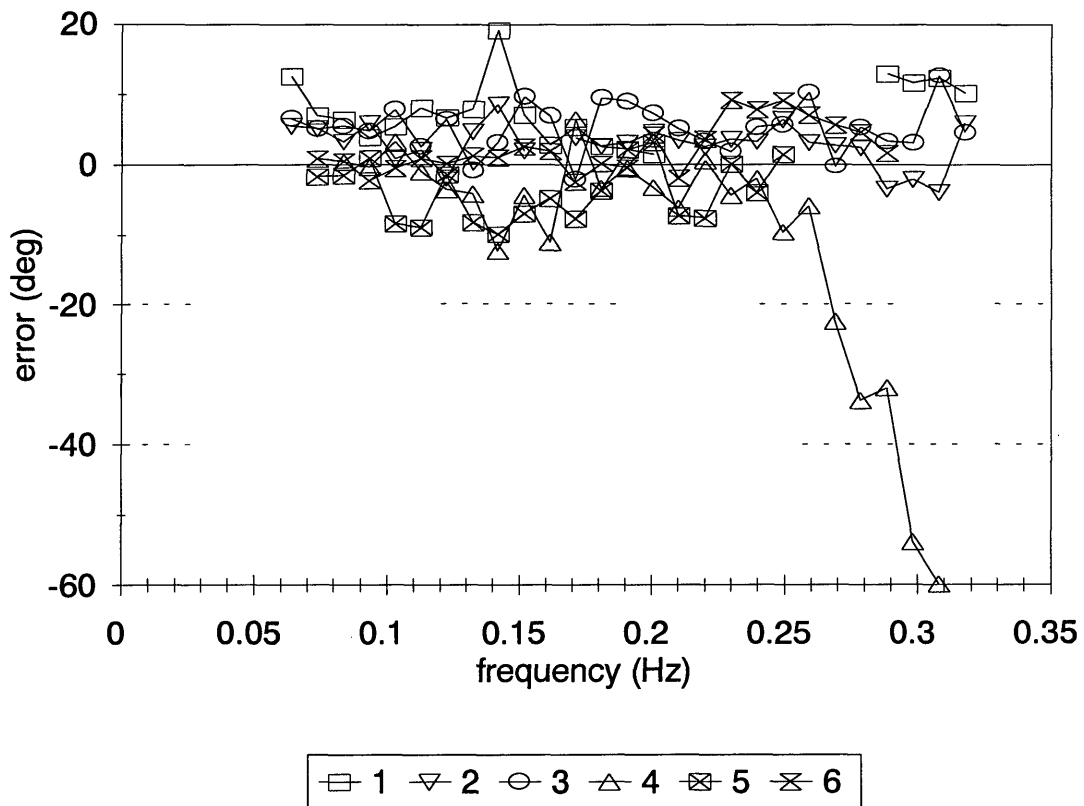


Figure 7.4-7 Errors in the ADCP-derived mean direction $\Theta(f)$ relative to the LA-derived mean direction for each case (see legend).

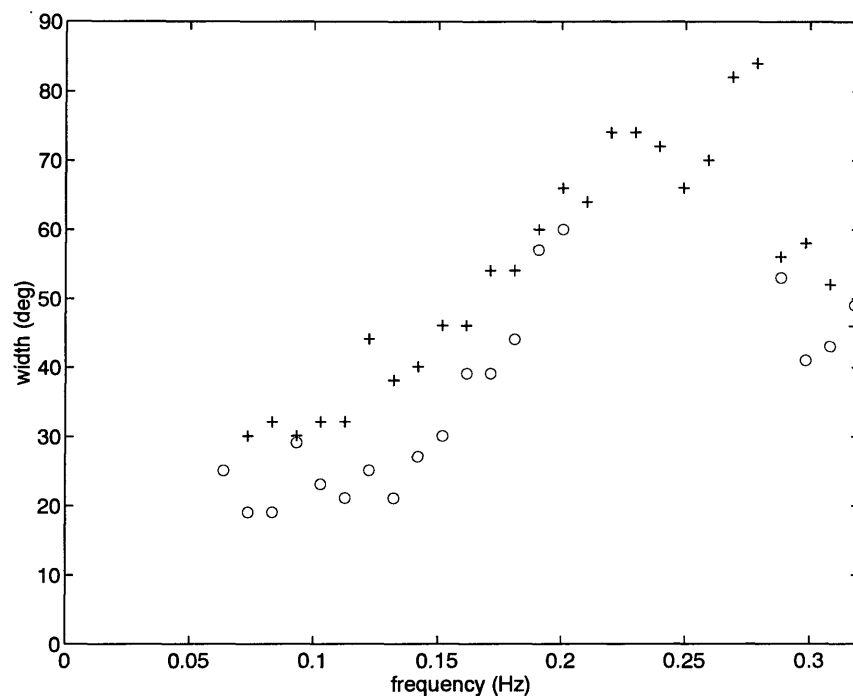


Figure 7.5-1 Case 1: Comparison of the directional widths $\Delta(f)$ from the LA ("+") and ADCP ("o") directional wave spectra.

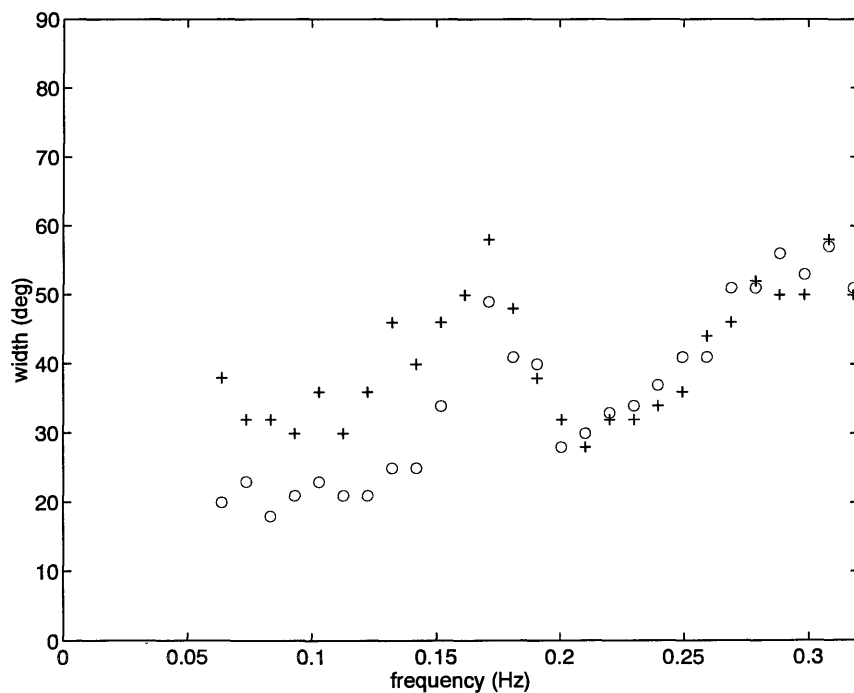


Figure 7.5-2 Case 2: Comparison of the directional widths $\Delta(f)$ from the LA ("+") and ADCP ("o") directional wave spectra.

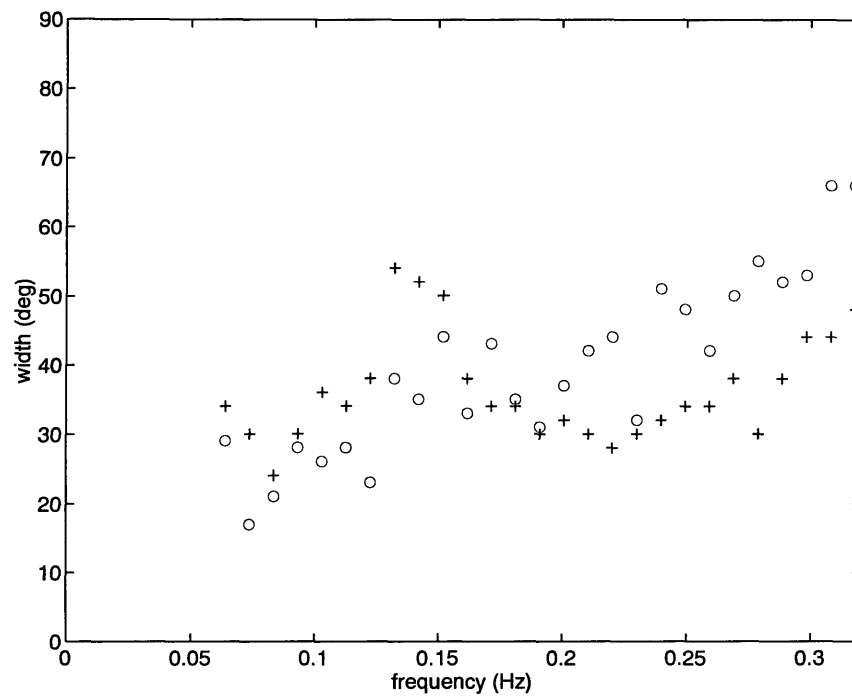


Figure 7.5-3 Case 3: Comparison of the directional widths $\Delta(f)$ from the LA ("+") and ADCP ("o") directional wave spectra.

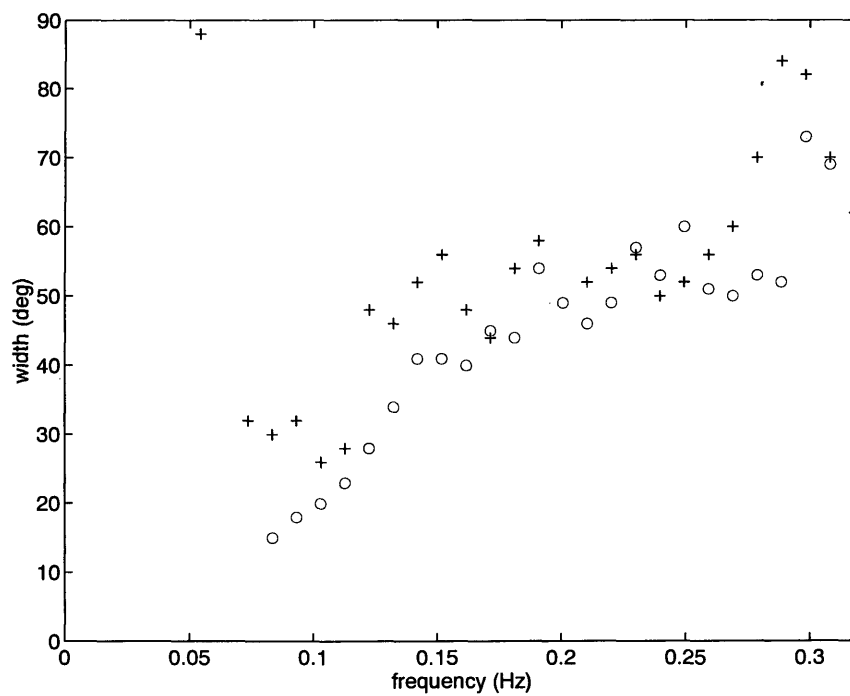


Figure 7.5-4 Case 4: Comparison of the directional widths $\Delta(f)$ from the LA ("+") and ADCP ("o") directional wave spectra.

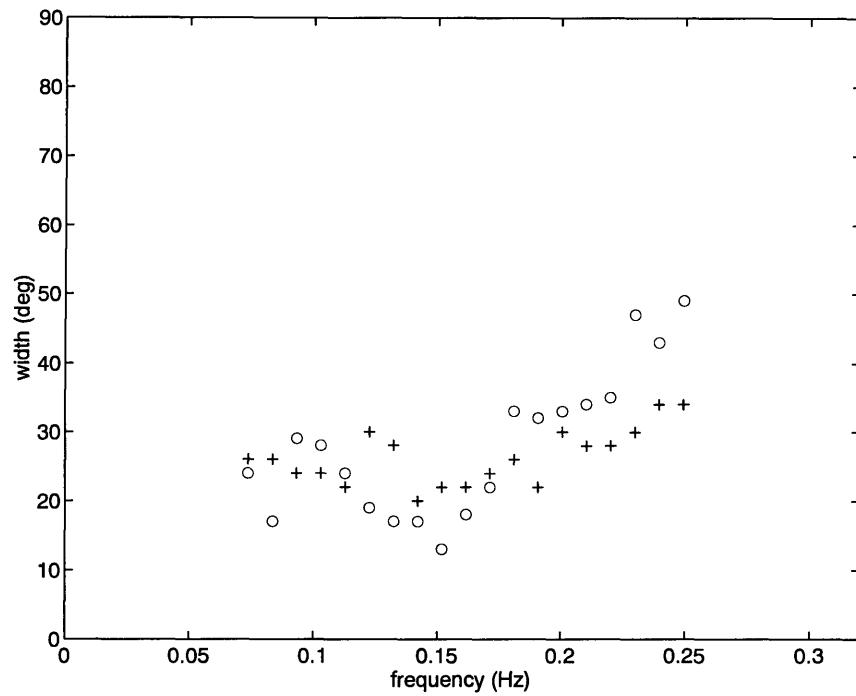


Figure 7.5-5 Case 5: Comparison of the directional widths $\Delta(f)$ from the LA ("+") and ADCP ("o") directional wave spectra.

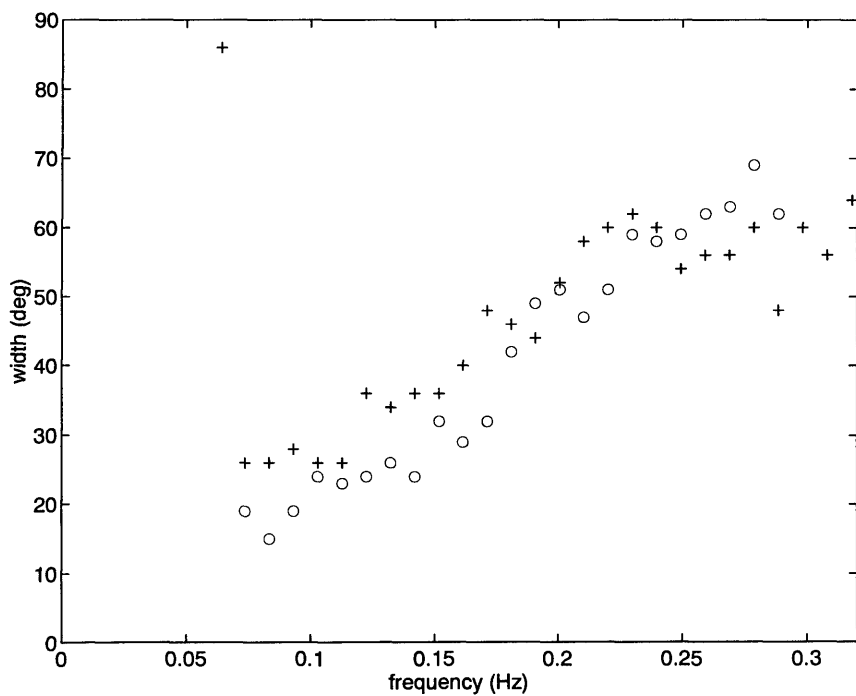


Figure 7.5-6 Case 6: Comparison of the directional widths $\Delta(f)$ from the LA ("+") and ADCP ("o") directional wave spectra.

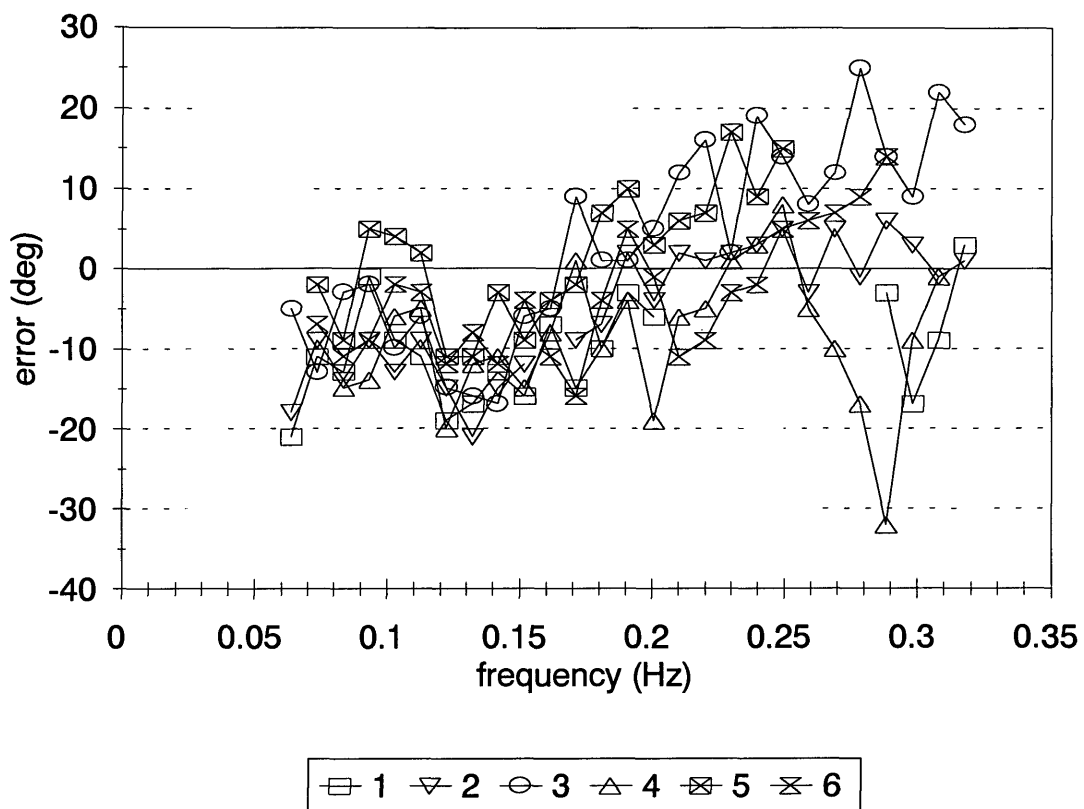


Figure 7.5-7 Errors in the ADCP-derived directional width $\Delta(f)$ relative to the LA-derived directional width for each case (see legend).

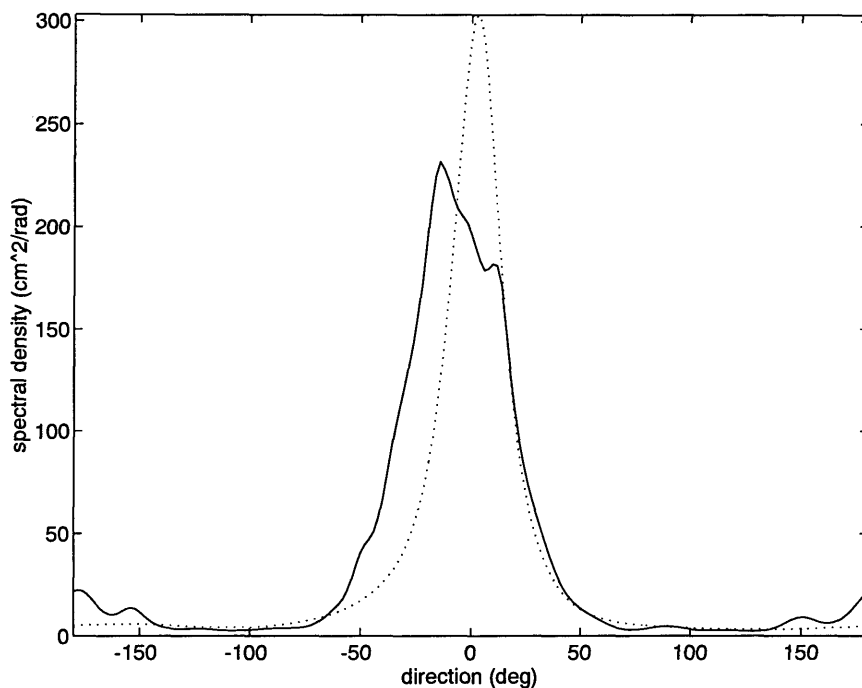


Figure 7.6-1 Case 1: Comparison of the frequency-integrated directional spectrum $S(\theta)$ from the LA (solid line) and ADCP (dotted line) directional wave spectra.

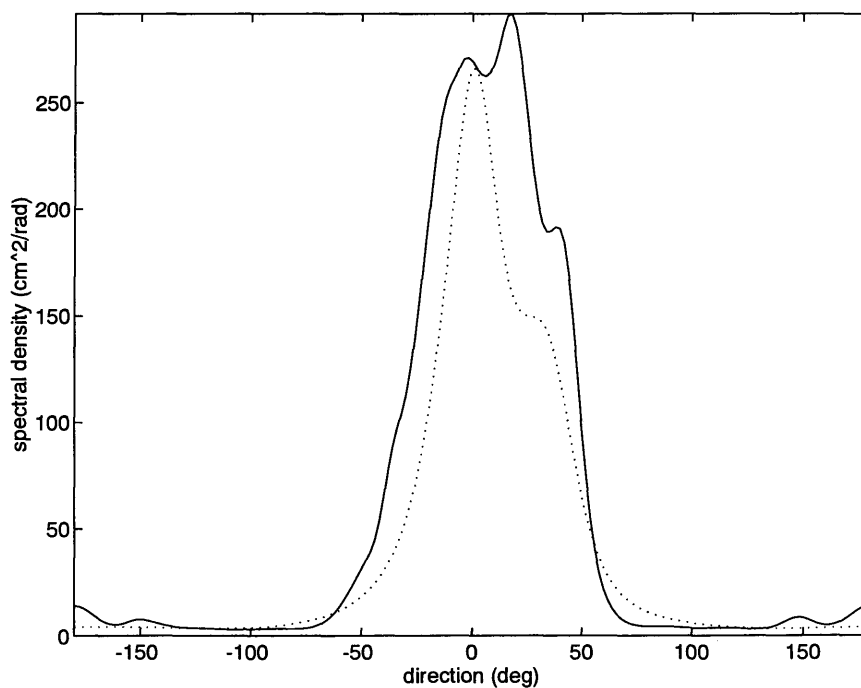


Figure 7.6-2 Case 2: Comparison of the frequency-integrated directional spectrum $S(\theta)$ from the LA (solid line) and ADCP (dotted line) directional wave spectra.

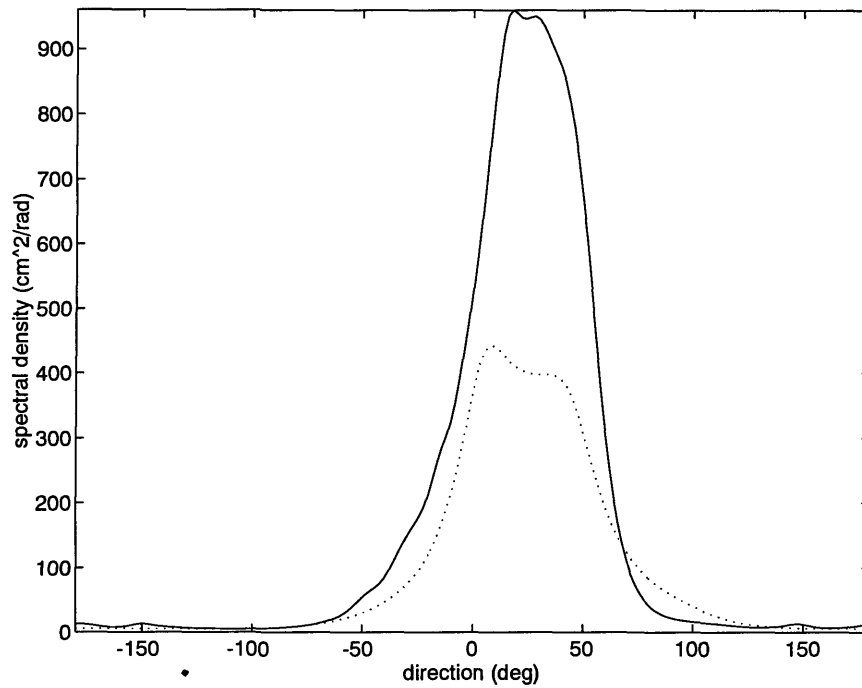


Figure 7.6-3 Case 3: Comparison of the frequency-integrated directional spectrum $S(\theta)$ from the LA (solid line) and ADCP (dotted line) directional wave spectra.

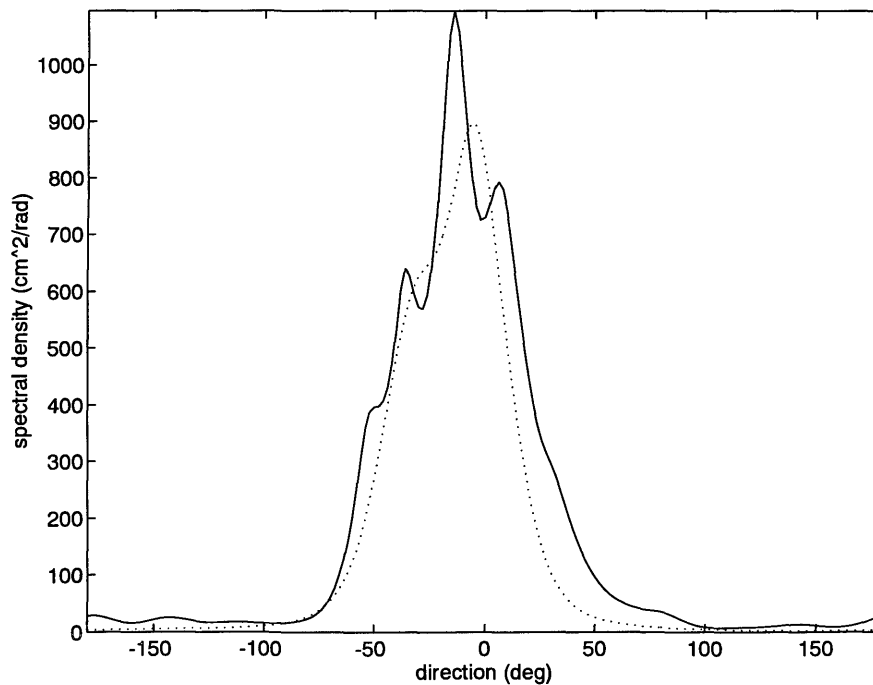


Figure 7.6-4 Case 4: Comparison of the frequency-integrated directional spectrum $S(\theta)$ from the LA (solid line) and ADCP (dotted line) directional wave spectra.

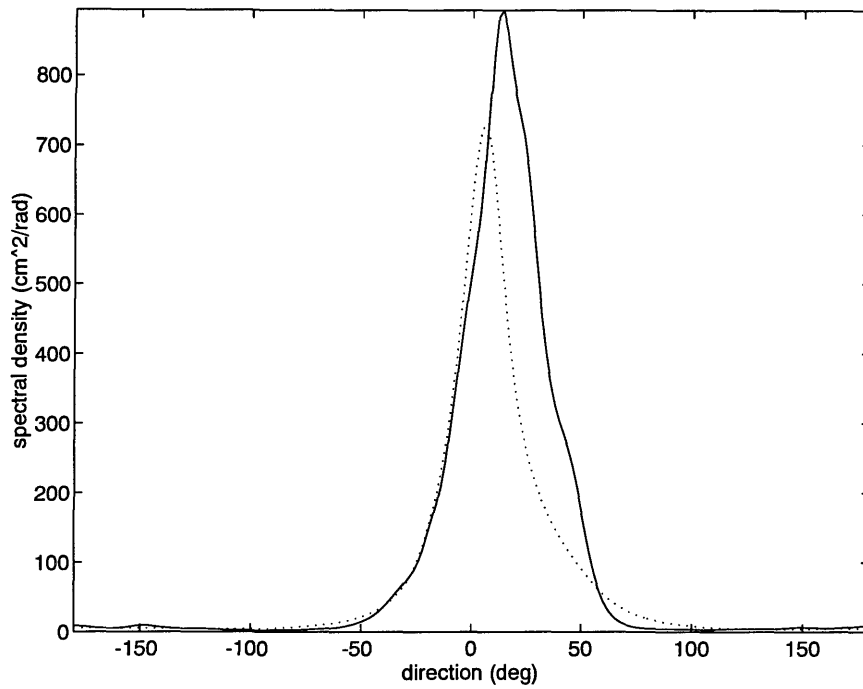


Figure 7.6-5 Case 5: Comparison of the frequency-integrated directional spectrum $S(\theta)$ from the LA (solid line) and ADCP (dotted line) directional spectra.

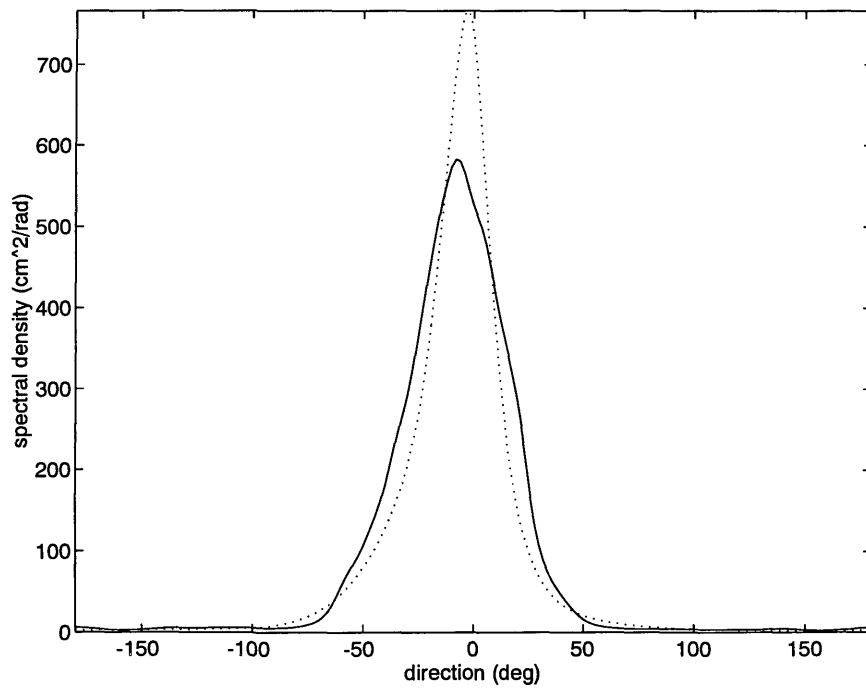


Figure 7.6-6 Case 6: Comparison of the frequency-integrated directional spectrum $S(\theta)$ from the LA (solid line) and ADCP (dotted line) directional wave spectra.

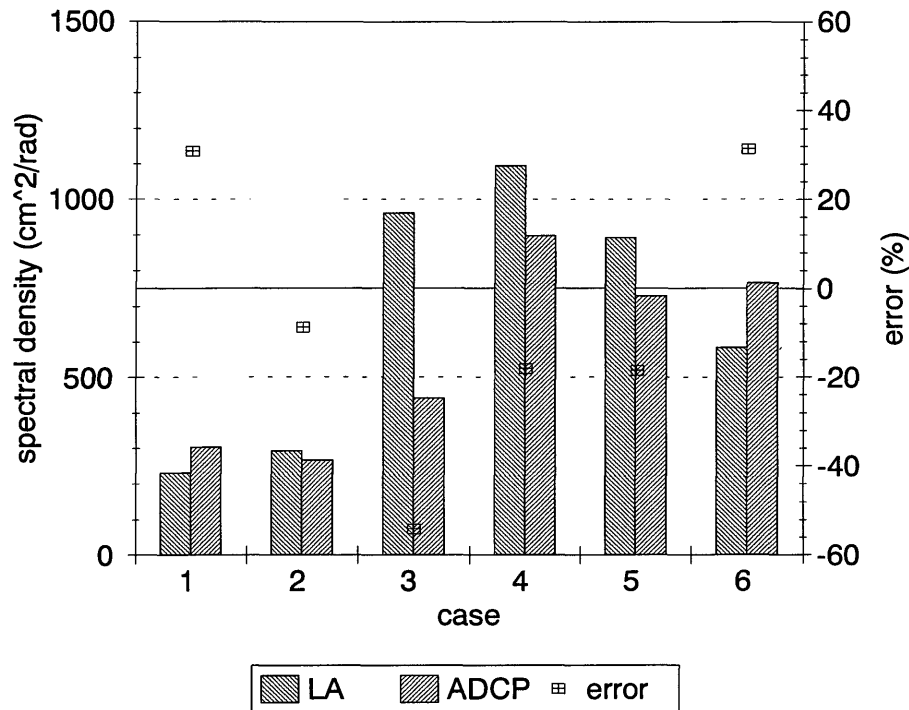


Figure 7.6-7 Comparison of the magnitude ($S_{p,d}$) of the largest peak in the LA- and ADCP-derived frequency-integrated directional spectra for each case.

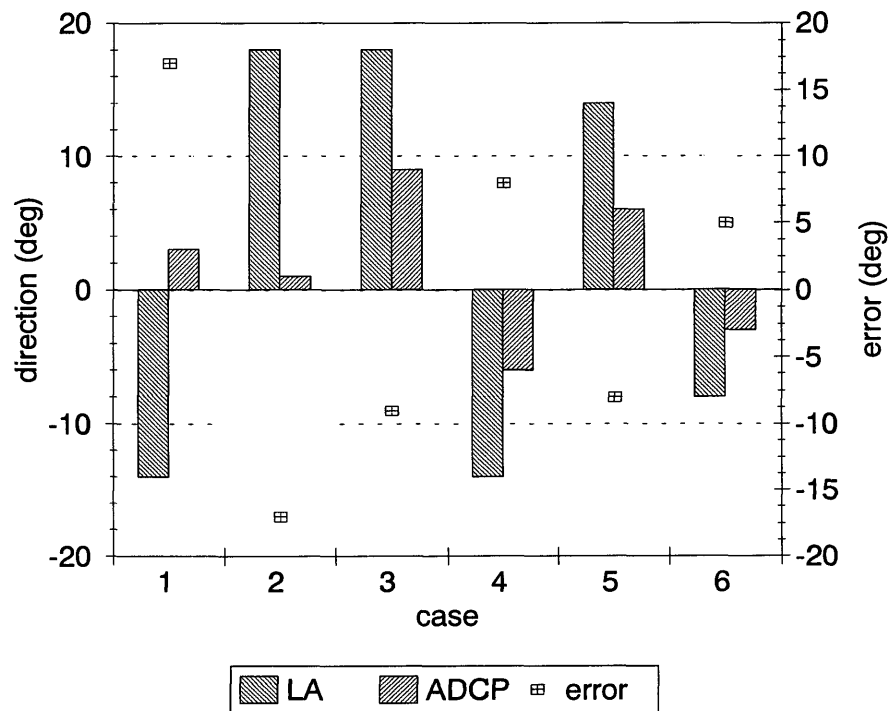


Figure 7.6-8 Comparison of the direction ($\Theta_{p,d}$) of the largest peak in the LA- and ADCP-derived frequency-integrated directional spectra for each case.

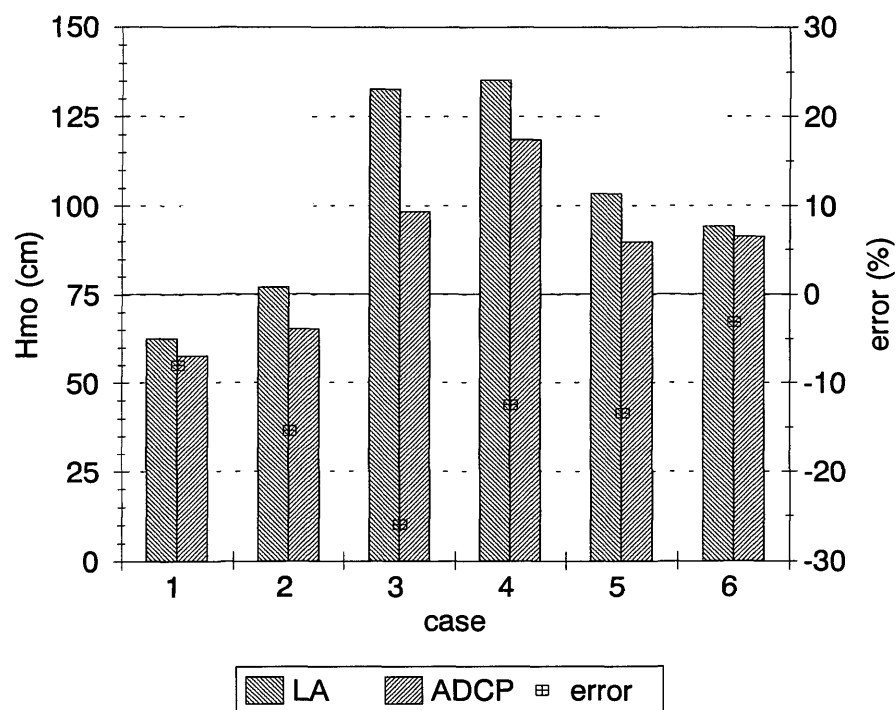


Figure 7.7-1 Comparison of the significant waveheight (H_{mo}) from the LA and ADCP directional wave spectra for each case.

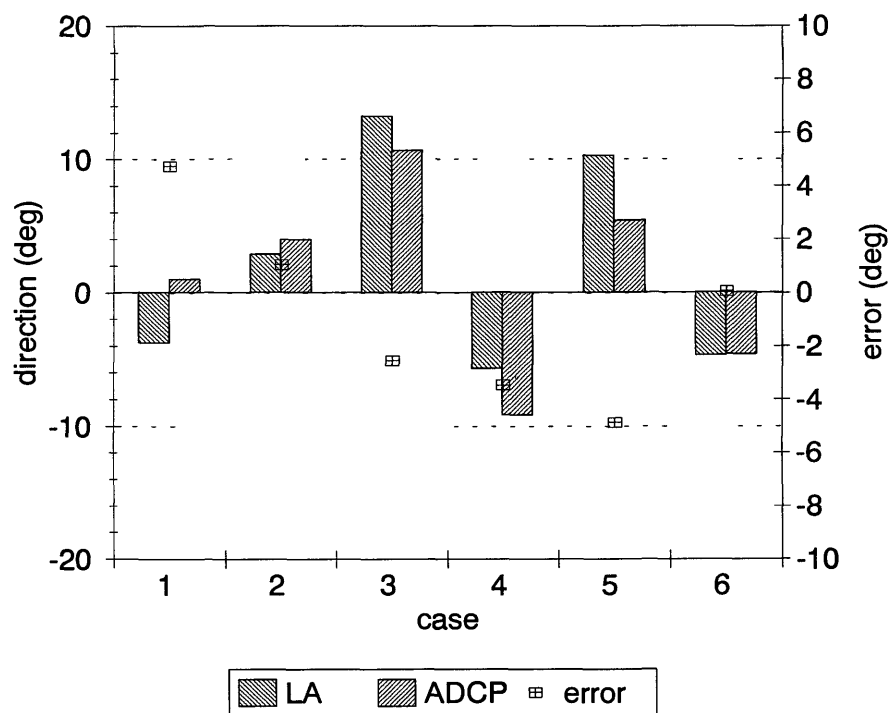


Figure 7.7-2 Comparison of the equivalent radiation stress angle ($\alpha_{xy,T}$) from the LA and ADCP directional wave spectra for each case.

8. DISCUSSION

Six cases are not enough to define the accuracy of the ADCP-based system for directional spectra estimation relative to the FRF Linear Array. A larger variety of environmental conditions and replicate cases within each environmental condition are required for this. These cases do indicate the potential for using an upward-looking, Janus-type ADCP to estimate directional wave spectra. From the results presented in chapters 6 and 7, it appears that useful information about the directional and nondirectional wave fields can be obtained from similar ADCP systems, particularly at low frequencies. This information includes the frequency and direction of localized peaks in the directional wave spectrum, the distribution of wave energy with frequency, and directional characteristics of the wavefield as functions of frequency.

However, these results also indicate two possibly connected shortcomings. The first is that the nondirectional wave spectra estimated from the ADCP autospectra (section 6.4) is inconsistent. The nondirectional wave spectra estimated from the ADCP autospectra of a single range bin should, in the absence of noise, be identical for different bins. The results presented in section 6.4 indicate a consistent bias between bins which increases with bin separation and with frequency (fig.s 6.4-7,8). The second shortcoming is that the nondirectional wave energy at high frequency ($f > 0.2$ Hz, say) computed from the ADCP directional wave spectrum is biased low in comparison to the nondirectional wave energy computed from the LA directional wave spectrum (sect. 7.2). This bias also appears to be frequency dependent.

These shortcomings may reflect errors in the parameters--e.g. total depth, bin depth--which determine the spatial δ -function model used here for the ADCP transfer functions or they may reflect shortcomings of the model itself. Possible causes for the frequency- and bin- dependent inconsistencies observed between the autospectra-derived nondirectional wave spectra calculated for different bins are discussed in section 8.1. Possible causes for the frequency-dependent bias in the nondirectional wave spectra computed from the ADCP

directional spectra are discussed in section 8.2.

8.1 Analysis of ADCP autospectra-derived nondirectional wave spectra

As noted above, the nondirectional wave spectra estimated from the ADCP autospectra for a range bin should, in the absence of noise, be identical for different bins. However, the results presented in section 6.4 indicate a consistent bias between bins which increases with bin separation and with frequency (fig.s 6.4-7,8). Several processing-related possibilities have been investigated to account for this behavior, but all seem to be inadequate to account for the observed behavior. Possible sources of errors in the processing which might generate the observed discrepancy include the use of the wrong total depth or the wrong bin depths for the normalization factor in eq. 3.13, the assumption of no instrument tilt, the uncorrected bias in the ADCP autospectra due to white noise, or the inadequacy of the current ADCP transfer function modelling.

From section 3.2, the wave frequency spectrum $S(\omega)$ and the sum of the ADCP autospectra $A_j(\omega, z)$ (using a slightly different notation from sect. 3.2--here j stands for beam number) for a bin at depth z are related (see eq. 3.13) by a proportionality factor $F(\omega, z, H)$ which depends on frequency ω , bin depth z , and total depth H . This relationship can be summarized as

$$S(\omega) = F(\omega, z, H) \sum_{j=1}^4 A_j(\omega, z) \quad (8.1)$$

An error in the total water depth, which also introduces a corresponding error of opposite sign in the bin depths, would affect the estimated wave frequency spectra through terms involving H (including the dispersion relation). The effect on the estimated wave frequency spectrum $\hat{S}(\omega, z)$ (i.e., calculated from the autospectra of the bin at depth z) of an error in total depth can thus be modelled as

$$\begin{aligned} \hat{S}(\omega ; z') &= F(\omega, z', H') \sum_{j=1}^4 A_j(\omega, z) \\ &= F(\omega, z', H') \left(\frac{S(\omega)}{F(\omega, z, H)} \right) \end{aligned} \quad (8.2)$$

where z and H are the true bin and total depths, while the primed quantities are the assumed values. Note that the ratio of the theoretical "estimated" spectra for two bins is independent of the true spectrum, but does depend on frequency, bin depth, and total depth.

A nominal depth of 8 m was used to compute the wave frequency spectra estimates (sect. 5.2). However, as noted in section 6.1, the mean depth at pressure gage 191 varies by over 1 m among the six cases (table 6.1-1). Consequently the actual mean water depth during a data interval could differ from the nominal depth by as much as a meter due to tidal variations. Using this as a "worst case" scenario, however, the results of eq. 8.2 for bin 1 and bin 5 (plotted as a ratio as in fig. 8.1-1) do not show the frequency-dependent discrepancy evident in the data results (fig. 6.4-7). Making an error in the total depth has very little effect on the ratio of the estimated wave frequency spectra from different bins. This should perhaps have been anticipated, because, for high frequencies, the depth attenuation of the wave-related currents becomes independent of the total depth. Similar results were obtained when a bias in the assumed bin depths was used in place of a bias in total depth (fig. 8.1-2).

Another hypothesis for the discrepancies observed in fig.s 6.4-7,8 focusses on the ADCP tilt. Equation 3.13 was developed on the assumption that the ADCP was not tilted, which means that each beam has the same inclination relative to vertical and that the beams are directed orthogonally in the horizontal. However, during the deployment, the ADCP was tilted slightly relative to vertical (table 6.1-1 and fig. 4-4). To investigate the effect of the ADCP tilt on the wave frequency spectra estimates, two sets of autospectra were simulated using eq. 3.11--one with no tilt and one with the same tilt as in case 1 (fig.s 8.1-3,4). The directional spectrum $S(\omega, \theta)$ used to generate the autospectra was chosen to be independent of frequency to simplify the simulation. The angular dependence of the directional spectrum was gaussian, with the peak taken at 20° off beam 1, a standard deviation of 10° , and an integrated amplitude of $1 \text{ m}^2/\text{Hz}$. For the untilted case, the autospectra magnitudes at each frequency are equal for beams 1 and 2 and for beams 3 and 4 (fig. 8.1-3). The effect of the tilt is to "split" the autospectra which had equal magnitude in the no tilt case (fig. 8.1-4). However, even though the magnitudes of the autospectra from the individual beams are have changed because of the tilt, their *sum* has not (fig. 8.1-5). Since it is the sum of the autospectra from a particular bin which is used to estimate the nondirectional wave frequency spectrum (eq. 8.2), this implies that, at least for small tilts of the type obtained

during this deployment, the effect of tilt on the estimated wave frequency spectra is negligible.

The final processing-related hypothesis for the observed behavior of the wave frequency spectra estimates stems from the bias introduced into the ADCP autospectra due to the ADCP instrument noise (see sect.s 3-1 and 3-3). If the true wave spectrum and the unbiased ADCP autospectra are related by eq. 8.1, the effect of a bias Q in the autospectra due to measurement noise is

$$\begin{aligned} \hat{S}(\omega ; z) &= F(\omega, z, H) \sum_{j=1}^4 \{A_j(\omega, z) \cdot Q\} \\ &= S(\omega) \left\{ 1 + 4F(\omega, z, H) \frac{Q}{S(\omega)} \right\} \end{aligned} \quad (8.3)$$

The ratio of eq. 8.3 for two bins depends not only on the "boost" factors for both bins, but also on the relative size of the bias and the true spectrum. The effect is illustrated in fig. 8.1-6. The estimated wave frequency spectra from bin 5 for case 2 has been used as a "true" spectrum to generate estimated spectra with a known bias. Estimated wave frequency spectra for bins 1, 3, and 5 were simulated assuming that the ADCP spectral noise density was 20 (cm/s)²/Hz, and the ratios of the simulated spectra from bins 1 and 3 relative to bin 5 were plotted. Also plotted are the corresponding ratios actually obtained for case 2. Although the simulated ratios demonstrate trends with frequency and depth, the magnitude of these trends is much smaller than was obtained for the ADCP results.

The discrepancy observed in the estimated wave frequency spectra consequently does not appear to be explained by processing artifacts or errors in the parameters used to define the δ -function model for the ADCP transfer functions. It is possible that the model itself is inadequate at high frequencies, a possibility which is addressed in the next section.

8.2 Analysis of nondirectional wave spectra from ADCP directional spectra

The nondirectional wave spectra computed from the ADCP directional wave spectra appear to be biased low at high frequencies ($f > 0.2$ Hz), relative to the LA-derived nondirectional spectra (section 7.2, fig.7.2-7). The magnitude of the bias appears to be greater in cases 2, 3, 4, and 5 than in cases 1 and 6. Two possible explanations for these

discrepancies are that the total depth used to compute the ADCP transfer functions is too small for these cases due to tidal variations in the total depth or that the modelling of the ADCP transfer functions as spatial δ -functions is inadequate.

The first possibility is suggested from the variation in the depth at pressure gage 191 in the LA over the cases (fig. 8.2-1 and table 6.1-1). The total depth is the smallest for case 6 and the greatest for cases 3 and 4, with the depth changes between cases 3 and 4 and case 6 over 1 m. Since a single nominal depth of 8 m was used to calculate the ADCP transfer functions for each case, the results could be biased due to a case-dependent error in the total depth.

To investigate the effect of the total depth on the nondirectional wave spectra computed from the ADCP directional spectra, it was assumed that the nominal depth corresponded to case 6 (since this case had the best agreement between the LA and ADCP nondirectional spectra results at high frequency) and cases 3 and 4 were reprocessed using a total depth of 9 m. The overall effect of this change was to boost the magnitude of features in the ADCP directional spectra without changing their directional characteristics appreciably.

The agreement between the frequency spectra computed from the LA and ADCP directional spectra is much improved when using the 9 m depth to compute the ADCP directional spectra, but the agreement is not perfect (fig.s 8.2-2,3). The ADCP results continue to underestimate the LA results. Comparing results from the full directional spectra, using 9 m for the total depth improves the agreement between the peak magnitudes of the LA and ADCP spectra in case 4 and the high frequency mode in case 3 (fig. 8.2-4), while it is worsened for the low frequency mode peak in case 3. Using the 9 m depth barely changes the directions associated with these peaks (fig. 8.2-5). The agreement between the results for characteristic waveheight H_{mo} is improved in both cases using the 9 m depth (fig. 8.2-6), while the results for $\alpha_{xy,T}$ are barely changed (fig. 8.2-7).

The second hypothesis proposed to account for the discrepancy between the magnitudes of the LA and ADCP directional and nondirectional spectra is that the modelling of the ADCP transfer functions as spatial δ -functions is inadequate. Because the ADCP beams are narrow (section 3.1), the next level of sophistication in modelling the ADCP transfer functions is to include the effect of the bin "width" in range, but to ignore the angular spread of the beams. In this model, the ADCP Doppler velocity estimate from a bin/beam pair is the

instantaneous average velocity along the beam direction, where a triangular weighting function is used to compute the average. The resulting transfer function model becomes

$$G_j(\omega, \theta) = \frac{\omega}{\sinh[kH]} \{ \cos(\alpha_j - \theta) \sin \beta_j I_{1,j}(\omega, \theta) - i \cos \beta_j I_{2,j}(\omega, \theta) \} \quad (8.4)$$

where

$$I_{1,j}(\omega, \theta) = \frac{1}{\delta z} \int_{-\delta z}^{\delta z} dz \left\{ 1 - \frac{|z|}{\delta z} \right\} \cosh[k(z_j \cdot z)] \exp \{ i \cos(\alpha_j - \theta) \tan \beta_j k(z_j \cdot z) \} \quad (8.5)$$

and

$$I_{2,j}(\omega, \theta) = \frac{1}{\delta z} \int_{-\delta z}^{\delta z} dz \left\{ 1 - \frac{|z|}{\delta z} \right\} \sinh[k(z_j \cdot z)] \exp \{ i \cos(\alpha_j - \theta) \tan \beta_j k(z_j \cdot z) \} \quad (8.6)$$

where δz is the vertical bin width.

To investigate the effect of the transfer function modelling on the resulting directional spectrum, case 3 was rerun using the transfer function model of eq.s 8.4-6 with a total depth of 8 m. The resulting ADCP directional spectrum, and consequently the corresponding frequency spectrum and directional content (fig.s 8.2-8,9), is virtually identical to that obtained using the simpler transfer function model (eq. 3.14).

It consequently appears that using a single nominal depth to process all six cases, regardless of tidal variations, introduced biases into the nondirectional ADCP wave spectra which resulted in underestimating the magnitude of the wave spectrum at each frequency relative to the LA results in the majority of cases. A pressure sensor located at the ADCP position could provide the requisite tidal variation to make this correction in future deployments (this had been suggested for the experiment reported here, but no instrument was available at the time).

It also appears that the simple modelling of the ADCP transfer functions as spatial δ -functions is quite adequate, at least relative to the next level of sophistication. Unfortunately, this leaves no satisfactory explanation for the biases obtained in the nondirectional spectra estimated from the autospectra of different ADCP bins. These biases are apparently not explainable in terms of errors in total depth, bin depth, ADCP tilt, transfer function modelling. The possibility of ADCP noise biasing the estimates from different bins showed trends in the correct directions, but the effect was too small. The cause of the observed biases thus remains unexplained and an area for future research.

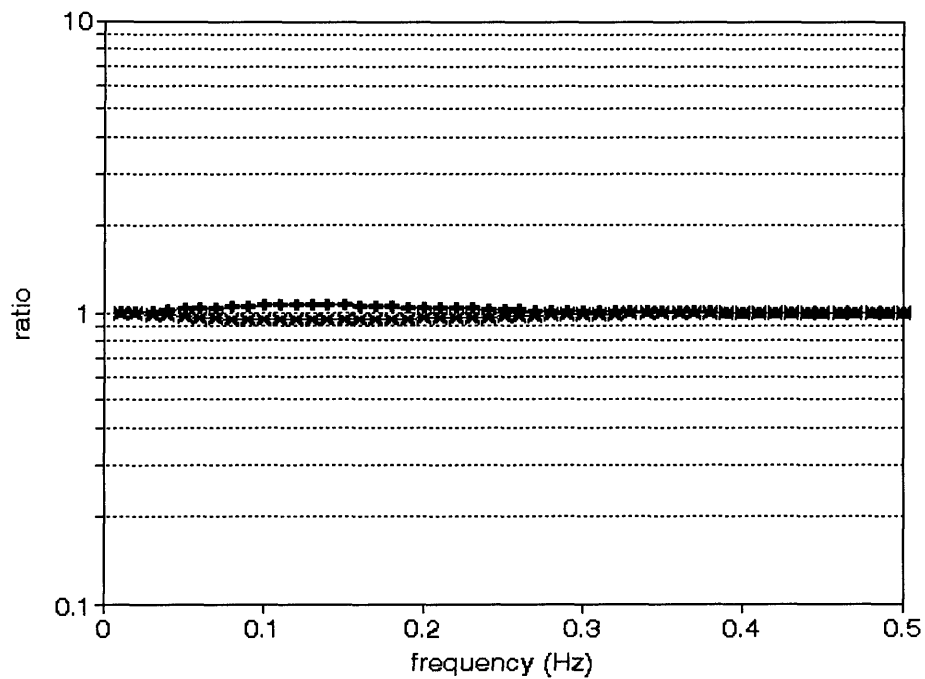


Figure 8.1-1 Frequency dependence of ratio of estimated wave frequency spectra (bins 1:5) when nominal total depth is 8 m and actual total depth is: $x = 7$ m, $+ = 9$ m.

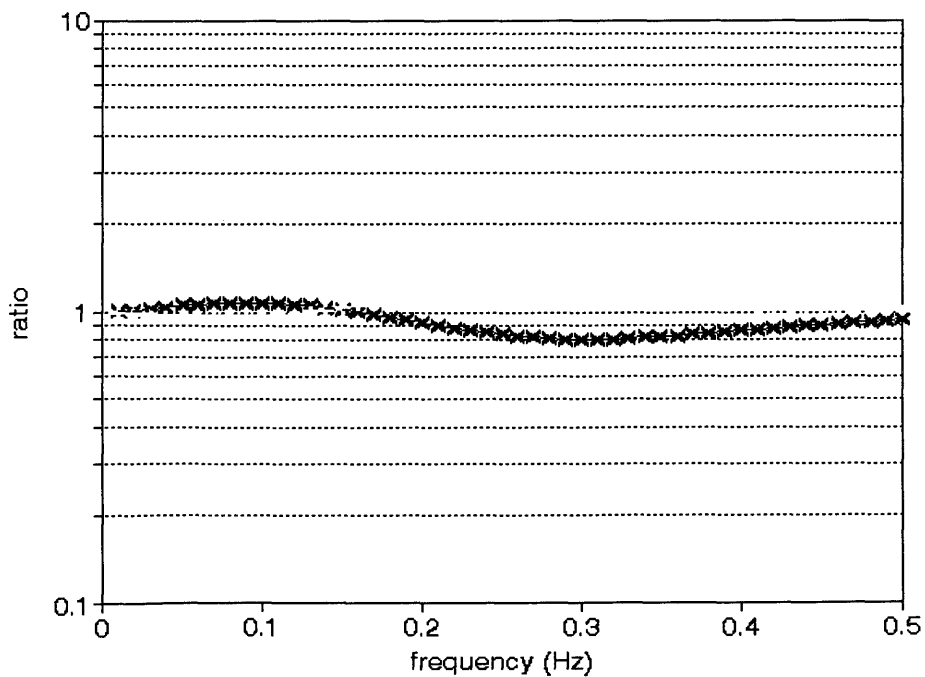


Figure 8.1-2 Frequency dependence of ratio of estimated wave frequency spectra (bins 1:5) when error in assumed bin depths is: $x = +1$ m, $+ = -1$ m.

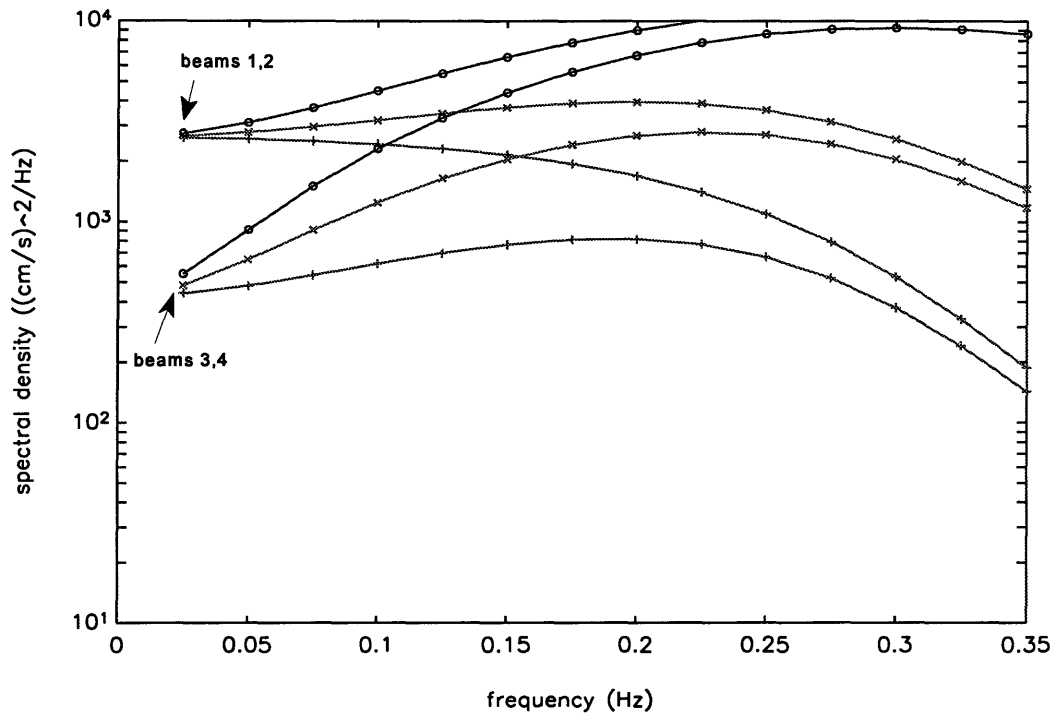


Figure 8.1-3 Simulated autospectra without tilt. + = bin 1, x = bin 3, o = bin 5.

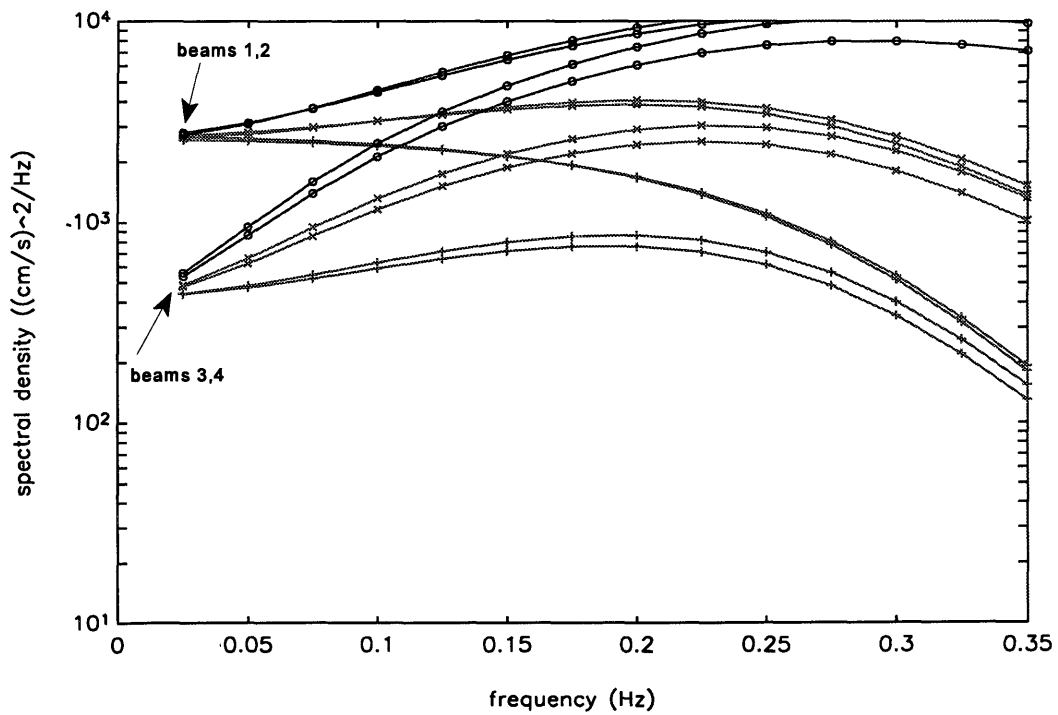


Figure 8.1-4 Simulated autospectra with tilt. + = bin 1, x = bin 3, o = bin 5.

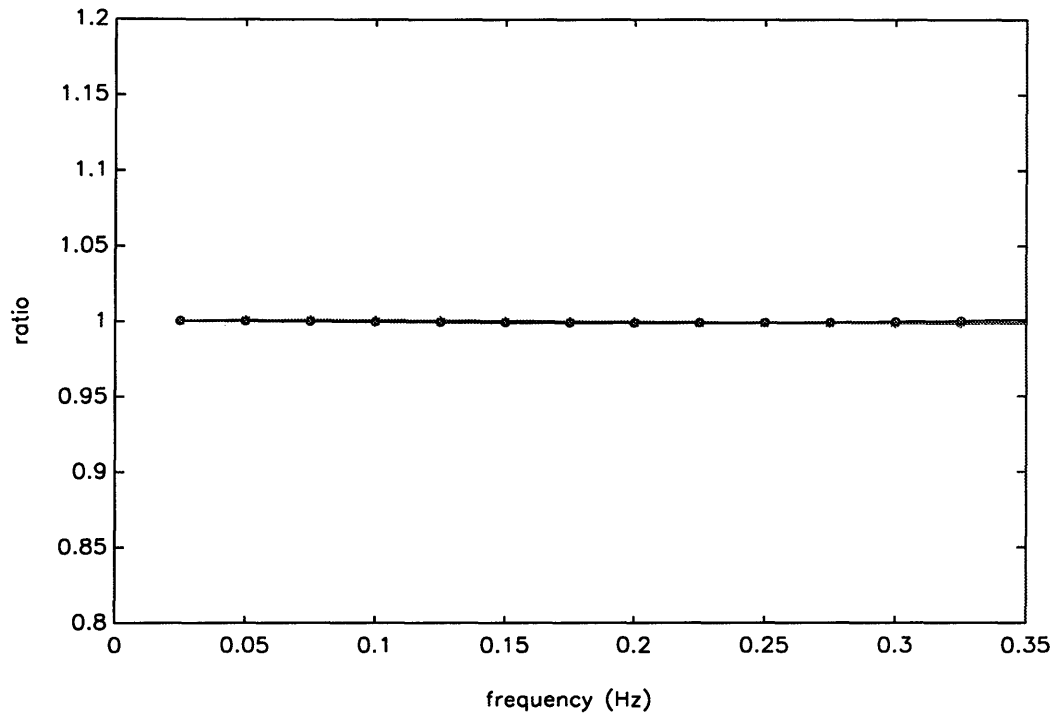


Figure 8.1-5 Ratio of sum of simulated autospectra with tilt to corresponding sum of autospectra without tilt. + = bin 1, x = bin 3, o = bin 5.

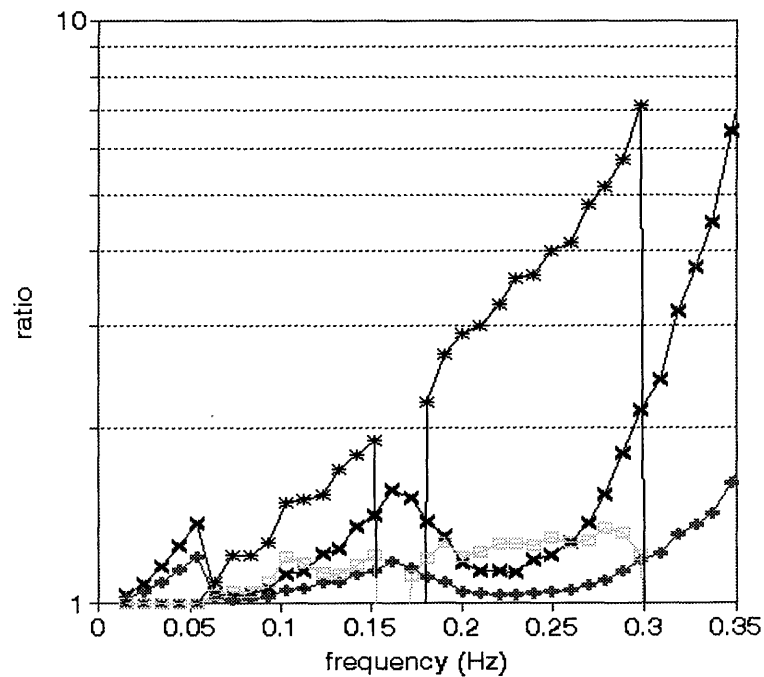


Figure 8.1-6 Effect of Q on ratios of ADCP wave frequency spectra: *, \square = ratios (bins 1:5,3:5) obtained for case 2; x, + = modeled ratios (bins 1:5,3:5) with noise bias.

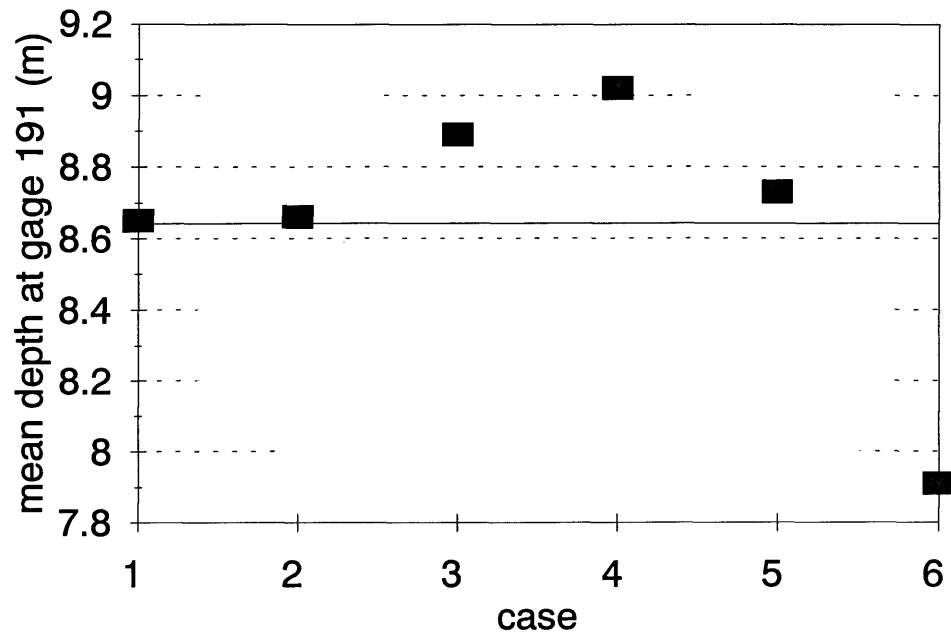


Figure 8.2-1 Mean depths at LA pressure gage 191 for each case.

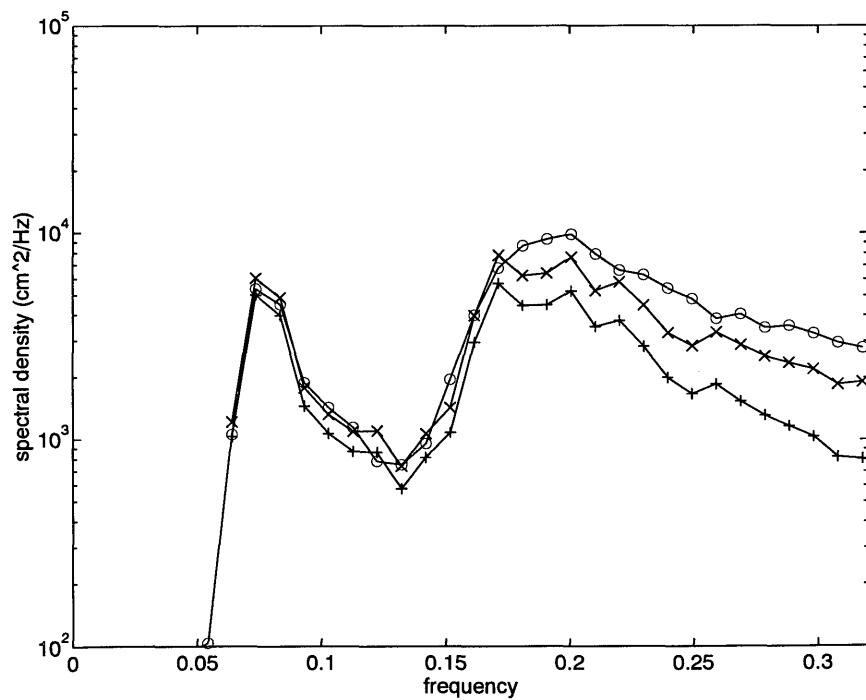


Figure 8.2-2 Nondirectional wave spectra for case 3 (from directional spectra): o = LA results, x,+ = ADCP results using total depth = 9,8 m respectively.

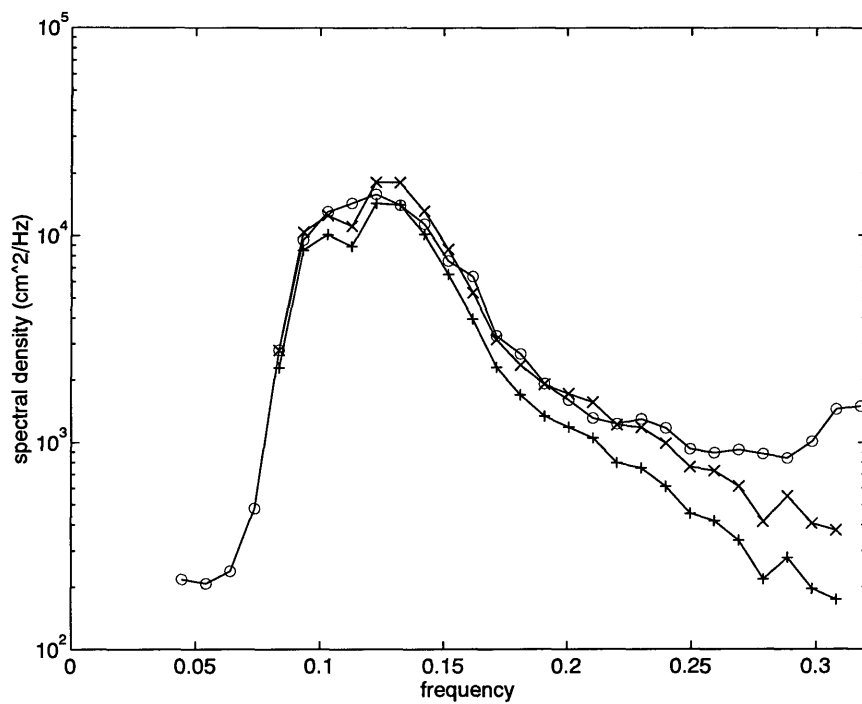


Figure 8.2-3 Nondirectional wave spectra for case 4 (from directional spectra): o = LA results, x,+ = ADCP results using total depth = 9,8 m respectively.

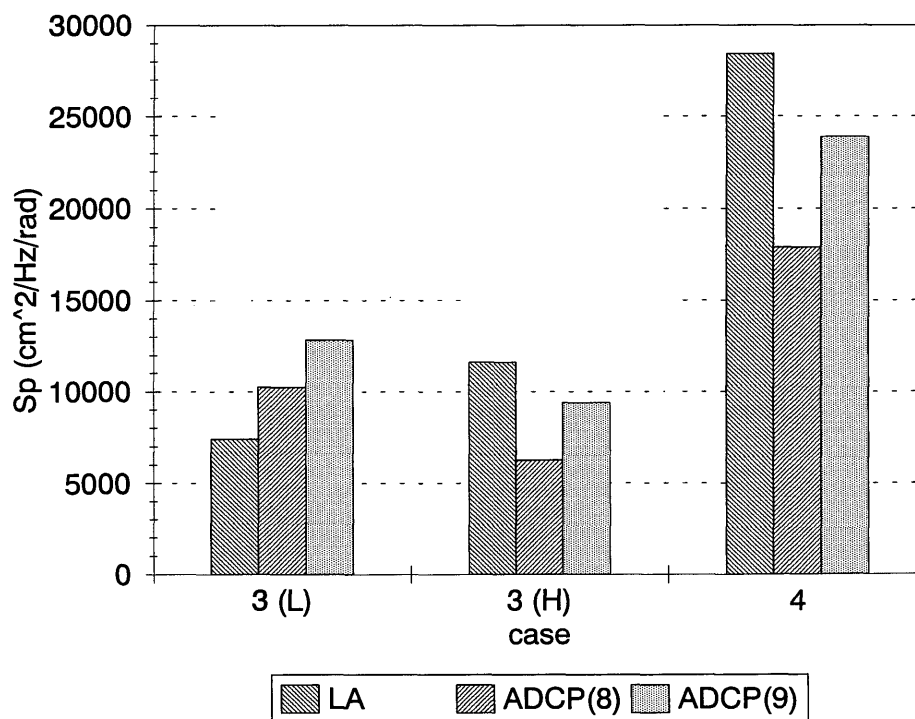


Figure 8.2-4 Comparison of peak magnitudes from directional wave spectra for case 3 (L = low freq., H = high freq.) and case 4. 8, 9 = assumed total depth (m).

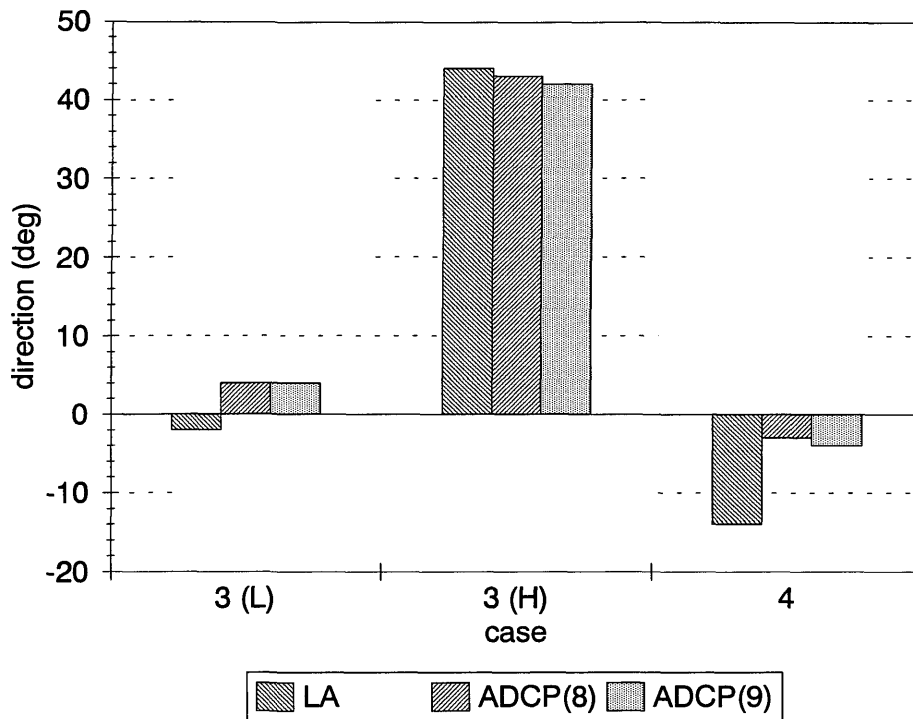


Figure 8.2-5 Comparison of peak directions from directional wave spectra for case 3 (L = low freq., H = high freq.) and case 4. 8, 9 = assumed total depth (m).

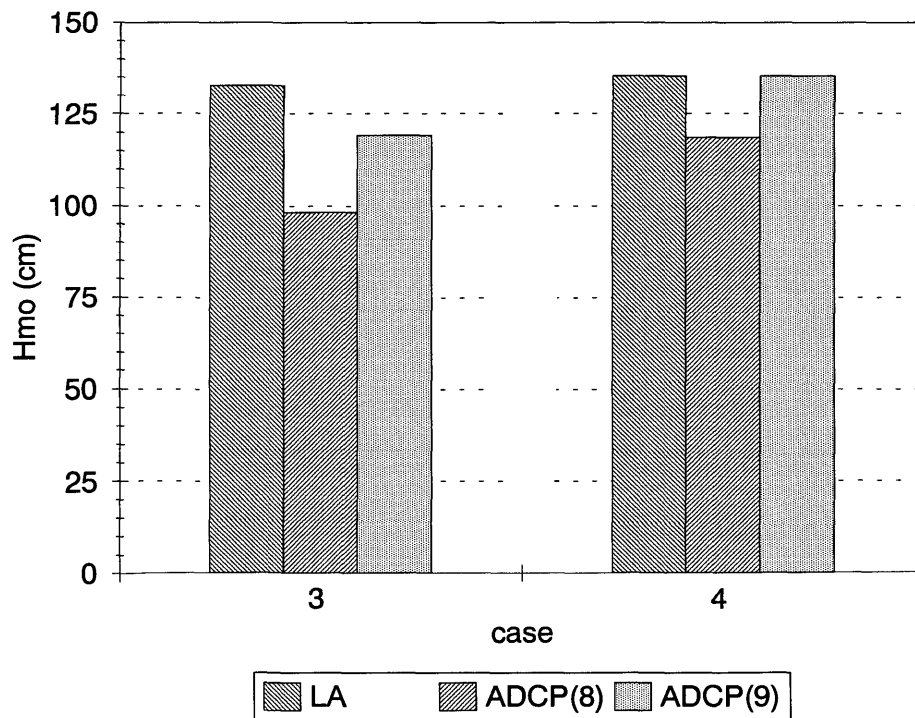


Figure 8.2-6 Comparison of characteristic waveheight H_{m0} from directional wave spectra for case 3 and case 4. 8, 9 = assumed total depth (m).

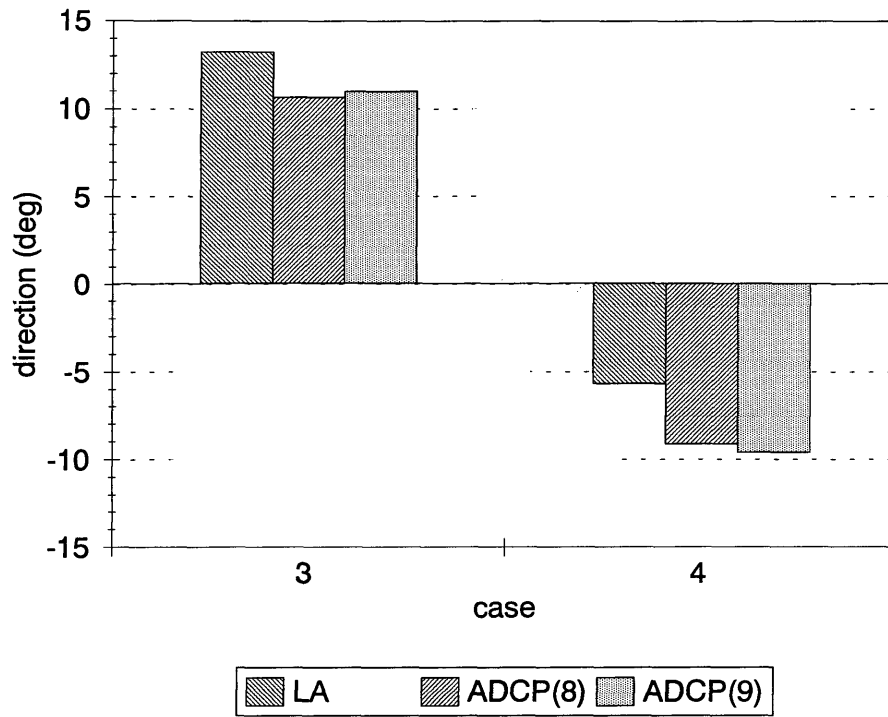


Figure 8.2-7 Comparison of total radiation stress angle $\alpha_{xy,T}$ from directional wave spectra for case 3 and case 4. 8, 9 = assumed total depth (m).

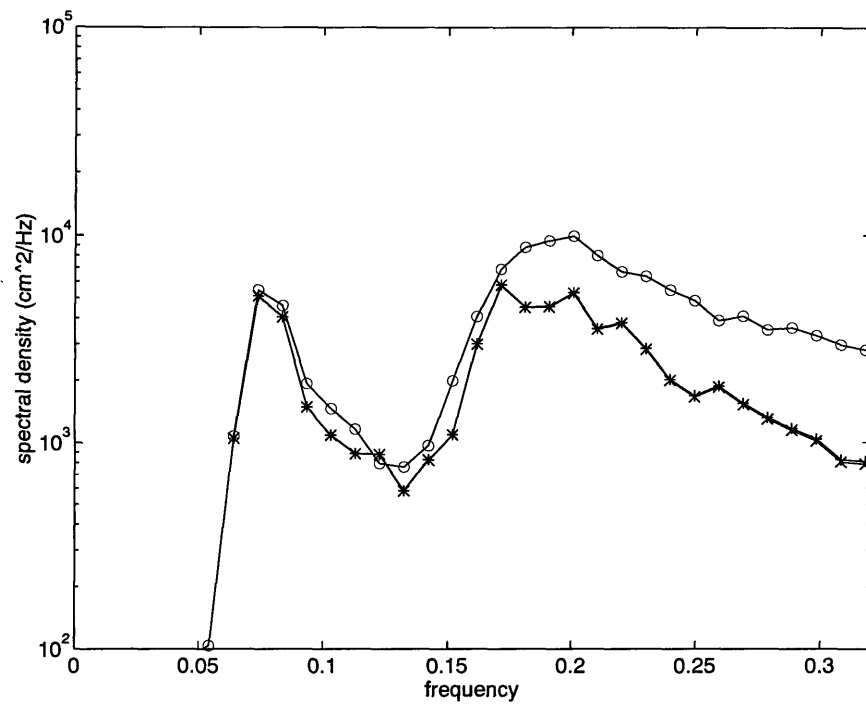


Figure 8.2-8 Comparison of nondirectional frequency spectra derived from directional spectra for case 3. o = LA, + = ADCP using eq. 3.14, x = ADCP using eq.s 8.4-8.6.

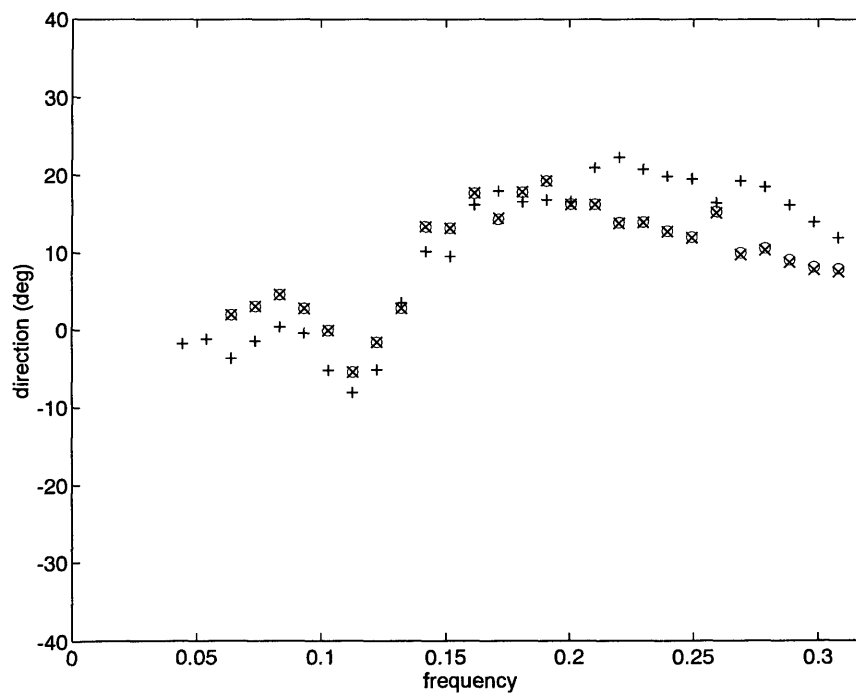


Figure 8.2-9 Comparison of mean direction vs. frequency derived from directional spectra for case 3: o = LA, + = ADCP using eq. 3.14, x = ADCP using eq.s 8.4-8.6.

9. SUMMARY AND CONCLUSION

ADCP Doppler velocity measurements are conventionally used to estimate low frequency (< 0.01 Hz) vertical profiles of current velocity. Estimates are typically averaged over tens to thousands of acoustic pulses and tens to hundreds of seconds to reduce associated random errors. In this study, it has been demonstrated that one can obtain reasonably accurate estimates of surface gravity wave directional spectra from high frequency (1 Hz) time series of ADCP Doppler velocity measurements.

In this study, transfer functions have been developed for a multibeam ADCP which model the connection between frequency cross spectra of ADCP Doppler velocity measurements and the directional wave spectrum. A sensitivity analysis based on these transfer functions has been presented for the RD Instruments 1200 kHz narrowband ADCP. This analysis indicates that it should be possible to estimate directional wave spectra via ADCP measurements in frequently encountered sea states. Directional wave spectra estimation algorithms based on the extended Maximum Likelihood Estimate method (Oltman-Shay and Guza, 1984) and the Iterative Maximum Likelihood Estimate method (Pawka, 1983 and Oltman-Shay and Guza, 1984) have been developed. Simulations indicate that directional resolution of ADCP-based directional spectra is better than some conventional directional spectra instruments such as the pitch-roll-heave buoy or U-V current meter/pressure gage combination.

As the final component of this study, an RD Instruments 1200 kHz ADCP was deployed at the US Army Corps of Engineers Waterways Experiment Station (WES) Coastal Engineering Research Center (CERC) Field Research Facility (FRF) at Duck, North Carolina, USA from October 28, 1992 to November 18, 1992. The ADCP was deployed within a Linear Array (LA) of pressure gages from which directional wave spectra are routinely estimated. Several ADCP datasets were collected from which directional wave spectra might be estimated. Six of these datasets were processed to estimate directional wave spectra using the equations and algorithms developed here. Comparison of the resulting

ADCP directional wave spectra with corresponding spectra estimated from LA measurements indicates that, while the ADCP-derived spectra are not identical to the LA-derived spectra, the overall agreement is rather good. Magnitudes of main peaks of wave energy in both types of spectra agree to within 50%, while the frequencies and directions associated with these peaks typically agree to within 10% and 10°, respectively. Other characteristics of the directional wave spectrum, such as the nondirectional wave spectrum, the frequency-dependent radiation stress angle, mean wave direction, and directional width, the frequency-integrated directional spectrum, the characteristic waveheight, and the total radiation stress angle also agree rather well between the ADCP and LA results for all six cases. A frequency-dependent bias apparent at frequencies > 0.2 Hz was noted between the ADCP and LA nondirectional wave spectra in several cases. This bias appears to be partly the result of not including tidal variations between cases in the total depth used for the ADCP directional spectra processing. It is consequently recommended that a pressure gage be included in future deployments of ADCPs to measure wave spectra in order to account for such variations in total water depth.

One issue unresolved in this study is that of the inconsistency among nondirectional wave spectra estimates obtained from the autospectra of different ADCP rangebins for the Duck datasets. Several explanations for this inconsistency were investigated, such as errors in the total depth or bin depths used to define the ADCP transfer functions, but none appeared conclusive. As a result, this issue remains an area for future investigation.

The six cases examined here indicate that estimating directional wave spectra using a commercially available ADCP is indeed possible and they give some indication of the accuracy one can expect, at least in relation to a conventional high resolution instrument array. However, more cases are clearly required, involving a larger variety of conditions and replicate cases, in order to more carefully assess the performance of the ADCP for directional spectra estimation.

APPENDIX A:
DIRECTIONAL WAVE SPECTRA FOR SURFACE GRAVITY WAVES

The physical observables associated with surface gravity waves in the ocean--e.g. sea surface elevation, orbital velocity components, perturbation pressure--are stochastic variables which vary in time and space. If they can be considered stationary during a period of observation, then the directional wave spectrum provides an important statistical description of these observables. The directional wave spectrum describes the distribution of the variance of sea surface elevation as a function of wave frequency and direction of travel. It also describes, to second order in the wave slope, the directional wave energy spectrum; wave energy is proportional to sea surface variance to this order (Phillips, 1966). In fact, "wave spectrum" and "energy spectrum" are frequently used interchangeably.

The directional wave spectrum is an example of a multidimensional wavenumber/frequency (WF) spectrum (Davis and Regier, 1977). The WF spectrum $S(\underline{k}, \omega)$ is the multi-dimensional Fourier transform of the spatial/temporal covariance of the sea surface elevation $R(\underline{r}, \tau)$. If $\eta(\underline{x}, t)$ is the sea surface elevation as a function of horizontal position $\underline{x} = (x, y)$ and time t , then

$$R(\underline{r}, \tau) = \langle \eta(\underline{x} + \underline{r}, t + \tau) \eta(\underline{x}, t) \rangle \quad (\text{A.1})$$

where $\langle \rangle$ denotes an ensemble average and $R(\underline{r}, \tau)$ and $S(\underline{k}, \omega)$ constitute a Fourier transform pair defined by

$$\begin{aligned} R(\underline{r}, \tau) &= \frac{1}{(2\pi)^3} \int d^2k d\omega S(\underline{k}, \omega) \exp[i(\underline{k} \cdot \underline{r} - \omega \tau)] \\ S(\underline{k}, \omega) &= \int d^2r d\tau R(\underline{r}, \tau) \exp[-i(\underline{k} \cdot \underline{r} - \omega \tau)] \end{aligned} \quad (\text{A.2})$$

The horizontal (angular) wavenumber $\underline{k} = (k_x, k_y)$ is the Fourier transform conjugate to the horizontal spatial separation $\underline{r} = (r_x, r_y)$, and the (angular) frequency ω is the conjugate to the

temporal separation τ . Because the wavenumber magnitude and the frequency are linked for small amplitude surface gravity waves by a dispersion relationship (see below), the directional waveheight spectrum can also be described as a function by frequency ω and direction of travel $\theta = \arctan^{-1}(k_y/k_x)$ alone. The WF spectrum can also be expressed in terms of the frequency cross-spectrum of sea surface variance $C(r, \omega)$, which is defined as the frequency transform of the spatial/temporal covariance function $R(r, \tau)$. The functions S , R , and C have the following relationships:

$$\begin{aligned} C(\underline{r}, \omega) &= \int d\tau R(\underline{r}, \tau) \exp(i\omega \tau) \\ S(\underline{k}, \omega) &= \int d^2r C(\underline{r}, \omega) \exp(-i\underline{k} \cdot \underline{r}) \\ C(\underline{r}, \omega) &= \frac{1}{(2\pi)^2} \int d^2k S(\underline{k}, \omega) \exp(i\underline{k} \cdot \underline{r}) \end{aligned} \quad (\text{A.3})$$

Additionally, the cross-spectra between different physical observables associated with small amplitude waves can be expressed as the Fourier transform of the wave spectrum weighted by a function of wavenumber and frequency. Measurements of these variables thus also lead to information about the waveheight spectrum. The relationships between the sea surface elevation and other wave-related observables are developed in the next section for deterministic small amplitude waves. The statistical relationships between the wave-related observables for a random sea are developed in the subsequent section.

A.1 Small Amplitude Surface Gravity Wave Theory

The theory of small amplitude surface gravity waves is well known. Phillips (1966), Apel (1987), and Kinsman (1984) are several of the many authors who provide a discussion of small amplitude wave theory. The key results of the theory as it pertains to directional wave spectra are developed herein.

$$0 = \nabla^2 \phi \quad (\text{A.4})$$

The linearized equations of motion for an incompressible, inviscid, and irrotational fluid with an impermeable flat bottom at $z = -h$ and a free surface at $z = \eta(\underline{x}, t)$ are

$$\vec{u}(\underline{x}, z, t) = \nabla \phi(\underline{x}, z, t) \quad (\text{A.5})$$

$$0 = \frac{\partial \phi}{\partial t} + \frac{1}{\rho} p_w \quad (\text{A.6})$$

with boundary conditions at $z = -h$

$$0 = \frac{\partial \phi}{\partial z} \quad (\text{A.7})$$

and at $z = 0$

$$0 = p_w(\underline{x}, 0, t) - \rho g \eta(\underline{x}, t) \quad (\text{A.8})$$

$$0 = \frac{\partial \phi}{\partial z} - \frac{\partial \eta}{\partial t} \quad (\text{A.9})$$

where \underline{u} is the wave orbital velocity vector, p_w is the perturbation pressure due to the waves, and ϕ is the velocity potential. A right-handed coordinate system is used; the z -axis points upward (opposite gravity) and the $z = 0$ plane is taken at mean sea level. It should be noted that these equations describe surface waves with frequencies much greater than the Coriolis parameter and the Brunt-Vaisala frequency and smaller than about 5 Hz, where surface tension effects become important (Phillips, 1966).

These equations are the first order equations in a perturbation expansion of the incompressible, inviscid, and irrotational Navier-Stokes equations in which boundary conditions at the sea surface are expanded about mean sea level in a Taylor series (Phillips, 1966). The assumption of linearity is often referred to (and will be referred to here) as a "small amplitude" assumption, although this is not strictly correct. If A is a typical wave amplitude and L is a typical wavelength, then the equations are valid when the wave slope or steepness A/L is small (i.e. $A/L \ll 1$) and the depth h is large compared to the wave amplitude (i.e. $A/h \ll 1$). Higher order terms are consequently needed to describe conditions approaching wave breaking (i.e. $A/L \gg 1$) and waves in the surf zone (i.e. $A/h \gg 1$).

Because the system of equations A.4-A.9 is linear, a solution for an arbitrary (consistent with the small amplitude assumption) initial sea surface may be regarded as a Fourier superposition of solutions to the problem of a single wave with wavenumber \underline{k} and frequency ω . For wave-related variables, the expansion

$$f(\underline{x}, z, t) = \frac{1}{(2\pi)^3} \int d^2k d\omega \hat{f}(\underline{k}, \omega, z) \exp[i(\underline{k} \cdot \underline{x} - \omega t)] \quad (\text{A.10})$$

is used, where \hat{f} is conjugate symmetric to ensure that f is a real function. If f is not a function of z , then \hat{f} is independent of z also. The wavenumber vector \underline{k} points in the direction of wave propagation. In component form, $\underline{k} = (k_x, k_y) = k (\cos \theta, \sin \theta)$, where k is the magnitude of \underline{k} and θ is the angle between \underline{k} and the positive x-axis. The integration is over $[-\infty, +\infty]$ for k_x , k_y , and ω . A subscript notation for f will be used to refer to specific wave-related variables, when convenient, with

$$\begin{bmatrix} f_0(\underline{x}, z, t) \\ f_1(\underline{x}, z, t) \\ f_2(\underline{x}, z, t) \\ f_3(\underline{x}, z, t) \\ f_4(\underline{x}, z, t) \end{bmatrix} = \begin{bmatrix} \eta(\underline{x}, t) \\ u(\underline{x}, z, t) \\ v(\underline{x}, z, t) \\ w(\underline{x}, z, t) \\ p_w(\underline{x}, z, t) \end{bmatrix} \quad (\text{A.11})$$

A subscripted f which refers to ϕ is not included here because the velocity potential is not an observable quantity and it will not be referred to beyond this section.

Substituting in equations of the form of eq. A.9 into the linearized equations A.3-A.8 and rearranging slightly, one obtains the following relationships for the Fourier amplitudes of the wave-related variables:

$$0 = \frac{1}{(2\pi)^3} \int d^2k d\omega \begin{Bmatrix} \hat{u}(\underline{k}, \omega, z) - ik_x \hat{\phi}(\underline{k}, \omega, z) \\ \hat{v}(\underline{k}, \omega, z) - ik_y \hat{\phi}(\underline{k}, \omega, z) \\ \hat{w}(\underline{k}, \omega, z) - \frac{\partial \hat{\phi}}{\partial z}(\underline{k}, \omega, z) \end{Bmatrix} \exp[i(\underline{k} \cdot \underline{x} - \omega t)] \quad (\text{A.12})$$

$$0 = \frac{1}{(2\pi)^3} \int d^2k d\omega \left\{ (k_x^2 + k_y^2 + \frac{\partial^2}{\partial z^2}) \hat{\phi}(\underline{k}, \omega, z) \right\} \exp[i(\underline{k} \cdot \underline{x} - \omega t)] \quad (\text{A.13})$$

$$0 = \frac{1}{(2\pi)^3} \int d^2k d\omega \left\{ -i\omega \hat{\phi}(\underline{k}, \omega, z) + \frac{1}{\rho} \hat{p}_w(\underline{k}, \omega, z) \right\} \exp[i(\underline{k} \cdot \underline{x} - \omega t)] \quad (\text{A.14})$$

$$0 = \frac{1}{(2\pi)^3} \int d^2k d\omega \left\{ \frac{\partial \hat{\phi}}{\partial z}(\underline{k}, \omega, z = -h) \right\} \exp[i(\underline{k} \cdot \underline{x} - \omega t)] \quad (\text{A.15})$$

$$0 = \frac{1}{(2\pi)^3} \int d^2k d\omega \left\{ \hat{p}_w(\underline{k}, \omega, z = 0) - \rho g \hat{\eta}(\underline{k}, \omega) \right\} \exp[i(\underline{k} \cdot \underline{x} - \omega t)] \quad (\text{A.16})$$

$$0 = \frac{1}{(2\pi)^3} \int d^2k d\omega \left\{ \frac{\partial \hat{\phi}}{\partial z}(\underline{k}, \omega, z = 0) - (-i\omega) \hat{\eta}(\underline{k}, \omega) \right\} \exp[i(\underline{k} \cdot \underline{x} - \omega t)] \quad (\text{A.17})$$

For the integrals to be zero in general, the terms within the parentheses must be zero.

Equation A.12 is separable in (\underline{k}, ω) and z . To satisfy eq. A.12, the velocity potential Fourier amplitudes can have the form

$$\hat{\phi}(\underline{k}, \omega, z) = A(\underline{k}, \omega) \cosh[k(z+h)] + B(\underline{k}, \omega) \sinh[k(z+h)] \quad (\text{A.18})$$

From the boundary condition at $z = -h$, eq. A.14, it is seen that $B(\underline{k}, \omega)$ in eq. A.17 must be identically zero. Plugging this result into eq. A.16, one obtains that

$$A(\underline{k}, \omega) = -i \frac{\omega}{k} \frac{\hat{\eta}(\underline{k}, \omega)}{\sinh[kh]} \quad (\text{A.19})$$

so that the velocity potential amplitudes are given by

$$\hat{\phi}(\underline{k}, \omega, z) = -i \frac{\omega}{k} \frac{\cosh[k(z+h)]}{\sinh[kh]} \hat{\eta}(\underline{k}, \omega) \quad (\text{A.20})$$

Substituting this result into eq. A.13 yields

$$\hat{p}_w(\underline{k}, \omega, z) = \frac{\omega^2}{k} \frac{\cosh[k(z+h)]}{\sinh[kh]} \hat{\eta}(\underline{k}, \omega) \quad (\text{A.21})$$

for the perturbation pressure amplitudes.

Finally, substituting this expression into eq. A.15 one obtains the constraint that

$$0 = \{ \omega^2 - gk \tanh[kh] \} \hat{\eta}(\underline{k}, \omega) \quad (\text{A.22})$$

Waves with nonzero amplitude must have \underline{k} and ω such that the term in parentheses is zero. For surface gravity waves, then, the frequency and wavenumber magnitude are related by

$$\omega^2 = g k \tanh[kh] \quad (\text{A.23})$$

This is known as the dispersion relationship for small amplitude surface gravity waves. The wavenumber magnitude k corresponding to surface gravity waves is thus a function of the wave frequency ω , i.e. $k = k(|\omega|)$. The vector wavenumber thus becomes $\underline{k} = \underline{k}(\omega, \theta)$. To simplify notation, we will drop the absolute value around ω with the understanding that $k(\omega) = k(|\omega|)$.

The Fourier amplitudes of the horizontal and vertical orbital velocity components are found from eq. A.11 to be

$$\hat{u}(\underline{k}, \omega, z) = i k_x \hat{\phi} = \omega \frac{k_x \cosh[k(z-h)]}{k \sinh[kh]} \hat{\eta}(\underline{k}, \omega) \quad (\text{A.24})$$

$$\hat{v}(\underline{k}, \omega, z) = i k_y \hat{\phi} = \omega \frac{k_y \cosh[k(z-h)]}{k \sinh[kh]} \hat{\eta}(\underline{k}, \omega) \quad (\text{A.25})$$

$$\hat{w}(\underline{k}, \omega, z) = \frac{\partial \hat{\phi}}{\partial z} = -i \omega \frac{\sinh[k(z-h)]}{\sinh[kh]} \hat{\eta}(\underline{k}, \omega) \quad (\text{A.26})$$

For a given set of Fourier amplitudes $\hat{\eta}$, the space/time dependence of the quantities η , ϕ , u , v , w and p_w is then obtained by substituting the corresponding "hatted" \underline{k}, ω space function into eq. A.7 and evaluating the integral. Because the \underline{k}, ω space amplitudes \hat{f}_i are proportional to $\hat{\eta}(\underline{k}, \omega)$ by different functions of \underline{k} , ω , and z , we adopt the notation

$$f_i(\vec{x}, z, t) = \frac{1}{(2\pi)^3} \int F_i(\underline{k}, \omega, z) \hat{\eta}(\underline{k}, \omega) e^{i(\underline{k}\vec{x} - \omega t)} d^2k d\omega \quad (\text{A.27})$$

where F_i is the proportionality function relating \hat{f}_i to $\hat{\eta}$ from eq.s A.19-A.20 and A.23-A.25. The F_i are known as transfer functions, since they transfer the properties of the waveheight Fourier amplitude to the \hat{f}_i .

The fundamental dispersion relation, eq. A.22, allows one to reduce the dimension of the integral in eq. A.26 from three to two. If $|\underline{k}|$ and ω are not related by the dispersion relation, then a solution to the equations of motion eq.s 2.3-2.8 exists only if $\hat{\eta}(\underline{k}, \omega)$ is zero.

Consequently $\hat{\eta}(\underline{k}, \omega)$ is nonzero only on the surface defined by the dispersion relation. Since $\hat{\eta}(\underline{k}, \omega)$ is nonzero only on a two-dimensional surface (whereas the integral in eq. A.26 is three-dimensional), in order that the waveheight in real space not be identically zero, the Fourier amplitude $\hat{\eta}(\underline{k}, \omega)$ must be expressible as

$$\hat{\eta}(\underline{k}, \omega) = 2\pi \delta(k - k(\omega)) \frac{2\pi}{k} \tilde{\eta}(\omega, \theta) \quad (\text{A.28})$$

where

$$\underline{k} = k(\cos\theta, \sin\theta) \quad (\text{A.29})$$

and $k(\omega)$ obeys the dispersion relation. Note that the Hermitian symmetry of $\hat{\eta}$ requires that $\tilde{\eta}$ is Hermitian under $(\omega, \theta) \rightarrow (-\omega, \theta + \pi)$. Substituting eq. A.27 into eq. A.26 yields the transformation

$$f(\underline{x}, z, t) = \frac{1}{2\pi} \int F_i(\omega, \theta, z) \tilde{\eta}(\omega, \theta) \exp[i(\underline{k}(\omega, \theta) \cdot \underline{x} - \omega t)] d\omega d\theta \quad (\text{A.30})$$

where

$$F_i(\omega, \theta, z) = F_i(\underline{k}(\omega, \theta), \omega, z) \quad (\text{A.31})$$

The transfer functions F_i ($i = 0, 1, 2, 3, 4$) corresponding to η , u , v , w , and p_w are

$$\begin{aligned} F_0(\omega, \theta, z) &= 1 \\ F_1(\omega, \theta, z) &= \omega \cos(\theta) \frac{\cosh[k(z-h)]}{\sinh[kh]} \\ F_2(\omega, \theta, z) &= \omega \sin(\theta) \frac{\cosh[k(z-h)]}{\sinh[kh]} \\ F_3(\omega, \theta, z) &= -i\omega \frac{\sinh[k(z-h)]}{\sinh[kh]} \\ F_4(\omega, \theta, z) &= \frac{\omega^2 \cosh[k(z-h)]}{k \sinh[kh]} \end{aligned} \quad (\text{A.32})$$

†

The equations just presented for the wave-related variables have been developed

assuming that no mean current exists. If a uniform horizontal current \underline{U} also exists, then eq.s A.3-A.8 are valid in a coordinate system moving with the current if \underline{u} and ϕ are regarded as describing only the wave motion. The solutions given by eq.s A.19-A.25 are also valid in the moving system. The Fourier amplitudes determined by eq.s A.19-A.20 and A.23-A.25 are valid in a fixed system which does not move with the current, as well, if its axes are parallel to those of the moving system and if both systems are contiguous at $t = 0$. However, the dispersion relationship between the wave frequency and the wavenumber is changed in the fixed coordinate system. The transformation from \underline{k}, ω space to real space relative to the fixed system becomes

$$f_i(\underline{x}, z, t) = \frac{1}{(2\pi)^3} \int F_i(\underline{k}, \omega, z) \hat{\eta}(\underline{k}, \omega) \exp[i(\underline{k} \cdot \underline{x} - n t)] d^2 k d\omega \quad (\text{A.32})$$

where the frequency n in the fixed system is a function of the fundamental frequency ω (the wave frequency in the system at rest with respect to the fluid), the wavenumber, and the current velocity \underline{U} by

$$n(\underline{k}, \omega, \underline{U}) = \omega + \underline{k} \cdot \underline{U} = \omega + k U \cos(\theta - \theta_u) \quad (\text{A.33})$$

The angles θ and θ_u are the directions of \underline{k} and \underline{U} relative to the x-axis of the fixed coordinate system. Because ω and k still must obey the fundamental dispersion relationship (eq. A.22), the integral in eq. A.32 can be reduced from three dimensions to two as was done to obtain eq. A.29.

Thus, with a current present, the observed frequency n of a wave will depend on its direction of travel relative to the current as well as its wavelength. The observed dispersion relationship is $n = n(\underline{k}(\omega, \theta), \omega, \underline{U})$. An example of the dependence of n on k for $|\underline{U}| = 2$ m/s is shown in fig. A-1. The dependence shown actually corresponds to the intersection of the observed dispersion curve and the plane in \underline{k}, n - space which contains the n -axis and the wavenumbers parallel to \underline{U} . The $k > 0$ axis corresponds to $\theta - \theta_u = 0$; the $k < 0$ axis corresponds to $\theta - \theta_u = \pi$. The fundamental dispersion curve (eq. A.22 or eq. A.32 for $|\underline{U}| = 0$) is also shown in the figure. One important feature of the fundamental dispersion curve is that, for a given θ , the relationship between k and ω is 1:1. When the current is not zero, two values of k , and thus two values of ω , may correspond to the same value of n .

Consequently, the wavenumber magnitude k and ω are double-valued functions of n when the direction of wave propagation has a component aligned against the current. If c_{gu} denotes the wave group speed component anti-parallel to the current, but relative to still water, then the maximum observed frequency n_m corresponds to the fundamental frequency ω_m for which $c_{gu} = U$. Values of ω larger than ω_m yield decreasing values of n . If c_u denotes the phase speed equivalent to c_{gu} , then n is negative for values of ω which yield $c_u < U$. This corresponds to a change in the direction of wave propagation: the waves appear to have a wavenumber component in the direction of the current, rather than opposite the current.

The occurrence of this phenomena is related to the decrease in wave phase speed with increasing ω and is stroboscopic in nature. The number of crests per unit time passing a fixed position, i.e. the observed frequency in hertz, for waves traveling directly against the current is $(c-U)/L = (1-U/c)(c/L)$, where L is the wavelength and c is the phase speed relative to still water. Waves with small fundamental frequencies have large phase speeds relative to the current. The ratio U/c is small and consequently the observed wave frequency is not affected much by the adverse current. For high frequency waves, however, the phase speed is smaller and U/c is larger. The waves are carried back by the current a much larger fraction of their wavelength per unit time than are the low frequency waves. Thus the number of crests passing a fixed position per unit time is much smaller, proportionately, for the high frequency waves than for the low frequency waves. The high frequency waves are thus observed to have a much smaller frequency than would be the case if no current were present. In fact, as noted above, for $c < U$ the waves appear to move backwards, i.e. *in* the direction of the current. As will be discussed in the next section, this could complicate the signal processing required to estimate the waveheight spectrum from measured data.

A.2 Linear Wave Spectrum Relationships

The general transform relationships in eq.s A.29 or A.32, presented in the previous section, are strictly valid only for deterministic Fourier amplitudes $\hat{\eta}(\mathbf{k}, \omega)$. Ocean surface waves are almost always random, in the sense that the physical observables associated with the waves may be regarded as random processes (Kinsman, 1984). To consider random waves, one must generalize the transform equations to describe η and the other wave-related variables as random processes in space and time. Further, what is of interest is not a

particular realization of this set of random processes. Rather, it is the statistics which underlie these processes which are important. Thus, while a generalization of eq.s A.29 and A.32 for wave-related random processes is presented, a statistical characterization of these processes is immediately developed and the characterization of any particular realization will be ignored.

The generalization to eq.s A.29 and A.32 for spatially and temporally stationary random processes is

$$f_i(\underline{x}, z, t) = \frac{1}{2\pi} \int F_i(\omega, \theta, z) dB_\eta(\omega, \theta) \exp[i(\underline{k}(\omega, \theta) \cdot \underline{x} - n(\omega, \theta, \underline{U}) t)] \quad (\text{A.34})$$

The integral in eq. A.34 is to be interpreted as a probabilistic Riemann-Stieltjes integral where $dB_\eta(\omega, \theta)$ is a normally distributed complex random variable with independent increments. The stochastic weights $dB_\eta(\omega, \theta)$ have zero mean, are independent for different values of (ω, θ) , and the variance at a particular value of (ω, θ) is proportional to the wave spectrum, i.e. the real-valued, nonnegative function $S(\omega, \theta)$. The relationship between $dB_\eta(\omega, \theta)$ and the wave spectrum $S(\omega, \theta)$ can be expressed as

$$\begin{aligned} \langle dB_\eta(\omega, \theta) \rangle &= 0 \\ \langle dB_\eta(\omega, \theta) dB_\eta(\omega', \theta') \rangle &= 2\pi S(\omega, \theta) \delta(\omega - \omega') \delta(\theta - \theta' + \pi) d\omega d\theta d\omega' d\theta' \\ \langle dB_\eta(\omega, \theta) dB_\eta^*(\omega', \theta') \rangle &= 2\pi S(\omega, \theta) \delta(\omega - \omega') \delta(\theta - \theta') d\omega d\theta d\omega' d\theta' \end{aligned} \quad (\text{A.35})$$

For *in situ* instrument arrays, the frequency cross-spectra of different sensors estimated from time series measurements constitute the principal "data" which spectral analysis techniques use to estimate the waveheight spectrum S . It will be shown that the cross-spectra for the wave observables have a simple canonical form.

The temporal cross-covariance of two zero mean wave-related quantities f_i and f_j at spatial positions \underline{x}_1, z_1 and \underline{x}_2, z_2 respectively can be expressed as

$$\begin{aligned} R_{ij}(\tau; \underline{x}_1, z_1, \underline{x}_2, z_2) &= \langle f_i(\underline{x}_1, z_1, t + \tau) f_j(\underline{x}_2, z_2, t) \rangle \\ &= \frac{1}{(2\pi)^2} \int [F_i(\omega, \theta, z_1) F_j^*(\omega', \theta', z_2)] \langle dB_\eta(\omega, \theta) dB_\eta^*(\omega', \theta') \rangle \\ &\quad \times \exp\{i[\underline{k} \cdot \underline{x}_1 - \underline{k}' \cdot \underline{x}_2 - (n[t + \tau] - n't)]\} \end{aligned} \quad (\text{A.36})$$

Using Eq. A.35 above and integrating over the primed quantities, the expression for the cross-correlation becomes

$$R_y(\tau; \underline{x}_1, z_1, \underline{x}_2, z_2, t) = \frac{1}{2\pi} \int d\omega d\theta [F_i(\omega, \theta, z_1) F_j^*(\omega, \theta, z_2)] S(\omega, \theta) \times \exp\{i [\underline{k} \cdot (\underline{x}_1 - \underline{x}_2) - n\tau]\} \quad (\text{A.37})$$

The frequency cross-spectra is the Fourier transform of the temporal cross-covariance and can be expressed as

$$C_y(n'; \underline{x}_1, z_1, \underline{x}_2, z_2) = \int d\tau R_y(\tau; \underline{x}_1, z_1, \underline{x}_2, z_2) e^{-in'\tau} \quad (\text{A.38})$$

Substituting eq. A.37 into eq. A.38 and evaluating the integral over τ , one obtains

$$C_y(n'; \underline{x}_1, z_1, \underline{x}_2, z_2) = \int d\omega d\theta \delta[n' - n(\omega, \theta, \underline{U})] [F_i(\omega, \theta, z_1) F_j^*(\omega, \theta, z_2)] \times S(\omega, \theta) \exp\{i [\underline{k}(\omega, \theta) \cdot (\underline{x}_1 - \underline{x}_2)]\} \quad (\text{A.39})$$

If $|\underline{U}| = 0$, then $n = \omega$, eq. A.39 can be integrated over ω , and the frequency cross-spectra can be written as

$$C_y(n' = \omega; \underline{x}_1, z_1, \underline{x}_2, z_2) = \int d\theta [F_i(\omega, \theta, z_1) F_j^*(\omega, \theta, z_2)] S(\omega, \theta) \times \exp\{i [\underline{k}(\omega, \theta) \cdot (\underline{x}_1 - \underline{x}_2)]\} \quad (\text{A.40})$$

or more generally

$$C_y(\omega; \underline{x}_1, z_1, \underline{x}_2, z_2) = \int d\theta g_i(\omega, \theta; \underline{x}_1, z_1) g_j^*(\omega, \theta; \underline{x}_2, z_2) S(\omega, \theta) \quad (\text{A.41})$$

where, in this case

$$g_i(\omega, \theta; \underline{x}, z) = F_i(\omega, \theta, z) e^{i\underline{k}(\omega, \theta) \cdot \underline{x}} \quad (\text{A.42})$$

This is a quite general form for the relation between the cross spectra of measurements and the underlying directional spectrum. It is shown in section 3 that the cross-spectra of the ADCP measurements can be cast into an identical form, but with a more complicated expression for the functions g_i .

As discussed in section A.1, when a uniform current is present ($|\underline{U}| \neq 0$), the observed wave frequency n may correspond to two values of the fundamental frequency ω . The δ -

function in eq. A.39 is thus possibly non-zero at two values of ω for a given θ . If we label these values as $|\omega_1| < |\omega_2|$, then integrating eq. A.39 over ω yields the equivalent expression to eq. A.40 for the case of waves on a uniform current \underline{U} :

$$C_{yy}(n'; \underline{x}_1, z_1, \underline{x}_2, z_2) = \sum_{m=1}^2 \int d\theta [F_i(\omega_m, \theta, z_1) F_j^*(\omega_m, \theta, z_2)] S_\eta(\omega_m, \theta) \times \exp\{i [\underline{k}(\omega_m, \theta) \cdot (\underline{x}_1 - \underline{x}_2)]\} \quad (\text{A.43})$$

The "canonical" form for the cross-spectra, eq. A.42, can thus be generalized to the case where a uniform current is present. In this case, the "canonical" form becomes

$$C_{yy}(n'; \underline{x}_1, z_1, \underline{x}_2, z_2) = \sum_{m=1}^2 \int d\theta g_i(\omega_m, \theta; \underline{x}_1, z_1) g_j^*(\omega_m, \theta; \underline{x}_2, z_2) S_\eta(\omega_m, \theta) \quad (\text{A.44})$$

The spectral analysis of eq. A.43 or A.44 is complicated beyond that of eq. A.40, when no current is present, because waves with different wavelengths now correspond to the same observed frequency. For *in situ* instrument arrays, the waveheight spectrum estimation problem comes down to estimating the spectrum $S(\omega, \theta)$ from a finite number of measured cross-spectra and integral relations based on eq. A.41 or eq. A.44.

Many of the concepts familiar from spectral analysis of time series data apply to the space-time data of wave measurements as well. Among these concepts are resolution and statistical stability. In analogy with time series analysis, and given certain constraints on the noise introduced by the measurement process, the expectation value of the estimated directional spectrum can be viewed as a "smeared" version of the true spectrum in which closely spaced features of the true spectrum may not be resolved.

The resolution of the spectral estimate is fundamentally linked to the space-time sampling geometry. In general, the resolution can be improved by increasing the number of "lags" $\{\tau_j, \tau_j\}$ at which the cross covariances in eq. A.38 can be estimated. It can also be improved or degraded to some extent by the estimation approach used. Because the space-time wave data is stochastic, however, the estimate of the spectrum will contain statistical fluctuations. These fluctuations can be reduced, and statistical stability improved, by increasing the number of samples which are included in the averaging process which determines the cross covariance at any given lag. If data can only be collected at a finite number of space-time points, this implies a tradeoff between resolution and stability. Stability is improved by choosing a sampling geometry which has many redundant sample

separations (at the expense of having fewer lags), whereas resolution is maximized by choosing a sampling geometry which has many lags (at the expense of having few samples with the same separation).

In situ instrument arrays can only provide information on the cross covariances of the physical observables at a finite number of lags $\{\tau_j\}$. Good temporal sampling is obtained fairly inexpensively by designing instruments which have adequate sampling rates and large data storage capacity. Adequate sampling rates are required to avoid aliasing wave energy from high frequencies to low frequencies. Large data storage capacity is required so that long time series can be collected to improve the frequency resolution of the WF spectra and the statistical stability of the covariance estimates. The temporal sampling for *in situ* arrays is usually adequate to meet these requirements.

However, the spatial sampling of these arrays is extremely sparse. Spatial sampling can be improved only by adding additional instruments to the array. This is an expensive proposition due not only to the cost of the instruments themselves but also due to the cost of deploying and maintaining each instrument. Fortunately the dispersion relation lessens the requirements on instrument separation to avoid spatially aliasing wave energy. Additionally, statistical stability may be improved by improving temporal, rather than spatial, sampling redundancy. Directional resolution, however, will be limited by the number and type of instruments deployed, by the geometry in which they are deployed, and by the spectral estimation approach used to estimate the WF spectrum.

APPENDIX B: ADCP ORIENTATION

The formalism for incorporating the ADCP pitch, roll, and heading information into the directional spectra estimation algorithms is discussed in this appendix.

Two fundamental cartesian coordinate systems are used in the ADCP directional spectra algorithms. The first will be referred to as the wave coordinate system (WCS); the second will be referred to as the ADCP coordinate system (ACS). The WCS (fig. B-1) is a "natural" coordinate system for expressing wave properties: the z -axis is antiparallel to gravity (i.e. vertical), $z = 0$ is the mean sea surface, and the x -axis is parallel to the onshore-directed shore-normal vector (e.g. fig. 4-2). The ACS (fig. B-2) is a "natural" coordinate system in which to express the ADCP beam orientation and bin/beam positions (see fig. 3-1): the z -axis points "up" from the ADCP transducers so that each beam is inclined 30° from it, $z = 0$ is defined at the (imaginary) intersection of the ADCP beams, and the x -axis is located in the plane formed by the z -axis and beam 1. If the ADCP were deployed with zero pitch and roll and with beam 1 directed onshore parallel to the shore normal, then the two coordinate systems would differ simply by the vertical distance δD between the imaginary point of beam intersection and the mean sea surface. With nonzero pitch and roll, and with beam 1 not directed onshore along the shore normal, the transformation of an orientation vector $\underline{\Phi}$ from the ACS to the WCS can be expressed mathematically as

$$\underline{\Phi}_W = T_{W \leftarrow A} \underline{\Phi}_A \quad (\text{B.1})$$

where the subscript on $\underline{\Phi}$ denotes the coordinate system the vector is expressed in and $T_{W \leftarrow A}$ is a rotation matrix. The transformation for a position vector \underline{P} from the ACS to the WCS can be expressed mathematically as

$$\underline{P}_W = T_{W \leftarrow A} \underline{P}_A + \delta D \underline{z}_W \quad (\text{B.2})$$

where \underline{z}_W is a unit vector along the WCS z -axis. The rotation matrix $T_{W \leftarrow A}$ can be expressed as the product of three intermediate transformation matrices:

$$T_{W \rightarrow A} = \begin{pmatrix} \cos(\gamma) & -\sin(\gamma) & 0 \\ \sin(\gamma) & \cos(\gamma) & 0 \\ 0 & 0 & 1 \end{pmatrix} \begin{pmatrix} 1 & 0 & 0 \\ 0 & \cos(\theta) & -\sin(\theta) \\ 0 & \sin(\theta) & \cos(\theta) \end{pmatrix} \begin{pmatrix} \cos(\phi) & 0 & \sin(\phi) \\ 0 & 1 & 0 \\ -\sin(\phi) & 0 & \cos(\phi) \end{pmatrix} \quad (\text{B.3})$$

The angles γ , θ , and ϕ are related to the mean ADCP pitch, roll, and heading angles (P, R, H) by

$$\begin{aligned} \gamma &= -H + C \\ \theta &= \tan^{-1} \left(\frac{\sin(P)}{\cos(P)/\cos(R)} \right) \\ \phi &= R \end{aligned} \quad (\text{B.4})$$

where C is the angle between the onshore-directed shore normal and magnetic east (H is assumed to be uncorrected for magnetic deviation and $H = 0$ implies that the ACS x -axis points due magnetic east). For the deployment in this experiment, C was -190° .

The orientation vector $\underline{\Phi}_j$ for the j th beam, relative to the ADCP coordinate system is given by

$$\underline{\Phi}_{j,A} = \begin{pmatrix} \cos(\alpha'_j) \sin(\beta') \\ \sin(\alpha'_j) \sin(\beta') \\ \cos(\beta') \end{pmatrix} \quad (\text{B.5})$$

where α'_j is 0° ($j = 1$), 180° ($j = 2$), 90° ($j = 3$), or -90° ($j = 4$) and $\beta' = 30^\circ$. The beam orientation vectors $\underline{\Phi}_{j,W}$ relative to the wave coordinate system are computed via eq.s B.1, B.3, and B.4. The beam orientation angles α_j , β_j in the WCS, i.e. the angles used in the transfer functions given in eq.s 3.14 and 5.5, are computed for beam j using

$$\begin{aligned} \alpha &= \tan^{-1} \{ (\Phi_{j,W})_2 / (\Phi_{j,W})_1 \} \\ \beta &= \cos^{-1} \{ (\Phi_{j,W})_3 \} \end{aligned} \quad (\text{B.6})$$

The position $\underline{P}_{j,k}$ of the midpoint of bin k on beam j in the ACS is given by

$$\underline{P}_{j,k,A} = \frac{(k \delta z + \Delta b + \Delta r)}{\cos(\beta)} \underline{\Phi}_{j,A} \quad (\text{B.7})$$

where δz is the vertical rangebin spacing, Δb is the vertical blanking distance, and Δr is the distance along the ACS z -axis from the origin to the transducers. In this study, Δr is set to

zero. The position vector \underline{x}_z used in the transfer functions, corresponding to a bin/beam pair, is in the WCS and is given by applying eq.s B-2,3 to eq. B-7.

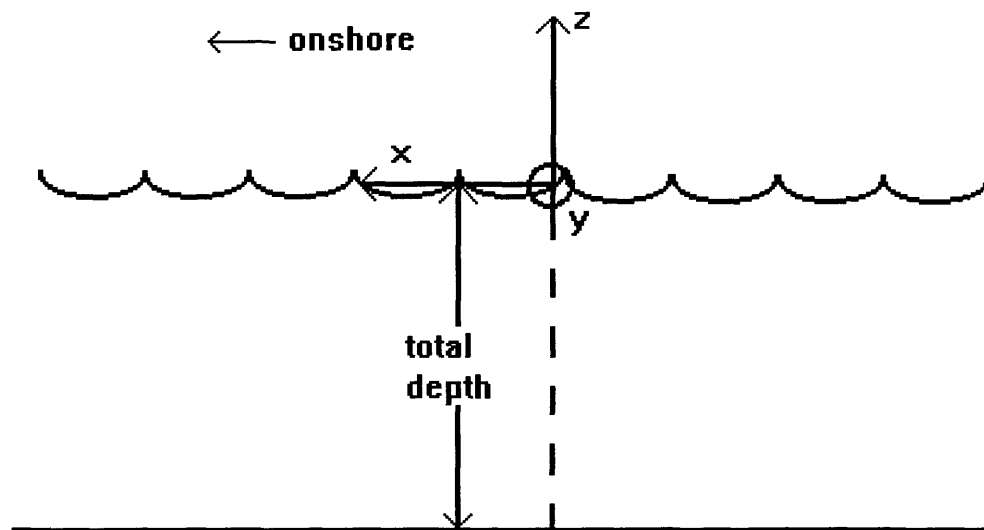


Figure B-1 Wave coordinate system (WCS) definition.

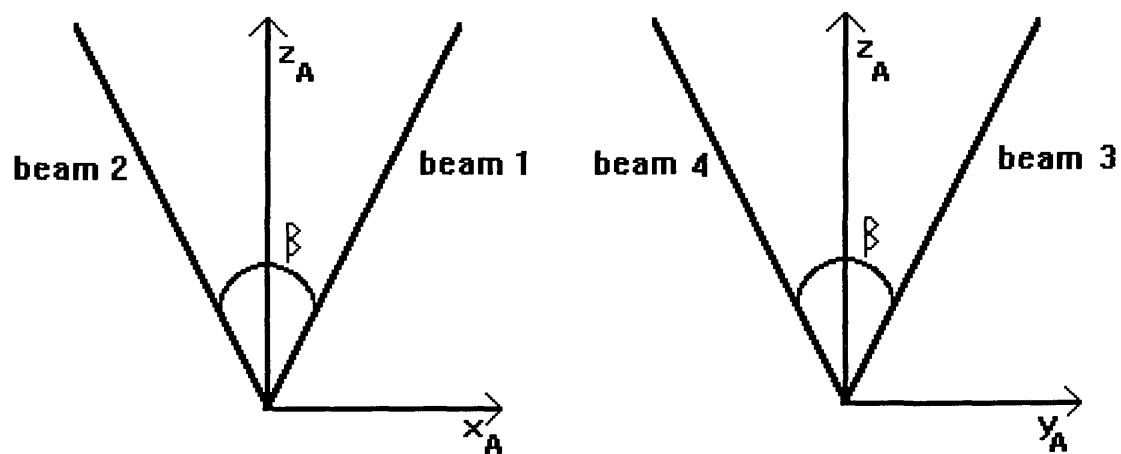


Figure B-2 Beam orientation in ADCP coordinate system (ACS).

LITERATURE CITED

- Apel, J.R., 1987: Principles of Ocean Physics, Academic Press, San Diego CA, 1987.
- Allender, J., T. Audunson, S.F. Barstow, S. Bjerken, H.E. Krogstad, P. Steinbakke, L. Vartdal, L.E. Borgman and C. Graham, 1989: The WADIC project: A comprehensive field evaluation of directional wave instrumentation, Ocean Engineering, **16**(5/6), pp. 505-536, 1989.
- Backus, G.E. and J.F. Gilbert, 1967: Numerical Applications of a formalism for geophysical inverse problems, Geophys. J. Roy. Astr. Soc., **13**, pp. 247-276, 1967.
- Barber, N.F., 1954: Finding the direction of travel of sea waves, Nature, **174**, pp. 1048-1050, 1954.
- Barber, N.F., 1963: The directional resolving power of an array of wave detectors, Ocean Wave Spectra, Prentice-Hall, Englewood Cliffs, NJ, pp.137-150, 1963.
- Boon, J.D., S.M. Kimball, K.D. Suh, and D.A. Hepworth, 1990: Chesapeake Bay Wave Climate Thimble Shoals Wave Station, Report and Summary of Wave Observations Sept. 27, 1988 through Oct. 17, 1989, VIMS Data Report #32, 1990.
- Borgman, L.E., 1979: Directional wave spectra from wave sensors, in Ocean Wave Climate, Earle, M.D. and A. Malahoff ed.s, pp. 269-299, 1979.
- Brubaker, J.M. and J.H. Simpson, 1988: Observations of circulation near a density front in a partially stratified estuary (abstract), EOS, **69**(44), p. 1256 Nov. 1, 1988.
- Burg, J.P., 1967: Maximum entropy spectral analysis, 37th Ann. Intern. Meeting. Soc. Explor. Geophys., Oklahoma City OK, 1967.
- Capon, J., R.J. Greenfield, and R.J. Kolker, 1967: Multidimensional maximum-likelihood processing of a large aperture seismic array, Proc. IEEE, **55**(2), pp. 192-211, 1967.
- Capon, J., 1969: High resolution frequency-wavenumber spectrum analysis, Proc. IEEE,

- 57(8), pp. 1408-1418, 1969.
- Cartwright, D.E., 1963: The use of directional spectra in studying the output of a wave recorder on a moving ship, in Ocean Wave Spectra, pp. 111-136, Prentice-Hall, Englewood Cliffs, N.J., 1963.
- Cartwright, D.E. and N.D. Smith, 1964: Buoy techniques for obtaining directional wave spectra, Buoy Technology, Washington DC, Mar. Technol. Soc., pp. 112-121.
- Constable, S.C., R.L. Parker and C.G. Constable, 1987: Occam's inversion: a practical algorithm for generating smooth models from electro-magnetic sounding data, Geophysics, 52(3), pp. 289-300, 1987.
- Davis, R.E. and L.A. Regier, 1977: Methods for estimating wave spectra from multi-element arrays, J. Mar. Res., 35(3), pp. 453-477, 1977.
- DeLeonibus, 1963: Power spectra of surface wave heights estimated from recordings made from a submerged hovering submarine, in Ocean Wave Spectra, pp. 111-136, Prentice-Hall, Englewood Cliffs, N.J., 1963.
- Earle and Bishop, 1984: A practical Guide to Ocean Wave Measurement and Analysis, Endeco, Inc., Marion MA, 1984.
- Grosskopf, W.G., D.G. Aubrey, M.G. Mattie, and M. Mathiesen, 1983: Field intercomparison of nearshore directional wave sensors, IEEE J. of Ocean Eng., OE-8(4), pp. 254-271, Oct. 1983.
- Guza, R.T., M.C. Clifton and F. Rezvani, 1988: Field intercomparisons of electromagnetic current meters, JGR, 93(C2), pp. 9302-9314.
- Haykin, S. and S. Kessler, 1983: Prediction-error filtering, in Nonlinear Methods of Spectral Analysis, S. Haykin ed., Springer-Verlag, New York NY, pp. 9-72, 1983.
- Herbers, T.H.C. and R.T. Guza, 1990: Estimation of directional wave spectra from multi-component observations, J. of Physical Oceanography, 20, pp. 1703-1724, Nov. 1990.
- Herbers, T.H.C., R.L. Lowe, and R.T. Guza, 1991: Field verification of acoustic Doppler surface gravity wave measurements, JGR, 96, C9, pp. 17023-17035, 1991.

- Higgins, A.L., R.J. Seymour, and S.S. Pawka, 1981: A compact representation of ocean wave directionality, Applied Ocean Research, **3**, pp. 105-112, 1981.
- Isobe M., K. Kondo and M. Horikawa, 1984: Extension of MLM for estimating directional wave spectra, Proc. symp. on Description and Modelling of Directional Seas, Lyngby, Denmark, no. A6, 1984.
- Jeffreys, E.R., G.T. Wareham, N.A. Ramsden and M.J. Platt, 1981: Measuring directional wave spectra with the MLM, Proc. Directional Wave Spectra Applications, Berkeley CA, ASCE, pp. 203-218, 1981.
- Jenkins, G.M. and D.G. Watts, 1968: Spectral Analysis and its Applications, Holden-Day, San Francisco CA, 1968.
- Kinsman, B., 1984: Wind Waves, Dover Publications, Inc., New York NY, 1984.
- Krogstad, H.E., R.L. Gordon, and M.C. Miller, 1988: High-resolution directional wave spectra from horizontally mounted acoustic doppler current meters, J. Atmos. and Oceanic Tech., **5**, pp. 340-352, 1988.
- Long, R.B. and K. Hasselman, 1979: A variational technique for extracting wave spectra from multi-component wave data, J. of Physical Oceanography, **9**, pp. 373-381, Mar. 1979.
- Long, R.B., 1980: The statistical evaluation of directional spectrum estimates derived from pitch/roll buoy data, J. of Physical Oceanography, **10**(6), pp. 944-952, 1980.
- Long R.B., 1986: Inverse modelling in ocean wave studies, Wave Dynamics and Radio Probing of the Ocean Surface, Phillips, O.M. and K. Hasselman ed.s, Plenum Press, New York, 1986.
- Longuet-Higgins, M.S., D.E. Cartwright, and N.D. Smith, 1963: Observations of the directional spectrum of sea waves using motions of a floating buoy, in Ocean Wave Spectra, pp. 111-136, Prentice-Hall, Englewood Cliffs, N.J., 1963.
- Lygre, A. and H.E. Krogstad, 1986: Maximum entropy estimates of the directional distribution in ocean wave spectra, J. Phys. Oceanography, **16**(12), pp. 2052-2060, 1986.

- McDonough, R.N., 1983: Application of the maximum-likelihood method and the maximum-entropy method to array processing, in Nonlinear Methods of Spectral Analysis, S. Haykin ed., Springer-Verlag, New York NY, pp. 181-244, 1983.
- Miller, K.S. and M.M. Rochwarger, 1972: A covariance approach to spectral moment estimation, IEEE Trans. Inform. Theory, **IT-18**(5), pp. 588-596, 1972.
- Mitsuyasu, H., F. Tasai, T. Suhara, S. Mizuno, M. Ohkuso, T. Honda, and K. Rikishi, 1975: Observations of the directional spectrum of ocean waves using a cloverleaf buoy, J. Phys. Oceanography, **5**, pp. 750-758, 1975.
- Mobarek, I.E., 1965: Directional spectra of laboratory wind waves, ASCE J. Waterways and Harbors, **3**, pp. 90-115, Aug. 1965.
- Nagata, Y., 1964: The statistical properties of orbital wave motions and their application for the measurement of directional wave spectra, J. Oceanogr. Soc. Japan, **19**, pp. 169-181, 1964.
- Oltman-Shay, J. and R.T. Guza, 1984: A data-adaptive ocean wave directional-spectrum estimator for pitch and roll type measurements, J. Phys. Oceanography, **14**, pp. 1800-1810, 1984.
- Pawka, S.S., 1983: Island shadows in wave directional spectra, JGR, **88**, C4, pp. 2579-2591, 1983.
- Pettigrew, N.R., R.C. Beardsley and J.D. Irish, 1986: Field evaluations of a bottom-mounted acoustic Doppler profiler and conventional current meter moorings, in Proc. of IEEE Third Working Conference on Current Measurement, G.F. Appell and W.E. Woodward, ed.s, IEEE, New York, 1986.
- Phillips, O.M., 1966: The Dynamics of the Upper Ocean, Cambridge University Press, London, 1966.
- Pinkel, R. and J.A. Smith, 1987: Open ocean surface wave measurement using Doppler Sonar, JGR, **92**, C12, pp. 12967-12973, 1987.
- Provost, C. and R. Salmon, 1986: A variational method for inverting hydrographic data, J. Mar. Res., **44**, pp. 1-34, 1986.

- RD Instruments, 1989a: Phase I SBIR Report: Measuring the Direction Spectrum of Ocean Waves using Doppler Sonar, RD Instruments, San Diego CA, 1989.
- RD Instruments, 1989b: Acoustic Doppler Current Profilers Principles of Operation: A Practical Primer, RD Instruments, San Diego CA, 1989.
- RD Instruments, 1991: Direct-Reading Acoustic Doppler Profiler (DR-ADCP) Technical Manual, RD Instruments, San Diego CA, 1991.
- Regier, L.A. and R.E. Davis, 1977: Observations of the power and directional spectrum of oceanic surface waves, J. Mar. Res., **35**(3), pp. 433-452, 1977.
- Rummler, W.D., 1968: Introduction of a new estimator for velocity spectral parameters, Bell Telephone Labs, Whippany NJ, Tech. Memo. MM-68-4121-15.
- Schott, F. and W. Johns, 1987: Half-year-long measurements with a buoy-mounted acoustic Doppler current profiler in the Somali current, JGR, **92**, C4, pp.5169-5176, 1987.
- Seymour, R.J. and A.L. Higgins, 1977: A slope array for measuring wave direction, Proc. Workshop on Coastal Processes Instrumentation, La Jolla, University of California, San Diego, Sea Grant Publ. No. 62, IMR Ref. No. 78-102, pp.133-142, 1977.
- Seymour, R.J., L.E. Borgman, W.L. Edge, V. Goldsmith, D.H. Harris, O.T. Magoon, D.T. Resio, and R.P. Savage, 1979: Nearshore Wave Measurements, in Ocean Wave Climate, M.D. Earle and A. Malahoff ed.s, pp. 269-299, 1979.
- Simpson, J.H., 1969: Observations of the directional characteristics of sea waves, Geophys. J. Roy. Astron. Soc., **17**, pp.93-120, 1969.
- Smith, J.A., R. Pinkel and R.A. Weller, 1987: Velocity structure in the mixed layer during MILDEX, J. Phys. Ocean., **17**(4), pp.425-439, 1987.
- Smith, J.A., 1989: Doppler Sonar and surface waves: range and resolution, J. Atmos. and Oceanic Tech., **6**, pp. 680-696, 1989.
- Terray, E.A., H.E. Krogstad, R. Cabrera, R.L. Gordon and A. Lohrmann, 1990: Measuring wave direction using upward-looking Doppler sonar, in Proc. of IEEE Fourth Working Conference on Current Measurement, G. Appell and T. Curtin, ed.s, IEEE, New York, 1992.

Therault, K.B., 1986: Incoherent multibeam Doppler current profiler performance, part 1: estimate variance, IEEE J. Ocean Eng., **OE-11(1)**, pp. 7-15, 1986.

VITA

Born at Ft. Belvoir, VA on March 3, 1960.

Graduated from West Springfield High School in Springfield, VA in 1978.

Graduated Summa Cum Laude from James Madison University in Harrisonburg, VA in 1982 with B.S. degrees in Physics and Mathematics.

Earned a M.S. degree in Physics from the University of California, Davis in 1984.

Worked for XonTech, Inc., Van Nuys, CA from 1984 to 1990.

Entered Master's program at VIMS in August, 1990.